THE UNIVERSITY OF LEEDS

Waveguide-Based Antenna Arrays in Multi-Chip Module Technology

by

Lukui Jin

Submitted in accordance with the requirements for the
degree of Doctor of Philosophy

in the
Faculty of Engineering
School of Electronic and Electrical Engineering

January 2014

The candidate confirms that the work submitted is his/her own, except where work which has formed part of jointly authored publications has been included. The contribution of the candidate and the other authors to this work has been explicitly indicated below. The candidate confirms that appropriate credit has been given within the thesis where reference has been made to the work of others.

The work in Chapter 1 of the thesis has appeared in publication as follows:

Lukui Jin, Razak M. Lee and Ian D. Robertson, Study of system in package technology for 60 GHz wireless transceivers, Millimeter wave technologies for gigabit per second wireless communications, 2012 IET seminar on , 11 Sept. 2012.

I was responsible for the literature survey on antennas and the text about 60 GHz antenna-in-package techniques. The other authors contributed the fabrication literature survey and write up.

The work in Chapter 4 of the thesis has appeared in publication as follows:

Jin, Lukui; Lee, Razak M.; Robertson, Ian D.; , Design and performance of log-periodic substrate integrated waveguide slot antennas, Microwave symposium Digest (MTT), 2012 IEEE MTT-S International , pp.1-3, 17-22 June 2012.

I designed and modelled a log-periodic antenna based on SIW in ordinary PCB technology. Razak fabricated it and we measured the antenna together under Ian's supervision.

The work in Chapter 5 of the thesis has appeared in publication as follows:

Jin, Lukui; Lee, Razak M.; Robertson, Ian D.; , Modelling of a Double-sided Dielectric Resonator Antenna Array Fed from Dielectric Insular Image Guide, Antennas and Propagation Conference (LAPC), 2012 Loughborough , 12-13 Nov. 2012.

I was responsible for the design and modelling of a novel DIIG antenna array, while Razak fabricated it using a novel LTCC technology under Ian's supervision.

“The artist is nothing without the gift, but the gift is nothing without work.”

Emile Zola (1840-1902)

THE UNIVERSITY OF LEEDS

Abstract

Faculty of Engineering
School of Electronic and Electrical Engineering

Doctor of Philosophy

by Lukui Jin

For mm-waves, two types of low-loss waveguide are analysed, designed and measured. One is the hollow substrate integrated waveguide (HSIW) in which the inner dielectric of a traditional substrate integrated waveguide (SIW) is removed to resemble the propagation characteristics of a standard rectangular waveguide (RWG). The measured attenuation of a WR28-like HSIW is 2 Np/m or 17 dB/m throughout the Ka band. The second is the dielectric insular image guide (DIIG) in which an insular layer is added between the dielectric and the metallic ground to further reduce the conductor loss. The measured attenuation of a Ka band DIIG is 26 dB/m at 35 GHz.

Based on the two waveguides, two high-gain antenna arrays operating in the Ka band are designed and measured. One is a 6 × 6 slot antenna array, centre-fed by the HSIW. The Taylor-distribution technique is applied in two orthogonal directions to suppress the sidelobe level. The measured gain of this antenna array is 17.1 dBi at the centre frequency of 35.5 GHz. The other is a double-sided 10-element dielectric insular resonator antenna (DIRA) array, end-fed by the DIIG. The Taylor-distribution technique is also applied here to achieve a gain of 15.8 dBi at the centre frequency of 36 GHz.

The great potential of these high-performance antennas is that they can be integrated with other microwave components (filters, power amplifiers, *etc.*) to form a complete front-end or transceiver in multi-chip module (MCM) technology.

Acknowledgements

The process of my Ph.D. study has been a long journey that brings about profound changes on myself and I do believe that will keep influencing me and eventually become an essential part of my life. There are so many people who helped me to make this come true, and I would like to take this opportunity to express my deepest gratitude to them.

First and foremost, I would like to give thanks to my supervisor, Prof. Ian D. Robertson for his insightful guidance and continuous support, without which I could not have gained so much. Prof. Robertson's wisdom and expertise has always inspired me in my research and will greatly benefit my future career.

Also, big thanks is given to Razak Lee, my colleague and teammate. We have been working together through all the odds and difficulties to come to today. Life is not easy, but without him, it would be worse.

I would also like to thank Prof. Qun Wu who introduced me into the field of microwave and mm-wave, his broad knowledge provides me a foundation of research, and his continuous support encourages me to move forwards.

I greatly appreciate Prof. Roger Pollard and Mr. Rolland Clarke for their selfish help on providing me with the essential measurement equipments, which is necessary for the completion of my thesis.

I gratefully acknowledge the funding I have received from Leeds University for financially supporting my research and life in Leeds. The name of this scholarship is FIRS (Fully-funded International Research Scholarship) which is a rare funding opportunity for international students. I do hope Leeds University and the UK government can increase the investment on the research funding so that more and more overseas students can come to study here fulfilling their dreams.

Acknowledgment should also go to members at IMP, especially the colleagues in my office. I greatly enjoy the discussions with you, both on research and on everyday life. You make my work life joyful and colorful. I would also like to thank Miss Louise Redmonds at IMP for providing clerical help.

I would like to thank my flatmates and friends from the Chinese community who make my life at Leeds so unforgettable.

Last but not the least, I would like to express my gratitude to my family and my girlfriend. Their continuous support is the source of everything I have gained, which I shall ever remember and treasure. It will be a great honor to invite them to come to my graduation ceremony and I will make them proud.

Contents

List of Figures

List of Tables

Abbreviations

DIG	**D**ielectric **I**mage **G**uide
DIIG	**D**ielectric **I**nsular **R**esonator **A**ntenna
DIRA	**D**ielectric **I**nsular **R**esonator **A**ntenna
DG	**D**ielectric **G**uide
DR	**D**ielectric **R**esonator
DRA	**D**ielectric **R**esonator **A**ntenna
HSIW	**H**ollow **S**ubstrate **I**ntegrated **W**aveguide
LTCC	**L**ow **T**emperature **C**ofired **C**eramic
MCM	**M**ulti-Chip **M**odule
PCB	**P**rinted **C**ircuit **B**oard
RWG	**R**ectangular **W**ave **G**uide
SIC	**S**ubstrate **I**ntegrated **C**ircuit
SIW	**S**ubstrate **I**ntegrated **W**aveguide
WLAN	**W**ireless **L**ocal **A**rea **N**etwork
WPAN	**W**ireless **P**ersonal **A**rea **N**etwork

Dedicated to my beloved family and girlfriend for their constant support and unconditional love. . . .

Chapter 1

Introduction

This chapter is organised as follows: Section 1.1 reviews the start and development of modern wireless communication in terms of the long-range cellular radio, medium-range wireless local area network (WLAN) and short-range wireless personal area network (WPAN). After that, Section 1.2 summarises three mm-wave on-chip technologies especially for the antenna applications, *i.e.*, semiconductor, printed circuit board (PCB) and low temperature co-fired ceramics (LTCC) technologies. A comparison is given among the three technologies in terms of performance, cost, yield, *etc.* Finally, a full transceiver system which integrates antennas and other active and passive components is also reviewed on the same technologies in Section 1.3.

1.1 A Short Review of Wireless Communication

In wireless communications, the ever increasing demand for a higher data rate and network capacity has always been a challenge for electronic engineers; it will be explicitly explained and profoundly proved after a look back at the history of cellular radio, WLAN and WPAN which have become indispensable elements in our daily life nowadays.

1.1.1 Evolution of Cellular Radio

As early as in the early 1940s, the concept of cellular radio was conceived by Bell Labs. After a period of mild progress, not until 1979 did the world see the first cellular radio system called MCS (Mobile Control Station) available to the mass market in Japan. Since then, the cellular radio era began and soon dominated the mobile communication. Transmitting analog signals by FM (Frequency Modulation), MCS provided radio coverage by seamless overlapping cells in the configuration of a honeycomb, which was employed by the following generations of cellular radios. Later on, some European countries and the United States developed their own cellular radio systems, such as TACS (Total Access Communication System), AMPS (Advanced Mobile Phone System), *etc.*, which were all commercially deployed but not compatible with each other. With an unexpected surge of subscribers in the early 1990s, the first-generation (1G) cellular radio system suffered severe congestion for insufficient frequency channels. Why did this happen? Take AMPS of the United States as an example: In AMPS systems, voice signals were modulated by FM with a transmission bandwidth of 30kHz and thus the whole channel was occupied by one subscriber. So within a certain frequency band, the number of channels was quite limited. Then, frequency reuse was introduced in a nearby cell cluster to boost the spectral efficiency and thus system capacity. However, since the FM signal needs a high SIR (Signal-to-Interference Ratio) (SIR = 18dB) to maintain the quality of service, the frequency reuse factor (the size of a cell cluster) could not be too small (K = 7). So the reuse efficiency was low and so was the improvement on spectral efficiency [1, 2].

A change from analog to digital operation brought about the 2G cellular radio system which included: the global system for mobile communication (GSM) in Europe, two digital-AMPS systems, D-AMPS TDMA (Time Division Multiple Access) and CDMA (Code Division Multiple Access), in the United States, and two personal digital cellular systems (PDC 800 and PDC 1500) in Japan. Take the upgraded version of AMPS, D-AMPS, as an example: Based on hybrid FDMA (Frequency Division Multiple Access)/TDMA or hybrid FDMA/CDMA, the same 30kHz bandwidth was divided into three timeslots to accommodate three channels of the digitised signal compared with one analog channel in the AMPS system. So the total number of voice channels in D-AMPS was increased by three times. Apart from that, the required SIR was reduced to less than 13 dB due to the digitisation and error correction coding and so is the frequency reuse factor. As a result, the spectral efficiency and thus system capacity was enhanced substantially. From another perspective, the congestion in mobile communications might not easily deteriorate, provided more spectrum resources could be allocated [1, 2].

As time passed by, instead of just voice exchange, people were more and more looking at a multimedia service and Internet access in mobile communications as they usually did in front of a computer screen. It could not be satisfied with the low data rate (*e.g.* 9.6 kbps for GSM) of the 2G scheme which was meant for voice, SMS (Short Messaging Service) and limited wireless data service. From mid-1990s, over the existing 2G systems that operated on the existing 2G spectrum only, some technology enhancements were developed, namely 2.5G, such as High-speed circuit-switched data (HSCSD, 64 kbps in circuit-switched mode), General packet radio service (GPRS, 115 kbps in packet-switched mode), Enhanced data rates for GSM evolution (EDGE, up to 384 kbps in wide-area applications and up to 554 kbps in local areas). In 1996, the International Telecommunication Union (ITU) presented a concept for a third-generation (3G) International Mobile Telecommunication System dubbed IMT-2000 and requested its members to submit respective proposals. After a lengthy discussion and debate, a consensus was reached that a new standard called Universal mobile telecommunications system (UMTS), with North Americans maintaining their own CDMA2000, which was established based on wideband CDMA (W-CDMA). As a result of the IMT-2000 consensus, UMTS provided broadband voice and data transmission in a frequency-division duplex (FDD) mode for large areas with a data rate up to 384 kbps, and in a time-division duplex (TDD) mode in areas with heavy traffic with speeds up to 2 Mbps [1–4].

This was, by no means, the end of the pursuit of a high data transmission in wireless communications. In March 2008, the Radio communications sector of ITU (ITU-R) specified a set of requirements for 4G standards, named the International Mobile Telecommunications Advanced (IMT-Advanced) specification, setting a peak speed for 4G service at 100 Mbps for mobile access and 1 Gbps for nomadic wireless access. At that time, there were two 4G candidate systems commercially deployed: The Mobile WiMAX standard (at first in South Korea in 2006), and the first-release Long Term Evolution (LTE) standard (in Scandinavia since 2009). They are recognised as “4G” by ITU-R, albeit they were not completely compliant to IMT-Advanced standard for a much lower bit rate. Yet, their enhanced versions, Mobile WiMAX Release 2 and LTE Advanced (LTE-A), fulfilled the requirements of IMT-Advanced and was deployed and operated in 2013. Possible applications include IP telephony, gaming services, high-definition mobile TV, video conferencing, *etc.* [3, 4].

In May 2013 (just a couple of months before the finalisation of this thesis), Samsung made an announcement of a technology breakthrough which might enable

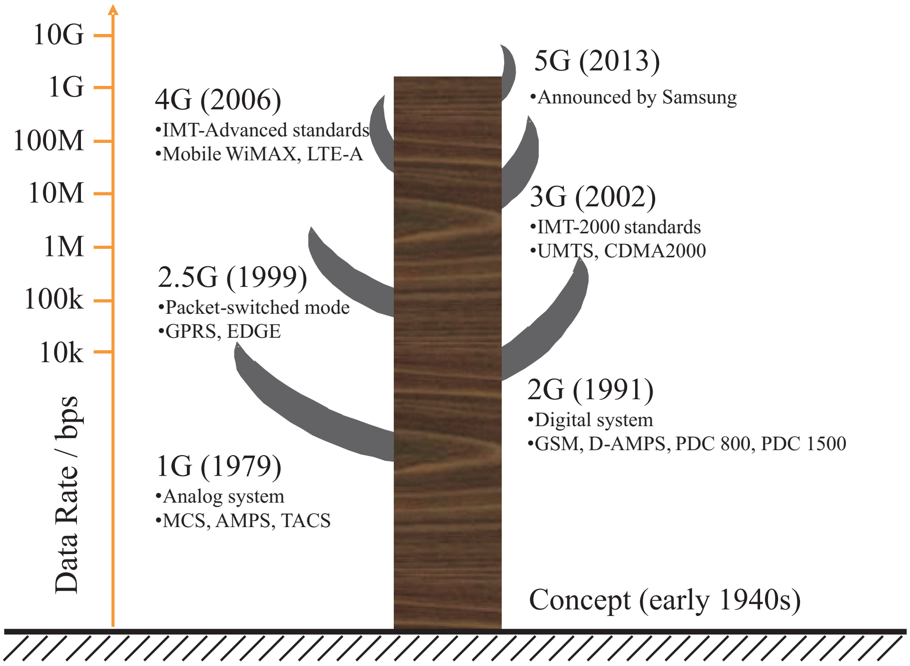

FIGURE 1.1: The evolution tree of the cellular radio.

the realisation of 5G mobile communication. This adaptive array transceiver technology used 64 antenna elements, along with signal-processing technology, to concentrate radio signals in a narrow, directional beam, thereby increasing received signal power without requiring more transmission power. The operating frequency was 28 GHz (Ka band) with a data rate of up to 1.056 Gbps to a distance of up to 2 kilometers. To take the pre-emptive moves, Samsung has made a plan to commercialise these technologies by 2020 [5–7].

The brief history of cellular radio can be summarised in Fig. 1.1, which clearly shows the trend of the ever growing data rate. Taking into account the evolution from the previous generation to the next one, how to enhance the spectral efficiency and thus the system capacity within a limited frequency band is also key to keeping a cellular system competitive in the industry of mobile communications.

1.1.2 IEEE Standards for WLAN

While cellular radio completely dominates the long-range wireless mobile communications, the WLAN has found itself hardly challenged when it comes to the short-range (within a company, university, house, *etc.*) data communications, which enables people to gain network access anytime anywhere. The idea of WLAN derived from a “wireless Ethernet” which was to sustain connectivity where wiring proved difficult to support wired LANs (Ethernet). Also, the allocation of the unlicensed 2.4 GHz industrial, scientific and medical (ISM) and Unlicensed National Information Infrastructure (U-NII) radio band by the Federal Communications Commission (FCC) facilitated the fast development of WLANs. As expected, the problem of incompatibility arises on the interfaces between WLANs and existing wired LANs and also in the wireless devices between different vendors. In order to provide interoperability, a universal communication standard was called for. The IEEE Standards Association (IEEE-SA), as one of the world's leading standards-makers, started a working group named IEEE 802.11 to work on the first wireless data communications standard in 1990 and introduced the first IEEE 802.11 standard in 1997. Later, amendments, supplements and enhancements of IEEE 802.11 were made to cope with the ever-growing demands for high data rate and other ever-emerging problems [2, 8–10].

Table. 1.1 summarises the IEEE 802.11 standard and its variants. There are five variants specifying the speed of the data transmission and bandwidth and a tendency toward a higher data rate and wider bandwidth is clearly indicated. As the newest variant of IEEE 802.11, the 802.11ac Draft 2.0 specification was just released in February 2012; it effectively supports more client devices and multiple HD (High Definition) video streams simultaneously with a peak data rate of 6.93 Gbps. A possible improvement to this standard is the working frequency. If it can be moved up to a higher ISM band, the data rate could be increased even further [11, 12].

1.1.3 IEEE Standards for WPAN

The WPAN is a short-range network centred on an individual person with wireless connection and communication among his/her personal electronic devices: cellular phones, digital cameras, music players, *etc*. The fast growing market of these small and inexpensive devices promotes the development of WPAN, just as that of laptops does to WLAN. There are similarities between WPAN and WLAN, such as they both belong to the family of short-range wireless mobile communication technologies, which could be the basis for their competition against each other. Differences, however, are also quite obvious, as illustrated in Table. 1.2 [9, 14].

The first WPAN technology, Bluetooth, was originally developed by Ericsson in 1994 and its development is now managed by the Bluetooth Special Interest Group (SIG). The driving force behind this is that some cell phone manufacturers wanted

Table 1.1: IEEE 802.11 and its variants [8–13]

Standard	Description
802.11	Specify a physical layer for the 2.4 GHz ISM band, 1 and 2 Mbps with a 20 MHz bandwidth
802.11a	Amendments to the physical layer for the 5 GHz U-NII band, 6 - 54 Mbps with a 20 MHz bandwidth
802.11b	Enhancements to the physical layer for the 2.4 GHz ISM band, 5.5 and 11 Mbps with a 20 MHz bandwidth
802.11c	Supplements to cover Media Access Control (MAC) bridge operation
802.11d	supplements to the MAC layer to promote greater worldwide use of WLANs
802.11e	Enhancements to the MAC layer for Quality of Service (QoS) support
802.11f	Interaccess point protocol in a multivendor environment
802.11g	Enhancements to the physical layer for the 2.4 GHz ISM band, 6 - 54 Mbps with a 20 MHz bandwidth
802.11h	Enhancements of spectrum and power management to the MAC layer of 802.11a
802.11i	Enhancements of security to the MAC layer
802.11j	Enhancements to 802.11a for operation in 4.9-5.0 GHz in Japan
802.11k	Radio resource management
802.11m	Technical corrections and clarifications
802.11n	High-throughput enhancements to the physical layer, 100 - 600 Mbps with a 20 or 40 MHz bandwidth
802.11r	A method for minimizing the terminal transfer from one access point (AP) to another
802.11ac	Enhancements to the physical layer of 802.11a for the 5 GHz U-NII band, 6.93 Gbps with a 160 MHz bandwidth

Table 1.2: Differences between WLAN and WPAN [9]

Aspects	WLAN	WPAN
Communication mode	Central access point (AP)	peer-to-peer connections or ad-hoc networks
Power consumption	High power consumption (on wall sockets or short battery operation)	Low power consumption (long battery operation)
Coverage	100 m with a transmit power of 100 mW and about 500 m for 1 W	about 10 m with transmitted power of about 1 mW
Power consumption	High power consumption (on wall sockets or short battery operation)	Low power consumption (long battery operation)
Control of the media	The mechanism for access to the medium must handle potential collisions (CSMNCA in IEEE 802.11)	The medium access protocol can be less tight
Lifespan of the networks	Constant existence independent of their constituent devices	Spontaneously created and lasting only for as long as needed

Table 1.3: The IEEE 802.15 standards [9, 14]

Standard	Description
802.15.1	Amendments to Bluetooth v.1.1
802.15.1a	Amendments to Bluetooth v.1.2
802.15.2	Recommended practice for WPAN to coexist with other systems
802.15.3	High-speed WPAN for the 2.4 GHz ISM band
802.15.3a	Amendments to the physical layer of 802.15.3 for the UWB band
802.15.4	Low-speed WPAN for the 2.4 GHz ISM band
802.15.4a	Enhancements to the physical layer of 802.15.4

make their products capable of wirelessly communicating with devices other than phones and thus increase the value. Working only as a cable replacement, Bluetooth wasn't after a high data rate (using the 2.4 GHz ISM band with a theoretical capacity up to 1 Mbps). Formed in July 1999, the IEEE 802.15 working group took Bluetooth into account and started to work on its own standards for WPAN. Table. 1.3 summarises the IEEE 802.15 standards, among which IEEE 802.15.3 was written to address a specific class of applications that did not have a wireless standard. Some of the applications were in response to the call for applications (CFA) sent out by 802.15.3, such as connecting digital still cameras to printers or kiosks, video camera display on a television, *etc.* For those applications, high throughput is the most demanding requirement, a typical data rate of greater than 20 Mbps. IEEE 802.11a/b/g seems to be capable of fulfilling that requirement, just from the standing point of data rate. The ability of low power consumption and ad hoc connectivity, however, deters 802.11 in a great deal. So the 802.15.3 group took advantage of that and recently began to work on a new physical layer 802.15.3a, providing a data rate over 100 Mbps, and up to 480 Mbps. This new standard will be based on ultra-wide band (UWB) technology, which is a 7500 MHz wide (3100-10600 MHz) band with an average radiated emission limit of -41.3 dBm/MHz released in February 2002 by the FCC. Suppose 802.15.3 could use a higher unlicensed band (e.g. 60 GHz), the data rate and bandwidth utilisation could be enhanced even more [8, 9, 15].

1.1.4 Conclusion

Take a look at the frequency bands already exploited for wireless mobile communications: 450/900/1800/1900/2100 MHz for cellular radio, the 2.4 GHz ISM band

and 5 GHz U-NII band for WLAN and WPAN. A common feature is that they are all in relatively low bands, whereas a higher frequency means a higher data rate, wider absolute bandwidth and smaller device size.

So, the mm-wave band (30 $\sim$ 300 GHz) is attracting more and more research interest nowadays, such as the Ka-band used for high-date-rate cellular communications (spotted by Samsung very recently) and the unlicensed 60 GHz band for short-range high-capacity WPANs.

Challenges and opportunities always go hand in hand when it comes to exploring new frontiers. Some cheap and simple technologies, such as PCB, are widely and maturely used in low frequencies. How to move it up to mm-wave band and maintain existing performances needs to be resolved. Some semiconductor processing technologies, such as gallium arsenide (GaAs) and silicon germanium (SiGe), should be no problem dealing with mm-wave antennas and other components. However, how to reduce the cost and make it available to the mass market is a big issue. Apart from those, the LTCC technology has been added to the shortlist capable of mm-wave processing. With its moderate cost and complexity, it seems quite promising in the mm-wave front-end technologies. All these technologies and their current research state will be elaborated in the following sections.

1.2 Mm-Wave Antenna Technology

Antennas play an important role in a radio system, as they are at the front end working as an interface between the designed systems and the radio channel. However, they always seem to be an obstacle to compact radio systems, as it is relatively bulky and hard to be incorporated into the system package. So it would be a huge step forward for system integrity if research on antenna in package (AiP), which would create complete system in package (SiP), could be finally proved successful [16]. The following section will focus on this key design factor.

This section is organised as follows: Section 1.2.1 illustrates a brief history and state of the art of the semiconductor technologies, among which a comparison is made when they are applied in mm-wave communications. Section 1.2.2 looks back at a brief history of the PCB technology with an overview of its applications in mm-wave antennas nowadays. After that, it's LTCC technology in Section 1.2.3. Finally, in the conclusion section, antenna performances implemented with different technologies are summarised and compared.

1.2.1 Semiconductor Technology

There is no doubt that semiconductors have changed and shaped our life beyond the wildest imagination. Although it's hard to trace back to the very origin of semiconductors and people may take a somewhat different viewpoint, there are some significant observations and discoveries on different materials contributing to the eventual invention of semiconductor devices: negative temperature coefficient of resistance (by Michael Faraday in 1833), photoconductivity ((by Becquerel in 1839)), rectification (by F. Braun and A. Schuster in 1874), photoelectromotive force (by W. G. Adams and R. E. Day in 1876), and the demonstration of the existence of electromagnetic waves (by H. Hertz in 1888). The sudden emerge of the vacuum tube, however, disturbed and delayed the progress of semiconductors (point contact detectors of radio waves at that time) until the 1920s. By the 1940s, substantial theoretical work has been developed, such as the theory of electrons in lattices, the theory of thermionic emission, models of the potential barrier and current flow through a metal-semiconductor junction, *etc.* Based on that, a lot of essential semiconductors, such as the p-n junction (by Russel Ohl), the bipolar transistor (by John Bardeen and Walter Brattain in 1947) *etc.* have been invented and soon put into industry production [17–20].

1.2.1.1 Mm-Wave Applications

Previously, III-V technologies, mostly based on GaAs and InP, were considered as the only suitable candidates to implement mm-wave systems. Only recently, Si-based technologies, such as SiGe HBT and Si CMOS technology, have emerged as strong contenders for mm-wave applications. III-V technologies are highly favoured for their high operation speed which is vital for fast-speed mm-wave systems. As the indicator of operation speed, the highest cutoff frequency f_T of two leading III-V technologies, HBT and HEMT, is 765 GHz and 610 GHz, respectively, much higher than all kinds of Si-based technologies (485 GHz for Si CMOS). Another favourable advantage of III-V technologies is the high resistivity of the substrates which can reduce transmission line loss and increase the Q-factor of passive devices. Despite these advantages, the relatively low reliability (resulting in potential non-planar structures and exposing active regions of devices) and high cost hamper its dominance in semiconductor technologies for mm-wave applications. In contrast, the Si-based technologies are growing fast with its low cost and high reliability. Also it is by far the most prevailing semiconductor

Table 1.4: Comparison among semiconductor technologies [21, 22]

Aspects	III-V technologies	Si-based technologies
Leading technologies	III-V HBT, III-V HEMT	SiGe HBT, Si CMOS
Substrate compounds	GaAs, InP, GaN, ... (25 in total)	SiGe, SiC, SiN, ...
f_T	765 GHz (HBT), 610 GHz (HEMT)	350 GHz (HBT), 485 GHz (CMOS)
Advantages	High operation speed and high substrate resistivity	Smooth monolithic integration without wire/flip-chip bonding and highly developed design environment to improve design efficiency and accuracy
Disadvantages	High cost and low reliability caused by non-planar structures and low thermal conductivity	Low operation speed

technology, which implies that the existing chip design procedure can be reused for mm-wave applications. Yet, there is still room for the operation speed to be improved [21, 22]. A detailed comparison is listed in Table. 1.4.

1.2.1.2 Mm-Wave Active Integrated Antennas

An active integrated antenna array together with a down-converter working at 39 GHz was successfully analyzed and made by R. Carrillo-Ramirez *et al.* in 2004. Using a silicon/BCB (benzocyclobutene) packaging technique, it is fabricated at a relatively-low cost, although it does introduce some additional loss and results in a low radiation efficiency[23]. Then at 60 GHz, Y. Zhang *et al.* presented on-chip inverted-F and quasi-Yagi antennas based on an improved Si CMOS technology in 2005. The same problem occurs with these two antennas as the radiation efficiency for the inverted-F antenna is only 3.5% and that for the quasi-Yagi antenna (through simulation) is 5.6%. Two reasons are accounted for this poor performance: a low resistivity (10 Ω·cm) silicon substrate is employed which results in a high transmission line loss; a long conductor line on top of the substrate is exposed to the air which contributes more to the whole loss in the mm-wave band [24].

Based on the semiconductor technology, researchers have been putting much effort in the improvement of the mm-wave antenna's radiation efficiency. M. Barakat *et al.* proposed a 60 GHz interdigitated dipole antenna on a high resistivity (> 1000 Ω·cm) silicon substrate utilising 0.13 μm CMOS SOI (silicon on insulator) technology in 2010. With a gain extraction method to mitigate the disturbs brought in by the V-connector, the radiation efficiency is calculated as 80%. However, one year later, they came up with a double slot antenna fabricated and measured with the same technology which exhibits an efficiency of only 20% [25, 26]. So it seems that their work still needs to be validated with further solid research. Another effort has been made by E. Herth *et al.* who employs a thick high-resistivity GaAs substrate for the feeding and wet-etched a cavity around the patch antenna. Another difference is that the radiating patch is on a low-dielectric glass substrate bonded with the GaAs substrate using benzocyclobutene (BCB) adhesive. As a result, the antenna is integrated inside the package and the simulated radiation efficiency has been improved up to 60%, although the bandwidth seems a bit narrower [27]. A similar cavity is built underneath the patch antenna by A. Adane *et al.* in [28] to maintain a high radiation efficiency, while a T-microstrip feeder is employed to increase the bandwidth up to 20%. Their later work features a reconfigurable patch antenna array on Si/BCB membrane with RF MEMS phase shifters for beamforming applications at 60 GHz [29]. Another high gain and broadband antenna is reported in [30] by B. Pan *et al.* as a CPW-fed horn antenna integrated on a silicon substrate using CMOS-compatible microfabrication steps. The dielectric (silicon) in the horn is etched away leaving an air cavity, which results in a even higher gain of 14.6 dB, flaring only in the H-plane, and the bandwidth is 10%.

It can be found that a high-resistivity, low-permittivity and thick substrate or superstrate with the AiP concept is highly preferred in the 60 GHz antenna design, as it substantially enhances the bandwidth and/or radiation efficiency.

1.2.2 PCB Technology

1.2.2.1 A Brief History

The history of PCB technology begins with a patent filed by Albert Hanson, a German inventor who was working in England, in 1903. The original idea was to replace the bulky point-to-point wiring in electronic components or systems. Although not a true “printed circuit” method, Mr. Hanson did come up with the concept of “conductive patterns laminated on an insulator” and also some concepts that can still be considered as modern PCB principles, such as “double-sided through-hole circuitry”. Over the next few decades, several other ideas were presented with the rise and boom of radios and wireless communication systems. In 1943, a low cost and mass production circuit process, later known as photo etching process, was developed by Paul Eisler in England which, however, didn’t come into widespread use until the 1950s when the transistor was introduced to commercial use to reduce the overall chip size. The through hole technology and its use in multi-layer PCBs were introduced by the U.S. firm Hazeltyne in 1961, which substantially enhanced the density of electrical tracks and electronic components. With the advent of integrated circuit chips in the 1970s, the chip density and complexity of PCBs could be increased to a higher level [31–33].

Through the development over more than 100 years, the PCB has become a cheap, basic and profound technology widely used for consumer electronics. With the 60 GHz band opened up, researchers all over the world are working hard to explore the new frontier and trying to keep in pace.

1.2.2.2 Mm-Wave PCB Antennas

A research group led by K. Wu is renowned for their innovative work on substrate integrated waveguide (SIW) and recently they have applied it to the mm-wave band. Although the microstrip patch antenna have been widely used for its easy fabrication and low cost, it suffers severe loss in the mm-wave band and the radiation efficiency of an array is roughly estimated to be lower than 20% at 60 GHz when a saturated gain of 35 dBi for planar antenna array is reached [34, 35]. So K. Wu *et al.* switched to the waveguide slot antenna which seems to be the least lossy among all planar antennas and presented a range of antenna arrays based on SIW and its variations, such as the half-mode SIW [36] and T-type folded SIW [37], *etc.* Among them, there is a 12 × 12 SIW array on Rogers RT/Duroid 6002 substrate with the standard PCB process. The measured gain is around 22 dBi at 60 GHz and an estimated radiation efficiency of 68% is achieved [38]. A similar 4 × 20 slot array is designed at 35 GHz and the measured gain is also 22 dBi [39]. Then, in order to break the barrier of the 35 dBi saturated gain, they proposed a novel 3D Yagi antenna by stacking the radiating patches on multiple Duroid 5880 layers. A single 4-element antenna and a 4 × 4 array were both fabricated and measured. The result shows that a gain of 18 dBi is attained for the array which could be further improved with more elements. The radiation efficiency is not clearly indicated. With a microstrip line as the feeding structure, however, it's not highly expected [40].

In 2009, another research group led by D. Liu *et al.* shifted their attention from SiGe to PCB technology to combine their previous work in [41] and [42] aiming for a low-cost, high-efficiency and wideband superstrate patch antenna for mm-wave applications. A cross sectional view is shown in Fig. 1.2. This is a multilayer PCB structure with the radiating patch attached on the bottom side of the superstrate. An air cavity is right beneath the patch to enhance the radiation efficiency and

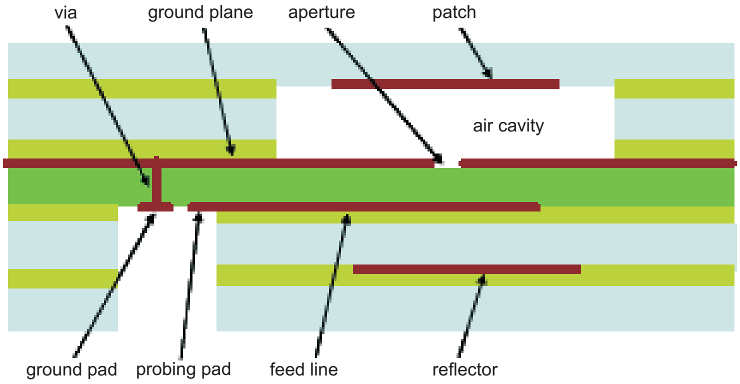

FIGURE 1.2: The cross sectional view of the superstrate patch antenna [43].

impedance bandwidth. The feeding structure is a aperture-coupled slot with a microstrip line underneath. Finally, a probing pad with a transition to the microstrip line feeds the energy in. A bandwidth of more than 15% and a radiation efficiency of more than 90% can be achieved from simulation [43]. Based on this antenna, two years later, they came up with another feeding structure and developed two 16-element circular arrays to achieve a peak gain of 17 dBi. Another interesting part of this design is that the room at the array centre has been reserved for an active RFIC chip, which could be integrated to allow beamforming and thus a reconfigurable antenna [44].

The dielectric resonator antenna (DRA) has been attracting much attention in mm-wave applications for its low loss, wide bandwidth and easy integration. PCB technology can also be applied to implement DRAs, although the permittivity (ϵ_r) of the dielectric resonator is normally higher ($10 \sim 100$) than the PCB materials. In [45], Q. Lai *et al.* present a novel feeding scheme for cylindrical DRAs, the half-mode SIW. A Duroid 5880 substrate is employed together with Duroid TMM10i for the cylinders to achieve a high radiation efficiency between 80% and 92%. A superstrate air cavity is introduced to enhance the gain of the DRA by 10.7 dBi to 16.71 dBi through simulation in [46]. Solid SIW cavities are also seen to help with low loss and high gain in [47].

Despite all the benefits the introduction of an air cavity could bring about, the realisation of it can be challenging and difficult especially when mainstream PCB processing technology is to be used; it will be even more challenging to realise a plastic or multilayer organic (MLO) package enclosing the antenna and the whole system [44]. So on one hand, further improvement should be made on the existing

PCB technology to easily accommodate air cavities without substantially increasing the cost; on the other hand, the search or development of a new technology which can inherently handle this problem should be carried out.

1.2.3 LTCC Technology

1.2.3.1 A Brief History

LTCC technology is a 3D integration technology with multilayered ceramic substrates which is applicable to electronic circuits. Fig. 1.3 shows a standard procedure for LTCC processing. The history of multilayer co-fired ceramic substrate technology dates back to the late 1950s when it was developed at RCA Corporation. Thereafter, this multilayer board, developed by IBM for its commercialized computers in the early 1980s, was co-fired at a high temperature of 1600 °C with low-conductivity high-melting-point materials (Mo, W, Mo-Mn), which was called High Temperature Co-fired Ceramics (HTCC). After that, the demand for conductive materials with low electrical resistance (Cu, Au, Ag) in the wiring process inspired the development of the LTCC technology (in contrast to HTCC), which fires all the materials below 1000 °C (typically 900 °C). By the early 1990s, the collaboration between LTCC tape producers (DuPont, Heraeus and Ferro) and packaging companies (Fujitsu and IBM) accelerated the commercialisation, mainly for mobile communication components. Up to present, the research on LTCC has been keeping pace with the development of high frequency wireless communications for its outstanding merits toward the high frequency band (*e.g.*, the mm-wave band) [48–50].

Here is the list of the unique characteristics which makes LTCC a promising technology for mm-wave applications [51–53]:

- Low thermal coefficient of expansion (TCE), which is close to semiconductors, to achieve high connection reliability in very-large-scale integration (VLSI) systems over a wide temperature span.
- Low loss tangent and hence low dielectric loss in the mm-wave band to give low loss performances.
- Good thermal conductivity, which is much better than organic PCBs and could be further improved with thermal vias, to easily dissipate heat.

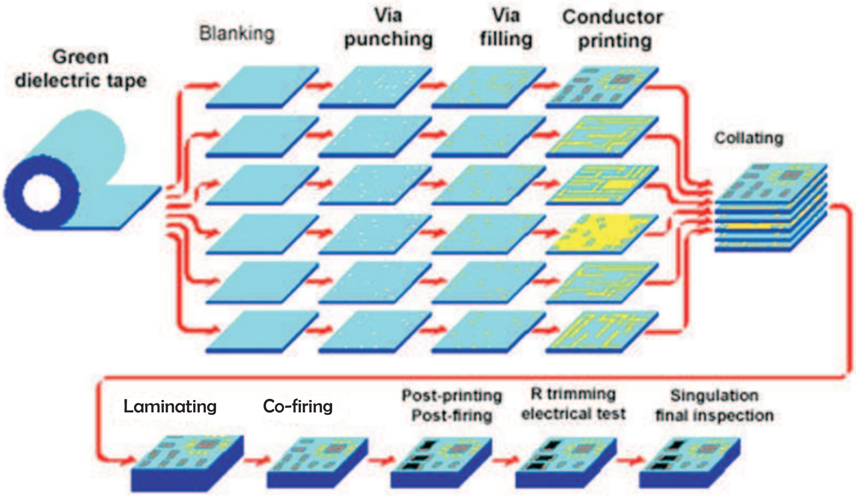

FIGURE 1.3: A standard procedure for LTCC processing [48].

- Easy to be 3D interconnected and packaged based on a multilayered structures.
- Easy to be integrated with various microwave components even of different types of materials.

1.2.3.2 Mm-Wave LTCC Antennas

After an attempt of an extremely low-efficiency on-chip antenna using the semiconductor technology, Y. Zhang *et al.* quickly switched to LTCC technology and came up with the concept of AiP in 2006 [16, 24]. AiP enables the codesign of the antenna, active chip and package at the same time, which makes a compact and efficient system with a low cost and high performance. Fig. 1.4 illustrates a 3D view of the basic AiP structure. Located in the recessed cavity is the active chip connected with the antenna through bond wires. There are also signal traces extending outside to be connected with power sources and other processing units. Finally, ceramic ball grid array (CBGA) technology is used to seal the package. With this novel AiP concept and technology, Y. Zhang *et al.* have successfully incorporated a Yagi antenna [54], a grid array antenna [55] and a triangular radiator [56] into a highly integrated 60 GHz radio system. Although the radiation efficiency of all three antennas is high (at least 85% without the active chip), the wire-bonding technique poses a real challenge and threat to the performance of the whole system as the introduced discontinuity and the thin wire itself could be lossy in the mm-wave band. In order to take advantage of the cheap and robust

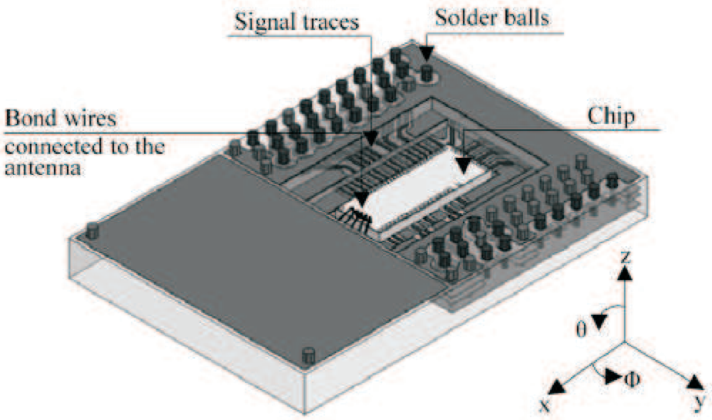

Figure 1.4: A 3D view of the basic AiP structure [54].

wire-bonding technology, a compensation scheme is introduced to minimize the mismatch and the length of the wire is also reduced to some extent in [56].

Apart from the research group led by K. Wu, another group with W. Hong *et al.* has also done some remarkable work on SIW and the collaboration between them is often seen. Recently, however, W. Hong *et al.* have fit their SIW designs into LTCC technology instead of PCB which they have been using for the last few decades. Published in 2011, this paper features a 8 × 8 cavity antenna array fed by a substrate integrated waveguide in the 60 GHz band. A total of 20 LTCC layers are used to achieve a bandwidth of 17.1% and a gain up to 22.1 dBi. The measured radiation efficiency is 44.4%, not as high as expected. The reason is not explained in the paper; yet the transition from WR 15 to SIW has certainly contributed to that [57]. Another high-gain LTCC antenna is demonstrated by A. Lamminen *et al.* who employs chain antenna array with SIW feed network to achieve a gain of 22 dBi at 62 GHz. The simulated radiation efficiency without the transition is 74%, higher than that of [57]; while the actual measured efficiency could be degraded greatly [58]. The highest-gain single-element LTCC antenna ever reported in the 60 GHz band is an improved Vivaldi antenna with a novel stepped dielectric director (SDD). This antenna features a broad bandwidth of 10% and a boresight gain of 10.25 dBi at 60 GHz [59]. While someone is pursuing a higher gain, the other one is looking at a smaller size. In [60], J. Lee *et al.* present a compact V-band front-end solution by integrating cavity filters/duplexers and antennas together. The measured channel-to-channel isolation is better than 49 dB across the RX/TX band. The proposed front-end can easily incorporate an active MMIC to complete a full RF transceiver in the near future.

Within the Easy-A project sponsored by the German Ministry of Education and Research (BMBF), M. Martinez *et al.* have carried out intensive work on mm-wave LTCC technology. Firstly, simulation and experiments are completed on the electrical and mechanical properties of the LTCC substrates, DuPont 943 and 9k7, at 60 GHz as the data is only available at the low frequency band. It is found that the actual permittivity of DuPont 943 at 60 GHz is slightly lower than that specified by DuPont at 40 GHz [61, 62]. With that in mind, they design and demonstrate a balanced-fed 2 × 1 60 GHz antenna array which could be integrated into an RF transceiver for high data rate WLAN systems [63, 64]. [65] presents another 2 × 2 patch array with a stripline-to-waveguide transition which could be integrated with front-end SiGe MMICs to complete a transceiver system. This array also shows good RF performance with a bandwidth of 12.5% and a radiation efficiency of 65%. A 60 GHz SIW fed steerable LTCC cavity antenna array is demonstrated in [66]. To reduce the mismatch at the interface between the SIW cavity and free space, an air cavity is etched to reduce the effective dielectric constant. Also, two passive elements are added at each column of the array to suppress the side lobe level. Finally, a prototype is made and tested. It should be noted, however, that only one column of the array is activated each time and the field superposition method is applied to calculate the far-field radiation pattern, which could be further improved.

1.2.4 Conclusion

Merits and drawbacks exist in all three major technologies. Semiconductor technology comes as the most expensive when it's applied in the mm-wave band; yet the integration level is the highest (24 times that of PCB). With the lowest integration level, PCB technology is cheapest in terms of both material and processing cost and has fulfilled every corner of modern microwave applications. The high TCE (Thermal Coefficient of Expansion) of PCB, however, has really dragged it down. A high TCE leads to thermal-mechanical fatigue defects and changes the mechanical and electrical properties of the board when it goes through thermal cycling or thermal shock. A trade-off is found in LTCC technology which has a moderate TCE, cost and performance and hence, a great potential in future mm-wave applications [67].

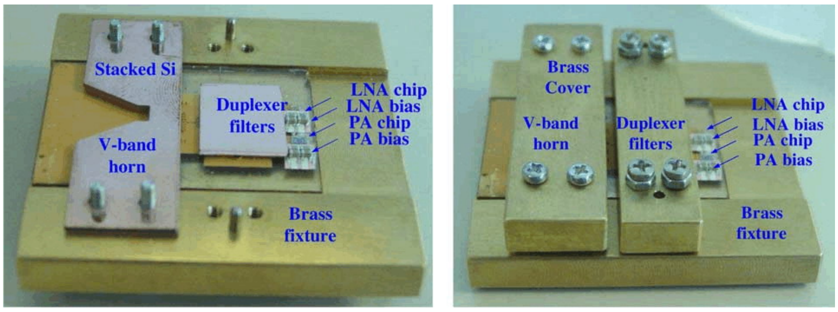

FIGURE 1.5: A 60 GHz transceiver before and after assembled with a brass fixture [71].

1.3 Mm-Wave Transceiver Technology

1.3.1 Semiconductor Transceivers

Utilizing 100 nm InAlAs/InGaAs HEMT technology on GaAs substrate, S. Koch *et al.* have realised and improved an integrated transceiver MIMIC with multiple antenna ports at 60 GHz from 2007 to 2009. There is a RF switch to change signal routes which has evolved from a DPDT, through 2:4, to 2:6 to achieve the capability of multiple bands. The newest version of this MIMIC is 2.5 × 5.5 mm ^{2}, which claims to be the highest integration level for a 60 GHz semiconductor transceiver chip to date [68–70]. With antennas incorporated, however, the transceiver chip will be much larger. Apart from their work on a high gain horn antenna in [30], B. Pan *et al.* also present a 60 GHz transceiver by integrating the horn antenna with a duplexer and active amplifiers as shown in Fig. 1.5. Although the design claims to be substrate-independent, they do use a silicon substrate to implement it. A gain of 14.5 dBi is achieved with a clearly bulky size; the horn itself is 14 × 12 mm^2 [71].

1.3.2 PCB Transceivers

K. Wu and his group demonstrate two single-layered transceiver front-ends with SIW technology in [72] and [73]. In [72], it's a dielectric rod antenna fed by substrate integrated image guide (SIIG) and hybridly integrated with an MMIC low-noise amplifier. The incorporation of a dielectric antenna is aiming at a low loss characteristic, which also inevitably increases the overall size of the system. The same problem emerges in their another design of a smart antenna receiver in [73], which integrates an antenna array, a Butler matrix, a bandpass filter,

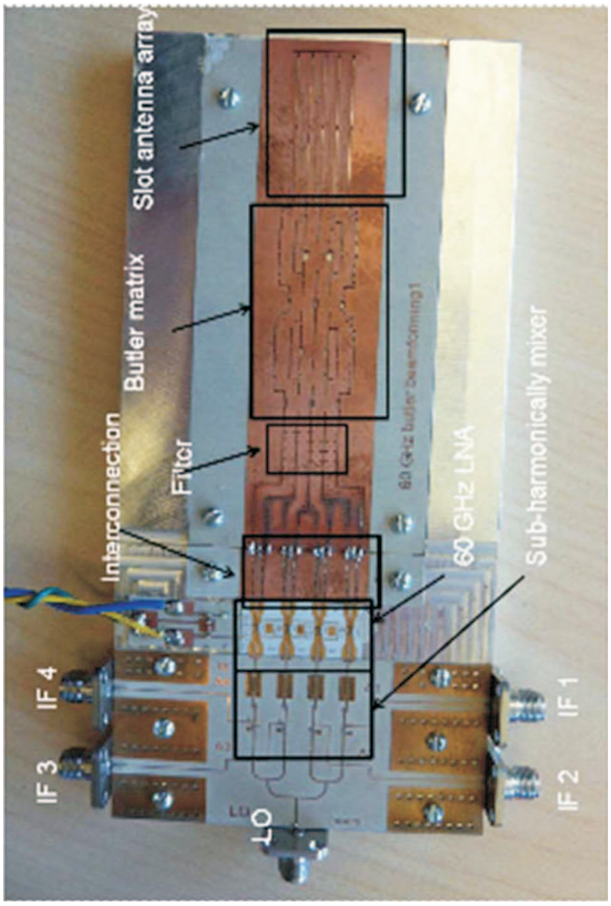

FIGURE 1.6: A 60 GHz receiver using the PCB technology [73].

and other active components in one single PCB layer as shown in Fig. 1.6. The obvious advantage is that it's low cost and easily fabricated; however, the large area it occupies is certainly a huge drawback and hinders its possible application in the space-demanding mm-wave band. A multilayer 60 GHz antenna embedded in a phased-array transmitter or receiver is presented in [74]. The size of the system has been reduced and a high data rate up to 5.3 Gbps using 16-quadrature amplitude modulation single-carrier and orthogonal frequency division multiplexing schemes has also been achieved.

None of the previously-mentioned systems can function as a real transceiver, as they can't transmit or receive signals at the same time. [75] demonstrates a transceiver system by integrating two separate RX/TX antennas into the same board, which could, however, be further improved by incorporating a single antenna and a duplexer as in [30, 60].

1.3.3 LTCC Transceivers

In 2003, K. Kunihiro *et al.* presented a fully integrated LTCC transceiver at 5 GHz suitable for WLAN systems at a data rate up to 54 Mbps. With the help of a high-permittivity LTCC (ϵ_r =17), the whole size of the system can be reduced to 8 × 10 × 1 mm. However, a high dielectric constant could hamper the antenna's radiation and reduces its efficiency [76]. Another similar design for Bluetooth applications with even smaller size was given by Y. Cho in 2008 [77]. Transceivers are also analysed and designed in X band [78] and Ku band [79] and Ka band [80], respectively. The SANTANA project is performed by some German researchers, which aims at electronically steerable antennas to realise multimedia terminals, *i.e.*, a transmitter operating at 30 GHz and a receiver at 20 GHz [81, 82]. One thing to be noted is that the transmitter and receiver are implemented as separated modules and hence no complete transceiver system has been demonstrated by far. When it comes to V band, however, no complete LTCC transceivers have been reported to date. In 2005, Y. Lee *et al.* demonstrated a highly integrated transmitter with a size of 36 × 12 × 0.9 mm^3, which is suitable for high speed multimedia communications, such as WPAN (Wireless Personal Area Network) [83]. Later, still using LTCC, J. Lee *et al.* designed and developed cavity-backed filters and antennas with the capability of integration into a full transceiver system [60, 84]. With the proposal of the AiP concept, Y. Zhang *et al.* have also contributed a lot to V-band LTCC antennas and come up with some models of AiP transmitters. Nevertheless, the final actual prototype still needs to be implemented [54–56].

1.4 Conclusion

After briefly reviewing the history of wireless communication, this chapter draws the conclusion that the operating frequency band should advance higher to the mm-wave band in pursuit of a higher data rate and wider bandwidth. Then, three main-stream technologies to implement mm-wave antennas and transceivers are reviewed and compared to find that the LTCC technology seems to be well-balanced in terms of its cost and performance, although they all have their own advantages and disadvantages.

LTCC technology is employed in this thesis to implement high-gain high-efficiency antenna arrays based on novel low-loss transmission lines (waveguides).

Chapter 2 presents a novel hollow SIW (HSIW) which removes most of the dielectrics inside SIW to achieve a lower loss. Detailed theoretical analysis and computer-aided simulation are provided and compared. Prototypes are also fabricated and measured to verify the concept.

Chapter 3 presents another type of low-loss transmission line, the dielectric insular image guide (DIIG). Detailed theoretical analysis and computer-aided simulation are provided and compared. Prototypes are also fabricated and measured to verify the concept.

Chapter 4 builds on Chapter 2 to present design and measurement of a slot antenna array. Similarly, a DRA antenna array is presented in Chapter 5 based on the DIIG in Chapter 3.

Chapter 6 concludes the whole thesis and gives some advice on the further and future work following this thesis.

Chapter 2

Hollow Substrate Integrated Waveguide

2.1 Introduction

The hollow substrate integrated waveguide (HSIW) proposed here derives from the newly-emerged substrate integrated waveguide (SIW) which is a key part of a general concept of a substrate integrated circuit (SIC). This concept was first introduced by K. Wu *etal.* to unify hybrid and monolithic integrations of various planar and non-planar circuits that are made in single and/or multi-layer substrates [85]. Since RF and millimetre-wave technologies are always searching for something that can bring about easy-fabrication, low-cost, and high-integrity *etc*, the SIC concept is certainly a good candidate.

As mentioned above, SIW is one of the various implementation forms of SICs and the most widely studied and used. In 1998, H. Uchimura *et al.* proposed a novel multilayer waveguide with sidewalls consisting of lined metal posts and named it as “laminated waveguide” [86]. Another similar waveguide was brought up by J. Hirokawa and M. Ando in the same year with the most obvious distinction being that the whole structure was single-layered [87]. That should be the origin of SIW even though it didn’t get its name then. After that, K. Wu *et al.* theoretically analysed SIW, extracted the complex propagation constant of each SIW mode and provided basic design rules in 2002 [88] and 2005 [89]. Then came an application boom for SIW. Antennas [66, 90], filters [91, 92], mixers [93], couplers [94], circulators [95], phase shifters [96], power amplifiers [97], and power dividers [98] have all seen SIW as their vital components.

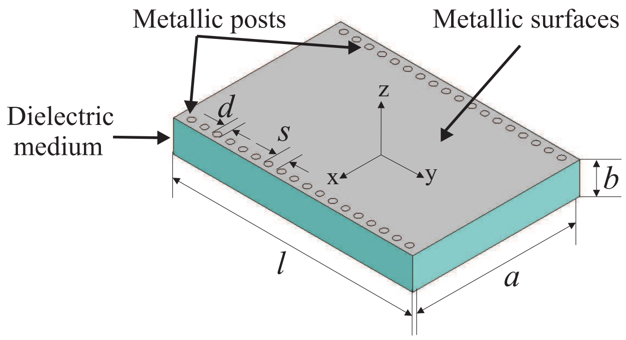

FIGURE 2.1: The 3D view of a standard SIW.

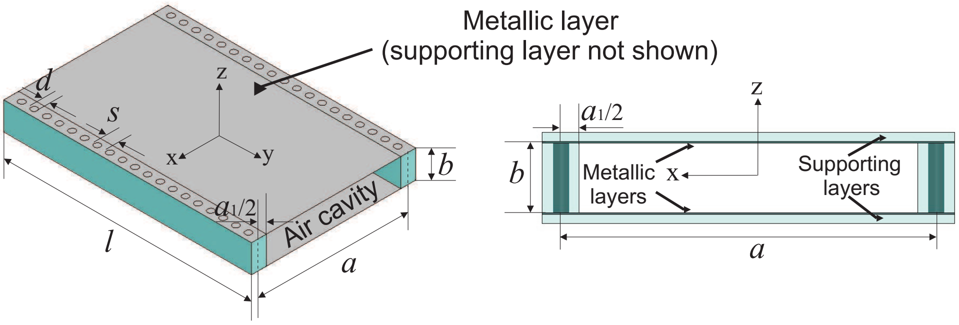

(a) (b)

FIGURE 2.2: (a) 3D and (b) cross-sectional view of the HSIW.

As can be seen in Fig. 2.1, SIW is based on a solid dielectric substrate with two parallel rows of metallic posts (vias) used to replace the side walls of a RWG. Here a novel HSIW is introduced where an air cavity is etched out inside the traditional SIW, as shown in Fig. 2.2(a). By incorporating this hollow cavity, the following advantages are expected:

1) Lower loss due to the removal of most of the lossy dielectric material.

2) The HSIW can be realized with high-permittivity substrates and at higher frequencies, where the size of SIW otherwise tends to be too small to accommodate the vias.

3) The HSIW can be directly connected with normal RWGs, whereas the SIW requires more complicated transitions with potentially more loss.

4) The low permittivity is advantageous for the design of many antennas

After the removal of the inner dielectric material, a supporting layer needs to be added on both top and bottom of the HSIW, which can be seen in Fig. 2.2 (b). To facilitate the fabrication process, the supporting layer can use the same material as the filled dielectric, in our case, LTCC ($\epsilon_r = 7.1$). Apart from that, the metallic vias and layers can use the same conductive material, in our case, silver paste ($\sigma = 3.7e7$).

The theoretical-analysis method of an HSIW is a combination of those of RWG and SIW; therefore, to analyse and design the HSIW (to find the width of the HSIW), two steps need to be followed. Firstly, HSIW is viewed as a two-dielectric loaded RWG. After solving this boundary value problem, the two-dielectric loaded RWG is transformed into a uniformly-filled RWG by introducing the effective dielectric constant (EDC), ϵ_e. Then, by modifying the empirical formula in [89] relating SIW and RWG, the dimension of HSIW can be finally determined. These are reflected in Section 2.2 and 2.3, respectively. In Section 2.4, an HSIW prototype resembling WR28 is also fabricated and measured to verify the theory.

2.2 Two-Dielectric Loaded RWG

This section deals with the boundary value problem of the two-dielectric loaded RWG to determine its width for a prescribed cutoff frequency. Firstly, by combining Maxwell's Equations and boundary conditions, the characteristic equations for both even and odd modes are set up. After analysing possible propagating modes inside the RWG, the TE_{10} mode is found to be fundamental when the height/width ratio, $b/a \leq 0.5$. Then the cutoff frequency of TE_{10} mode is determined through either exact or empirical method. With the introduction of the EDC, ϵ_e, the two-dielectric loaded RWG is redistributed uniformly and the loss characteristics of TE_{10} mode can be immediately obtained through ready formulas in [99]. Finally, the design process for a single-mode dielectric-filled RWG is given.

2.2.1 Characteristic Equations

As shown in Fig. 2.3, a metallic RWG is longitudinally filled with two symmetrical dielectrics and hence, divided into three regions: 1, 2, and 3. a, b stands for the width and height of the two-dielectric loaded RWG, respectively, while the widths of Dielectric 1 and 2 are represented by a_1 and a_2, respectively. Then,

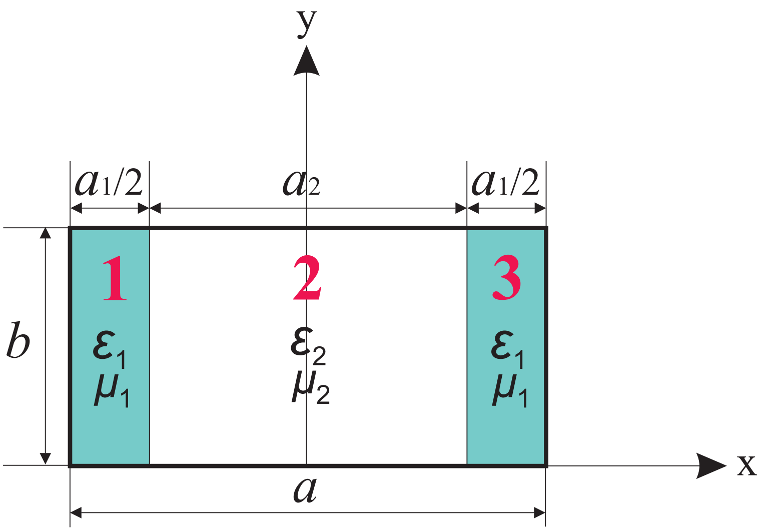

FIGURE 2.3: The cross-sectional view of the dielectric-filled RWG.

assume both dielectrics are linear, isotropic, homogeneous and lossless with a pair of permittivities and permeabilities of ϵ_1, μ_1 and ϵ_2, μ_2, respectively. The metal encompassing the dielectrics is initially assumed to be perfectly electric conductor (PEC), whereas the attenuation due to a finite conductivity can be analysed later by the perturbation method discussed in [99].

Assuming time-harmonic fields with an $e^{j\omega t}$ dependence propagate in the dielectric-loaded RWG shown in Fig. 2.3, the electric and magnetic fields can be expressed as follows:

$$\bar{A}(x, y, z) = [\bar{A}_x(x, y) + \bar{A}_y(x, y) + \bar{A}_z(x, y)]e^{-j\beta z} \tag{2.1}$$

where $\bar{A}$ denotes $\bar{E}$ or $\bar{H}$ and β is the phase constant of the travelling wave.

Since the RWG is source-free, the electric and magnetic fields should also satisfy the Helmholtz's equation:

$$\nabla^2 \bar{A} + k_i^2 \bar{A} = 0, \quad i = 1, 2 \tag{2.2}$$

where $\bar{A}$ denotes $\bar{E}$ or $\bar{H}$ and

$$k_i = \omega\sqrt{\mu_i \epsilon_i} = 2\pi/\lambda_i, \quad i = 1, 2 \tag{2.3}$$

stands for the wavenumber with λ_i as the wavelength in its corresponding dielectric.

Following (2.1) and (2.2), the transverse components of the fields, *i.e.* E_x, E_y, H_x, H_y can be solved in terms of the longitudinal components, *i.e.* E_z, H_z:

$$\begin{aligned}
E_x &= \frac{-j}{k_{ci}^2}\left(\beta\frac{\partial E_z}{\partial x} + \omega\mu\frac{\partial H_z}{\partial y}\right)\\
E_y &= \frac{j}{k_{ci}^2}\left(-\beta\frac{\partial E_z}{\partial y} + \omega\mu\frac{\partial H_z}{\partial x}\right)\\
H_x &= \frac{j}{k_{ci}^2}\left(\omega\epsilon\frac{\partial E_z}{\partial y} - \beta\frac{\partial H_z}{\partial x}\right)\\
H_y &= \frac{-j}{k_{ci}^2}\left(\omega\epsilon\frac{\partial E_z}{\partial x} + \beta\frac{\partial H_z}{\partial y}\right)
\end{aligned} \tag{2.4}$$

where

$$k_{ci}^2 = k_i^2 - \beta^2, \quad i = 1, 2 \tag{2.5}$$

is defined as the cutoff wavenumber in its corresponding dielectric.

Boundary conditions at the PEC walls and dielectric interfaces should also be included to solve this problem, which are as follows:

$$E_x|_{y=0,\,b} = E_y|_{x=\pm a/2} = E_z|_{x=\pm a/2} = E_z|_{y=0,\,b} = 0 \tag{2.6a}$$

$$A_{p1} = A_{p2}|_{x=-a_2/2},\ A_{p2} = A_{p3}|_{x=a_2/2} \tag{2.6b}$$

where A denotes E or H and p denotes y or z.

By applying the method of separation of variables to (2.2) together with boundary conditions at a PEC wall, (2.6a), the longitudinal field components in three different regions, *i.e.* E_{zi}, H_{zi}, $i = 1, 2, 3$, can be derived as follows:

$$\begin{aligned}
E_{z1} &= A_1 \sin\left[k_{x1}(x + a/2)\right] \sin\left(n\pi y/b\right)\\
E_{z2} &= \left[A_2 \cos\left(k_{x2}x\right) + A_4 \sin\left(k_{x2}x\right)\right] \sin\left(n\pi y/b\right)\\
E_{z3} &= A_3 \sin\left[k_{x1}(x - a/2)\right] \sin\left(n\pi y/b\right)\\
H_{z1} &= B_1 \cos\left[k_{x1}(x + a/2)\right] \cos\left(n\pi y/b\right)\\
H_{z2} &= \left[B_2 \cos\left(k_{x2}x\right) + B_4 \sin\left(k_{x2}x\right)\right] \cos\left(n\pi y/b\right)\\
H_{z3} &= B_3 \cos\left[k_{x1}(x - a/2)\right] \cos\left(n\pi y/b\right)
\end{aligned} \tag{2.7}$$

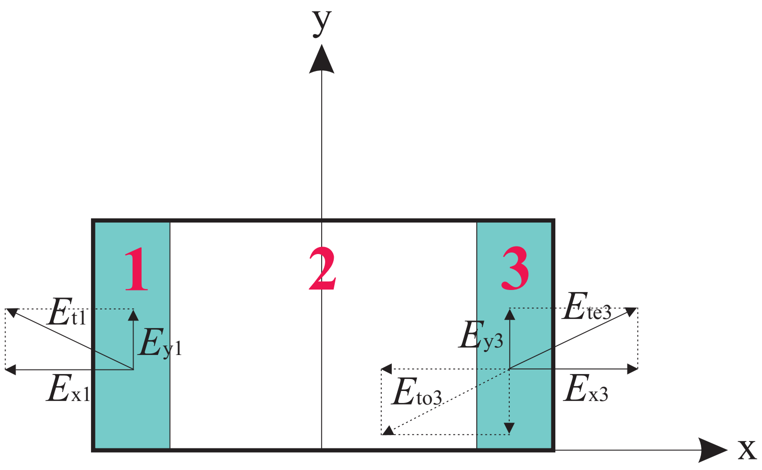

FIGURE 2.4: The odd/even mode of the transverse electric field.

where $n = 0, 1, 2, \cdots$ and k_{xi}, $i = 1, 2$ (the x-direction wavenumber in the corresponding dielectric) also satisfies the following separation equations:

$$\begin{aligned} k_1^2 &= \epsilon_r k_0^2 = k_{x1}^2 + (n\pi/b)^2 + \beta^2 \\ k_2^2 &= k_0^2 = k_{x2}^2 + (n\pi/b)^2 + \beta^2 \end{aligned} \tag{2.8}$$

where k_0 is the wavenumber in free space.

Since the dielectric-loaded RWG is symmetrical in terms of material and geometry with respect to the plane of $x = 0$, the fields within it are either symmetrical or asymmetrical, namely even or odd, with respect to the same plane. Here on a regular basis, the transverse electric fields, namely E_x and E_y, are taken to determine the odd/even nomenclature of the travelling wave.

Suppose $\bar{E}_{x1}$ and $\bar{E}_{y1}$ and their vector sum, $\bar{E}_{t1}$, are depicted in Region 1, as shown by Fig. 2.4. For the even mode of the transverse fields, $\bar{E}_{te3}$ in Region 3 is symmetrical to $\bar{E}_{t1}$ with respect to the plane $x = 0$. This results in an even-E_y pair ($E_{y1} = E_{y3}$) and an odd-E_x pair ($E_{x1} = -E_{x3}$), as shown in Fig. 2.4. With the aid of (2.4) and (2.7), it is then found that

$$A_3 = -A_1, \; B_3 = -B_1. \tag{2.9}$$

The odd-mode field in Region 3 represented by $\bar{E}_{to3}$ in Fig. 2.4, therefore, brings about an opposite relation:

$$A_3 = A_1, \; B_3 = B_1. \tag{2.10}$$

These two modes will be analysed individually as follows.

a) Even mode

In this case, the transverse fields are symmetrical with respect to the plane of $x = 0$, which results in a relation among the unknown field coefficients as expressed by (2.9).

Based on that, we apply boundary conditions at dielectric interfaces, (2.6b), for E_z

$$E_{z1} = E_{z2}|_{x=-a_2/2}, \;\; E_{z2} = E_{z3}|_{x=a_2/2} \tag{2.11}$$

to obtain

$$\begin{aligned} A_1 \sin(k_{x_1} a_1/2) &= A_2 \cos(k_{x_2} a_2/2) - A_4 \sin(k_{x_2} a_2/2) \\ A_1 \sin(k_{x_1} a_1/2) &= A_2 \cos(k_{x_2} a_2/2) + A_4 \sin(k_{x_2} a_2/2) \end{aligned} \tag{2.12}$$

which gives

$$\begin{aligned} &A_4 = 0 \\ &A_1 \sin(k_{x1} a_1/2) - A_2 \cos(k_{x2} a_2/2) = 0 \end{aligned} \tag{2.13}$$

Again, we apply (2.6b) for H_z to obtain

$$\begin{aligned} &B_2 = 0 \\ &B_1 \cos(k_{x1} a_1/2) + B_4 \sin(k_{x2} a_2/2) = 0 \end{aligned} \tag{2.14}$$

Hence, two unknown field coefficients have been removed by the assumption of even mode and the boundary equations have also been greatly simplified compared with the method presented in [100].

Once again, we apply boundary conditions, (2.6b), for E_y and H_y to obtain

$$\begin{aligned} A_1 \left[\frac{\beta}{k_{c1}^2}\frac{n\pi}{b}\sin(k_{x1} a_1/2)\right] - A_2 \left[\frac{\beta}{k_{c2}^2}\frac{n\pi}{b}\cos(k_{x2} a_2/2)\right] & \\ + B_1 \left[\frac{\omega\mu_1}{k_{c1}^2} k_{x1} \sin(k_{x1} a_1/2)\right] + B_4 \left[\frac{\omega\mu_2}{k_{c2}^2} k_{x2} \cos(k_{x2} a_2/2)\right] &= 0 \end{aligned} \tag{2.15a}$$

$$\begin{aligned} A_1 \left[\frac{\omega\epsilon_1}{k_{c1}^2} k_{x1} \cos(k_{x1} a_1/2)\right] - A_2 \left[\frac{\omega\epsilon_2}{k_{c2}^2} k_{x2} \sin(k_{x2} a_2/2)\right] & \\ - B_1 \left[\frac{\beta}{k_{c1}^2}\frac{n\pi}{b}\cos(k_{x1} a_1/2)\right] - B_4 \left[\frac{\beta}{k_{c2}^2}\frac{n\pi}{b}\sin(k_{x2} a_2/2)\right] &= 0 \end{aligned} \tag{2.15b}$$

Combining (2.13), (2.14), and (2.15), a homogeneous linear equation array is produced with 4 unknowns: A_1, A_2, B_1, B_4. In order to obtain nontrivial solutions, the determinant of the coefficient matrix must be zero, which yields the characteristic equation:

$$\begin{aligned}\left[\frac{K_\mu k_{x1}\tan(k_{x1}a_1/2)}{k_{c1}^2} - \frac{k_{x2}}{k_{c2}^2\tan(k_{x2}a_2/2)}\right]\left[\frac{K_\epsilon k_{x1}}{k_{c1}^2\tan(k_{x1}a_1/2)}\right.\\ \left.-\frac{k_{x2}\tan(k_{x2}a_2/2)}{k_{c2}^2}\right] + \left(\frac{\beta c_2 n\pi}{\omega b}\right)^2\left(\frac{1}{k_{c2}^2}-\frac{1}{k_{c1}^2}\right)^2 = 0\end{aligned} \tag{2.16}$$

where $K_\mu = \mu_1/\mu_2$, $K_\epsilon = \epsilon_1/\epsilon_2$ and c_2 is the speed of light in Dielectric 2.

At an arbitrary given frequency, the electromagnetic fields can be solved by combining (2.8) and (2.16) for a two-dielectric loaded RWG with a specific shape and material.

b) Odd mode

In this case, the transverse fields are asymmetrical with respect to the plane of $x = 0$, which results in a relation among the unknown field coefficients as expressed by (2.10).

Following a similar route, apply boundary conditions at the dielectric interfaces, (2.6b), for E_z, H_z, E_y, and H_y to obtain the characteristic equation:

$$\begin{aligned}\left[\frac{K_\mu k_{x1}\tan(k_{x1}a_1/2)}{k_{c1}^2} + \frac{k_{x2}\tan(k_{x2}a_2/2)}{k_{c2}^2}\right]\left[\frac{K_\epsilon k_{x1}}{k_{c1}^2\tan(k_{x1}a_1/2)}\right.\\ \left.+\frac{k_{x2}}{k_{c2}^2\tan(k_{x2}a_2/2)}\right] + \left(\frac{\beta c_2 n\pi}{\omega b}\right)^2\left(\frac{1}{k_{c2}^2}-\frac{1}{k_{c1}^2}\right)^2 = 0\end{aligned} \tag{2.17}$$

In the same way, with the help of the separation equation, (2.8), the odd-mode fields can also be derived for a specific two-dielectric loaded RWG.

2.2.2 Propagating Modes

A special case of the propagating modes inside the two-dielectric loaded RWG when $n = 0$ should be mentioned here. If $n = 0$, the longitudinal electric component, E_z, vanishes according to (2.7), generating TE_{m0} modes.

For other modes with $n \neq 0$, both E_z and H_z will exist and thus, brings about a hybrid mode, EH_{mn}, where $m, n \neq 0$. The reason why $m \neq 0$ results from the fact that the two-dielectric loaded RWG is not homogeneous along the x-direction.

Consequently, the lowest cut-off frequency is from either (a) TE_{10} mode or (b) EH_{11o} and EH_{11e} modes. It can be found that the cut-off frequency of the TE modes is independent of the y dimension, *i.e.*, b, while that of the EH modes decreases with an increasing b. Therefore, it is foreseen that the TE and EH modes will exchange their role as the dominant mode at a certain point.

Suppose Dielectric 1 is the Dupont$^{\mathrm{TM}}$ GreenTape$^{\mathrm{TM}}$ 9K7 LTCC system with a relative dielectric constant ϵ_{r1} of 7.1 and Dielectric 2 is air. Thus, $K_\mu = 1$, $K_\epsilon = 7.1$. Let

$$p = \frac{2a_1}{a} \tag{2.18}$$

represents the filling factor of Dielectric 1, the influence of which on the cutoff wavelength of possible fundamental modes is shown in Fig. 2.5. Also in this figure, the influence of b is clearly depicted.

As can be seen in Fig. 2.5, there are three groups of curves representing three possible fundamental modes: TE_{10}, EH_{11o}, and EH_{11e}. In each group, each of the five curves, from top to bottom, corresponds to a filling factor, p, from 1 to 0 in a descending order. The cutoff wavelength, λ_c, ($= \lambda_{c2}$, the cutoff wavelength in Region 2) has been normalised to that of the RWG with a 0-loaded ratio, *i.e.*, $p = 0$, while the height, b, has been normalised to the width a. Higher cutoff wavelengths mean lower cutoff frequencies. Intersections are clearly seen and marked by those green squares for the curves with the same load ratio. These are the turning points, to the left of which TE_{10} mode has a lower cutoff frequency and thus, is the fundamental one and to the right EH_{11o} is the fundamental one. The EH_{11e} mode always prompts a higher cutoff frequency than EH_{11o} mode provided with the same p. It's worth noting that when the RWG is completely occupied by one dielectric, *i.e.*, $p = 1$ and $p = 0$, the EH_{11o} mode is converted to TE_{01} mode, with the EH_{11e} mode being TE_{11}.

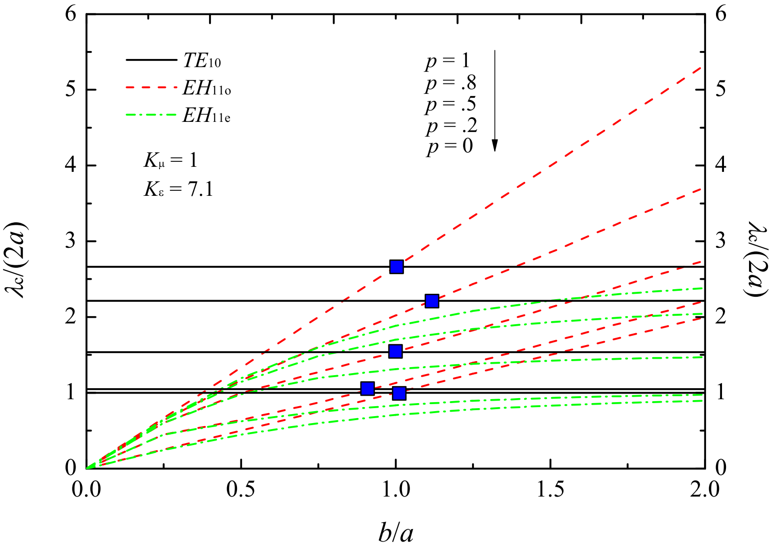

FIGURE 2.5: The cut-off wavelength with the change of height, b, and load ratio, p, of the two-dielectric loaded RWG.

It can also be found that those turning points occur when b/a approximates 1, which means the height and the width of a RWG is about the same. On a regular basis, the width of a RWG is larger than its height and laid on its wider side. Therefore, if Dielectric 2 is placed vertically as shown in Fig. 2.3, the dominant mode is probably TE_{10}; however, if Dielectric 2 is placed horizontally on the top and bottom of a RWG, the EH_{11o} mode will probably be the dominant one. The single-mode bandwidth will depend on how much longer a is than b; the longer a is or the shorter b is, the wider the bandwidth is.

Simulation by Ansoft HFSS$^{\mathrm{TM}}$ has also been carried out to verify this theory and the discrepancy is within 0.1%. So the results are not plotted in Fig. 2.5, otherwise they will be overlapping and obscuring those from theoretical calculations.

2.2.3 TE_{10} Mode

For TE_{m0} modes, $n = 0$ removes the longitudinal electric component, E_z, and hence, the E_x and H_y components (based on (2.4)), leading to

$$k_{yi} = 0, \ k_{ci}^2 = k_{xi}^2, \quad i = 1, 2 \tag{2.19}$$

Since the TE_{10} mode has a symmetrical distribution of transverse electric fields, it belongs to the even-mode group.

Applying boundary conditions at dielectric interfaces, (2.6b) for the even TE_{m0} modes to obtain

$$\begin{gathered}B_1 \cos\left(k_{x1}a_1/2\right) + B_4 \sin\left(k_{x2}a_2/2\right) = 0 \\ B_1 K_\mu k_{x2} \sin\left(k_{x1}a_1/2\right) + B_4 k_{x1} \cos\left(k_{x2}a_2/2\right) = 0\end{gathered} \tag{2.20}$$

and setting the determinant of its coefficient matrix to 0, the simplified characteristic equation for the even TE_{m0} modes can be obtained as follows

$$K_\mu k_{x2} \tan\left(k_{x1}a_1/2\right) \tan\left(k_{x2}a_2/2\right) - k_{x1} = 0, \quad \text{even mode} \tag{2.21}$$

A similar process can be taken to derive the characteristic equation for the odd TE_{m0} modes

$$K_\mu k_{x2} \tan\left(k_{x1}a_1/2\right) + k_{x1} \tan\left(k_{x2}a_2/2\right) = 0, \quad \text{odd mode} \tag{2.22}$$

The four unknown coefficients can then be solved for the even modes in terms of B_1, suppose all the other terms are known, to give the field components as follows:

$$\begin{aligned}
H_{z1} &= A\cos\left[k_{x1}(x+a/2)\right] \\
H_{z2} &= -A\frac{\cos\left(k_{x1}a_1/2\right)}{\sin\left(k_{x2}a_2/2\right)}\sin\left(k_{x2}x\right) \\
H_{z3} &= -A\cos\left[k_{x1}(x-a/2)\right] \\
E_{y1} &= -A\frac{j\omega\mu_1}{k_{x1}}\sin\left[k_{x1}(x+a/2)\right] \\
E_{y2} &= -A\frac{j\omega\mu_2}{k_{x2}}\frac{\cos\left(k_{x1}a_1/2\right)}{\sin\left(k_{x2}a_2/2\right)}\cos\left(k_{x2}x\right) \\
E_{y3} &= A\frac{j\omega\mu_1}{k_{x1}}\sin\left[k_{x1}(x-a/2)\right] \\
H_{x1} &= A\frac{j\beta}{k_{x1}}\sin\left[k_{x1}(x+a/2)\right] \\
H_{x2} &= A\frac{j\beta}{k_{x2}}\frac{\cos\left(k_{x1}a_1/2\right)}{\sin\left(k_{x2}a_2/2\right)}\cos\left(k_{x2}x\right) \\
H_{x3} &= -A\frac{j\beta}{k_{x1}}\sin\left[k_{x1}(x-a/2)\right] \\
E_x &= E_z = H_y = 0
\end{aligned} \tag{2.23}$$

where A is an arbitrary constant.

For the convenience of later designs, suppose Dielectric 2 is air and Dielectric 1 is a nonmagnetic material with a relative permeability, $\mu_r = 1$, and a relative permittivity, ϵ_r. Then, $K_\mu = 1$ and $K_\epsilon = \epsilon_r$.

To determine the cutoff frequency of the even TE$_{m0}$ modes, set β to 0 for (2.21). Therefore, the separation equations can also be rewritten as

$$k_{x1}^2 = \epsilon_r k_0^2,\ \ k_{x2}^2 = k_0^2$$

which yields the final characteristic equation for even modes as

$$\sqrt{\epsilon_r} k_0 a_1/2 = \arctan\left[\sqrt{\epsilon_r}/\tan\left(k_0 a_2/2\right)\right] + m'\pi, \quad m' = 0, 1, 2, \cdots \tag{2.24}$$

Note in this equation, there are four unknowns, a, p, ϵ_r, and k_0. With three of them given, the remaining one will be solved out immediately. This, in another way, has offered a high degree of flexibility when designing the two-dielectric loaded RWG.

If k_0 is the target and when it has been worked out, the cutoff frequency can then be derived as

$$f_c = \frac{k_0 c_0}{2\pi} \tag{2.25}$$

where c_0 is the speed of light in free space. It is also worth noting that m' has nothing to do with m; the introduction of m' is just for the convenience of solving (2.21). In fact, when m' takes one single value, it could correspond to a series of continuous guided modes depending on the number of curve intersections represented by the two sides of (2.24).

Since the HSIW has most of its inner dielectric removed and behaves like an air-filled RWG, the dielectric-loaded RWG considered here should also be lightly loaded, *i.e.*, the product of p and $\sqrt{\epsilon_r}$ is small. So the cutoff wavenumber k_c is close to that of an air-filled RWG, *i.e.*, $m\pi/a$. If

$$k_{x1} a_1/2 = \sqrt{\epsilon_r} k_c a p/2 = \sqrt{\epsilon_r} m\pi p/2 \ll 1$$

i.e.,

$$p\sqrt{\epsilon_r} \ll 2/(m\pi),$$

$\tan\left(k_{x1} a_1/2\right) \approx k_{x1} a_1/2$, which can simplify (2.24) to

$$k_0 a_2/2 = \arctan\left[2/(k_0 a_1)\right] + m'\pi, \quad m' = 0, 1, 2, \cdots \tag{2.26}$$

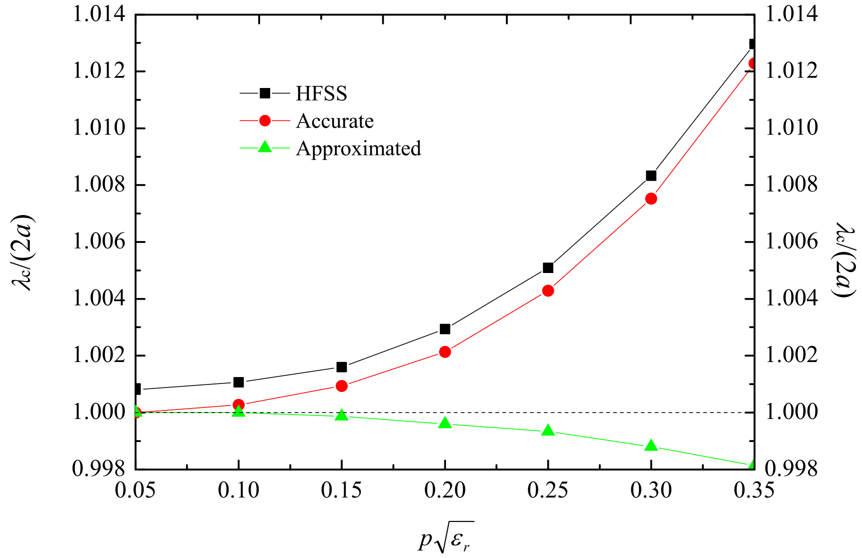

FIGURE 2.6: The comparison of cut-off wavelength with $p\sqrt{\epsilon_r}$ ($\epsilon_r = 7.1$).

When m takes a high value, it's very hard to meet that simplification condition. So it is only realistic for low-order modes.

Regarding the TE$_{10}$ mode, Fig. 2.6 describes the accuracy of (2.26) compared with the accurate (2.24) and the simulation results from HFSS. Dielectric 1 used here is the LTCC material as before with $\epsilon_r = 7.1$. As in Fig. 2.5, the cut-off wavelength λ_c has been normalised to that of the RWG with a 0-loaded ratio, *i.e.*, $2a$. The λ_c derived from the approximated (2.26) has a different trend from those obtained by (2.24) and HFSS simulation, with the increase of $p\sqrt{\epsilon_r}$. Nevertheless, the discrepancy is not much, about 1% at $p\sqrt{\epsilon_r} = 0.35$. It can also be found, however, that the cutoff wavelength of an air-filled RWG is closer to that of the accurate model.

In a word, the TE$_{10}$ mode of an air-filled RWG can probably replace that of a dielectric-loaded RWG in terms of cut-off frequency when $p\sqrt{\epsilon_r} \leq 0.35$ (1% discrepancy approximately).

To further explore the cut-off characteristics and obtain a more accurate expression for this dielectric-loaded RWG, a series of different permittivities has been theoretically calculated with the accurate (2.24), as shown in Fig. 2.7. The relative dielectric constant ϵ_r starts at 2 and endes at 12 with a step of 2. Generally, when ϵ_r increases, the normalised cut-off wavelength λ_c decreases and behaves more like the TE$_{10}$ mode of an air-filled RWG. However, note that the maximum λ_c doesn't appear at the lowest ϵ_r, as it resembles, again, an air-filled RWG when

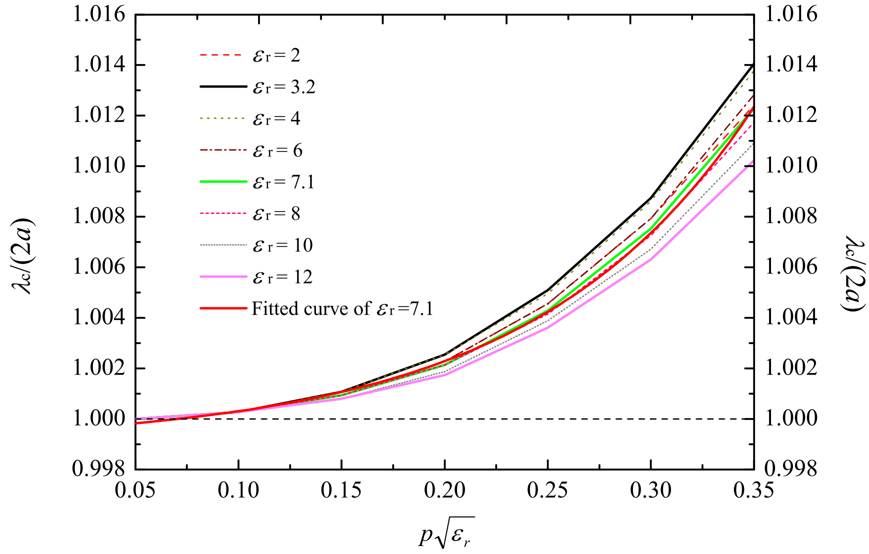

FIGURE 2.7: The comparison of cut-off wavelength with different permittivities and the curve fitting.

ϵ_r approaches 1. It is therefore searched through accurate calculation that $\epsilon_r = 3.2$ gives the maximum λ_c.

Since the accurate (2.24) needs to be numerically calculated and thus, is complicated, a curve-fitting technique is used here to derive a simplified approximation. For $2 \leq \epsilon_r \leq 12$ which accounts for most of the regular dielectric materials, $\epsilon_r = 7.1$ is chosen to be curve-fitted, as it stands close to the middle and will later be used for the HSIW design. The fitted curve takes the form of an exponential function, shown as the red solid line in Fig. 2.7. The approximated empirical expression for the cutoff wavelength of TE_{10} mode is

$$\lambda_c = 2a\left[0.999 + 4.946\text{e}(-4)\exp\left(9.409p\sqrt{\epsilon_r}\right)\right], \quad p\sqrt{\epsilon_r} \leq 0.35 \tag{2.27}$$

with a discrepancy less than 0.2%. After that, the cutoff frequency is obtained as:

$$f_c = \frac{c_0}{\lambda_c}. \tag{2.28}$$

2.2.4 EDC, ϵ_e, of TE_{10} Mode

A waveguide needs to be single-moded to be practically in use. For a two-dielectric loaded waveguide with $b/a \leq 0.5$, the cut-off frequency of higher modes, *i.e.*, TE_{20},

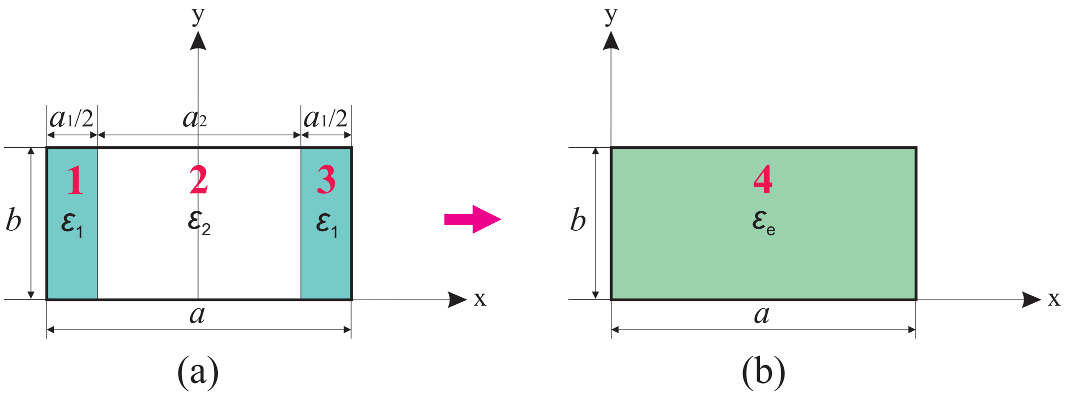

FIGURE 2.8: The transformation from a two-dielectric loaded RWG into a uniformly filled one with EDC, ϵ_e.

EH$_{11o}$, *etc.*, will at least double that of the TE$_{10}$ mode for a lightly-loaded case (refer to Fig. 2.5 to get a sense). So the single-mode band is from the cut-off frequency f_c to $2f_c$. In order to characterise the propagation of a lightly-loaded RWG ($p\sqrt{\epsilon_r} \leq 0.35$) in its single-mode band, a concept of EDC, ϵ_e, is proposed, which transforms a two-dielectric loaded RWG into a uniformly-filled one, as shown in Fig. 2.8.

2.2.4.1 Derivation of ϵ_{re}

In a situation where no dielectric loss exists, $\epsilon_e = \epsilon_{re}$. Therefore, the propagation constant, β, can now be rewritten as

$$\beta = \sqrt{\epsilon_{re} k_0^2 - (\pi/a)^2} \tag{2.29}$$

Take (2.21) with a simplified separation equation (2.30):

$$\begin{aligned} \epsilon_r k_0^2 &= k_{x1}^2 + \beta^2 \\ k_0^2 &= k_{x2}^2 + \beta^2 \end{aligned} \tag{2.30}$$

to solve for β and hence, ϵ_{re}.

Calculation and HFSS simulation on ϵ_{re} have been carried out for $\epsilon_r = 7.1$ along a frequency range of $f_c \sim 2f_c$, as shown in Fig. 2.9 (For simplicity, results from HFSS simulation are not displayed as they tend to overlap those from theoretical calculation). Fig. 2.9 shows that ϵ_{re} curves take the form of an exponential function and tend not to be flat with high $p\sqrt{\epsilon_r}$ values in the single-mode band. A

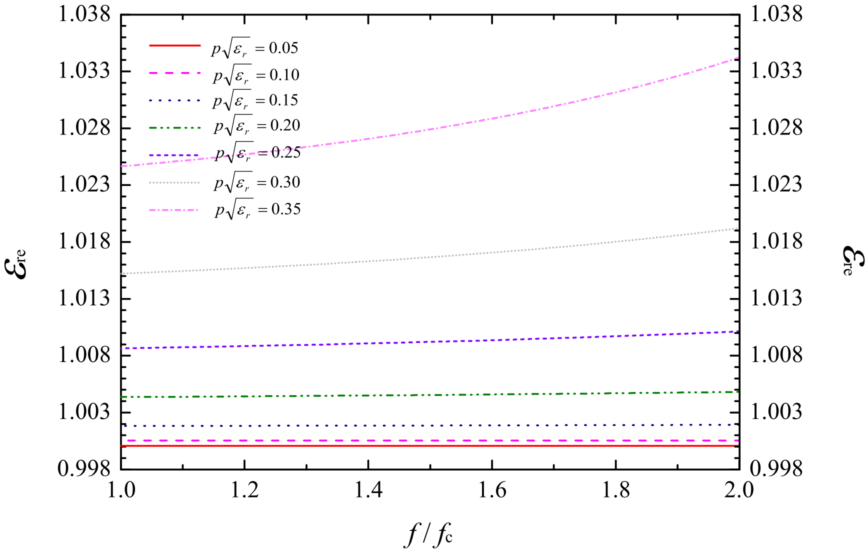

FIGURE 2.9: The EDC, ϵ_{re}, of a lightly-loaded RWG with different $p\sqrt{\epsilon_r}$ values ($\epsilon_r = 7.1$).

TABLE 2.1: The coefficients' values for the fitted ϵ_{re} ($\epsilon_r = 7.1$).

$p\sqrt{\epsilon_r}$	ϵ_{r0}	A	B
0.05	1.00007	0	0
0.10	1.00052	4.357e-6	0.832
0.15	1.00173	4.045e-5	0.779
0.20	1.00402	1.441e-4	0.855
0.25	1.00776	3.320e-4	0.983
0.30	1.01334	5.975e-4	1.142
0.35	1.02131	8.700e-4	1.349

curve-fitting technique has also been applied here to extract an empirical expression for ϵ_{re} with different $p\sqrt{\epsilon_r}$ values:

$$\epsilon_{re} = \epsilon_{r0} + A\exp\left(Bf'\right) \tag{2.31}$$

where $f' = f/f_c$ and the values for the coefficients are listed in Tab. 2.1.

Similar to the analysis of the cut-off characteristics, a series of ϵ_r has also been calculated to obtain ϵ_{re} and shown in Fig. 2.10. Since ϵ_{re} varies with changing frequency toward high $p\sqrt{\epsilon_r}$, a fixed frequency point at $f/f_c = 1.5$ has been chosen to evaluate ϵ_{re}. It is seen in Fig. 2.10 that a cluster of curves, with $2 \leq \epsilon_r \leq 12$, tend to open up toward higher $p\sqrt{\epsilon_r}$ values, which is similar to that depicted in Fig. 2.7. ϵ_{re} from $\epsilon_r = 7.1$ stands in the middle with the maximum deviation,

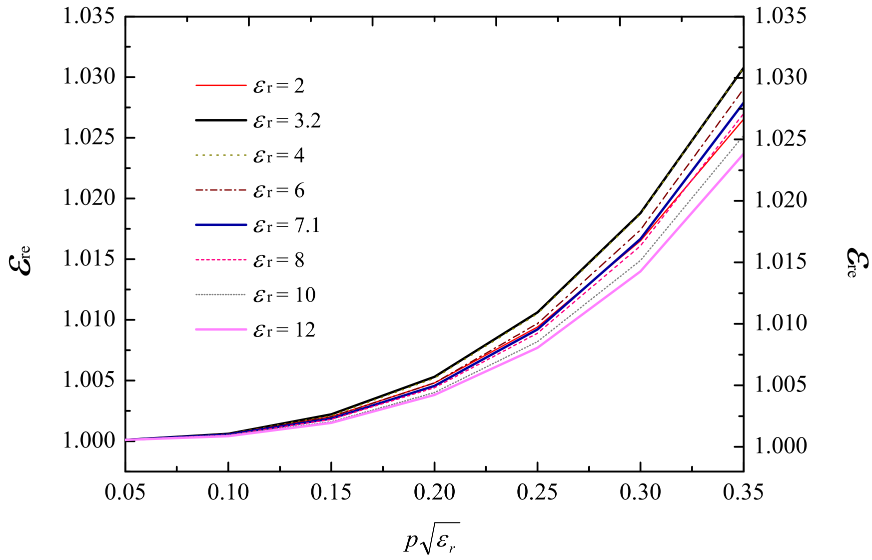

FIGURE 2.10: The EDC, ϵ_{re}, of a lightly-loaded RWG with different ϵ_r.

0.4%, occurring at $p\sqrt{\epsilon_r} = 0.35$. Note that this deviation is achieved at $f/f_c = 1.5$. As the frequency rises, the deviation is expected to be escalated toward the end of the single-mode band, $f/f_c = 2$.

2.2.4.2 Derivation of $\tan\delta_{re}$

If the dielectric loss exists which is the normal case in practice, ϵ and ϵ_e become complex

$$\epsilon = \epsilon' - j\epsilon'' = \epsilon_0\epsilon_r(1 - j\tan\delta) \tag{2.32a}$$

$$\epsilon_e = \epsilon_e' - j\epsilon_e'' = \epsilon_0\epsilon_{re}(1 - j\tan\delta_e) \tag{2.32b}$$

Hence, from [99], the time-average power dissipated per unit length due to the dielectric loss of the two RWGs shown in Fig. 2.8 should be equal to each other and found to be

$$\begin{aligned} P_d &= \frac{\omega\epsilon''}{2}\left(\int_{S_1}|E_{y1}|^2\mathrm{d}s + \int_{S_3}|E_{y3}|^2\mathrm{d}s\right) && \text{Fig. 2.8 (a)} \\ &= \frac{\omega\epsilon_e''}{2}\int_{S_4}|E_{ye}|^2\mathrm{d}s && \text{Fig. 2.8 (b)} \end{aligned} \tag{2.33}$$

where E_{ye} is given by Eq. (3.89b) in [99] as

$$E_{ye} = -\frac{j\omega\mu a}{\pi} B_1' \sin\frac{\pi x}{a} \tag{2.34}$$

Solve (2.33) using (2.23) to find ϵ_e'' as

$$\epsilon_e'' = \epsilon'' \frac{B_1^2}{B_1'^2} \frac{(\pi/a)^2}{k_{x1}^2} \frac{a_1 - \sin(k_{x1}a_1)/k_{x1}}{a} \tag{2.35}$$

To obtain $B_1^2/B_1'^2$, a power condition needs to be taken into consideration, which is the power flow down the two RWGs in Fig. 2.8 are also the same, *i.e.*,

$$\begin{aligned} P_o &= \frac{1}{2}\mathrm{Re}\left(\int_{S_1} E_{y1}H_{x1}^*\mathrm{d}s + \int_{S_3} E_{y3}H_{x3}^*\mathrm{d}s\right) && \text{Fig. 2.8 (a)} \\ &= \frac{1}{2}\mathrm{Re}\int_{S_4} E_{ye}H_{xe}^*\mathrm{d}s && \text{Fig. 2.8 (b)} \end{aligned} \tag{2.36}$$

where H_{xe} is given by Eq. (3.89c) in [99] as

$$H_{xe} = \frac{j\beta a}{\pi} B_1' \sin\frac{\pi x}{a} \tag{2.37}$$

Solve (2.36) using (2.23) to find $B_1^2/B_1'^2$ and substitute it into (2.35) to find ϵ_e'' as

$$\epsilon_e'' = \epsilon'' \left[1 + \frac{k_{x1}^2}{k_{x2}^2} \frac{a_2 + \sin(k_{x2}a_2)/k_{x2}}{a_1 - \sin(k_{x1}a_1)/k_{x1}} \frac{\cos^2(k_{x1}a_1/2)}{\sin^2(k_{x2}a_2/2)}\right]^{-1} \tag{2.38}$$

hence,

$$\begin{aligned} \tan\delta_e &= \frac{\epsilon_e''}{\epsilon_e'} = \frac{\epsilon_e''}{\epsilon_{re}} \\ &= \tan\delta\left(\frac{\epsilon_r}{\epsilon_{re}}\right)\left[1 + \frac{k_{x1}^2}{k_{x2}^2} \frac{a_2 + \sin(k_{x2}a_2)/k_{x2}}{a_1 - \sin(k_{x1}a_1)/k_{x1}} \frac{\cos^2(k_{x1}a_1/2)}{\sin^2(k_{x2}a_2/2)}\right]^{-1} \end{aligned} \tag{2.39}$$

To simplify (2.39), a series of $\tan\delta_e$ normalised to the actual dielectric loss tangent, $\tan\delta$, has been calculated using (2.39) with different $p\sqrt{\epsilon_r}$ values when $\epsilon_r = 7.1$, as shown in Fig. 2.11. It can be found in Fig. 2.11 that the curves take the form of an exponential function and tend not to be flat with high $p\sqrt{\epsilon_r}$ values in the single-mode band. A curve-fitting technique has also been applied here to extract

TABLE 2.2: The coefficients' values for the fitted $\tan\delta_e/\tan\delta$ ($\epsilon_r = 7.1$).

$p\sqrt{\epsilon_r}$	δ_0	A'	B'
0.05	0.00008	0	0
0.10	0.00060	1.380e-5	0.739
0.15	0.00195	8.565e-5	0.830
0.20	0.00451	2.707e-4	0.963
0.25	0.00866	5.739e-4	1.146
0.30	0.01499	9.247e-4	1.380
0.35	0.02433	1.190e-3	1.674

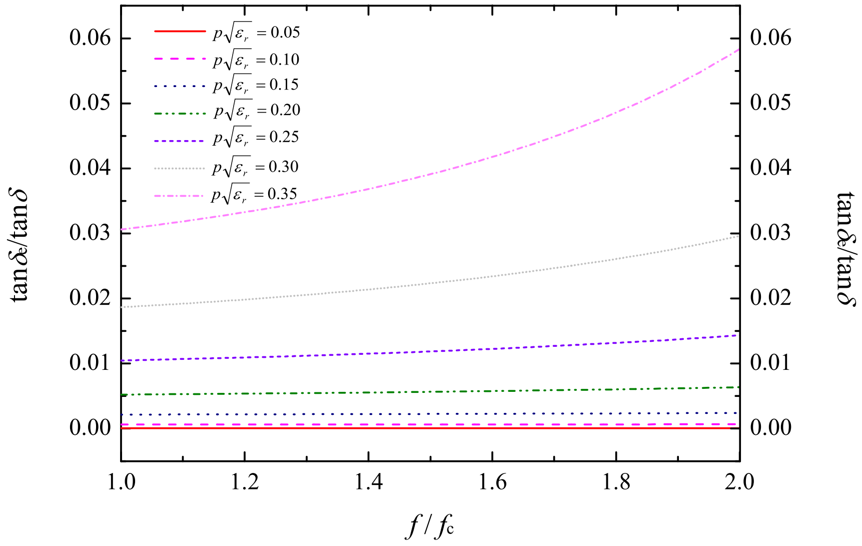

FIGURE 2.11: The normalised $\tan\delta_e$ of a lightly-loaded RWG with different $p\sqrt{\epsilon_r}$ values.

an empirical expression for $\tan\delta_e/\tan\delta$ with different $p\sqrt{\epsilon_r}$ values:

$$\frac{\tan\delta_e}{\tan\delta} = \delta_0 + A'\exp(B'f') \tag{2.40}$$

where $f' = f/f_c$ and the values for the coefficients are listed in Tab. 2.2.

Similar to the analysis of ϵ_{re}, a series of ϵ_r has also been calculated to obtain $\tan\delta_e/\tan\delta$ and shown in Fig. 2.12. Since $\tan\delta_e/\tan\delta$ varies with changing frequency toward high $p\sqrt{\epsilon_r}$, a fixed frequency point at $f/f_c = 1.5$ has been chosen to evaluate it. It is seen in Fig. 2.12 that a cluster of curves, with $2 \leq \epsilon_r \leq 12$, tend to flare up toward higher $p\sqrt{\epsilon_r}$ values, which is similar to that depicted in Fig. 2.10. The only difference lies in that $\tan\delta_e$ is monotonically increasing with

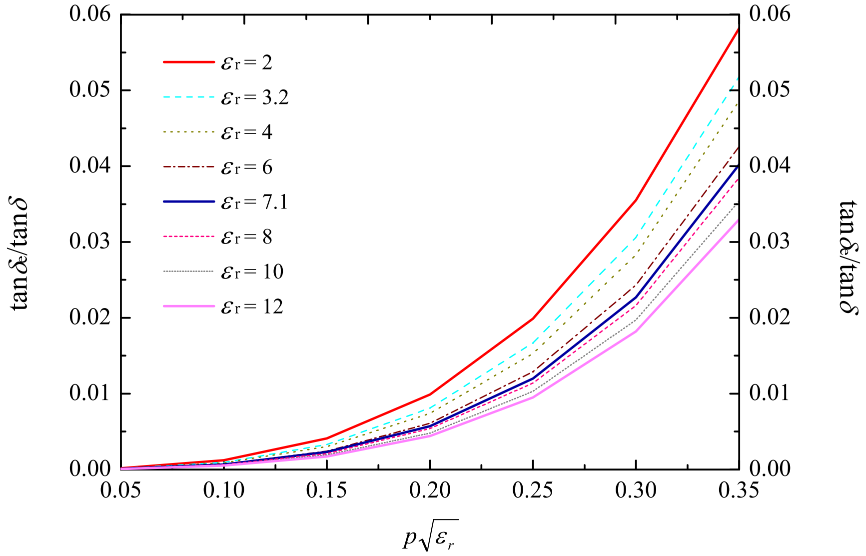

FIGURE 2.12: The normalised $\tan\delta_e$ of a lightly-loaded RWG with different ϵ_r values.

the decrease of ϵ_r. $\tan\delta_e$ from $\epsilon_r = 7.1$ stands in the middle with the maximum deviation, 2%, occuring at $p\sqrt{\epsilon_r} = 0.35$. Note that this deviation is achieved at $f/f_c = 1.5$. As the frequency rises, the deviation is expected to be escalated toward the end of the single-mode band, $f/f_c = 2$.

2.2.4.3 Combination of ϵ_{re} and $\tan\delta_{re}$

To summarise the EDC method in a lossy situation, a complex dielectric constant is introduced as (2.32b), where ϵ_{re} can be derived through (2.21), (2.29), and (2.30) and $\tan\delta_e$ is found by (2.39). Nevertheless, if approximation is allowed, ϵ_e can be transformed into a simplified empirical expression as

$$\begin{aligned}\epsilon_e &= \epsilon_{re}(1 - j\tan\delta_e)\\ &= [\epsilon_{r0} + A\exp(Bf')]\left\{1 - j\tan\delta\left[\delta_0 + A'\exp(B'f')\right]\right\}\end{aligned} \tag{2.41}$$

where $f' = f/f_c$ and the coefficients' values are listed in Tab. 2.1 and 2.2 for different $p\sqrt{\epsilon_r}$ values. Note that this approximated formula will give exact solutions when $\epsilon_r = 7.1$ and a maximum 0.4% discrepancy for ϵ_{re} and 2% for $\tan\delta_e$ when $2 \le \epsilon_r \le 12$ and $f' \le 1.5$.

2.2.5 Loss of TE_{10} Mode

Generally, for a matched transmission line, the loss is composed of three components: conductor loss, α_c, dielectric loss α_d, and radiation loss, α_r, attributed by a finite conductivity, σ, imperfect dielectric material, ϵ'', and an open structure, respectively. As to the dielectric-loaded RWG, the radiation loss can be ignored as the structure is sealed within a metallic surface.

With the introduction of EDC, ϵ_e, the two-dielectric loaded RWG can be viewed as one uniformly-filled with a new dielectric in its single-mode band, *i.e.*, TE_{10} mode. Hence, the attenuation constant due to conductor loss, α_c, of the TE_{10} mode can be expressed as (3.96) in [99]

$$\alpha_c = \frac{R_s}{a^3 b \beta k \eta}(2b\pi^2 + a^3 k^2) \tag{2.42}$$

where

$$\begin{aligned}
\omega &= k_0 c_0 \\
k &= \sqrt{\epsilon_{re}} k_0 \\
R_s &= \sqrt{\frac{\omega\mu}{2\sigma}}, \quad \text{the wall-surface resistance} \\
\eta &= \sqrt{\frac{\mu}{\epsilon_0 \epsilon_{re}}}, \quad \text{the intrinsic impedance of the filling material} \\
c_0 &= \frac{1}{\sqrt{\mu_0 \epsilon_0}}, \quad \text{the speed of light in free space}
\end{aligned} \tag{2.43}$$

Fig. 2.13 shows the conductor loss constant, α_c, of dielectric-loaded RWGs with different widths. As can be seen, α_c is high in the proximity of cut-off frequency and decreases drastically to a stable value across the single-mode band. As the width a decreases or in other words, the operating frequency increases, α_c gets higher which means that the attenuation due to finite conductivity tend to be severe toward high frequencies. This fact has become a serious constraint for the application of RWGs in mm-wave and higher frequency bands. The result from HFSS simulation has also been presented in Fig. 2.13. A minor deviation has been observed between results from the calculation and simulation and it gets worse toward narrower RWGs, which is probably resulted from the fact that ϵ_{re} is not derived from the standing point of power.

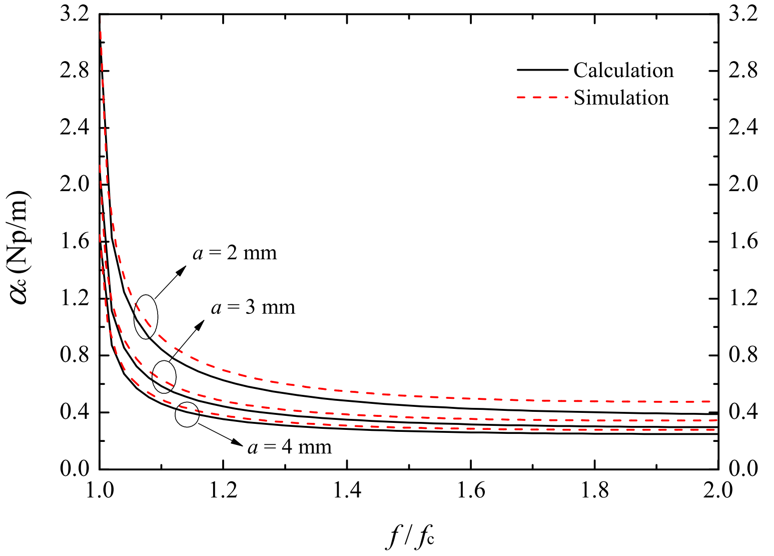

FIGURE 2.13: The conductor loss constant, α_c, when $\epsilon_r = 7.1$, $\sigma = 5.8\text{e}7$ S/m, $p\sqrt{\epsilon_r} = 0.3$, and $b = 1$ mm.

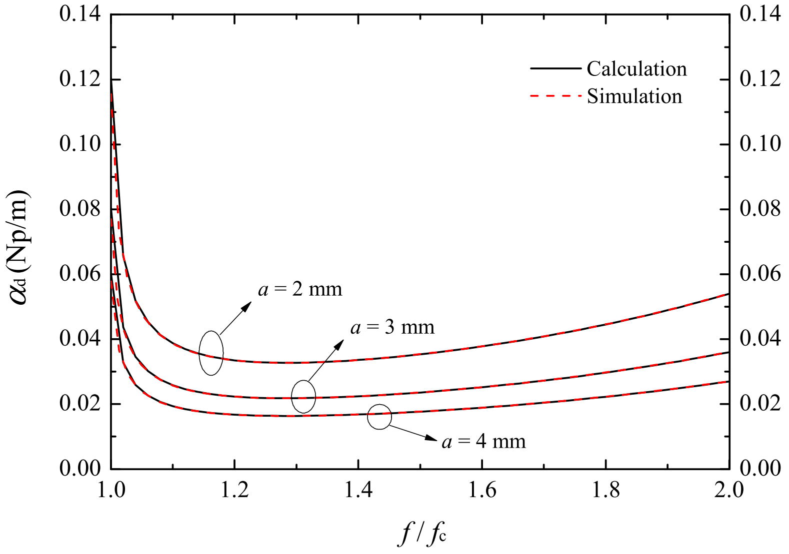

FIGURE 2.14: The dielectric loss constant, α_d, when $\epsilon_r = 7.1$, $\tan\delta = 0.001$, $p\sqrt{\epsilon_r} = 0.3$, and $b = 1$ mm.

With $\tan\delta_e$ known from either (2.39) or (2.41), the attenuation constant due to dielectric loss, α_d, for the TE$_{10}$ mode is modified from (3.29) in [99] to give

$$\alpha_d = \frac{\epsilon_{re} k_0^2 \tan\delta_e}{2\beta} \tag{2.44}$$

Fig. 2.14 shows the dielectric loss constant, α_d, of dielectric-loaded RWGs with different widths. As can be seen, α_d is high in the proximity of cut-off frequency, drops drastically to a relatively-stable value and then rises again toward the end of the single-mode band. Similar to α_c, as the operating frequency increases, α_d gets higher which means high dielectric attenuation at high frequencies. Compared with α_c for a specific case ($p\sqrt{\epsilon_r} = 0.3$), α_d is negligible, at the order of 10% of α_c. It is clear that with the removal of most of the dielectric in the RWG, the dielectric attenuation is very low. The result from HFSS simulation has also been presented in Fig. 2.14. A perfect agreement has been found and the curves are actually overlapping each other.

2.2.6 Design of Two-Dielectric Loaded RWG

To design a dielectric-loaded air-filled RWG with $b/a \leq 0.5$, as shown in Fig. 2.3, one can follow a rigorous route:

1) Figure out p and ϵ_r based on the materials and techniques available.
2) Use (2.24) to find the width, a, for a prescribed cut-off frequency. Numerical analysis is needed to solve this transcendental equation.
3) Use (2.21), (2.29), (2.30), and (2.39) to find the phase constant, β, and the complex EDC, ϵ_e. ϵ_e at several discrete frequency points can be solved first and then extrapolated to be a continuous curve.
4) Use (2.42) and (2.44) to find the loss characteristics, *i.e.*, α_c and α_d.
5) Use HFSS to build up 3D models and make necessary adjustments upon simulation.

Alternatively, if approximation is allowed, a simpler route can be taken as follows (exact solutions throughout the single-mode band when $\epsilon_r = 7.1$):

1) Choose one value from 0.05 to 0.35 with a 0.05 step for $p\sqrt{\epsilon_r}$, based on the materials and techniques available as long as $2 \leq \epsilon_r \leq 12$.
2) Use (2.27) to find the width a for a prescribed cut-off frequency with a discrepancy less than 0.2%.

3) Choose one equation from a set of (2.41) to find the complex EDC, ϵ_e, based on the $p\sqrt{\epsilon_r}$ value you already chose in Step 1), and hence, (2.29) to find the propagation constant, β, when $f_c \leq f \leq 1.5f_c$. The maximum discrepancy of 0.4% for ϵ_{re} and 2% for $\tan\delta_e$ occurs at $f = 1.5f_c$.

4) Same as the exact method.

5) Same as the exact method.

2.3 SIW

In this section, a multimode calibration method proposed in [89] is used to analyse and extract the propagation characteristics of the SIW. After that, a modified formula on K. Wu's method in [88] and [89] is given to better adapt our design with LTCC as the filling dielectric.

As stated in Section 2.1, the main difference between an SIW and a completely dielectric-loaded RWG lies in that the solid side walls of a RWG are replaced by two rows of periodic metal posts. As can be seen in Fig. 2.1, the diameter of the posts is d and the pitch between two adjacent posts is s. In addition, a, b, and l represents the width, height, and length of the SIW, respectively.

Based on [89], only TE_{m0} modes can propagate within an SIW, since the discrete posts will cut off the surface currents of all other modes. Various methods have been applied to analyse the propagation characteristics of this newly-introduced structure. By assuming a uniform longitudinal electric current on the post surface, J. Hirokawa *et. al.* used the dyadic Green's function to solve the fields generated by a unit cell of the SIW. This method is completely numerical without giving any closed-form formula [87]. K. Wu has used the BI-RME method in [88], the FDTD method, and a multimode calibrated FEM method in [89]. Apart from the numerical nature of these two methods, approximated numerical formulas are derived to determine the equivalent RWG width of an SIW, which is simple and straightforward within a certain accuracy.

The multimode calibrated FEM method is employed here to characterise the SIW. Two lowest-order modes will be considered, where HFSS based on the FEM method will implement the calculation.

The multimode calibration method is essentially a multiline method, where the basic principle is that one can determine the propagation constant through uncalibrated S-parameter measurements of at least two transmission lines [101, 102]. Instead of a simple and less-accurate formula for a single-mode case:

$$\alpha = \frac{\ln |S_{21}^i / S_{21}^j|}{\Delta l}, \quad \beta = \frac{\angle(S_{21}^i / S_{21}^j)}{\Delta l}, \tag{2.45}$$

where S_{21}^i and S_{21}^j are for SIW i and SIW j with a length difference of Δl, a matrix method is introduced to take on board all the elements of the S-matrix aiming for a more-accurate solution.

Under a premise of two-mode calibration, define T_0^i,

$$T_0^i = \mathrm{diag}[e^{-\gamma_1 l_i} \quad e^{\gamma_1 l_i} \quad e^{-\gamma_2 l_i} \quad e^{\gamma_2 l_i}] \tag{2.46}$$

as the cascade T-parameter matrix for an ideal transmission line i, where γ_1, γ_2 are the propagation constant for mode 1 and mode 2, respectively, and l_i is the length of transmission line i. Then, define T^i

$$T^i = X T_0^i Y \tag{2.47}$$

as an uncalibrated cascade T-parameter matrix, where matrices X and Y represent imperfections and errors from practical measurements or modelling-software simulations. It is worth noting that X and Y are assumed unchanged for each measurement and simulation of both transmission line i and j. The definition of T_0^j and T^j takes a similar manner [102].

Since the S-parameter matrix is generally obtained directly from measurements or simulations, the conversion from a S-matrix into a T-matrix is necessary. In this case, the conversion will be performed in a two-mode environment, which is intended to yield a more-accurate result than that from a single-mode calibration and clearly identify the single-mode band of the transmission line.

Recall the definition of a single-mode S-parameter matrix:

$$\begin{pmatrix} b_1 \\ b_2 \end{pmatrix} = \begin{pmatrix} S_{11} & S_{12} \\ S_{21} & S_{22} \end{pmatrix} \begin{pmatrix} a_1 \\ a_2 \end{pmatrix} \tag{2.48}$$

and interchange b_2 and a_1, then a_2 and b_2 to obtain the T-parameter matrix as:

$$\begin{pmatrix} b_1 \\ a_1 \end{pmatrix} = \begin{pmatrix} T_{11} & T_{12} \\ T_{21} & T_{22} \end{pmatrix} \begin{pmatrix} a_2 \\ b_2 \end{pmatrix} \tag{2.49}$$

Now, extend the single-mode S-parameter and T-parameter matrix into the two-mode case:

$$\begin{pmatrix} b_1^1 \\ b_1^2 \\ b_2^1 \\ b_2^2 \end{pmatrix} = \begin{pmatrix} S_{11} & S_{12} & S_{13} & S_{14} \\ S_{21} & S_{22} & S_{23} & S_{24} \\ S_{31} & S_{32} & S_{33} & S_{34} \\ S_{41} & S_{42} & S_{43} & S_{44} \end{pmatrix} \begin{pmatrix} a_1^1 \\ a_1^2 \\ a_2^1 \\ a_2^2 \end{pmatrix} \tag{2.50}$$

$$\begin{pmatrix} b_1^1 \\ b_1^2 \\ a_1^1 \\ a_1^2 \end{pmatrix} = \begin{pmatrix} T_{11} & T_{12} & T_{13} & T_{14} \\ T_{21} & T_{22} & T_{23} & T_{24} \\ T_{31} & T_{32} & T_{33} & T_{34} \\ T_{41} & T_{42} & T_{43} & T_{44} \end{pmatrix} \begin{pmatrix} a_2^1 \\ a_2^2 \\ b_2^1 \\ b_2^2 \end{pmatrix} \tag{2.51}$$

where the superscript 1 and 2 indicate the corresponding mode 1 and mode 2, respectively.

To solve for the elements of the T-matrix, it needs to be decomposed into separate equations. Take the solution of T_{11} for example.

First,

$$b_1^1 = T_{11}a_2^1 + T_{12}a_2^2 + T_{13}b_2^1 + T_{14}b_2^2 \tag{2.52}$$

Then,

$$T_{11} = \frac{b_1^1}{a_2^1}\Big|_{a_2^2 \;=\; b_2^1 \;=\; b_2^2 \;=0} \tag{2.53}$$

Substitute a_2^2, b_2^1, and b_2^2 in the S-matrix, (2.50), with 0 to solve for b_1^1 in terms of a_2^1, suppose the S-matrix is known. In the end, T_{11} can be found as

$$T_{11} = S_{11}\frac{S_{43}S_{32} - S_{42}S_{33}}{S_{42}S_{31} - S_{41}S_{32}} + S_{12}\frac{S_{41}S_{33} - S_{43}S_{31}}{S_{42}S_{31} - S_{41}S_{32}} + S_{13} \tag{2.54}$$

As can be seen, the algebraic expression for the whole T-matrix in terms of S-parameters will be too complex to be presented here. Nevertheless, one can always follow the same method discussed above to solve for the T-matrix.

With T^i and T^j solved from the S-matrix, they can thus be combined into an eigenvalue equation:

$$T^{ij} = XT_0^{ij}X^{-1} \tag{2.55}$$

where

$$T^{ij} = T^j(T^i)^{-1}, \quad T_0^{ij} = T_0^j(T^i)_0^{-1} \tag{2.56}$$

The eigenvalues of T^{ij}, λ_{1T}^{ij}, λ_{2T}^{ij}, λ_{3T}^{ij}, λ_{4T}^{ij}, are equal to those of $XT_0^{ij}X^{-1}$, which, after a simple derivation, equal those of T_0^{ij}, *i.e.*, the diagonal elements: $e^{-\gamma_1\Delta l}$, $e^{\gamma_1\Delta l}$, $e^{-\gamma_2\Delta l}$, and $e^{\gamma_2\Delta l}$.

Hence, the propagation constant γ_1 and γ_2 are given as:

$$\gamma_1 = \ln(\lambda_1^{ij})/\Delta l, \quad \gamma_2 = \ln(\lambda_2^{ij})/\Delta l \tag{2.57}$$

where $\Delta l = l_j - l_i$ and λ_1^{ij}, λ_2^{ij} are the mean value of the first and second pair of T^{ij}'s eigenvalues, respectively:

$$\lambda_1^{ij} = \frac{1}{2}\left(\lambda_{1T}^{ij} + \frac{1}{\lambda_{2T}^{ij}}\right), \quad \lambda_2^{ij} = \frac{1}{2}\left(\lambda_{3T}^{ij} + \frac{1}{\lambda_{4T}^{ij}}\right) \tag{2.58}$$

Following this two-mode calibration method, the properties of three SIWs with different widths, $a = 2,\ 3$, and 4 mm are calculated and compared with results obtained from [89], while the other parameters are chosen as $b = 1$ mm, $d = 0.25$ mm, $s = 0.5$ mm, $\sigma = 3.7e7$, $\tan\delta = 0.001$, and $\epsilon_r = 7.1$.

Fig. 2.15 shows the propagation constants of the three SIWs with the frequency normalised to their own cutoff. The attenuation constant, α, is for the TE$_{10}$ mode. Mode 2 starts to appear at $f/f_c = 2$, where the single-mode band ends. Based on the phase constant, β, of TE$_{10}$ mode in Fig. 2.15, we can use

$$a_e = \frac{\pi}{\sqrt{\epsilon_r k_0^2 - \beta^2}} \tag{2.59}$$

to find the equivalent width of a RWG completely filled with the same dielectric material, as shown in Fig. 2.16.

An interesting phenomenon is discovered here that the equivalent width, a_e, is weakly increasing with the frequency and tends to merge with a constant value given by [89] at the end of the single-mode band, *i.e.*, $f/f_c = 2$ (Note that results given by Formulas (8) and (9) are overlapping each other and thus, presented in one curve.). Therefore, a maximum discrepancy is indicated at the cutoff frequency,

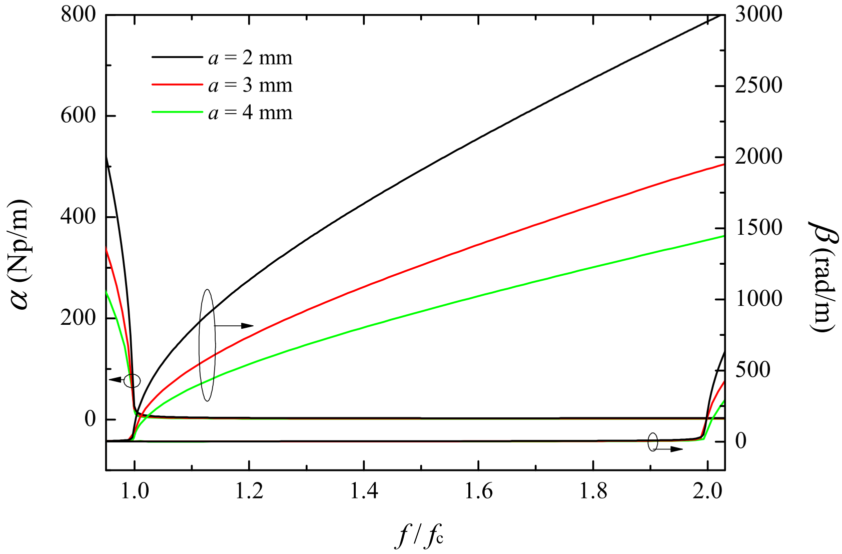

FIGURE 2.15: The propagation constants of three SIWs with different widths, $a = 2,\ 3$, and 4 mm.

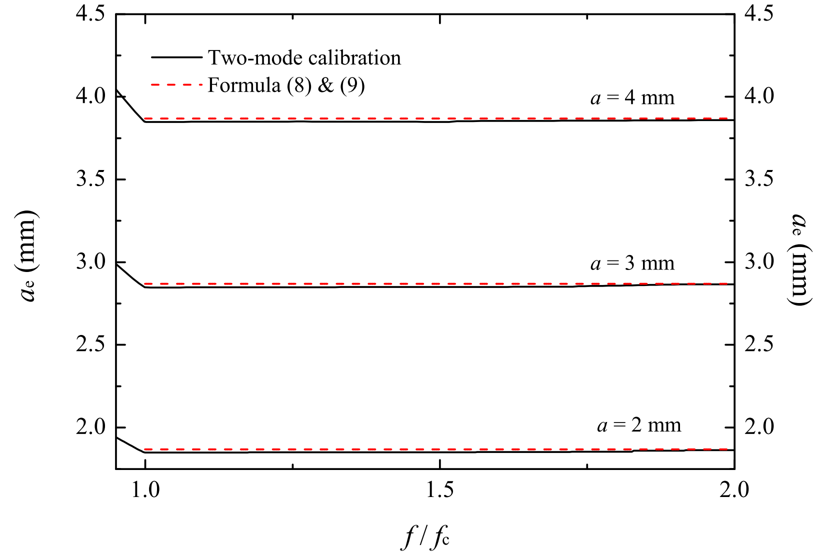

FIGURE 2.16: The equivalent width, a_e, of three SIWs with different widths (Formulas (8) and (9) are from K. Wu's method [89]).

TABLE 2.3: The equivalent width, a_e, from two-mode calibration method and K. Wu's method [89].

a (mm)	2	3	4
a_e (mm, Formula (8) in [89])	1.868	2.868	3.868
a_e (mm, two-mode calibration)	1.847	2.847	3.848

i.e., $f/f_c = 1$. In an ideal situation, the definition of the cutoff is where the phase constant, β, equals 0. In HFSS simulation, however, β takes a small positive value below the cutoff. Therefore, the new definition of the cutoff is where the largest leap of β happens, which is also where a_e stops dropping and tends to be stable in Fig. 2.16. To accurately determine the cutoff frequency, a_e at $f/f_c = 1$ is required.

a_e from both two-mode calibration method and [89] is shown in Tab. 2.3. A maximum discrepancy of 1.1% can be observed. Apparently, however, Formula (8) will match our results if the coefficient of the second term is adjusted slightly as

$$a_e = a - \frac{d^2}{0.817 \cdot s} \tag{2.60}$$

Other basic design rules with respect to s/d and a/d in [89] can be followed to minimize the leakage loss, ensure a proper TE_{m0} mode, *etc*.

2.4 HSIW

Combining the analysis in Sections 2.1 and 2.3, this section designs, fabricates and measures HSIWs at the mm-waves to achieve a low-loss transmission line comparable with an air-filled RWG.

2.4.1 Design

With the introduction of the EDC, ϵ_e, the partially-filled RWG can be viewed as one completely filled with an equivalent dielectric; while the SIW is also connected with its corresponding RWG based on the theory in [89]. So the theoretical analysis of HSIW can be the combination of them. Design steps of exact solutions for a HSIW with $b/a \leq 0.5$ are as followed:

1) Determine the cutoff frequency f_c of the TE$_{10}$ mode and hence, the single-mode band is $f_c \sim 2f_c$.

2) Determine s, d, a_1, and ϵ_r based on the materials and techniques available and make sure $s/d \leq 2$, $a_1/d \geq 2$.

3) Use (2.24) to find the width of the two-dielectric loaded RWG, a_p, for f_c and check if $a_p/d \geq 5$. If not, reduce f_c, d, or a_1 until it satisfies the condition. Numerical analysis is needed to solve this transcendental equation.

4) Use (2.21), (2.29), (2.30), and 2.39 to find the phase constant, β, and the complex EDC, ϵ_e. ϵ_e at several discrete frequency points can be solved first and then extrapolated to be a continuous curve. Now the partially-filled RWG has been transformed into one completely filled with a single dielectric.

5) Use (2.60) to find the width of the HSIW, a_h. Note that $a_e = a_p$. The height of the HSIW, b_h, enjoys a certain degree of flexibility and can be selected to the convenience of fabrication, loss requirements, *etc*.

6) Use the two-mode calibration method to find the loss characteristics, *i.e.*, α_c, α_d and α_r, where α_r is the radiation loss. HFSS based on the FEM method is needed to perform the 3D modelling.

Alternatively, if approximation is allowed, a much simpler route can be taken as follows (exact solutions throughout the single-mode band when $\epsilon_r = 7.1$):

1) Same as the exact method.

2) Choose one value from 0.05 to 0.35 with a 0.05 step for $p\sqrt{\epsilon_r}$ and determine s and d based on the materials and techniques available as long as $2 \leq \epsilon_r \leq 12$ and $s/d \leq 2$.

3) Use (2.27) to find the width of partially-filled RWG, a_p, for a prescribed cut-off frequency with a discrepancy less than 0.2%. Check if $a_p/d \geq 5$ and $pa_p \geq 2d$. If not, reduce f_c, d or increase p until it satisfies the condition.

4) Choose one equation from a set of (2.41) to find the complex EDC, ϵ_e, based on the $p\sqrt{\epsilon_r}$ value you already chose in Step 1), and hence, (2.29) to find the phase constant, β, when $f_c \leq f \leq 1.5f_c$. The maximum discrepancy of 0.4% for ϵ_{re} and 2% for $\tan\delta_e$ occurs at $f = 1.5f_c$. Now the partially-filled RWG has been transformed into one completely filled with a single dielectric.

TABLE 2.4: The configurational parameters (in mm) of WR28-like and WR15-like HSIWs.

HSIW	d	s	a_1	ϵ_r	a_p	a_h	a	b
WR28-like	0.30	0.60	0.70	7.1	7.08	7.26	7.11	1.32
WR15-like	0.25	0.50	0.50	7.1	3.71	3.87	3.76	1.32

5) Same as the exact method.

6) Same as the exact method.

Based on the steps discussed above, two HSIWs have been designed which have the same cutoff frequency as the standard WR28 (21.10 GHz) and WR15 (39.89 GHz), respectively. Both the exact and approximated method have been used. The results tend to be the same as ϵ_r of the dielectric is selected as 7.1.

Tab. 2.4 shows the configurational parameters of WR28-like and WR15-like HSIWs, where a is the width of a standard RWG. The propagation characteristics are shown in Fig. 2.17. The frequency has been normalised to the calculated cutoff, which is 21.21 GHz for WR28-like and 40.20 GHz for WR15-like. The loss tangent of LTCC is $\tan\delta = 0.001$ and the conductivity of silver paste is $\sigma = 3.7\text{e}7$ S/m. Standard WR28 and WR15 and corresponding dielectric-filled SIWs with the same cutoff frequencies have also been simulated by HFSS and results are shown as a comparison. Note that the height of the RWGs and SIWs is also 1.32 mm, the same as the HSIW.

In Fig. 2.17(a), the loss of SIW implied by the attenuation constant, α, is significantly larger than that of the HSIW. This has clearly verified the reduction of loss by removing the inner dielectric of the SIW. Compared with standard RWGs, the WR28-like HSIW is very close to a standard one in terms of attenuation; while WR15 is separated apart slightly. A possible explanation is that the conductor loss from the surface current flowing along the metallic posts gets severe, as the frequency rises. Another point to be noted is that the loss of WR15-like HSIW is obviously larger than that of WR28-like. This is probably results from the fact that the conductor loss, which rises with frequency, has accounted for the majority of the loss, as the dielectric has mostly been removed.

In Fig. 2.17(b), the cutoff frequency defined by the largest derivative of the phase constant, β, is close to that of standard RWGs (0.11 GHz deviation for WR28-like

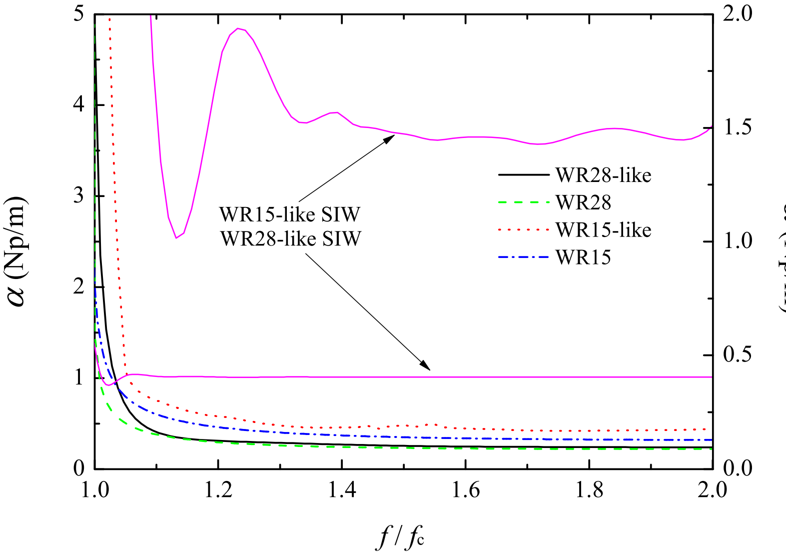

(a) the attenuation constant, α

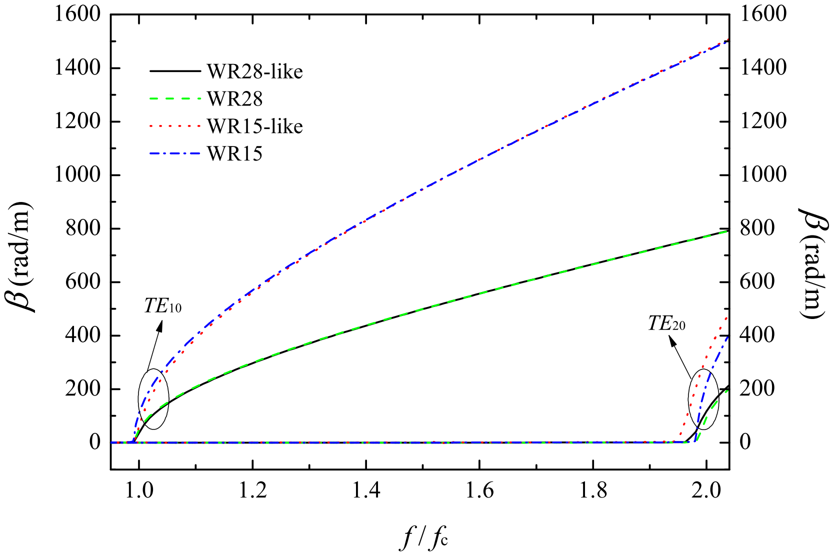

(b) the phase constant, β

FIGURE 2.17: The propagation characteristics of the WR28-like and WR15-like HSIWs in contrast with standard RWGs and SIWs.

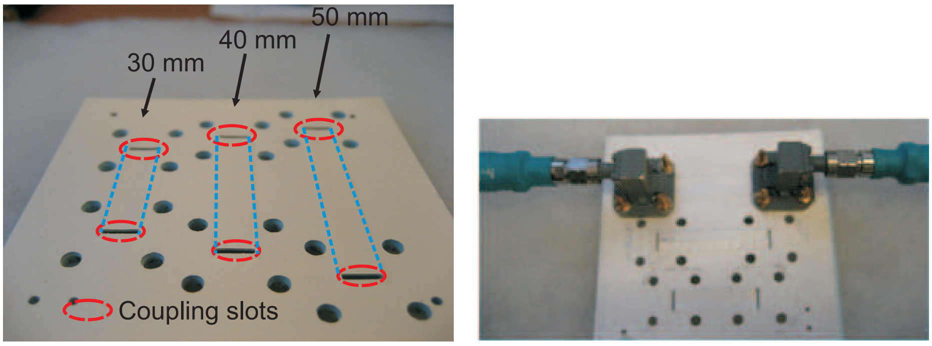

(a) sample (b) measurement fixture

FIGURE 2.18: The fabricated three WR28-like HSIWs.

HSIW and 0.31 GHz for WR15-like) for the TE_{10} mode. For the TE_{20} mode, however, that deviation doubles and can be clearly seen in Fig. 2.17(b).

2.4.2 Measurement

Due to the restriction of measurement equipments, only a WR28-like HSIW sample has been made and measured to verify the design, as shown in Fig. 2.18. Three HSIWs with an equal difference in length of 10 mm, *i.e.*, 30 mm, 40 mm, and 50 mm, are built into one panel using a progressive-lamination LTCC technique. The Dupont^{TM} GreenTape^{TM} 9K7 LTCC system with a relative dielectric constant of 7.1 is employed as the dielectric, while the silver paste with a conductivity of 3.7e7 S/m is adopted as the conductive material.

Regarding the feeding scheme, a back-to-back transversal slot-pair is employed to couple the energy in and out. The transmission loss, S_{21}, for each HSIW is measured, as shown in Fig. 2.19. As can be seen, the transmission loss has a relatively flat response in the frequency range of 30 - 35 GHz apart from multiple resonances probably due to the two feeding slots.

After that, the propagation constant of this WR28-like HSIW is thus extracted with the single-mode multiline calibration technique introduced in Section 2.3, since the measured result cannot differentiate those fundamental and higher-order modes. The result is shown in Fig. 2.20. To compare with the measurement, the simulated propagation constant using the two-mode multiline calibration technique has also been plotted in the same figure.

In Fig. 2.20, the measured phase constant, β, stays very close to the simulated one, including the cutoff frequency. As for the measured loss constant, α, it ripples

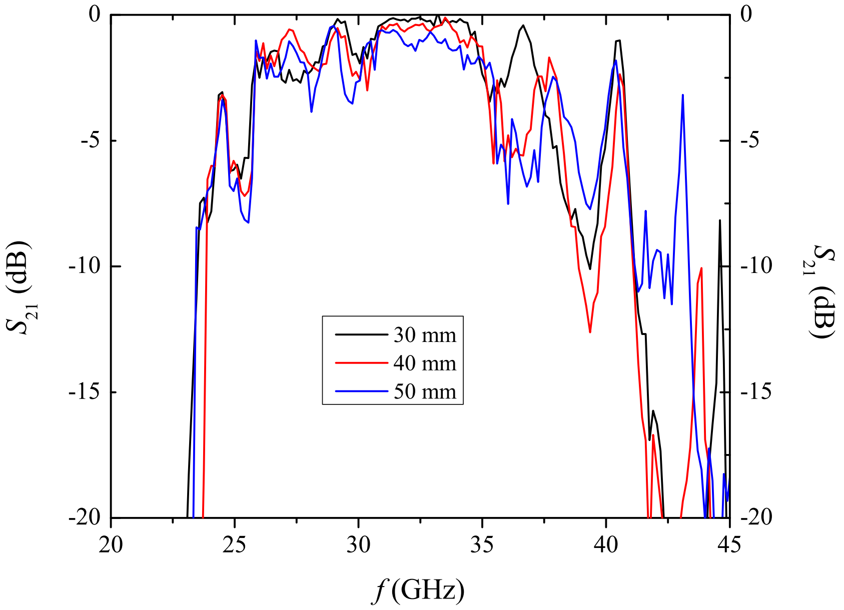

FIGURE 2.19: Measured S_{21} of the three HSIWs with lengths of 30 mm, 40 mm, and 50 mm.

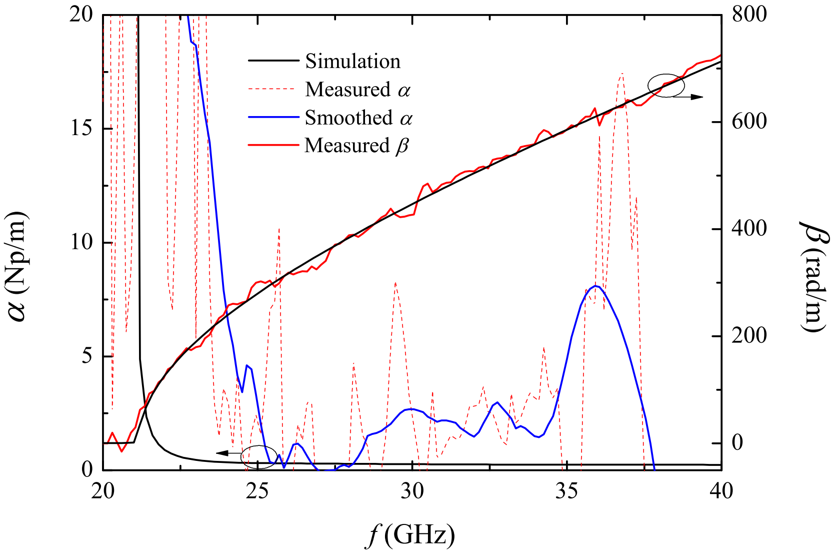

FIGURE 2.20: Extracted propagation constant of the WR28-like HSIW.

greatly and a Savitzky-Golay smoothing technique [103] has to be used to find out the figure shape and tendency, which is indicated by the blue line. As can be seen, α from 30 to 35 GHz ripples around 2 Np/m, whereas the simulated one is only 0.5 Np/m, which implies that the actual sample is more lossy. It is then assumed that α in other frequency ranges are about the same if the multiple resonances could be eliminated. The shape and tendency of the measured α agree with that of the simulated one, especially for the frequencies below 35 GHz, in that they both have a sharp drop near the cutoff frequency and tend to be flat afterwards. Finally, possible reasons for the high loss may lie in that the loss characteristics of materials (LTCC, silver paste) tend to be worsening at higher frequencies and minor fabrication errors are inevitable. Nevertheless, an average α of 2 Np/m or 17 dB/m is still an excellent loss performance.

2.5 Conclusion

By decomposing the HSIW into the two-dielectric loaded RWG and a standard SIW, this chapter builds up a systematic theory for the analysis and design of HSIW. A prototype operating in the Ka band is fabricated and the measured results suggest that the HSIW can work similarly to a standard RWG with the same cutoff frequency and slightly higher loss. The potential of HSIW to be integrated with other microwave components is highly desired and advantageous over standard RWGs.

Chapter 3

Dielectric Insular Image Guide

This chapter is organised as follows: firstly, a short review of the history and methodology for the dielectric guides is presented in Section 3.1. Then in Section 3.2, a traditional rectangular DIG is analysed in terms of both approximate and numerical methods among which the widely-used EDC method is improved and generalised for all aspect ratios. Finally, the DIIG is analysed and designed to show an improved loss performance on the DIG with measurement given to verify the validility in Section 3.3.

3.1 Introduction

3.1.1 History

The study of the dielectric guide (DG) started as early as 1910 when Hondros *et al.* analysed the propagation characteristics of electromagnetic waves along cylindrical DGs. Although further investigations were carried out both theoretically and experimentally in the following decades, the progress of the DG in practice was overshadowed by the rapid development of metal waveguides during the 1940s [104].

The 1950s saw the revival of the DG used for microwave and millimetre wave integrated circuits as they are easier to be manufactured compared with 3D metal waveguides. A metallic layer or surface, however, is inevitable for transmission lines in microwave and millimetre wave circuits for use as a mechanical support, heat sink, DC bias and for integration with other components. This brings about

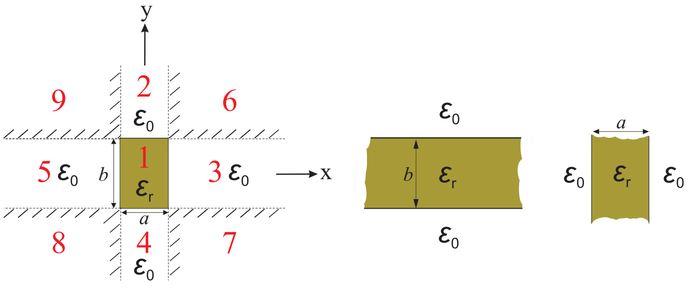

(a) (b)

FIGURE 3.1: (a) Marcatili's DG model, (b) equivalent horizontal and vertical slab guides (For simplicity, the surrounding dielectric is assumed to be air.)

a new configuration on the DG by incorporating a large pure metallic layer at the bottom of the dielectric guide, popularly referred to as the dielectric image guide (DIG) which is the simplest millimetre-wave dielectric integrated guide structure [104] and was first proposed by King in 1952 [105]. After that, a variety of dielectric transmission lines was proposed based on this rectangular DIG, including dielectric insular image guide (DIIG) [106–109], dielectric slab guide [107, 110], inverted strip dielectric waveguide [108], cladded rectangular dielectric image guide [111], *etc.*

3.1.2 Theoretical Methods

Together with the development of DG applications came various theoretical investigations to qualitatively and quantitively characterise the propagation and dispersion characteristics of the electromagnetic wave inside and in the vicinity of the DG in its various forms. Since there are no closed-form solutions to rigorously describe the wave behaviour, unlike the case in the metallic waveguide, the methods to be reviewed here are all essentially approximate, although they are all reasonably close to the actual field distribution.

3.1.2.1 Approximate Methods

Marcatili's paper [112] in 1969 is the earliest and most comprehensive effort to give a deep insight into the waveguiding mechanisms of the low-permittivity rectangular DG during this period. In this paper, Marcatili introduced an approximate solution by neglecting the electromagnetic fields of certain field regions as shown in Fig. 3.1(a). Firstly, E. Marcatili divides the DG and its surroundings into 9 regions. Then, he simplifies this boundary value problem by making two assumptions:

(a) For well-guided modes, the fields decay exponentially in Regions 2, 3, 4 and 5 and hence, a small portion of the energy travels in these regions with even less in the shaded Regions 6, 7, 8 and 9. Consequently, the fields are matched only along the sides of the DG and only a small error should be introduced into the field calculation if the shaded regions were removed from this DG model. These assumptions will inherently lead to the following wavenumber relations:

$$k_x = k_{x1} = k_{x2} = k_{x4} \tag{3.1a}$$

$$k_y = k_{y1} = k_{y3} = k_{y5} \tag{3.1b}$$

where k_{xi} and k_{yi}, i=1, 2, $\cdots$ 5, are the transverse propagation constants along the x- and y-direction in the ith region, respectively.

(b) The permittivity of the dielectric rod must be low, which guarantees the internal total reflection at grazing angles within the dielectric rod.

We take a deeper look at Marcatili's Assumption (a) and found that there is always one of the subequations, (3.1a) and (3.1b) slightly more accurate than the other for a specific configuration (except when $b/a = 1$), although they are all reasonably correct. Suppose the aspect ratio, $b/a \ll 1$, the wave behaviour will certainly approach the horizontal slab guide rather than the vertical one, resulting in (3.1a) rather than (3.1b). It is the other way around when $b/a \gg 1$. So, it is expected that (3.1a) holds more strongly when b/a <1 and (3.1b) is closer to the actual situation when $b/a > 1$.

Based on all the preceding assumptions, Marcatili has calculated the propagation constants and provided a solution for both a single and two coupled DGs in the form of transcendental equations, which is further approximated into a closed form. With the establishment of characteristic equations for this boundary value problem, it is then found that this DG model can be split into two independent and simpler slab guides with infinite extension along one single direction, respectively, *i.e.*, the horizontal and vertical slab guides, as shown in Fig. 3.1(b) [112].

In 1970, Knox *et al.* followed Marcatili's approximation and introduced an EDC method, which was applied to the DIG shown in Fig. 3.2(a) and showed possible microwave and millimetre wave applications. Up until now, it is still the most commonly used method for calculating the propagation characteristics of the rectangular DG [113]. Through the image theory, it can be inferred that DIG

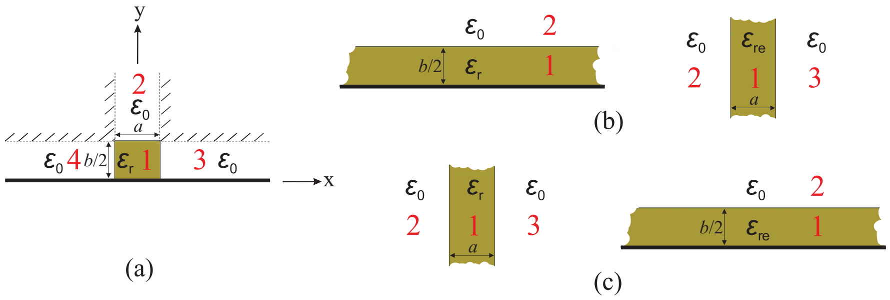

FIGURE 3.2: (a) Knox's DIG model, (b) equivalent horizontal (ϵ_r) and vertical (ϵ_{re}) slab guides (c) equivalent vertical (ϵ_r) and horizontal (ϵ_{re}) slab guides.

represents the top half of a rectangular DG of twice the height, except that certain modes are shorted out by the metallic ground plane and hence suppressed. This is a distinct advantage over the DG, giving a much wider frequency bandwidth for single mode operation [104].

In addition to Marcatili's assumptions, Knox *et al.* assume that the aspect ratio of the DIG, $b/a \leq 1$ (low aspect ratio), which aims for a non-variation of the fields in the x direction and in other words, (3.1b) holds. Then the DIG model can be split into two infinite slab guides, as is the case for Marcatili's DG model. Fig. 3.2(b) shows this transformation and the difference from Marcatili's model, where the dielectric constant of the vertical slab guide is an EDC, ϵ_{re} [113]. It's also worth noting that a modification to Knox's DIG model is made here where the ground plane is removed from the vertical slab guide to accommodate the tangential electric components, *i.e.*, E_x and E_z.

The derivation process is demonstrated in [113] and summarised as follows:

Firstly, the infinite horizontal slab guide shown in Fig. 3.2(b) is analysed. k'_x (=0) and k_y are the guided propagation constant in the x and y direction, respectively. Then, the propagation constant in the z direction, namely phase constant under a low-loss situation, β', satisfies

$$\begin{aligned}\beta'^2 &= \epsilon_r k_0^2 - k_y^2 \\ &= k_0^2 \left[\epsilon_r - \left(\frac{k_y}{k_0} \right)^2 \right] \\ &= k_0^2 \epsilon_{re} \end{aligned} \tag{3.2}$$

where ϵ_{re} is defined by

$$\epsilon_{re} = \epsilon_r - \left(\frac{k_y}{k_0} \right)^2 \tag{3.3}$$

and k_0 is the free space wavenumber.

Secondly, since an effective dielectric constant, ϵ_{re} is introduced, a new uniform medium is generated, which is a new vertical slab guide shown in Fig. 3.2(b). Here contrary to that in the horizontal slab guide model, $k'_y = 0$, while k_x is nontrivial. Likewise, the propagation constant of the final DIG satisfies:

$$\begin{aligned} \beta^2 &= \beta'^2 - k_x^2 \\ &= \epsilon_{re} k_0^2 - k_x^2 \end{aligned} \tag{3.4}$$

With a deep look into this process, it's found that k_x is obtained from the horizontal guide and then k_y is from the vertical guide, which is exactly the same route with Marcatili's method. A different dielectric constant, however, will certainly differentiate the two methods.

In fact, Knox *et al.* have only presented one type of this EDC method, *i.e.*, EDC-H which starts with a horizontal slab guide. As shown in Fig. 3.2(c), one may also start the analysis with a vertical slab guide whose dielectric constant is ϵ_r and then form a horizontal slab guide with a uniform effective dielectric constant, ϵ_{re}. This supplementary EDC method is named as EDC-V. The key to this analysis order lies with the aspect ratio. If the aspect ratio, b/a, is smaller than 1, better to start with the horizontal guide and vice versa. This will result in a more accurate result by Marcatili's first assumption. With this flexibility, the EDC method takes an advantage to be potentially more accurate through suitable analysis order over Marcatili's method which doesn't account for the aspect ratio.

The characteristic equations as to find solutions of k_x and k_y will be explicitly explained in Section 3.2.

An improvement on these approximation methods was made near the cutoff frequency in 1988 by J. Xia *et al.* They introduced a new factor F_0/F_1, (which equals 1 at high frequencies as in Marcatili's and EDC method; while deviates from 1 at low frequencies) into the transcendental characteristic equation and found that the propagation losses will be lowered and the fields will be more effectively confined within the guide in the vicinity of the cutoff frequency. So it will be helpful to design the DIG in a way so that it operates near the cutoff to achieve a low-loss performance [114].

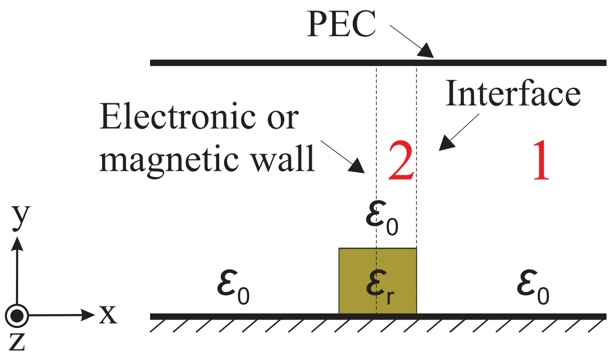

FIGURE 3.3: The cross-sectional view of the DIG model for applying the mode-matching method [115].

3.1.2.2 Rigorous Methods

Attention should be paid to how the approximation is made in Marcatili's and EDC methods so as to improve the accuracy by taking into account what's been neglected, although closed-form solutions can't be achieved and the workload is substantially increased. Research on this subject has been carried out, which gives rise to the mode-matching method [109, 115, 116], the generalised telegrapher's equations [107] and the finite element iterative method [117], *etc.* All these numerical methods tolerate the existence of geometrical discontinuities which enable the coupling among different modes and create hybrid ones [118].

Here the mode-matching method is taken as an example. In order to define a proper eigenvalue problem, a perfect electric conductor (PEC) is placed on top of the DIG, which is also parallel to the ground plane. A large distance from the PEC to the ground plane is chosen to minimize the field distortion by the PEC, as shown in Fig. 3.3. The guided modes in the DIG generally have all the components of E and H fields. Because of the symmetry of the structure, however, they can be divided into even and odd modes and only half plane of the structure (divided by an electronic or magnetic wall) needs to be considered. Further, the region under consideration continues to be divided into two subregions (1 and 2) and the fields in each region can be expanded in terms of its eigenfunctions, which is a set of infinite harmonics. Finally, the fields at the interface are matched by applying boundary conditions and solved for the propagation constant as well as for the field distribution. Ideally, this mode-matching method will bring about an exact solution for the characterization of DIGs. In practice, however, one must choose a limited number of harmonics. Consequently, an approximated solution will be yielded with its accuracy depending on the volume of harmonics and the capacity of the computers [109, 115].

Through rigorous analysis, it's found that all 6 components of electric and magnetic fields exist in the rectangular DG/DIG [118]. By neglecting one of the weakest electric or magnetic component, however, the modes of the DG/DIG can be grouped into TE-like and TM-like ones, which is essentially how the approximate methods solve this problem.

As for the wave pattern, it tends to be standing inside the DG/DIG, whereas decaying exponentially with distance outside it in the x and y directions; while in the z direction, it's travelling suppose the transmission line is infinitely long or perfectly matched.

3.2 DIG

In this section, both the approximate and numerical methods disscussed in Section 3.1 are used to characterise the DG/DIG in terms of propagation and attenuation. Results are presented and comparisons are made amongst various methods.

As for the characterisation of the rectangular DG/DIG, there are mainly two approximate methods, namely Marcatili's method and the EDC method, which are widely accepted and applied. The basic rules are followed here, whereas reasonable modifications and extensions are also made.

In this thesis, only the DIG model will be discussed, as it has the potential to be applied and integrated in the microwave band. In fact, with the existence of the metallic ground plane, certain modes that are guided in the DG are shorted out in the DIG. Apart from that, the DIG and DG of twice its height are equivalent.

As discussed in Chapter 2, the electric and magnetic fields are characterised by (2.1) for a infinitely-long and uniformly-distributed transmission line. The transverse and longitudinal field components can be further decomposed and retain a relation regulated by (2.4).

Before the boundary conditions are formulated, take on board that the DIG model can be approximately split into two infinite slab guides, as shown in Fig. 3.2.

Then, the boundary condition for the horizontal slab guide is given as follows:

$$\begin{aligned} &E_p|_{y=0} = 0,\ E_p|_{y\to\infty} \to 0 \\ &A_{p1} = A_{p2}|_{y=b/2} \end{aligned} \tag{3.5}$$

and that for the vertical slab guide is:

$$E_q|_{x\to\infty} \to 0 \tag{3.6a}$$

$$A_{q1} = A_{q2}|_{x=-a/2},\ A_{q1} = A_{q3}|_{x=a/2} \tag{3.6b}$$

where A denotes E or H, p denotes x or z and q denotes y or z.

After the establishment of this boundary value problem, the theoretical analysis will be based on the two slab guides individually. An infinite slab guide can only support the TM or TE mode, which means none of the TEM or hybrid modes exists [99]. Therefore, the propagating modes in the DIG will be grouped into two families: TM-like (with E_y and H_x as the main field components) and TE-like (with E_x and H_y as the main field components), which is in line with the conclusions in [104, 112]. Note that the TE/TM modes for a slab guide are conventionally defined with respect to the z direction ($\mathrm{TM}^z/\mathrm{TE}^z$), while those for the DIG are defined with respect to the y direction ($\mathrm{TM}^y/\mathrm{TE}^y$).

The following analysis will start with the TM^y_{mn} mode, followed by the TE^y_{mn} mode in a similar manner.

3.2.1 TM^y_{mn} Mode

The TM^y_{mn} mode in the DIG will require a TM^z_n mode in the horizontal slab guide and a TE^z_m mode in the vertical one, based on the consistency of main field components in each guide. Hence, the analysis will be based on the two guides individually and then combine them together to generate the overall characterisation.

Suppose the aspect ratio, $b/a < 1$ and thus the EDC-H method is employed, which demands the horizontal slab guide to be first analysed. If $b/a > 1$, the vertical slab guide will be studied first with the EDC-V method. Either method is suitable for the case of $b/a = 1$. As for the Marcatili's method, it's not sensitive to the analysis order.

3.2.1.1 Horizontal Slab Guide

Since there is no field variation in the x direction, the Helmholtz's equation (2.2) for the TM_n^z mode can be simplified as

$$\left(\frac{\partial^2}{\partial y^2}+k_{yi}^2\right)E_z=0, \quad i=1,\ 2 \tag{3.7}$$

where $k_{yi},\ i=1,\ 2$, is the cutoff wavenumber in Regions 1 and 2, respectively, and defined as

$$\begin{aligned} k_{y1}&=\sqrt{\epsilon_r k_0^2-\beta_h^2}\\ k_{y2}&=\sqrt{k_0^2-\beta_h^2} \end{aligned} \tag{3.8}$$

where β_h is the phase constant of the horizontal slab guide.

Since the fields in Region 2 of the horizontal guide are exponentially attenuating along the y direction, k_{y2} is essentially a pure imaginary number. Hence, to obtain a positive real number, k_{y0} is introduced as

$$\begin{aligned} k_{y0}&=\sqrt{\beta_h^2-k_0^2}\\ &=\sqrt{(\epsilon_r-1)k_0^2-k_{y1}^2} \end{aligned} \tag{3.9}$$

Solve (3.7) and apply the boundary condition, (3.5), to obtain the field components, E_z, E_y, and H_x as

$$\begin{aligned} E_{z1}&=A_1\sin(k_{y1}y)\\ E_{z2}&=A_1\sin(k_{y1}b/2)\mathrm{e}^{k_{y0}(b/2-y)}\\ E_{y1}&=\frac{-jA_1\beta_h}{k_{y1}}\cos(k_{y1}y)\\ E_{y2}&=\frac{-jA_1\beta_h}{k_{y0}}\sin(k_{y1}b/2)\mathrm{e}^{k_{y0}(b/2-y)}\\ H_{x1}&=-\frac{\omega\epsilon}{\beta_h}E_{y1}\\ H_{x2}&=-\frac{\omega\epsilon_0}{\beta_h}E_{y2} \end{aligned} \tag{3.10}$$

where A_1 is an arbitrary constant. ϵ (complex if lossy) and ϵ_0 are the permittivity of the DIG and free space, respectively. The characteristic equation is then found to be

$$1 - \frac{k_{y1}}{\epsilon_r k_{y0}} \tan(k_{y1}b/2) = 0 \tag{3.11}$$

or for the convinience of calculation, transformed into

$$k_{y1}b = -2\arctan\left(\frac{k_{y1}}{\epsilon_r k_{y0}}\right) + n\pi \tag{3.12}$$

where

$$n = 2n' - 1, \quad n' = 1,\ 2,\ 3,\ \cdots$$

Note that n, which stands for the number of field variations in the y direction, can only be odd for the TM^y_{mn} mode in the DIG.

3.2.1.2 Vertical Slab Guide

In this case, the electromagnetic fields are non-variant along the y direction, which reduces the Helmholtz's equation (2.2) for the TE^z_m mode into

$$\left(\frac{\partial^2}{\partial x^2} + k_{xi}^2\right) H_z = 0, \quad i = 1,2,3 \tag{3.13}$$

where $k_{xi},\ i = 1,\ 2,\ 3$, is the cutoff wavenumber in Regions 1, 2, and 3, respectively, and defined as

$$\begin{aligned} k_{x1} &= \sqrt{\epsilon_r' k_0^2 - \beta_v^2} \\ k_{x2} = k_{x3} &= \sqrt{k_0^2 - \beta_v^2} \end{aligned} \tag{3.14}$$

where β_v is the phase constant of the vertical slab guide and ϵ_r' is the new relative dielectric constant defined as

$$\begin{aligned} \epsilon_r' &= \epsilon_r, & &\text{Marcatili's method} \\ &= \epsilon_{re} = \epsilon_r - \left(\frac{k_{y1}}{k_0}\right)^2, & &\text{EDC method} \end{aligned} \tag{3.15}$$

Since the fields in Regions 2 and 3 of the vertical guide are exponentially attenuating along the x direction, a positive real number, k_{x0}, is introduced to replace

k_{x2} and k_{x3}, where

$$\begin{aligned} k_{x0} &= \sqrt{\beta_v^2 - k_0^2} \\ &= \sqrt{(\epsilon_r' - 1)k_0^2 - k_{x1}^2} \end{aligned} \tag{3.16}$$

Since the vertical slab guide has a finite symmetrical structure (the dielectric rod), the fields can be either symmetrical or asymmetrical, namely even or odd. Note that the classification of even/odd modes here is based on the transversal electric component, E_y. Then, the even mode is chosen to be analysed first.

Solve (3.13) and apply the boundary condition, (3.6a), to obtain the general solutions of H_z as:

$$\begin{aligned} H_{z1} &= A_1' \sin(k_{x1}x) + A_2' \cos(k_{x1}x) \\ H_{z2} &= A_3' \mathrm{e}^{k_{x0}(x+a/2)} \\ H_{z3} &= A_4' \mathrm{e}^{-k_{x0}(x-a/2)} \end{aligned} \tag{3.17}$$

and then, E_y, in Regions 2 and 3 as:

$$\begin{aligned} E_{y2} &= \frac{-jA_3'\omega\mu}{k_{x0}} \mathrm{e}^{k_{x0}(x+a/2)} \\ E_{y3} &= \frac{jA_4'\omega\mu}{k_{x0}} \mathrm{e}^{-k_{x0}(x-a/2)} \end{aligned} \tag{3.18}$$

where μ is the permeability of the DIG.

(a) Even mode

Under the circumstances of the even mode,

$$E_{y2}|_{x=-x_0} = E_{y3}|_{x=x_0}, \quad a/2 \leq x_0 < \infty \tag{3.19}$$

which gives

$$A_4' = -A_3' \tag{3.20}$$

Now, we apply the boundary condition of continuous E_y at two interfaces, (3.6b), to obtain

$$\begin{aligned} \frac{j\omega\mu}{k_{x1}}\left[A_1'\cos(k_{x1}a/2) + A_2'\sin(k_{x1}a/2)\right] &= \frac{-jA_3'\omega\mu}{k_{x0}} \\ \frac{j\omega\mu}{k_{x1}}\left[A_1'\cos(k_{x1}a/2) - A_2'\sin(k_{x1}a/2)\right] &= \frac{-jA_3'\omega\mu}{k_{x0}} \end{aligned} \tag{3.21}$$

which gives

$$A_2' = 0 \tag{3.22a}$$

$$A_1'k_{x0}\cos(k_{x1}a/2) + A_3'k_{x1} = 0 \tag{3.22b}$$

Again, we apply the boundary condition of continuous H_z at the interface between Regions 1 and 2 or 1 and 3, (3.6b), to obtain

$$A_1'\sin(k_{x1}a/2) + A_3' = 0 \tag{3.23}$$

Then, we combine (3.22b) and (3.23) to obtain the characteristic equation as:

$$1 - \frac{k_{x1}}{k_{x0}}\tan\left(k_{x1}a/2\right) = 0 \tag{3.24}$$

or for the convinience of calculation, transformed into

$$k_{x1}a = -2\arctan\left(\frac{k_{x1}}{k_{x0}}\right) + m\pi \tag{3.25}$$

where

$$m = 2m' - 1, \quad m' = 1,\ 2,\ 3,\ \cdots$$

Note that m, which represents the number of field variations in the x direction, can only be odd for the even TM^y_{mn} mode in the DIG.

Finally, the field components of even mode for the vertical slab guide are given as

$$\begin{aligned}
H_{z1} &= A_2 \sin(k_{x1}x) \\
H_{z2} &= -A_2 \sin(k_{x1}a/2)\mathrm{e}^{k_{x0}(x+a/2)} \\
H_{z3} &= A_2 \sin(k_{x1}a/2)\mathrm{e}^{-k_{x0}(x-a/2)} \\
E_{y1} &= \frac{jA_2\omega\mu}{k_{x1}} \cos(k_{x1}x) \\
E_{y2} &= \frac{jA_2\omega\mu}{k_{x0}} \sin(k_{x1}a/2)\mathrm{e}^{k_{x0}(x+a/2)} \\
E_{y3} &= \frac{jA_2\omega\mu}{k_{x0}} \sin(k_{x1}a/2)\mathrm{e}^{-k_{x0}(x-a/2)} \\
H_{xi} &= -\frac{\beta_v}{\omega\mu}E_{yi}, \quad i = 1,\ 2,\ 3
\end{aligned} \tag{3.26}$$

where A_2 has replaced A_1' as an arbitrary constant.

(b) Odd mode

The analysis of the odd mode is following the same route as that of even mode. In this case,

$$A_4' = A_3' \tag{3.27}$$

and the characteristic equation is thus derived as

$$1 + \frac{k_{x0}}{k_{x1}} \tan\left(k_{x1}a/2\right) = 0 \tag{3.28}$$

or for the convinience of calculation, transformed into

$$k_{x1}a = -2\arctan\left(\frac{k_{x1}}{k_{x0}}\right) + m\pi \tag{3.29}$$

where

$$m = 2m', \quad m' = 1,\ 2,\ 3,\ \cdots$$

Note that for the odd TM_{mn}^{y} mode in the DIG, m can only be even.

Finally, the field components of odd mode for the vertical slab guide are given as

$$\begin{aligned}
H_{z1} &= A_3 \cos(k_{x1}x) \\
H_{z2} &= A_3 \cos(k_{x1}w/2)\mathrm{e}^{k_{x0}(x+w/2)} \\
H_{z3} &= A_3 \cos(k_{x1}w/2)\mathrm{e}^{-k_{x0}(x-w/2)} \\
E_{y1} &= \frac{-jA_3\omega\mu}{k_{x1}} \sin(k_{x1}x) \\
E_{y2} &= \frac{-jA_3\omega\mu}{k_{x0}} \cos(k_{x1}w/2)\mathrm{e}^{k_{x0}(x+w/2)} \\
E_{y3} &= \frac{jA_3\omega\mu}{k_{x0}} \cos(k_{x1}w/2)\mathrm{e}^{-k_{x0}(x-w/2)} \\
H_{xi} &= -\frac{\beta_v}{\omega\mu}E_{yi}, \quad i = 1,\ 2,\ 3
\end{aligned} \tag{3.30}$$

where A_3 has replaced A_2' as an arbitrary constant.

With all three characteristic equations given, it can then be summarised that for the TM^y_{mn} mode, n can only be odd and if m is odd, the TM^y_{mn} mode is even; vice versa.

3.2.1.3 Phase Constant, β

Now the solutions from horizontal and vertical slab guides are combined to find the phase constant, β, of the DIG as shown in Fig. 3.2(a). In order to do that, the field components in both guides must agree. From the preceding analysis, it can be found that the field components for the TM modes in horizontal guide are E_z, E_y, and H_x, while those for the TE mode in vertical guide are H_z, E_y, and H_x. With Marcatili's Assumption (b), however, this disagreement can be resolved. Since the dielectric constant of DIG, ϵ_r, is low and close to 1, only modes impinging at grazing angles can be propagating, which means

$$\beta_h \gg k_{y1}, \quad \beta_v \gg k_{x1} \tag{3.31}$$

Hence, through (3.10), (3.26), and (3.30),

$$\begin{aligned}
&E_y,\ H_x \gg E_z, \quad \text{Horizontal slab guide} \\
&E_y,\ H_x \gg H_z, \quad \text{Vertical slab guide}
\end{aligned} \tag{3.32}$$

Therefore, E_z and H_z are neglidible in their corresponding guide and the main field components agree on E_y and H_x for the TM^y mode in the DIG.

From the analysis of horizontal slab guide, the wavenumber of the DIG in the y direction, k_y, is found out, *i.e.*, $k_y = k_{y1}$; while that in the x direction, k_x, is obtained as $k_x = k_{x1}$. Hence, that in the z direction in a lossless situation, β, also known as phase constant, is derived as

$$\begin{aligned} \beta &= \sqrt{\epsilon_r k_0^2 - k_x^2 - k_y^2} \\ &= \sqrt{\epsilon_r k_0^2 - k_{x1}^2 - k_{y1}^2} \end{aligned} \tag{3.33}$$

In terms of the expressions for field components in each region of Fig. 3.2(a), they are now restrained by both x and y dimensions and are actually the product of field expressions in each slab guide. The only difference lies in that the amplitude of the new field expressions should take the square root of the product. Since the TM$^y_{11}$ mode has a symmetrical distribution of transverse electric fields, it belongs to the even-mode family and is given as

$$\begin{aligned} E_{y1} &= A\sqrt{\frac{\omega\mu\beta_h}{k_{x1}k_{y1}}}\cos(k_{x1}x)\cos(k_{y1}y) \\ E_{y2} &= A\sqrt{\frac{\omega\mu\beta_h}{k_{x1}k_{y0}}}\sin(k_{y1}b/2)\cos(k_{x1}x)\mathrm{e}^{-k_{y0}(y-b/2)} \\ E_{y3} &= A\sqrt{\frac{\omega\mu\beta_h}{k_{x0}k_{y1}}}\sin(k_{x1}a/2)\cos(k_{y1}y)\mathrm{e}^{-k_{x0}(x-a/2)} \\ E_{y4} &= A\sqrt{\frac{\omega\mu\beta_h}{k_{x0}k_{y1}}}\sin(k_{x1}a/2)\cos(k_{y1}y)\mathrm{e}^{k_{x0}(x+a/2)} \\ H_{x1} &= \sqrt{\frac{\epsilon\beta_v}{\mu\beta_h}}E_{y1} \\ H_{xi} &= \sqrt{\frac{\epsilon_0\beta_v}{\mu\beta_h}}E_{yi}, \quad i = 2,\ 3,\ 4 \end{aligned} \tag{3.34}$$

where A has substituted $\pm\sqrt{A_1 A_2}$ as an arbitrary constant.

The derivation of field expression for the odd mode can follow a similar route and will not be presented here for simplicity.

By this stage, the propagation characteristic of the rectangular DIG has been analysed and demonstrated.

3.2.1.4 Attenuation Constant, α

Due to the finite conductivity, the complex dielectric constant and the open boundary, attenuation in the rectangular DIG is inevitable, which is characterised by the attenuation constant, α. Consequently, α is composed of three constituents: α_c, conductor loss, α_d, dielectric loss, and α_r, radiation loss.

To find the attenuation constant, α_c, α_d and α_r, the perturbation method in [99] will be applied here.

By assuming that the fields of low-loss transmission lines are not greatly different from those of lossless lines, which is accurate enough, the attenuation constant, α, can be derived as:

$$\alpha = \frac{P_l}{2P} = \frac{P_{lc} + P_{ld} + P_{lr}}{2P} = \alpha_c + \alpha_d + \alpha_r \tag{3.35}$$

where P is the total power flow and P_l is the total power loss at a certain cross section along the transmission line. Then P_l can be decomposed into P_{lc}, conductor power loss, P_{ld}, dielectric power loss, and P_{lr}, radiation power loss.

Firstly, find P through

$$\begin{aligned} P &= P_1 + P_2 + P_3 + P_4 \\ &= \frac{1}{2}\mathrm{Re}\int_S \bar{E} \times \bar{H}^* \cdot \hat{z}\ \mathrm{d}s \end{aligned} \tag{3.36}$$

where S is an area that encompasses Regions 1, 2, 3, and 4, as depicted in Fig. 3.2(a) and P_i, $i = 1,\ 2,\ 3,\ 4$, is their corresponding power flow:

$$\begin{aligned} P_1 &= \frac{1}{2}\mathrm{Re}\int_{S_1} E_{y1}H_{x1}^*\ \mathrm{d}s \\ &= \frac{|A|^2\omega\sqrt{\mu\beta_h\beta_v\mathrm{Re}(\epsilon)}}{16}\,\frac{k_{x1}a + \sin(k_{x1}a)}{k_{x1}^2}\,\frac{k_{y1}b + \sin(k_{y1}b)}{k_{y1}^2} \end{aligned} \tag{3.37a}$$

$$\begin{aligned} P_2 &= \frac{1}{2}\mathrm{Re}\int_{S_2} E_{y2}H_{x2}^*\ \mathrm{d}s \\ &= \frac{|A|^2\omega\sqrt{\mu\epsilon_0\beta_h\beta_v}}{8}\,\frac{k_{x1}a + \sin(k_{x1}a)}{k_{x1}^2}\,\frac{\sin^2(k_{y1}b/2)}{k_{y0}^2} \end{aligned} \tag{3.37b}$$

$$\begin{aligned} P_3 &= P_4 \\ &= \frac{1}{2}\mathrm{Re}\int_{S_4} E_{y4}H_{x4}^{*}\ \mathrm{d}s \\ &= \frac{|A|^2\omega\sqrt{\mu\epsilon_0\beta_h\beta_v}}{16}\frac{\sin^2(k_{x1}a/2)}{k_{x0}^2}\frac{k_{y1}b+\sin(k_{y1}b)}{k_{y1}^2} \end{aligned} \tag{3.37c}$$

where it's assumed that $\mathrm{Re}(\epsilon) = \epsilon_r\epsilon_0 \approx |\epsilon|$ in a low-loss situation and hence, $\mathrm{Re}(\sqrt{\epsilon}) \approx \sqrt{\mathrm{Re}(\epsilon)}$.

Secondly, find P_{lc} through

$$\begin{aligned} P_{lc} &= P_{lc1} + P_{lc3} + P_{lc4} \\ &= \frac{R_s}{2}\int_C |\bar{H}_t|^2\ \mathrm{d}l \end{aligned} \tag{3.38}$$

where R_s is surface impedance of the ground metal with a conductivity of σ, $R_s = \sqrt{\omega\mu/(2\sigma)}$ and $\bar{H}_t$ is tangential magnetic field with respect to the integral route, C, which is a line along the ground plane at a certain cross section that encompasses Lines 1, 3, and 4, as depicted in Fig. 3.2(a). P_{lci}, $i = 1,\ 3,\ 4$, is their corresponding power loss due to a finite σ:

$$\begin{aligned} P_{lc1} &= \frac{R_s}{2}\int_{C_1} |H_{x1}|^2\ \mathrm{d}l \\ &= \frac{R_s}{4}\frac{|A|^2\omega\beta_v\mathrm{Re}(\epsilon)}{k_{y1}}\frac{k_{x1}a+\sin(k_{x1}a)}{k_{x1}^2} \end{aligned} \tag{3.39a}$$

$$\begin{aligned} P_{lc3} &= P_{lc4} \\ &= \frac{R_s}{2}\int_{C_4} |H_{x4}|^2\ \mathrm{d}l \\ &= \frac{R_s}{4}\frac{|A|^2\omega\epsilon_0\beta_v}{k_{y1}}\frac{\sin^2(k_{x1}a/2)}{k_{x0}^2} \end{aligned} \tag{3.39b}$$

Thirdly, find P_{ld} through

$$\begin{aligned} P_{ld} &= P_{ld1} \\ &= \frac{\omega\epsilon''}{2}\int_S |\bar{E}|^2\ \mathrm{d}s \end{aligned} \tag{3.40}$$

where $\epsilon'' = \epsilon_0\epsilon_r\tan\delta$ is the imaginary part of ϵ and $\tan\delta$ represents the dielectric loss tangent. Here S is only Region 1 where the lossy dielectric exists and P_{ld_1} is the corresponding dielectric power loss:

$$\begin{aligned} P_{ld1} &= \frac{\omega\epsilon''}{2}\int_{S_1} |E_{y1}|^2 \, \mathrm{d}s \\ &= \frac{|A|^2\omega^2\mu\epsilon''\beta_h}{16}\frac{k_{x1}a+\sin(k_{x1}a)}{k_{x1}^2}\frac{k_{y1}b+\sin(k_{y1}b)}{k_{y1}^2} \end{aligned} \tag{3.41}$$

Finally, the power loss due to the radiation comprises the whole power flow in Region 2 and that in Regions 3 and 4 excluding the conductor loss:

$$\begin{aligned} P_{lr} &= P_2 + P_3 + P_4 - P_{lc3} - P_{lc4} \\ &= \frac{|A|^2\omega\sqrt{\mu\epsilon_0\beta_h\beta_v}}{8}\frac{k_{x1}a+\sin(k_{x1}a)}{k_{x1}^2}\frac{\sin^2(k_{y1}b/2)}{k_{y0}^2} \\ &\quad + \frac{|A|^2\omega\sqrt{\mu\epsilon_0\beta_h\beta_v}}{8}\frac{\sin^2(k_{x1}a/2)}{k_{x0}^2}\frac{k_{y1}b+\sin(k_{y1}b)}{k_{y1}^2} \\ &\quad - \frac{R_s}{2}\frac{|A|^2\omega\epsilon_0\beta_v}{k_{y1}}\frac{\sin^2(k_{x1}a/2)}{k_{x0}^2} \end{aligned} \tag{3.42}$$

With all the power losses found out, the next step is to apply (3.35) to obtain the attenuation constants individually and then, collectively. Since the preceding power equations all seem to be complicated, simplification is made, which lets

$$\begin{aligned} M_x &= \frac{k_{x1}a+\sin(k_{x1}a)}{k_{x1}^2}, \quad M_y = \frac{k_{y1}b+\sin(k_{y1}b)}{k_{y1}^2} \\ N_x &= \frac{\sin^2(k_{x1}a/2)}{k_{x0}^2}, \quad N_y = \frac{\sin^2(k_{y1}b/2)}{k_{y0}^2} \\ T &= (\sqrt{\epsilon_r}M_xM_y + 2M_xN_y + 2N_xM_y)^{-1} \end{aligned} \tag{3.43}$$

After that,

$$\begin{aligned} \alpha_c =& 2R_s\sqrt{\frac{\epsilon_0\beta_v}{\mu\beta_h}}\frac{(\epsilon_r M_x + 2N_x)T}{k_{y1}} \\ \alpha_d =& \frac{\omega}{2}\sqrt{\frac{\mu\epsilon_0\beta_h}{\beta_v}}(\tan\delta)\epsilon_r M_xM_yT \\ \alpha_r =& \left(M_xN_y + N_xM_y - 4R_s\sqrt{\frac{\epsilon_0\beta_v}{\mu\beta_h}}\frac{N_x}{k_{y1}}\right)T \end{aligned} \tag{3.44}$$

$$\begin{aligned}\alpha =&\alpha_c + \alpha_d + \alpha_r \\ =&\left[M_x N_y + N_x M_y + 2R_s\sqrt{\frac{\epsilon_0\beta_v}{\mu\beta_h}}\frac{\epsilon_r M_x}{k_{y1}}\right. \\ &\left.+\frac{\omega}{2}\sqrt{\frac{\mu\epsilon_0\beta_h}{\beta_v}}(\tan\delta)\epsilon_r M_x M_y\right]T\end{aligned} \tag{3.45}$$

By this stage, the attenuation characteristic of the rectangular DIG has been analysed and demonstrated.

3.2.2 TE$^y_{mn}$ Mode

The analysis of the TE$^y_{mn}$ mode follows a similar manner as that of the TM$^y_{mn}$ mode and hence, the detailed derivation process will not be mentioned here. Instead, results and conclusions are directly presented.

The TE$^y_{mn}$ mode in the rectangular DIG will require a TE^z_n mode in the horizontal slab guide and a TM^z_m mode in the vertical one, based on the consistency of main field components in each guide. Hence, the characteristic equation of the horizontal slab guide is given as

$$1 + \frac{k_{y0}}{k_{y1}}\tan\left(k_{y1}b/2\right) = 0 \tag{3.46}$$

or for the convenience of calculation, transformed into

$$k_{y1}b = -2\arctan\left(\frac{k_{y1}}{k_{y0}}\right) + n\pi \tag{3.47}$$

where

$$n = 2n', \quad n' = 1,\ 2,\ 3,\ \cdots$$

can only be even for the TE$^y_{mn}$ mode in the DIG. Then, that of the vertical slab guide is derived as

$$\begin{aligned}&1 + \frac{\epsilon_r' k_{x0}}{k_{x1}}\tan\left(k_{x1}a/2\right) = 0, \quad \text{Even Mode} \\ &1 - \frac{k_{x1}}{\epsilon_r' k_{x0}}\tan\left(k_{x1}a/2\right) = 0, \quad \text{Odd Mode}\end{aligned} \tag{3.48}$$

or for the convenience of calculation, transformed into

$$k_{x1}a = -2\arctan\left(\frac{k_{x1}}{\epsilon_r' k_{x0}}\right) + m\pi \tag{3.49}$$

where

$$\begin{aligned} &m = 2m', && m' = 1,\ 2,\ 3,\ \cdots && \text{even mode} \\ &m = 2m' - 1, && m' = 1,\ 2,\ 3,\ \cdots && \text{odd mode} \end{aligned}$$

and the classification of even/odd modes is based on the symmetry/asymmetry of E_x which is now the main transverse electric-field component.

With k_{x1} and k_{y1} solved, the phase constant, β, and attenuation constant, α, can hence be found out through the same method used in preceding sections. Detailed results are not presented here for simplicity and also for the reason that TE^y_{mn} modes are not to be focused on.

In the DIG, it can be found that the TM^y_{mn} and TE^y_{mn} modes are now separated, which means one specific pair of "mn" can only refer to either the TM^y or TE^y mode, since n can only be odd for TM^y_{mn} modes and even for TE^y_{mn} modes. In other words, half the numerous modes of the DG are eliminated. This is especially useful for microwave applications, as it opens up a possible wideband for single-mode operation, where only the TM^y_{11} mode is guided. By contrast, the DG will probably have a much narrower single-mode band with both the TE^y_{11} and TM^y_{11} modes interfering on each other.

3.2.3 Comparisons and Calculations

3.2.3.1 Comparison on Marcatili's and EDC Method

Marcatili's method and the EDC method differ at the second stage of the analysis process in terms of the relative dielectric constant, ϵ_r', as shown in Section 3.2.1.2. Marcatili keeps it unchanged, which means he treats the two slab guides independently and the order of solving the two characteristic equations can also be random; while Knox takes advantage of the preceding result, which integrates the two guides together and follows a specific order. The difference is summarised as follows

$$\begin{aligned} k_{y1}^2 &= \epsilon_r k_0^2 - \beta_h^2, && \text{Both} \\ k_{x1}^2 &= \epsilon_r k_0^2 - \beta_v^2, && \text{Marcatili's method} \\ &= \epsilon_{re} k_0^2 - \beta_{ve}^2, && \text{EDC method} \\ &= \beta_h^2 - \beta_{ve}^2, && \text{EDC method} \end{aligned} \tag{3.51}$$

By recalling Marcatili's Assumption (a), it is found that Marcatili's method will always generates a wavenumber which is poor in accuracy, unless the aspect ratio b/a is 1. The EDC method, however, can choose the direction with a larger dimension to start with and utilise the result in the analysis of the other direction, as demonstrated in [113].

3.2.3.2 Theoretical Calculations and Comparisons

The rectangular DIG shown in Fig. 3.2(a) with various aspect ratios is theoretically analysed with Marcatili's method, the EDC method (including EDC-H and EDC-V Methods) and rigorous numerical analysis using HFSS$^{\text{TM}}$, which is based on the FEM method.

The Dupont$^{\text{TM}}$ GreenTape$^{\text{TM}}$ 9K7 LTCC system is used as the dielectric material of the DIG, which has a relative dielectric constant, ϵ_r of 7.1 at 10 GHz. Its loss tangent is also characterised at 10 GHz to be $\tan\delta = 0.001$. The material used as the metallic ground plane here is copper plated on a RT/duroid 5880 board, which has a conductivity of $\sigma = 5.8\text{e}7$ S/m, a relative dielectric constant of 2.2 and a loss tangent of 0.001 at 10 GHz.

Results and comparisons are shown from Figs. 3.4 to 3.6, where the normalized guided wavelength, *i.e.*, the free-space to guided wavelength ratio, λ_0/λ_g, is shown as a function of the normalised dimension, D, of the DIG, where

$$D = \frac{a+b}{\lambda_0}\sqrt{\epsilon_r - 1} \tag{3.52}$$

For well-guided modes, the wavelength ratio, λ_0/λ_g, varies in the following range:

$$1 \leq \lambda_0/\lambda_g \leq \sqrt{\epsilon_r}$$

When $\lambda_0/\lambda_g = 1$, it indicates that the field is completely leaking into the free space around it, whereas when $\lambda_0/\lambda_g = \sqrt{\epsilon_r}$, the field is completely confined inside the dielectric.

(a) Phase constant, β

In Fig. 3.4, where MAR is short for Marcatili's method, the normalised guided wavelength λ_g/λ_0 of the fundamental mode, TM_{11}^y, is calculated for five different aspect ratios, b/a. It can be seen that while results from all the four methods tend to agree well beyond a certain D (at least triple the cutoff frequency), which means that they are equally accurate for the DIGs with an electrically-large cross-section, the obvious discrepancy occurs near the cutoff. Marcatili's method will always give a higher cutoff than the other three methods and have a sharper intersection with the horizontal axis, which brings about a poor accuracy regardless of the aspect ratio, b/a. On the contrary, cutoffs from the two EDC methods tend to be lower and those from the rigorous FEM method tend to stand in the middle.

Between the two EDC methods, EDC-H and EDC-V, the aspect ratio, b/a, clearly shows its influence on the accuracy with respect to results from the FEM method. In Fig. 3.4(a) when $b/a < 1$, the EDC-H method which analyses the horizontal slab guide first is more accurate, as expected in Section 3.1.2.1; while in Fig. 3.4(b) when $b/a > 1$, the EDC-V method is more accurate. Furthermore, it can be predicted that the accuracy of the corresponding EDC method will increase when b/a deviates more from 1 in the corresponding direction. When $b = a$, results from both methods agree well.

So only the EDC and FEM methods are used to explore higher-order modes in the rectangular DIG to find out a wide single-mode band, where only the fundamental mode propagates and the isolation from other modes is as high as possible.

In Fig. 3.5, the normalised guided wavelength of three lowest-order modes are plotted for various aspect ratios. Note that when $b/a = 1$, the two higher-order modes, the TM_{21}^y and TE_{12}^y modes should have the same cutoff frequency theoretically and hence tend to be clustered.

It is then observed in Fig. 3.5 that the single-mode band when $a = b$ is the widest, which is in line with the conclusion in [113]. It's worth noting that the normalised dimension D in Fig. 3.5(b) is only half of those in Figs. 3.5(a) and 3.5(b) and hence, should be doubled. When b/a deviates from 1 in both directions, the width of the single-mode band narrows. Another feature to be observed is that the

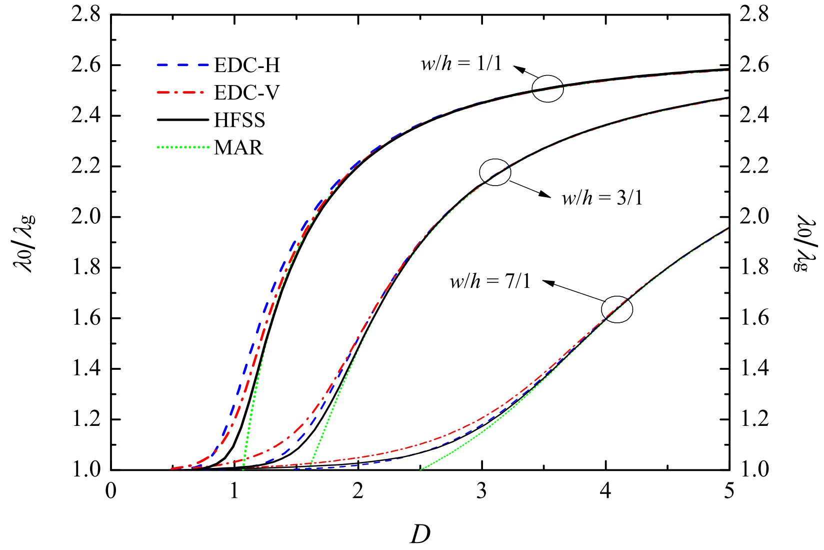

(a) $b/a = 1/7,\ 1/3,\ 1$

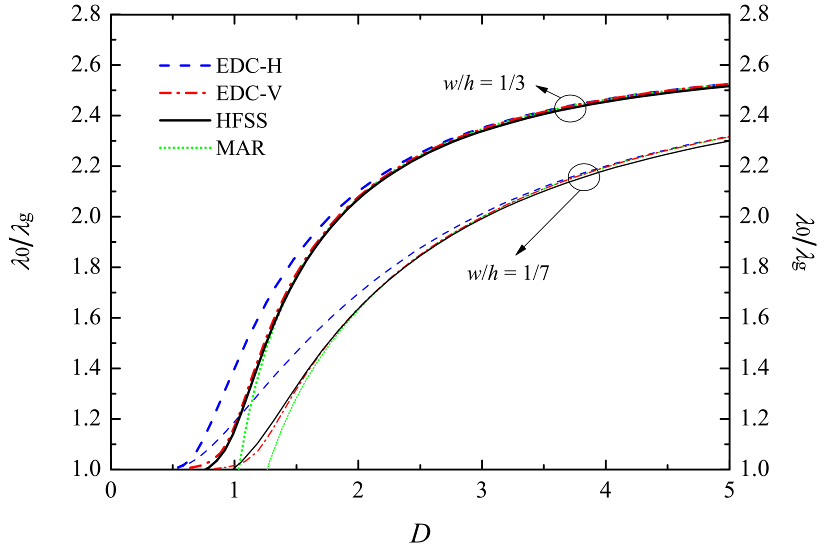

(b) $b/a = 3/1,\ 7/1$

FIGURE 3.4: The normalised guided wavelengths of the TM_{11}^{y} mode vs. the normalised dimension D of the rectangular DIG for various aspect ratios.

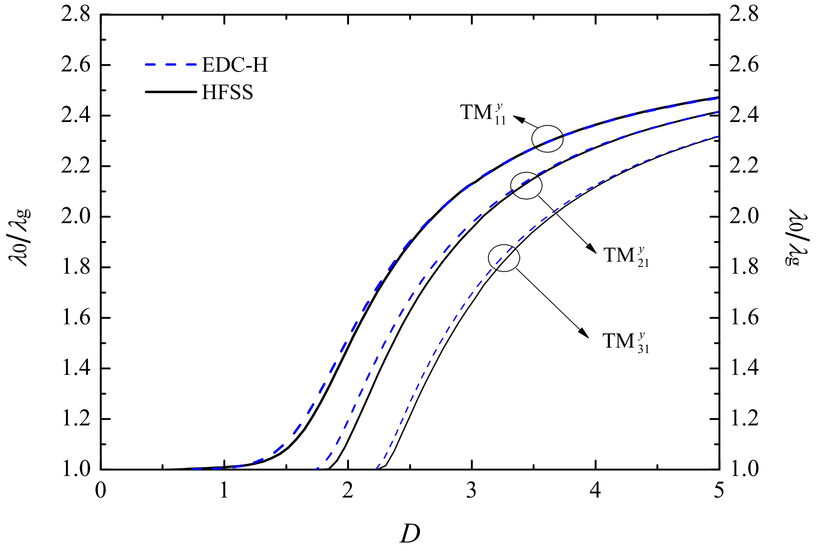
2.8
2.6
2.4
2.2
2.0
1.8
1.6
1.4
1.2
1.0
0
1
2
3
4
5
EDC-H
HFSS
TM_{11}^{y}
TM_{21}^{y}
TM_{31}^{y}
$\lambda 0/\lambda_g$
D

(a) $b/a = 1/3$

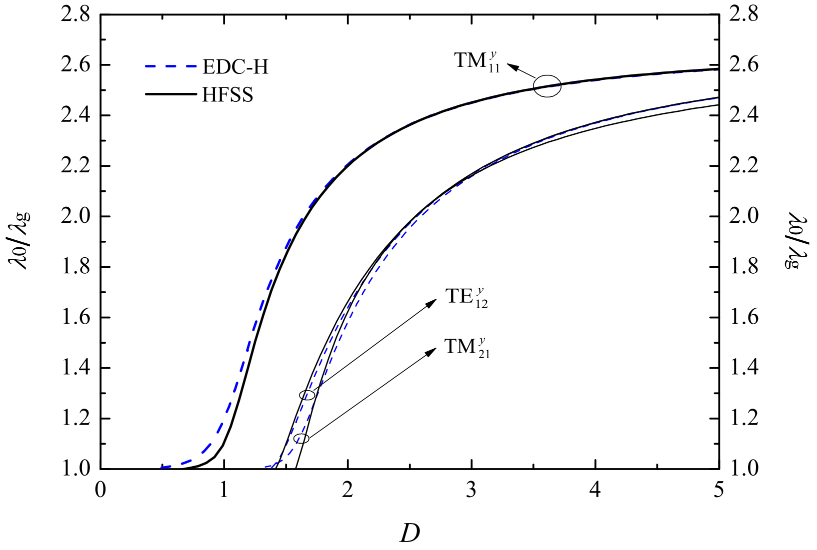
2.8
2.6
2.4
2.2
2.0
1.8
1.6
1.4
1.2
1.0
0
1
2
3
4
5
EDC-H
HFSS
TM_{11}^{y}
TE_{12}^{y}
TM_{21}^{y}
$\lambda 0/\lambda_g$
D

(b) $b/a = 1$

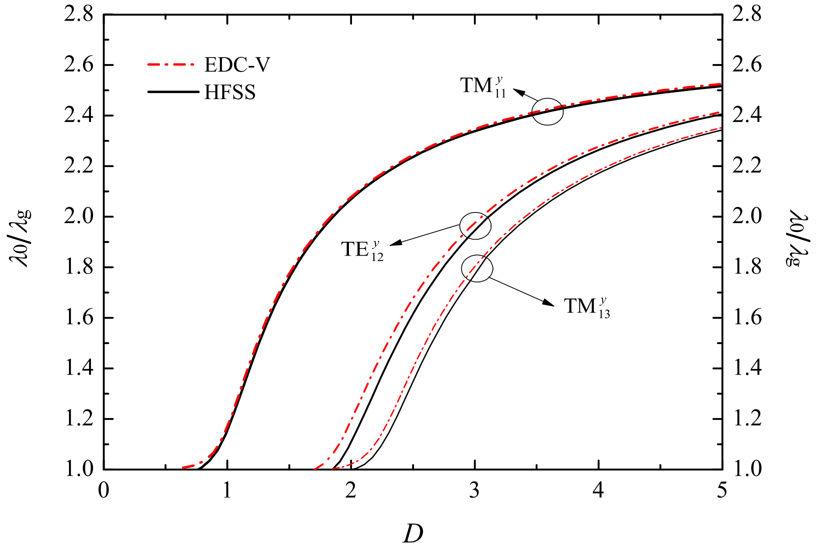

(c) $b/a = 3/1$

Figure 3.5: The normalised guided wavelengths vs. the normalised dimension D of the rectangular DIG for three lowest-order modes and various aspect ratios.

isolation in Fig. 3.5(a) is much smaller than that in Fig. 3.5(c), which indicates the isolation amongst adjacent modes deteriorates as b/a decreases. So it is better to choose an aspect ratio smaller than 1 when $b/a = 1$ can't be realised in practice.

To provide a direct view of the field distribution within the cross-section of the DIG, Fig. 3.6 shows three lowest-order modes for three different aspect ratios obtained through the rigorous FEM method. As the nomenclature of the DIG modes follows that of the DG, the field variations in the y direction in Fig. 3.6 is in fact doubled, represented by n.

(b) Attenuation constant, α

The attenuation constant, α, of the fundamental TM_{11}^{y} mode is calculated here for the aspect ratio of $b/a = 1$ which exhibits the widest single-mode band and $b/a = 3/1$ which has a high isolation between the fundamental and second-lowest modes. Both the EDC and FEM methods will be employed.

As for the two methods, results shown in Fig. 3.7 agree well, especially for α_c and α_r toward the higher end of the normalised dimension. Near the cutoff, a relatively high deviation can be observed, which gradually converges as D increases.

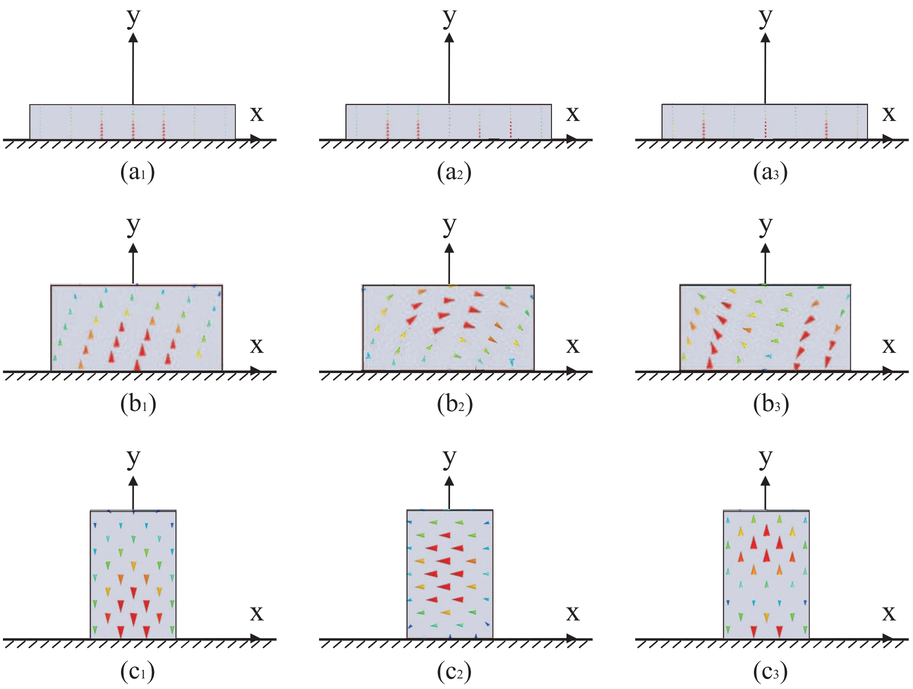

FIGURE 3.6: The field distribution inside the DIG: **(a)** $b/a = 1/3$, (a$_1$) TM$^y_{11}$, (a$_2$) TM$^y_{21}$, (a$_3$) TM$^y_{31}$; **(b)** $b/a = 1$, (b$_1$) TM$^y_{11}$, (b$_2$) TE$^y_{12}$, (b$_3$) TM$^y_{21}$; **(c)** $b/a = 3/1$, (c$_1$) TM$^y_{11}$, (c$_2$) TE$^y_{12}$, (c$_3$) TM$^y_{13}$.

Among the four attenuation constants, α_d (the dielectric loss) accounts for a large percentage (more than 60%) of the total attenuation, α. Furthermore, that percentage goes up as D increases. So it's expected that $\alpha_d \approx \alpha$ at a frequency far enough from the cutoff, although α_c (the conductor loss) will also be rising. As for α_r due to the radiation loss, it's low enough to be negligible.

Now, results from the two aspect ratios are compared. It can be seen in Fig. 3.7 that the loss of the DIG of $b/a = 3/1$ is considerably lower than that of $b/a = 1$. Even if we transform the horizontal axis into normalised frequency, f/f_c, the DIG with a higher height still has a lower loss. This characteristic can be used in search of a low-loss dielectric transmission line.

In the end, results from the EDC method have also been compared with those from Knox's other paper in 1976 [106], as shown in Fig. 3.8. It is observed that both the conductor loss and dielectric loss from the EDC method deviate from Knox's results at the low values of the normalised dimension, D, and approaches closer when D increases. This is similar to what has been observed in Fig. 3.7 when compared with the HFSS simulation. It's worth noting that dielectric and conductor loss cannot be differentiated in practice, so all this analysis and comparison are based on the theory.

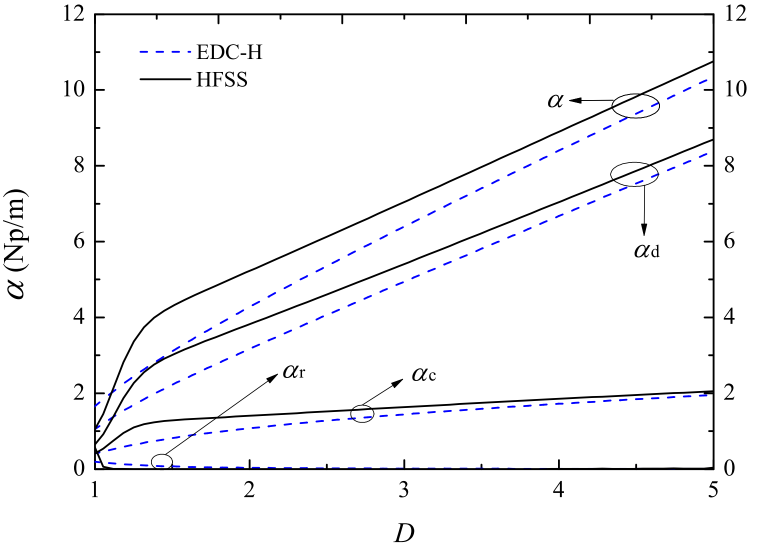

(a) $b/a = 1$, $a = 1$ mm

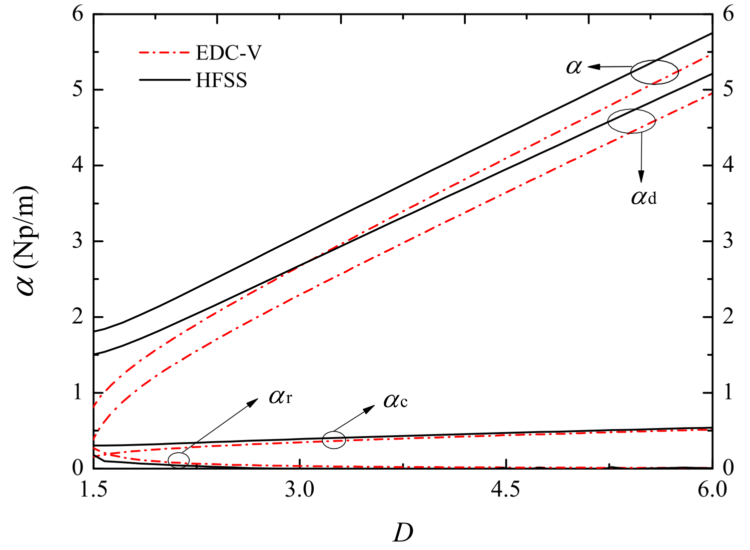

(b) $b/a = 3/1$, $a = 1$ mm

FIGURE 3.7: The attenuation constant, α, of the TM^y_{11} mode vs. the normalised dimension D of the rectangular DIG.

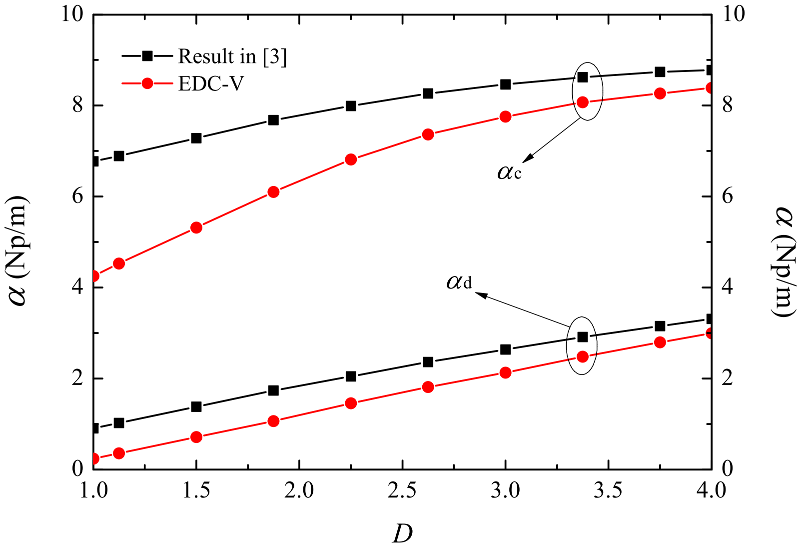

FIGURE 3.8: Comparison of the attenuation constant, α, of the TM_{11}^{y} mode with Knox's results in [106] ($b/a = 2/1$, $\epsilon_r = 9.8$, $\tan\delta = 0.0001$, and $\sigma = 3.72e7\mathrm{S/m}$).

3.3 DIIG

In search of a low-loss transmission line, the DIG is not a perfect solution. The reason is that the DIG suffers from the conductor loss with a large field concentration near the metallic ground plane when it's operating in the fundamental TM_{11}^{y} mode. This can be further reduced by introducing a low-permittivity (normally lower than that of the dielectric rod) low-loss dielectric layer between the dielectric rod and the ground plane [106]. This layer works as an insulator which keeps the fields away from the ground plane and hence, this new type of DIG is named as dielectric insular image guide (DIIG) [104].

3.3.1 Theoretical Analysis

As shown in Fig. 3.9(a), an insular layer with a low dielectric constant of ϵ_{r_2} and a thickness of $d/2$ is added below the original DIG dielectric (ϵ_{r_1}). Using the EDC-H method, the DIIG can be divided into three constituent regions each of which can be then extended into infinite horizontal slab guides. After the equivalent dielectric constants, ϵ_{re_1} and ϵ_{re_2} are extracted, the vertical slab guides can also be established in Fig. 3.9(b). The EDC-V method may also be applied if the height, a, of the DIIG is larger than the width, b. However, note that the subsequent

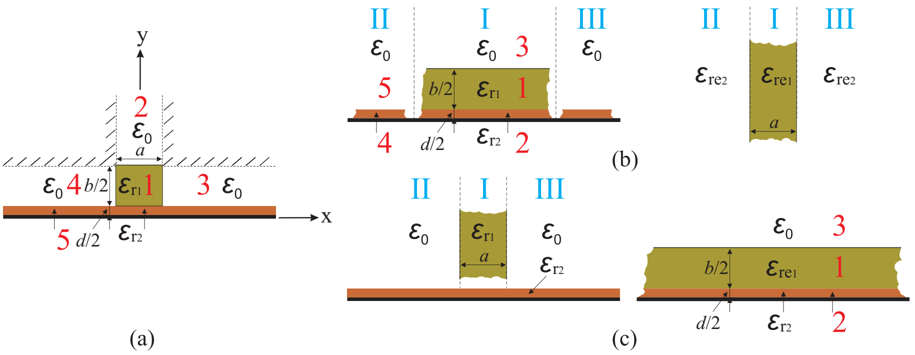

FIGURE 3.9: (a) The DIIG model, (b) equivalent horizontal and vertical slab guides using the EDC-H method, (c) equivalent vertical and horizontal slab guides using the EDC-V method.

results are not accurate as applied in the DIG case since the infinite horizontal insular layer is against the assumption made by the EDC-V method. This is shown in Fig. 3.9(c).

The theoretical analysis is similar to that demonstrated in Section 3.2 and the generated results are shown as follows.

3.3.1.1 TM^y_{mn} Mode

(a) EDC-H method

In this case, the aspect ratio, b/a, is smaller than 1 and the DIIG is firstly extended into infinite horizontal slab guides, as shown in Fig. 3.9(b). Hence, the characteristic equations for the horizontal slab guides in the three regions are given as:

$$1+\frac{k_{y2}}{\epsilon_{r2}k_{y3}}\tanh\left(k_{y2}d/2\right)-\frac{k_{y1}}{\epsilon_{r1}k_{y3}}\tan\left(k_{y1}b/2\right)$$
$$+\frac{\epsilon_{r1}k_{y2}}{\epsilon_{r2}k_{y1}}\tanh\left(k_{y2}d/2\right)\tan\left(k_{y1}b/2\right)=0,\ \text{Region I} \tag{3.53a}$$

$$1-\frac{k_{y4}}{\epsilon_{r2}k_{y5}}\tan\left(k_{y4}d/2\right)=0,\ \text{Regions II \& III} \tag{3.53b}$$

where

$$\begin{aligned}
k_{y1} &= \sqrt{\epsilon_{r1}k_0^2 - \beta_{h1}^2} \\
k_{y2} &= \sqrt{(\epsilon_{r1} - \epsilon_{r2})k_0^2 - k_{y1}^2} \\
k_{y3} &= \sqrt{(\epsilon_{r1} - 1)k_0^2 - k_{y1}^2} \\
k_{y4} &= \sqrt{\epsilon_{r2}k_0^2 - \beta_{h2}^2} \\
k_{y5} &= \sqrt{(\epsilon_{r2} - 1)k_0^2 - k_{y4}^2}
\end{aligned} \tag{3.54}$$

With k_{y1} and k_{y4} solved, Regions I, II, and III are then transformed into three uniformly-distributed media whose equivalent relative dielectric constants are

$$\begin{aligned}
\epsilon_{re1} &= \epsilon_{r1} - \left(\frac{k_{y1}}{k_0}\right)^2 \\
\epsilon_{re2} &= \epsilon_{r2} - \left(\frac{k_{y4}}{k_0}\right)^2
\end{aligned} \tag{3.55}$$

As a result, the infinite vertical slab guide is built up to obtain its characteristic equation as:

$$1 + \frac{k_{x0}^2 - k_{x1}^2}{k_{x0}k_{x1}} \tan\left(k_{x1}a/2\right) - \tan^2\left(k_{x1}a/2\right) = 0 \tag{3.56}$$

which can then be split into

$$\begin{aligned}
1 - \frac{k_{x1}}{k_{x0}} \tan\left(k_{x1}a/2\right) = 0, &\quad \text{even mode} \\
1 + \frac{k_{x0}}{k_{x1}} \tan\left(k_{x1}a/2\right) = 0, &\quad \text{odd mode}
\end{aligned} \tag{3.57}$$

where

$$\begin{aligned}
k_{x1} &= \sqrt{\epsilon_{re1}k_0^2 - \beta^2} \\
k_{x0} &= \sqrt{(\epsilon_{re1} - \epsilon_{re2})k_0^2 - k_{x1}^2}
\end{aligned} \tag{3.58}$$

Note that β is the final phase constant of the DIIG.

It's also worth noting that the transendental equations, (3.53) and (3.56), have infinite roots. The TM_{mn}^y mode is determined by the mth root of k_{x1} through (3.56) and the nth root of k_{y1} through (3.53).

(b) EDC-V method

In this case, it's assumed that the aspect ratio, b/a, is larger than 1 and the DIIG is firstly extended into infinite vertical slab guides, as shown in Fig. 3.9(c). Note that the insular layer can't be vertically extended, as the wavenumber in the y direction varies along the x direction. This will potentially result in poor accuracy as shown later on.

The characteristic equation for the vertical slab guide is given the same as (3.56), wherein the difference is

$$\begin{aligned} k_{x1} &= \sqrt{\epsilon_{r1} k_0^2 - \beta_v^2} \\ k_{x0} &= \sqrt{(\epsilon_{r1} - 1) k_0^2 - k_{x1}^2} \end{aligned} \tag{3.59}$$

With k_{x1} known, Regions I, II, and III are then transformed into one uniform media whose equivalent dielectric constant is

$$\epsilon_{re1} = \epsilon_{r1} - \left(\frac{k_{x1}}{k_0} \right)^2 \tag{3.60}$$

After that, the infinite horizontal slab guide is established and the characteristic equation is obtained the same as (3.53a), except that ϵ_{r_1} is now replaced by ϵ_{re_1} and

$$\begin{aligned} k_{y1} &= \sqrt{\epsilon_{re1} k_0^2 - \beta^2} \\ k_{y2} &= \sqrt{(\epsilon_{re1} - \epsilon_{r2}) k_0^2 - k_{y1}^2} \\ k_{y3} &= \sqrt{(\epsilon_{re1} - 1) k_0^2 - k_{y1}^2} \end{aligned} \tag{3.61}$$

The TM_{mn}^y mode is also determined by the mth root of k_{x1} through (3.56) and the nth root of k_{y1} through (3.53).

It can be seen that there is one less characteristic equation in the EDC-V method due to the fact that the insular layer can't be extended vertically. The influence prompted will be shown later.

(c) Field components

Similar to the analysis of the DIG, E_y and H_x are the dominating field components from Marcatili's Assumption (b). Furthermore, the wave behaviours in Areas 1, 2, 3, and 4 (shown in Fig. 3.9(a)) are the same as those in the DIG. The fields in Area 5, however, are different: for the part underneath the dielectric, the fields stand along the x direction and decay along the y direction; for that extending toward infinity, the fields decay on both directions.

Since TM_{11}^{y} is the dominating mode in the single-mode frequency band and belongs to the even-mode family, only the field expressions of even TM_{mn}^{y} modes are given. Referring to the derivation process of the DIG through the EDC-H method, the field expressions in five areas shown in Fig. 3.9(a) are as follows:

Main electric field, E_y,

$$
\begin{aligned}
E_{y1} &= A_1\sqrt{\frac{\omega\mu\beta_{h1}}{k_{x1}k_{y1}}}\cos(k_{x1}x)\big\{\cos\left[k_{y1}(y-d')\right]+A_2\sin\left[k_{y1}(y-d')\right]\big\}\\
E_{y2} &= A_1A_3\sqrt{\frac{\omega\mu\beta_{h1}}{k_{x1}k_{y3}}}\cos(k_{x1}x)\mathrm{e}^{-k_{y3}[y-(b'+d')]}\\
E_{y3} &= A_1\sqrt{\frac{\omega\mu\beta_{h1}}{k_{x0}k_{y1}}}\sin(k_{x1}a')\big\{\cos\left[k_{y1}(y-d')\right]+A_2\sin\left[k_{y1}(y-d')\right]\big\}\mathrm{e}^{-k_{x0}(x-a')}\\
E_{y4} &= A_1\sqrt{\frac{\omega\mu\beta_{h1}}{k_{x0}k_{y1}}}\sin(k_{x1}a')\big\{\cos\left[k_{y1}(y-d')\right]+A_2\sin\left[k_{y1}(y-d')\right]\big\}\mathrm{e}^{k_{x0}(x+a')}\\
E_{y5} &= A_1A_4\sqrt{\frac{\omega\mu\beta_{h1}}{k_{x1}k_{y2}}}\cos(k_{x1}x)(\mathrm{e}^{k_{y2}y}+\mathrm{e}^{-k_{y2}y}), \qquad -a'\leq x\leq a'\\
&= A_1A_4\sqrt{\frac{\omega\mu\beta_{h1}}{k_{x0}k_{y2}}}\sin(k_{x1}a')\mathrm{e}^{k_{x0}(x+a')}(\mathrm{e}^{k_{y2}y}+\mathrm{e}^{-k_{y2}y}), \quad -\infty\leq x\leq -a'\\
&= A_1A_4\sqrt{\frac{\omega\mu\beta_{h1}}{k_{x0}k_{y2}}}\sin(k_{x1}a')\mathrm{e}^{-k_{x0}(x-a')}(\mathrm{e}^{k_{y2}y}+\mathrm{e}^{-k_{y2}y}), \quad a'\leq x\leq\infty
\end{aligned}
\tag{3.62}
$$

Main magnetic field, H_x,

$$
\begin{aligned}
H_{x1} &= \sqrt{\frac{\epsilon_1\beta}{\mu\beta_{h1}}}E_{y1}\\
H_{xi} &= \sqrt{\frac{\epsilon_0\beta}{\mu\beta_{h1}}}E_{yi}, \quad i=2,\ 3,\ 4\\
H_{x5} &= \sqrt{\frac{\epsilon_2\beta}{\mu\beta_{h1}}}E_{y5}
\end{aligned}
\tag{3.63}
$$

where

$$\begin{aligned}
A_2 &= \frac{k_{y1}\tan(k_{y1}b') - \epsilon_{r1}k_{y3}}{k_{y1} + \epsilon_{r1}k_{y3}\tan(k_{y1}b')} \\
A_3 &= \frac{\epsilon_{r1}k_{y3}}{k_{y1}\cos(k_{y1}b') + \epsilon_{r1}k_{y3}\sin(k_{y1}b')} \\
A_4 &= \frac{\epsilon_{r1}k_{y2}\mathrm{sech}(k_{y2}d')}{2\epsilon_{r2}k_{y1}} \\
a' &= a/2,\ \ b' = b/2,\ \ d' = d/2
\end{aligned} \tag{3.64}$$

(d) Attenuation constant, α

Following the perturbation method in [99], the attenuation constant, α, of the DIIG is given by (3.35). In this case, the number of areas to be studied has increased to 5 suplemented by the insular layer, as depicted in Fig. 3.9(a). The field expressions have also been given by (3.62) and (3.63) through the EDC-H method.

Before α is derived, the simplification quantities, M_y and N_y, as shown in (3.43) need to be redefined as:

$$\begin{aligned}
M_y &= \frac{(1+A_2^2)k_{y1}b + (1-A_2^2)\sin(k_{y1}b) + 2A_2\left[1-\cos(k_{y1}b)\right]}{k_{y1}^2} \\
N_y &= \frac{A_3^2}{k_{y3}^2} \\
T &= \left[\sqrt{\epsilon_{r1}}M_xM_y + 2M_xN_y + 2N_xM_y + 2\sqrt{\epsilon_{r2}}Q_y(M_x+2N_x)\right]^{-1}
\end{aligned} \tag{3.65}$$

where Q_y is a new simplification quantity which is defined as

$$Q_y = \frac{A_4^2(2k_{y2}d + \mathrm{e}^{k_{y2}d} - \mathrm{e}^{-k_{y2}d})}{k_{y2}^2} \tag{3.66}$$

After that,

$$\begin{aligned}
\alpha_c =& 4R_s\sqrt{\frac{\epsilon_0\beta}{\mu\beta_{h1}}}\frac{\epsilon_{r2}(M_x+2N_x)T}{k_{y2}} \\
\alpha_d =& \frac{\omega}{2}\sqrt{\frac{\mu\epsilon_0\beta_{h1}}{\beta}}\left[(\tan\delta_1)\epsilon_{r1}M_xM_y + 2(\tan\delta_2)\epsilon_{r2}Q_y(M_x+2N_x)\right]T
\end{aligned} \tag{3.67}$$

$$\begin{aligned}
\alpha_r = & \Bigg[M_x N_y + N_x M_y - 8R_s \sqrt{\frac{\epsilon_0 \beta}{\mu \beta_{h1}}} \frac{\epsilon_{r2} N_x}{k_{y2}} \\
& -2\omega \sqrt{\frac{\mu \epsilon_0 \beta_{h1}}{\beta}} (\tan \delta_2) \epsilon_{r2} N_x Q_y \Bigg] T \\
\alpha = & \alpha_c + \alpha_d + \alpha_r \qquad (3.68) \\
= & \Bigg\{ M_x N_y + N_x M_y + 4R_s \sqrt{\frac{\epsilon_0 \beta}{\mu \beta_{h1}}} \frac{\epsilon_{r2} M_x}{k_{y2}} \\
& + \frac{\omega}{2} \sqrt{\frac{\mu \epsilon_0 \beta_{h1}}{\beta}} \left[(\tan \delta_1) \epsilon_{r1} M_x M_y + 2 (\tan \delta_2) \epsilon_{r2} M_x Q_y \right] \Bigg\} T
\end{aligned}$$

where $\tan \delta_1$ and $\tan \delta_2$ are the loss tangents of the main dielectric and insular layer, respectively.

3.3.1.2 TE$^y_{mn}$ Mode

(a) EDC-H method

According to the TM$^y_{mn}$ mode, the characteristic equations for the TE$^y_{mn}$ mode can be obtained in a similar format.

For the horizontal slab guides,

$$\begin{aligned}
1 + \frac{k_{y3}}{k_{y2}} \tanh(k_{y2} d/2) + \frac{k_{y3}}{k_{y1}} \tan(k_{y1} b/2) & \\
- \frac{k_{y1}}{k_{y2}} \tanh(k_{y2} d/2) \tan(k_{y1} b/2) = 0, & \quad \text{Region I} \qquad (3.69a) \\
1 - \frac{k_{y4}}{k_{y5}} \tan(k_{y_4} d/2) = 0, & \quad \text{Regions II \& III} \qquad (3.69b)
\end{aligned}$$

where the defination of $k_{y1} \sim k_{y5}$ is the same as that in the TM$^y_{mn}$ mode given by (3.54).

For the vertical slab guide,

$$1 + \frac{(\epsilon_{re1} k_{x0})^2 - (\epsilon_{re2} k_{x1})^2}{\epsilon_{re1} \epsilon_{re2} k_{x0} k_{x1}} \tan(k_{x1} a/2) - \tan^2(k_{x1} a/2) = 0 \qquad (3.70)$$

which can then be split into

$$\begin{aligned} &1+\frac{\epsilon_{re_1}k_{x0}}{\epsilon_{re_2}k_{x1}}\tan\left(k_{x1}a/2\right)=0, \quad \text{even mode} \\ &1-\frac{\epsilon_{re_2}k_{x1}}{\epsilon_{re_1}k_{x0}}\tan\left(k_{x1}a/2\right)=0, \quad \text{odd mode} \end{aligned} \tag{3.71}$$

where the definition of ϵ_{re1}, ϵ_{re2}, k_{x0}, and k_{x1} is the same as that in the TM^y_{mn} mode given by (3.55) and (3.58).

Finally, by finding out the mth root of k_{x1} through (3.70) and the nth root of k_{y1} through (3.69), the TE^y_{mn} mode is determined.

(b) EDC-V method

Firstly, extend the DIIG vertically and then apply the EDC-V method to obtain the characteristic equation the same as (3.70) except that ϵ_{re1} and ϵ_{re2} are now replaced by ϵ_{r1} and 1. The definition of k_{x0} and k_{x1} is the same as that in the TM^y_{mn} mode given by (3.59).

Secondly, extend the DIIG horizontally to find the characteristic equation as (3.69a), where the definition of ϵ_{re1}, k_{y1}, k_{y2}, and k_{y3} is the same as that in the TM^y_{mn} mode given by (3.60) and (3.61).

For simplicity, the field components and attenuation constant, α, will not be displayed here.

3.3.2 Calculations and Comparisons

The rectangular DIIG with an aspect ratio of $b/a = 1$ is analysed, where various values of the insular ratio, $p = d/b$, are considered. The materials used here are the same as those for the DIG, which means that $\epsilon_{r1} = 7.1$, $\epsilon_{r2} = 2.2$, $\tan\delta_1 = \tan\delta_2 = 0.001$ and $\sigma = 5.8\mathrm{e}7$ S/m.

3.3.2.1 Phase Constant, β

Fig. 3.10 shows the normalised phase constant, β, as a function of the normalised dimension, D. In Fig. 3.10(a), the EDC-H, EDC-V, and FEM methods are applied and compared for the case of $b/a = 1$ and $p = 0.1$. It's seen that the EDC-V method gives rise to poor agreement with the rigorous FEM method for the TM^y modes. That deviation won't converge even at very high frequencies. For the TE^y modes, results from the EDC-V and EDC-H agree well with a small gap from the FEM method that narrows down gradually. Generally speaking, due to the fact that the DIIG doesn't fully conform to Marcatili's Assumption (a), the EDC-V method easily brings about poor accuracy and is not suitable for theoretical analysis of the DIIG.

In Fig. 3.10(b), the EDC-H method is applied to find out how different insular ratios may affect the propagating characteristics. As can be seen, the normalised guided wavelength, λ_0/λ_g which is equal to β/k_0, of the TM^y modes goes upward with the increase of p; while that of the TE^y modes are on the contrary. This will unwantedly narrow down the width of the single-mode band. So the insular ratio, p, cannot be too large to maintain a reasonable single-mode bandwidth.

To provide a direct view of the field distribution within the cross-section of the DIIG, Fig. 3.11 shows three lowest-order modes for with an aspect ratio of $b/a = 1$ obtained through the rigorous FEM method. Same as the nomenclature of the DIG modes, the field variations in the y direction in Fig. 3.11 is in fact doubled, represented by n.

3.3.2.2 Attenuation Constant, α

The attenuation constant, α, of the fundamental TM^y_{11} mode is calculated here for the aspect ratio of $b/a = 1$ which exhibits the widest single-mode band. Both the EDC-H and FEM methods will be employed.

Fig. 3.12(a) shows the calculated attenuation constant from the EDC-H and FEM methods in terms of α_d and α_c. A slowly-diminishing gap (about 10%) can be seen between two α_d's, which is similar to the case in the DIG. By contrast, the agreement of α_c is much better.

Now the three constituent constants of α, α_d, α_c, and α_r are studied individually.

With the introduction of an insular layer, α_d decreases for all p's compared with that for $p = 0$ (the DIG)) at low D's and the higher p is, the lower α_d is. Then comes a turning point where α_d with high p's overtakes and approaches that of the DIG. So it can be predicted that the dielectric loss of the DIIG can be higher with a sufficiently-thick insular layer. However, given that a transmission line normally works in its single-mode band and that turning point is beyond it, the introduction of an insular layer can only reduce the dielectric loss.

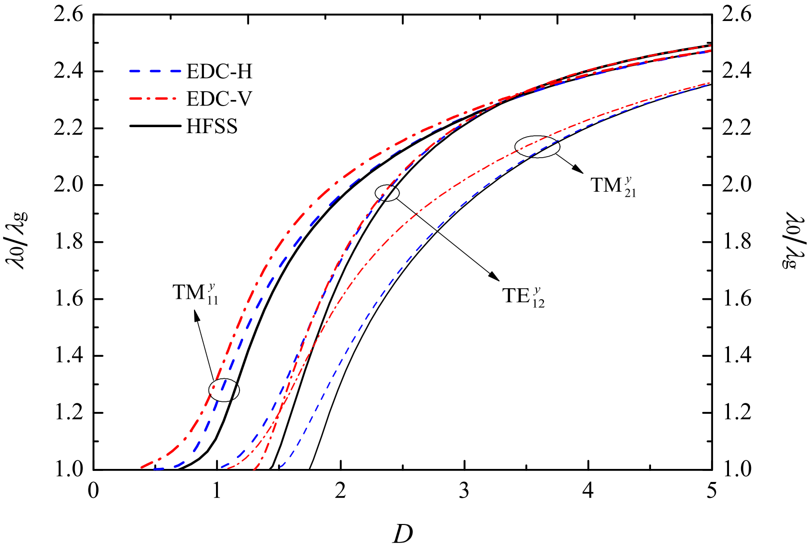

(a) comparisons among three methods

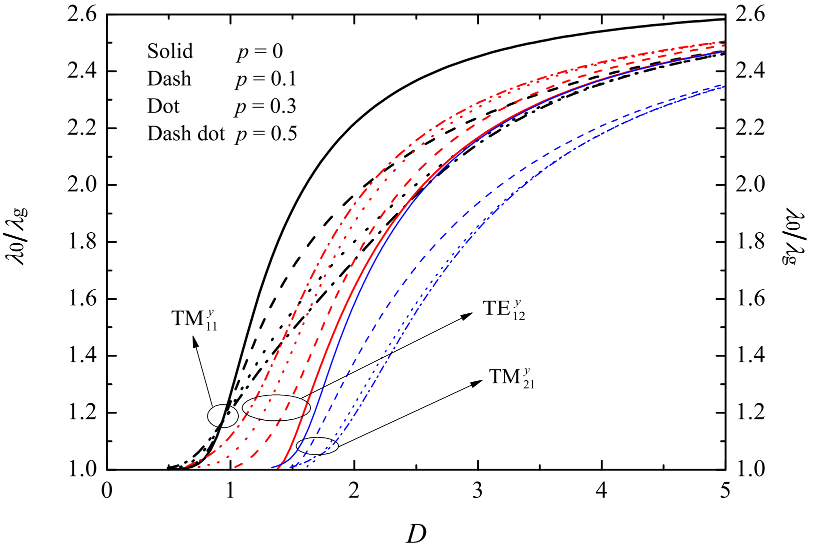

(b) various p's for the EDC-H method

FIGURE 3.10: The normalised guided wavelength vs. the normalised dimension D of the rectangular DIIG for $b/a = 1$.

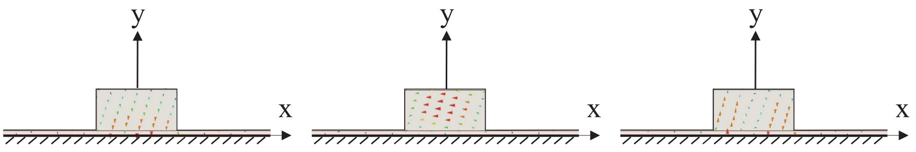

(a) (b) (c)

FIGURE 3.11: The field distribution inside the DIIG of $b/a = 1$: (a) TM$^y_{11}$, (b) TE$^y_{12}$, (c) TM$^y_{21}$.

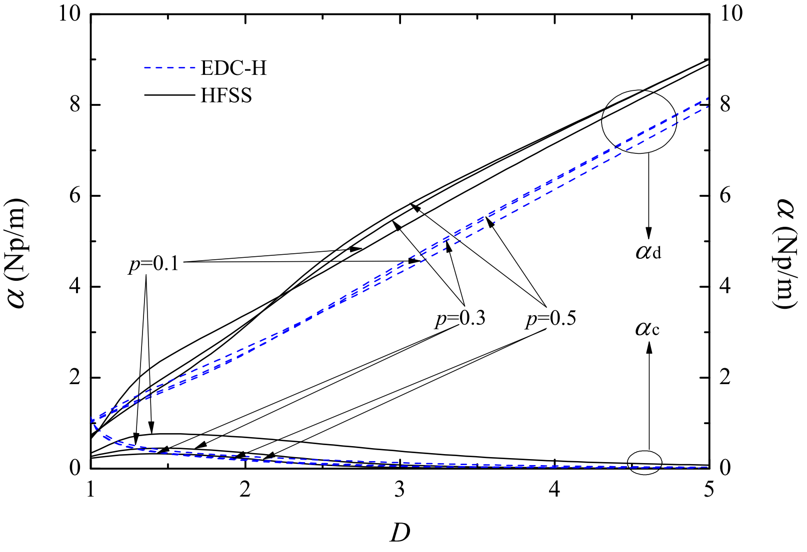

(a) comparisons between the EDC-H and FEM method

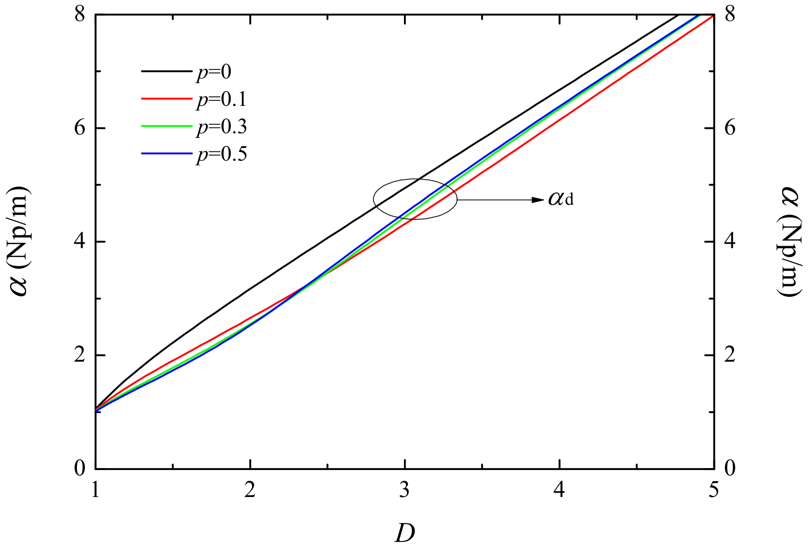

(b) α_d

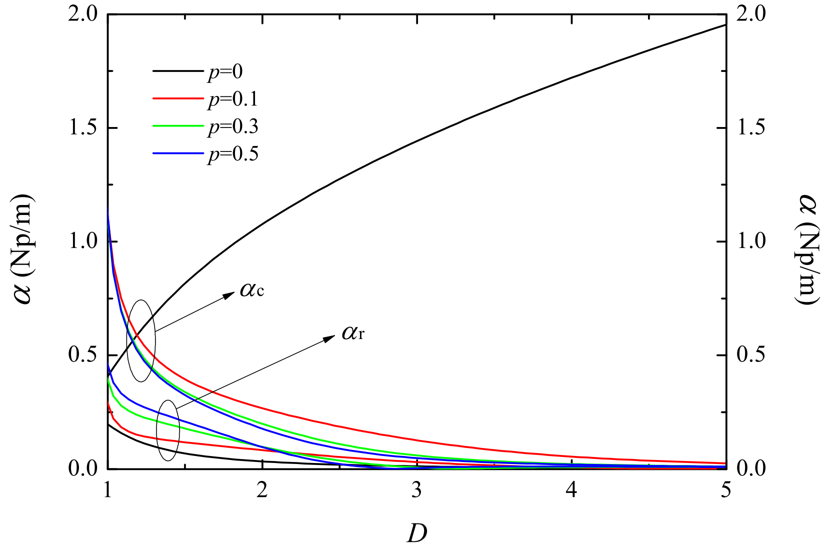

(c) α_c and α_r

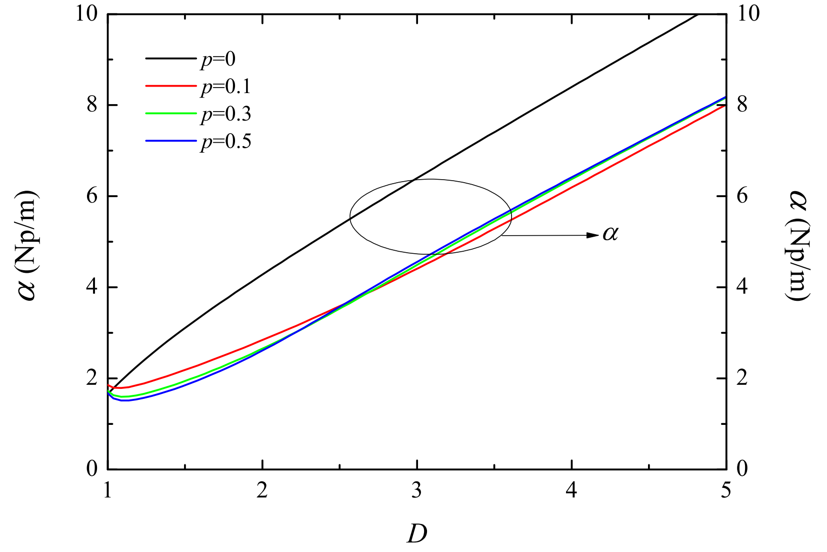

(d) α

FIGURE 3.12: The attenuation constant, α, of the TM_{11}^{y} mode vs. the normalised dimension D of the rectangular DIIG for $b/a = 1$.

The most obvious improvement by employing an insular layer is the significant reduction of the conductor loss, α_c, as observed in Fig. 3.12(c). For the DIG where $p = 0$, α_c increases with D; while for the DIIG, α_c decreases and tend to be 0 at high D's. Furthermore, the higher p is, the lower α_c is. This is because the thicker the insular layer is, the more separation it creates. However, the radiation loss deteriorates for the DIIG. The reason for this is that the introduction of a low-permittivity dielectric loosens the confinement of electromagnetic fields and make them easily radiate. Since α_r is considerably low, the deterioration doesn't affect much.

Finally, for the combination, α, significant reduction for all p's compared with the DIG can be observed in Fig. 3.12(d), especially before the turning point. Since the single-mode band falls before the turning point, a thicker insular layer will yield a lower loss for the DIIG.

3.3.2.3 Conclusion

In search of a low-loss transmission line, a low-permittivity low-loss insular layer is introduced. On one hand, the attenuation constant, α is significantly reduced and will be further reduced by increasing the thickness of the insular layer; on the other hand, the phase constant, β, of the fundamental and adjacent modes tend to get closer when the insular layer gets thicker, which narrows the single-mode bandwidth. The reduction of loss is in fact at the cost of a reduced single-mode bandwidth. This conflict will probably end up with a compromise of the insular ratio, p. Recommended value is between 0.1 and 0.3.

3.3.3 Measurement

Three DIIGs with an equal difference in length of 20 mm, *i.e.*, 20 mm, 40 mm, and 60 mm, are manufactured, as shown in Fig. 3.13, using a standard LTCC technique. The Dupont$^{\mathrm{TM}}$ GreenTape$^{\mathrm{TM}}$ 9K7 LTCC system with a relative dielectric constant of 7.1 is employed as the dielectric, while the RT/duroid 5880 board, which has a relative dielectric constant of 2.2 and a thickness of 0.254 mm is adopted as the insular layer. Due to the restrictions of the LTCC technique, the thickness of the DIIG is chosen as 1.54 mm, which is 7 layers of LTCC (0.22 mm for each layer after firing). So the insular ratio, p, is 0.16 which falls into the

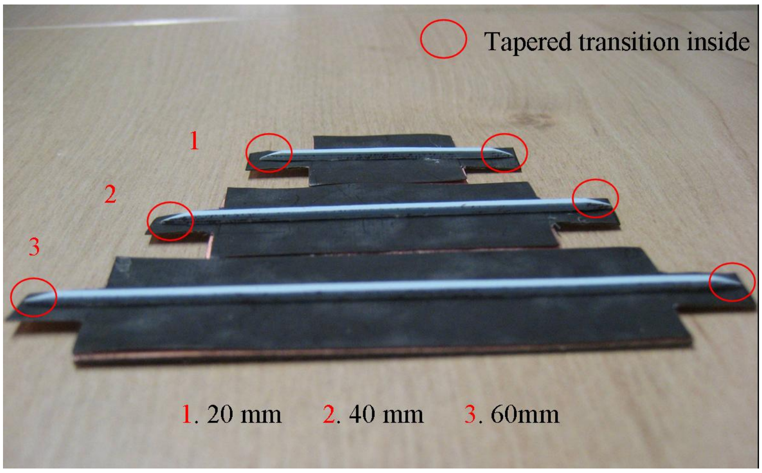

FIGURE 3.13: Three fabricated DIIG samples of 20 mm, 40 mm, and 60 mm.

recommended range. To ensure the DIIG works in the Ka band, the width of the DIIG is derived as 1.3 mm through the theoretical calculation.

As can be seen in Fig. 3.13, tapered transitions are added at both ends of the DIIG in order to be fed from a standard WR28. Note that the transitions are tapered at both horizontal and vertical planes to ensure a smooth feeding. The transmission loss, S_{21}, for each DIIG is measured, as shown in Fig. 3.14. As can be seen, the transmission loss has a sharp rise near 25 GHz and an obvious drop after it. For the rest of the operating frequency band, S_{21} tends to be relatively stable yet with constant ripples.

Through the single-mode multiline calibration technique introduced in Section 2.3, the propagation constant of the DIIG can be extracted, as illustrated in Fig. 3.15. To compare with the measurement, the simulated propagation constant using the two-mode multiline calibration technique has also been plotted in the same figure.

In Fig. 3.15, the measured phase constant, represented by the normalised guided wavelength, stays close to the simulated one, although there are some gentle ripples above and below. As for the measured loss constant, α, it ripples greatly and a Savitzky-Golay smoothing technique [103] has to be used to find out the figure shape and tendency, which is indicated by the blue line, as performed in Section 2. As can be seen, α throughout the Ka band ripples around 3 Np/m, whereas the simulated one gradually increases from 0.3 to 0.8 Np/m, which implies that the actual sample is more lossy. The shape and tendency of the measured α agree with that of the simulated one in that they both have a sharp drop near the cutoff frequency and tend to be flat afterwards. Possible reasons may lie in that the loss characteristics of materials (LTCC, silver paste) tend to be worsening at higher

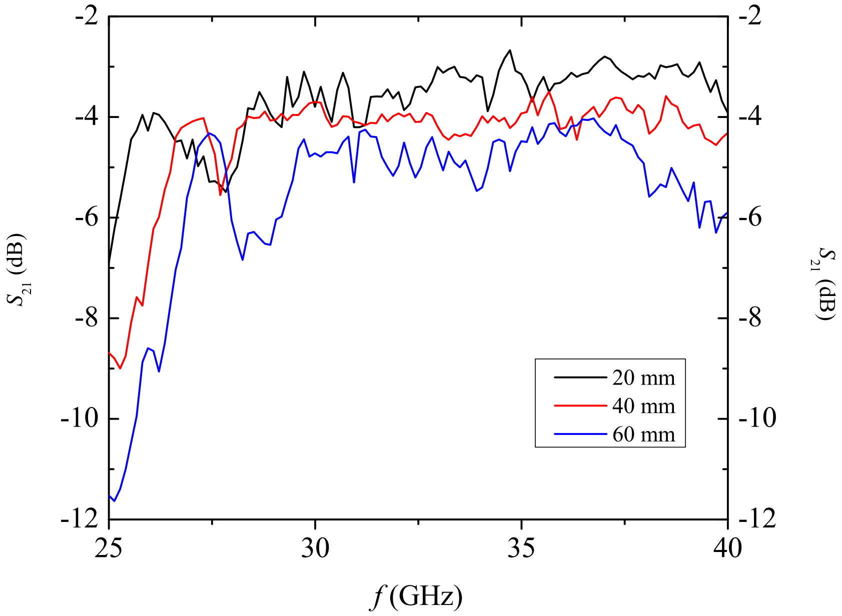

FIGURE 3.14: Measured S_{21} of the three DIIGs with lengths of 20 mm, 40 mm, and 60 mm.

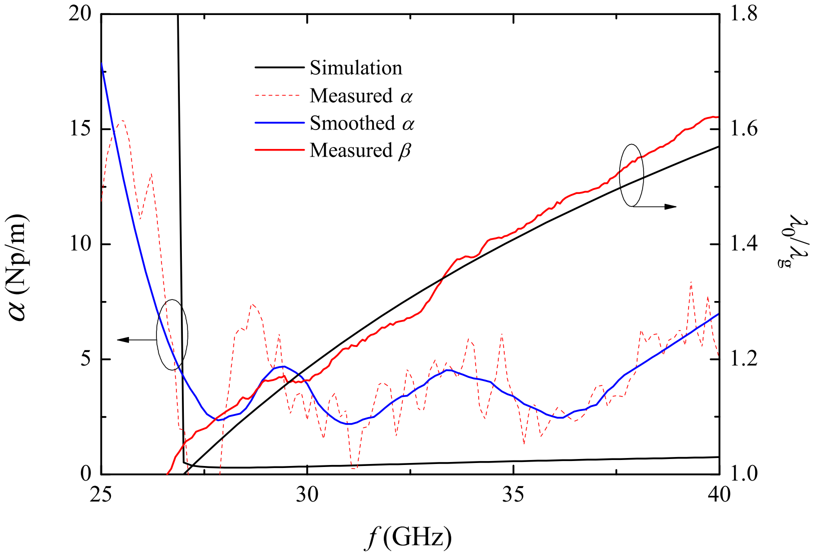

FIGURE 3.15: Extracted propagation constant of the Ka band DIIG.

frequencies, the bond between the LTCC and PCB board might not be completely intact and the surface of the insular layer might not be exactly flat. Nevertheless, an α of 3 Np/m or 26 dB/m at 35 GHz is still an excellent loss performance.

3.4 Conclusion

By reviewing the traditional approximate methods on the analysis of the DG/DIG, this chapter improves the EDC method by extending it for all aspect ratios. As a result, the EDC method is now complete. Apart from that, the analytical expression of the attenuation constant, α, of the rectangular DIG has also been given and can be directly used. The rectangular DIG with various aspect ratios have been calculated and compared with the results from the rigorous FEM method and published literatures. Good agreement has been observed, which verifies the validility of this new EDC method.

After that, the new EDC method is applied to the DIIG which gives rise to lower loss than the DIG. Detailed analytical expression of α has also been given. Three DIIG samples are made to extract the propagation constant and compared with the result from the rigorous FEM method.

Chapter 4

A Slot Antenna Array Based on HSIW

This chapter starts with a brief introduction of the history and general radiation characteristics of the waveguide slot antennas in Section 4.1. After that, a single waveguide slot is analysed theoretically and numerically in Section 4.2. The analysis starts with a thin slot on RWG, then extends to thick slot on RWG and finally to thick slot on HSIW. All the analysis is in the Ka band which is in line with the design and fabrication in Chapter 2. Finally, a linear slot array is designed taking mutual coupling into account and then extends to a 6×6 planar array aiming at high gain and high efficiency. Fabrication and measurement are also carried out to verify the results from theory and simulation in Section 4.3.

4.1 Introduction

4.1.1 Historical Review

The first waveguide slot antenna array was developed at McGill University in Montreal in April, 1943, according to W. Watson [119]. That 50-element radiator attempted to leak high power from large-aperture antennas, mainly for military radar use. Fortunately, the experiment on the array was carried out successfully and theoretical analysis was derived later on by A. Stevenson in 1948 [120]. For the first time, waveguide slots were proved to be equivalent to series or shunt resistance or conductance in a transmission line and simple closed expressions are obtained, although Stevenson's waveguide is assumed to be zero thickness. Following his work, A. Oliner demonstrated more explicit results and circuit representations on a variety of broad-wall waveguide-slots through variational techniques in 1957 [121]. More importantly, he has accounted for the finite wall-thickness in real world and laid out ground foundation for the applications of slot antennas.

After World War II and with the strong support of theory, waveguide slot antennas received extensive interest and many studies were reported. Now it has been widely used in applications of radar, communications, meteorology, and navigation, *etc.* What makes slot antennas stand out is their simple geometry, easy fabrication, conformal installation, low cross-polarization, and high efficiency [122]. This is becoming more and more intriguing nowadays, as it's more and more demanding for the antenna to be light-weight, low-profile, and low-cost.

4.1.2 Radiation Characteristics

Fig. 4.1(a) shows a single rectangular slot cut in a infinitely-large ground plane, where the slot is free to radiate on both sides of the plane. A balanced transmission line can be imagined to feed the slot at the central points, P_1 and P_2.

Assuming that $w \ll l$, and $w \ll \lambda$, where λ is the guided wavelength, the slot itself resembles a section of balanced two-wire line, where the two "wires" are semi-infinite ground planes extending from edges at $x = \pm w/2$ and shorted at $z = \pm l/2$. Then, the electric field distribution inside the slot is found to be maximum at the centre and vanishing at both ends (resembling a sinusoid), which is identical to the electric current distribution on the complementary wire; in other words, with the wire in free space being a electric dipole, the slot in a large ground works as a complementary magnetic dipole [121–123]. Detailed analysis on the relation between slot and wire antennas can be found in [124].

Fig. 4.1(b) shows various waveguide slot configurations and their equivalent circuit models. Since the slots are cut on either the broad or edge wall of a waveguide, they cannot radiate freely in both directions. The influence on the impedance and radiation pattern could be significant and should be taken into account in the design process. Nevertheless, the waveguide doesn't just work as a base of the slots but also the feeding system, which simplifies the design since baluns or matching networks are not required [122].

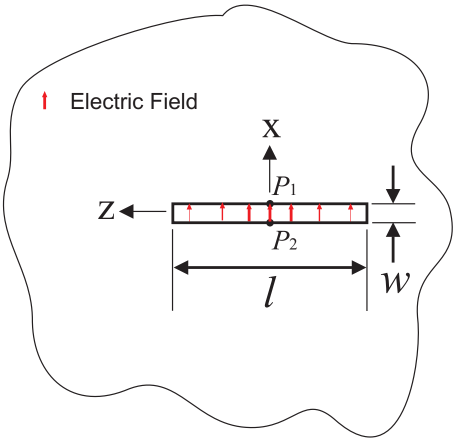

(a) A free-radiating slot

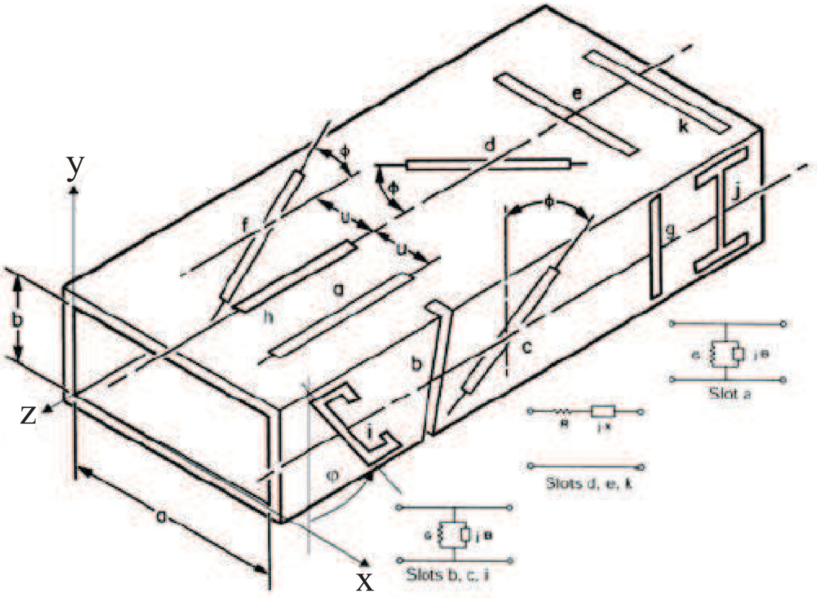

(b) Waveguide slots [122]

FIGURE 4.1: The electric field distribution of a free-radiating slot and the equivalent circuit models of waveguide slots.

Among the slots in Fig. 4.1, Slots d, g, and h do not radiate. The reason is that Slot d lies symmetrically across the waveguide centreline and the radiation cancels out, Slot g does not cut through any surface current, and the current around Slot h is zero. Apart from those, since Slots a, b, c, i, and j disturb the transverse currents (J_x and J_y), they can be represented by two-terminal shunt admittances, whereas Slots e, and k interrupt J_z and are represented by series impedance. Both J_x and J_z excite slot f and A π- or T-impedance network can represent it.

Not all of the above slot types are commonly seen and widely used, so in this thesis, only the longitudinal Slot a is chosen and will be employed for the antenna design.

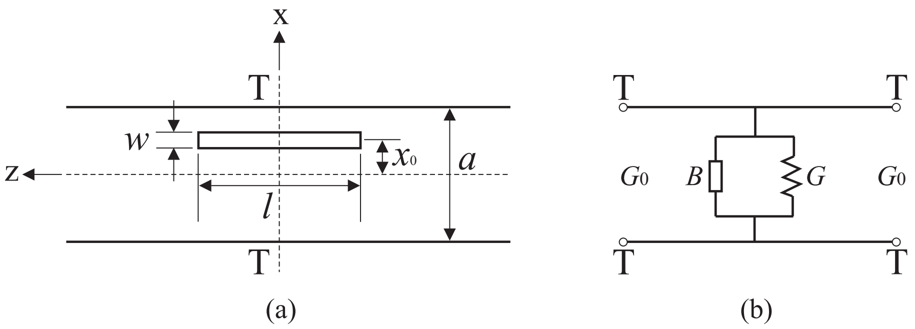

FIGURE 4.2: A single longitudinal slot on the broadwall of a waveguide: (a) the geometry, (b) the equivalent circuit model.

4.2 Single Waveguide Slot

4.2.1 Thin Slot

4.2.1.1 Theory

As shown in Fig. 4.2(a), a longitudinal slot offset by x_0 from the centre line is cut on the broad wall of a rectangular waveguide with a dimension of $a \times b$. Assume that the thickness of the metallic wall is small and thus negligible, which gives rise to a thin slot. Also, the metal has an infinite conductivity, *i.e.*, PEC (Pefect Electric Conductor). Apart from that, the previous assumptions on the narrow dimension of the slot still hold.

On these premises, the electric field inside the slot follows a symmetrical distribution and satisfies [121, 123]:

$$\bar{E}(x,y,z) = \hat{x}\frac{V_s}{w}\cos\left(\frac{\pi z}{l}\right), \tag{4.1}$$

where V_s is the peak slot voltage and then it results in a symmetrical reflection and transmission upon the slot, suppose there is an incident wave and a matched load. This symmetry implies that the slot works as a shunt element on a two-wire transmission line [123], as shown in Fig. 4.2(b).

The normalised admittance of the shunt element can then be derived as [123]:

$$\frac{Y}{G_0} = \frac{G + jB'}{G_0} = -\frac{2B}{A+B}, \tag{4.2}$$

where G_0 is the characteristic conductance of the transmission line and A, B, and C are the complex amplitudes of the incidence, reflection and transmission, respectively.

The slot is believed to be resonant when $B' = 0$ or in connection with (4.2), Y/G_0 is pure real. In this case, the normalised resonant conductance can be deduced in a closed form with the approximation, $kl \approx \pi$, as:

$$g_r = \frac{G_r}{G_0} = 2.09\frac{a\lambda_g}{b\lambda}\cos^2\left(\frac{\pi\lambda}{2\lambda_g}\right)\sin^2\left(\frac{\pi x_0}{a}\right), \tag{4.3}$$

where λ and λ_g are the wavelength unbounded and bounded by the waveguide, respectively.

From (4.3), it can be found that although the resonant conductance is offset-dependent, the resonant length is assumed constant around $\lambda/2$, which has been verified by experiments in [125]. This, in another way, means that the radiation pattern doesn't change much with different offsets [123].

As for the radiated power, P_r, of the narrow slot (normalised to the incident power) at its resonant frequency, it is easily derived from the equivalent circuit from Fig. 4.2. As assumed, one end of the two-port network is matched and thus the power absorbed by the admittance is

$$P_r = \frac{G}{1+G}. \tag{4.4}$$

4.2.1.2 Calculation and Simulation

Here the radiation characteristic of a single slot based on a standard WR28 (7.11 × 3.55 mm^2) is calculated and simulated.

Note that there is no simple closed-form formula to refer to in search of the resonant length, l_r (formulas provided by [120, 121] are too complicated to be followed). With the help of the HFSS simulation based on the FEM method, however, this can be an easy job to do. The only preparation is to rewrite (4.2) in terms of S parameters as:

$$\frac{Y}{G_0} = -\frac{2S_{11}}{1+S_{11}}, \tag{4.5}$$

where $S_{11} = B/A$ and can be directly given by the HFSS simulation.

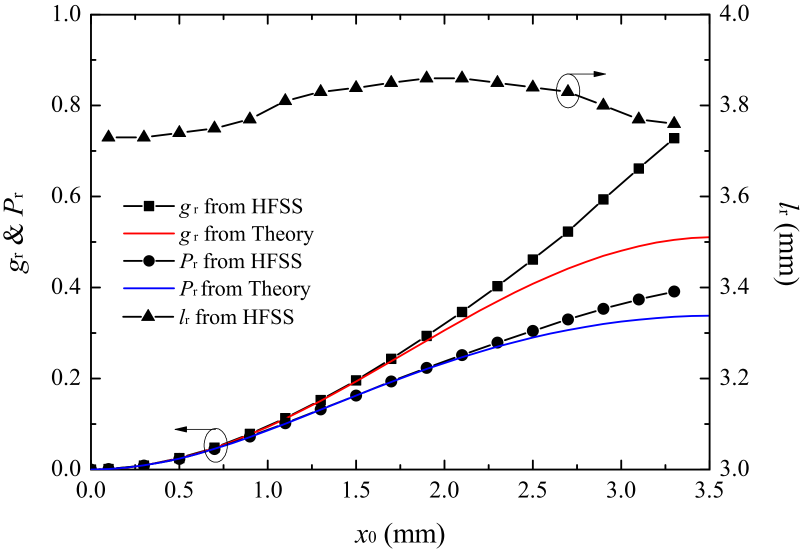

FIGURE 4.3: g_r, P_r, and l_r vs. x_0 of a single longitudinal slot based on a standard WR28 at 35 GHz ($b = 3.55$ mm and $w = 0.3$ mm).

As shown in Fig. 4.3, the normalised conductance, g_r, and normalised radiated power, P_r, at the resonance rise up with an increasing offset, x_0 and reach their peaks at the maximum x_0. Results from both HFSS simulation and theoretical calculation agree well when x_0 is below about half the maximum value, *i.e.*, $a/2$. After that, the deviation becomes noticeable and keeps increasing, which indicates that (4.3) is not suitable to be applied to large offsets. This has been observed in [126] and attributed to the distortion of the field symmetry in the slot.

As for the resonant length, l_r, of the waveguide slot at 35 GHz, it doesn't vary much with the offset. Nevertheless, it does have relatively high values at the offset of around $a/4$ and decreases (less than 4%) toward both ends. Compared with the free-space wavelength at 35 GHz, 8.57 mm, the resonant slot is about 45% long, where $kl_r \approx \pi$ still holds as expected.

In Fig. 4.4, g_r, P_r, and l_r are simulated by HFSS to see how the changing of w affects the radiation characteristic of a waveguide slot. It's found that none of the three quantities significantly changes as w increases from 0.1 to 0.5 mm. This, to some extent, can be expected from (4.3), as no involvement of w can be found in it. Further, this also indicates that w is not a key factor to be considered in the antenna design and can be flexibly chosen to the convenience of fabrication, measurement, *etc.*

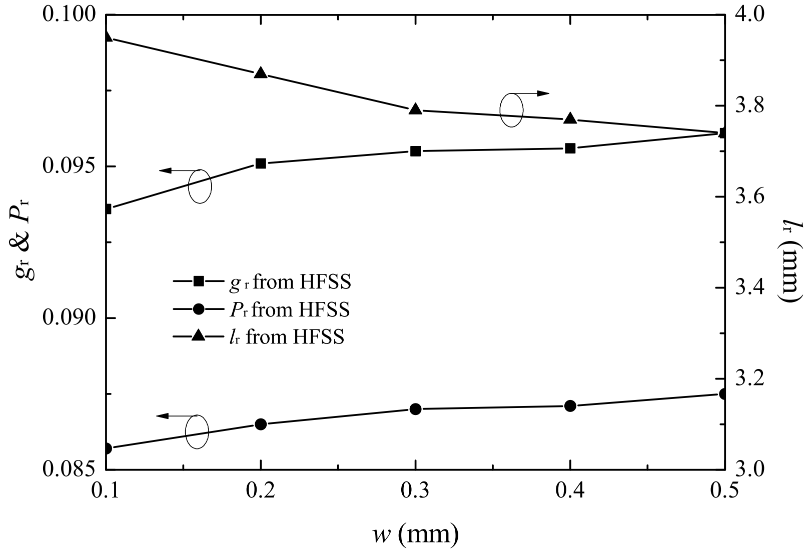

FIGURE 4.4: g_r, P_r, and l_r vs. w of a single longitudinal slot based on a standard WR28 at 35 GHz ($b = 3.55$ mm and $x_0 = 1$ mm).

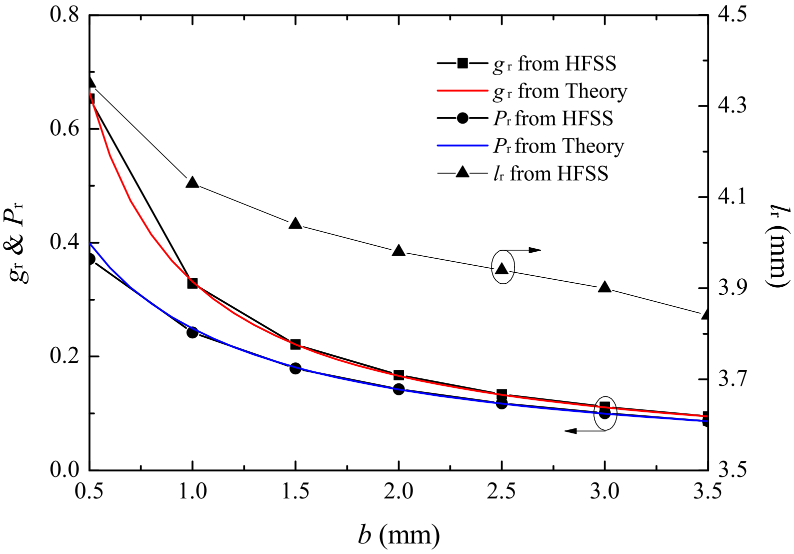

FIGURE 4.5: g_r, P_r, and l_r vs. b of a single longitudinal slot based on a standard WR28 at 35 GHz ($x_0 = 1$ mm and $w = 0.3$ mm).

The influence from b on the radiation characteristics is studied and shown in Fig. 4.5. In contrast to w, it's obvious that b has produced a massive effect. Take the resonant length, l_r, as an example: It drops from 4.35 to 3.80 mm when b increases from 0.5 to 3.5 mm, which is 12.6%. The changes of g_r and P_r are significant as well. This phenomenon is also mentioned in [126], which concludes that the shunt-element model in Fig. 4.2 is not valid for reduced-height waveguide ($b < \lambda/10$). As shown in Fig. 4.5, the disagreement of results between HFSS and theory start to be seen when $b < 1$ mm (about 0.12λ at 35 GHz). Apart from that, the agreement is still very good, since the offset, x_0, is 1 mm (small offset). Also in [126], a wave method dealing directly with field theory instead of circuit models is recommended in the end aiming at validility and high accuracy.

Since the radiation pattern of the slot antenna is very stable, the change of w and b has little effect as long as the aspect ratio of the slot stays in a reasonable region.

Given the lack of accurate theory at large offsets, numerical methods based on electromagnetic field theory, such as FEM (realised by HFSS) will be the first option to be considered in later analysis and design.

4.2.2 Thick Slot

In practice, the waveguide or HSIW supporting the slots will have a finite thickness which brings about a noticeable effect on the radiation characteristics. This problem is solved by the microwave network theory in [121, 127] and summarised here. As before, only the longitudinal shunt slot is considered.

As shown in Fig. 4.6, the basic principle is to divide the thick slot into three constitutions: A, the feeding waveguide with a T-junction on the broad wall; B, a section of waveguide with a length of t and a cross section of $l \times w$; C, the radiating junction into a half space connected with A through B. Based on this theory, it's predicted that the radiation pattern of the slot won't change much.

After that, closed-form expressions for normalised conductance, susceptance, *etc.*, are given. As expected, they are even more complicated than those of the thin slot. Hence, (4.5) based on the HFSS simulation continues to be used here in order to characterise the thick waveguide slot.

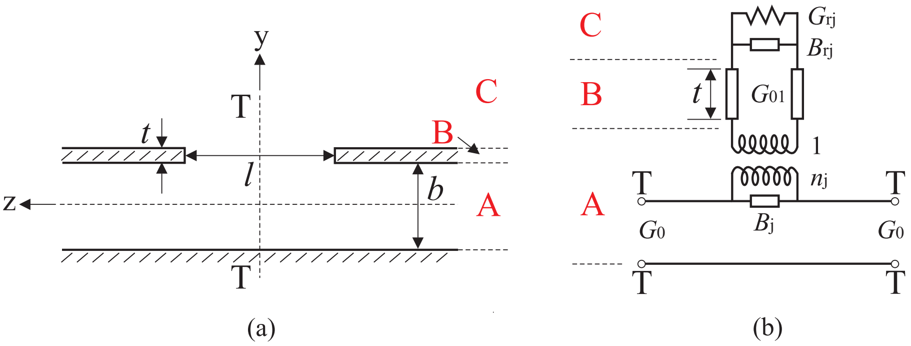

FIGURE 4.6: A thick longitudinal slot on the broadwall of a waveguide or HSIW: (a) the geometry, (b) the equivalent circuit model [121].

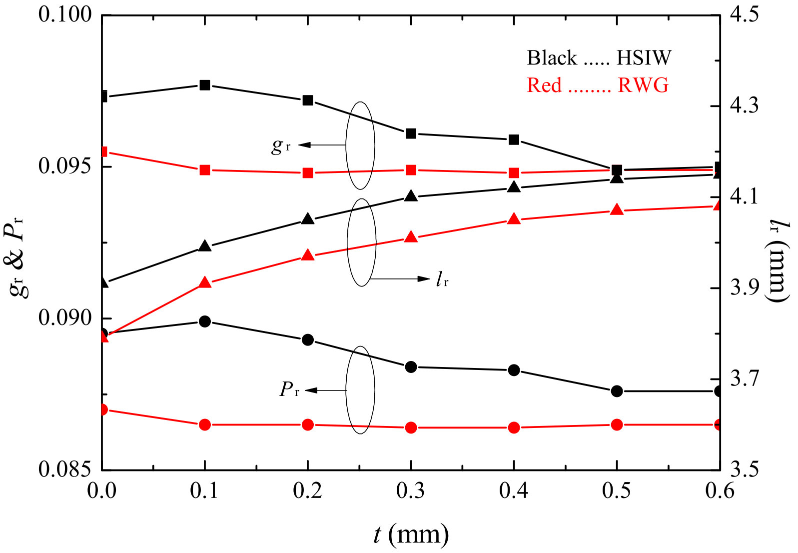

FIGURE 4.7: g_r, P_r, and l_r vs. t of a single longitudinal slot based on a standard WR28 and HSIW at 35 GHz ($x_0 = 1$ mm, $w = 0.3$ mm and $b = 3.55$ mm).

4.2.2.1 Thick RWG slot

Here, the wall thickness of WR28 is taken into account and assumed to change from 0.1 to 0.6 mm. The effect of this changing on the radiation characteristics is shown in Fig. 4.7. As can be seen, the resonant length, l_r, gradually moves upward with the increasing thickness, t, while g_r and P_r barely change except when t jumps from 0 to 0.1 mm.

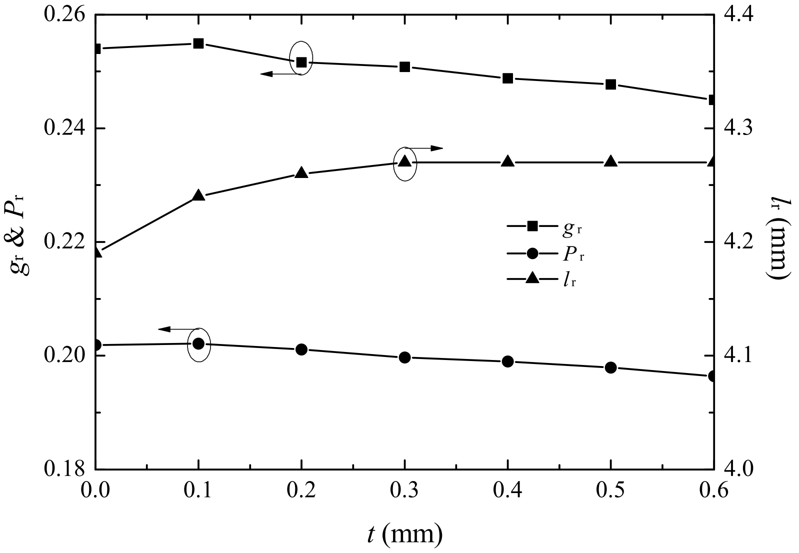

FIGURE 4.8: g_r, P_r, and l_r vs. t of a single longitudinal slot based on an HSIW at 35 GHz ($x_0 = 1$ mm, $w = 0.3$ mm and $b = 1.32$ mm).

4.2.2.2 Thick HSIW slot

Following the design of a Ka-band HSIW in Chapter 2, a longitudinal shunt slot is now cut on its broad wall to radiate.

Firstly, an HSIW slot with the same height as WR28 ($b = 3.55$ mm, other geometrical and physical parameters can be found in Table 2.4) is analysed and compared with the WR28 slot, as shown in Fig. 4.7. It can be seen that g_r, P_r, and l_r are all approximately following the same trend as those of the WR28 slot, except that those of the HSIW slot are all slightly higher. This obviously is introduced by the structural change: the side walls of WR28 replaced by two rows of metallic posts and this might be preferred as high capability of power radiating facilitate the Taylor distribution to each array element.

Then, the slot based on the HSIW designed in Chapter 2 (now $b = 1.32$ mm) is analysed and results are shown in Fig. 4.8. As expected, g_r, P_r, and l_r are following a similar trend as those of the HSIW with $b = 3.55$ mm, except that all the values are now even higher, since b has been reduced.

4.3 Waveguide Slot Array

Waveguide slot arrays are classified into two groups in terms of the wave pattern inside the waveguide: (a) standing-wave arrays, (b) travelling-wave arrays [122].

For standing-wave arrays, each element is spaced $\lambda_g/2$ apart and left/right-offset alternatively on the broadwall to ensure that each element is fed in phase and jointly radiate a broadside beam. As for the feeding scheme, standing-wave arrays can be fed either at one end or the centre of the waveguide with the rest end(s) terminated with a matched load or short circuit. Short-circuit terminations provide for a more efficient array since the incident power can be potentially all radiated instead of absorbing by the matched load. If a slightly larger bandwidth is desired, however, matched-load terminations are preferred, as they minimize reflected waves that potentially could cause the array to radiate another beam in the opposite direction and thus narrow down the bandwidth. It's also worth noting that due to the dispersive nature of the waveguide, the main beam will shift from the broadside with frequency if the array is fed at one end, which is called “Long-Line Effect” [128, 129] by M. Ando, *et.al*. This can be significantly improved by the centre feeding, also known as corporate feeding [128–133].

For travelling-wave arrays, the main difference is that they are designed to radiate at scanning angles to the broadside with frequency. This means that the inter-element spacing should deviate from $\lambda_g/2$ slightly and avoid $\lambda_g/2$ paticularly. As for the feeding scheme, they can be fed only at one end of the waveguide. With the use of wideband terminations, however, the bandwidth is noticeably wider than that of standing-wave arrays.

Waveguide slot arrays can also be classified into two groups in terms of the configuration: (a) linear array, (b) planar array.

A linear array, by its very nature, is one dimensional by including multiple radiating elements on the same waveguide, while a planar array is two dimensional, which comprise multiple linear arrays placed side by side.

In this section, the high-efficiency and load-saving standing-wave array will be focused on. Within standing-wave arrays, A single waveguide slot antenna is extended firstly into a linear slot array and then a planar array to realise a high gain and high selection (pencil beam).

4.3.1 Linear Array

4.3.1.1 Mutual Coupling

When a slot is set in an array, its radiation characteristics will be inevitably affected by the other slots from the same branch line or across branches. This is known as "mutual coupling", which includes external and internal coupling.

In 1978, R. Elliott did a first look into the external mutual coupling between waveguide longitudinal slots and produced two decisive equations for small antenna array designs. The drawback of these two equations, however, is that they can only be applied to air-filled waveguide because of the analogy of slot to the complimentary dipole [134]. Later in 1983, he improved that design procedure by extending it to dielectric-filled waveguide. At the end of this paper, the new iterative procedure is presented in the presence of external mutual coupling [135]. In the situation of reduced-height waveguide, the internal coupling becomes strong and has to be accounted for. R. Elliott quickly spotted and investigated that in 1986 and concluded that "the effects are ignorable for full-height guide, marginally detectable for half-height guide, but significant for quarter-height guide" [136]. In addition to Elliott's work, a similar conclusion on internal higher-order mode coupling of waveguide slots was achieved in 1991 [137].

All these methods above are complex, less-accurate and rely heavily on computer programming. Take the design procedure in [135] for example. It needs the normalised admittance of the shunt slot at all locations, (x_0, l) beforehand, which either comes from measurement or simulation. That already is time-consuming. After that, at least 3 to 4 iterations are needed before a suitable set of slot dimension can be found. With the advent of commercial 3D softwares, the design process could get easier and more accurate.

4.3.1.2 Design Procedure

The basic principle is to firstly design the linear array ignoring the mutual coupling effects and then optimise it taking coupling into account, all with the aid of HFSS.

1) Characterisation of a single slot

The influence of the thickness, t, of a single HSIW slot may bring to the radiation characteristic has been studied in Section 4.2.2. Now t is fixed to 0.44 mm

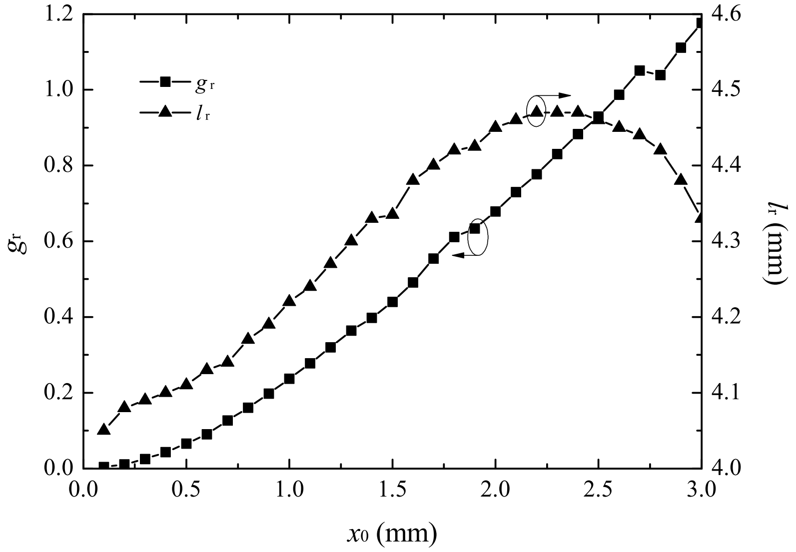

FIGURE 4.9: g_r and l_r vs. x_0 of a single longitudinal slot based on an HSIW at 35 GHz ($t = 0.44$ mm and $w = 0.3$ mm).

which is roughly two layers of LTCC tapes after firing. The resonant length and corresponding normalised conductance are re-simulated through HFSS and given in Fig. 4.9.

As shown in Fig. 4.9, g_r and l_r follow a similar tendency as those shown in Fig. 4.3. The only difference lies in that the values of g_r and l_r are all noticeably higher with a reduced b and thickened t. Particularly, g_r gets over 1 when x_0 is larger than 2.7 mm, which will certainly rule out these offsets in standing-wave array design for the sake of input match.

2) Design without mutual coupling

In the design of a standing-wave slot array, the end of the supporting waveguide is short-circuited and the distance to the centre of the end slot is always $\lambda_g/4$, which transforms a short circuit into an open circuit. Hence, the total of the normalised resonant conductance, g_t, suppose each slot is at its own resonance, for an input-matched linear array of N slot elements is

$$\begin{aligned} g_t = \sum_{n=1}^{N} g_{rn} &= 1, \quad \text{End-fed Array} \\ &= 2, \quad \text{centre-fed Array} \end{aligned} \tag{4.6}$$

Table 4.1: The radiation characteristics for each slot in the centre fed 6-element linear array.

	S_1	S_2	S_3	S_4	S_5	S_6
P_r	0.0387	0.1594	0.3019	0.3019	0.1594	0.0387
g_r	0.0774	0.3188	0.6038	0.6038	0.3188	0.0774
l_r / mm	4.12	4.27	4.42	4.42	4.27	4.12
x_r / mm	0.55	1.20	1.78	1.78	1.20	0.55
l_{ro} / mm	4.25	4.42	4.55	4.55	4.42	4.25
x_{ro} / mm	0.56	1.23	1.83	1.83	1.23	0.56

and for each slot,

$$g_{ri} = 2P_{ri}/V^2, \quad i = 1,\ 2,\ \cdots,\ N \tag{4.7}$$

where V is the input voltage. Hence, g_r is proportional to the radiated power of the slot.

Based on the prescribed array performance, such as the beamwidth, gain, and sidelobe level, *etc.*, the approximated number of elements can be determined by empirical knowledge. After that, through either Dolph-Chebyshev or Taylor distribution, the aperture distribution and thus radiated power for each slot can be obtained. Since the normalised conductance is proportional to the radiated power, g_r is also known. Finally, refer to Fig. 4.9 (some data interpolation technique may be needed to obtain sufficient data points) to find the initial corresponding resonant length, l_r, and offset, x_r. Note all this synthesis is based on the centre frequency of the interested band (35 GHz here).

According to [122], the number of slots that can be arrayed in a single waveguide is limited, as the impedance bandwidth narrows down quickly with the increasing number of elements. Furthermore, the main beam with the centre-fed scheme doesn't shift with frequency.

So a small centre-fed array of 6 elements centred at 35 GHz is chosen here to realise at least 10 dB gain. The aperture distribution is calculated based on a 25-dB Taylor distribution ($\tilde{n} = 4$). After that, P_r, g_r, l_r, and x_r without accounting for mutual coupling can be derived and shown in Table 4.1. The geometrical configuration and equivalent circuit model are shown in Fig. 4.10. It can be observed that the aperture distribution and geometry are symmetrical.

The 6-element array is fed by a standard WR28 from the backside of the HSIW, so the feeding slot is actually the cross-sectional size of WR28 (7.11×3.55 mm^2). Note there is a blockage area on top of the feeding slot, which enlarges the distance

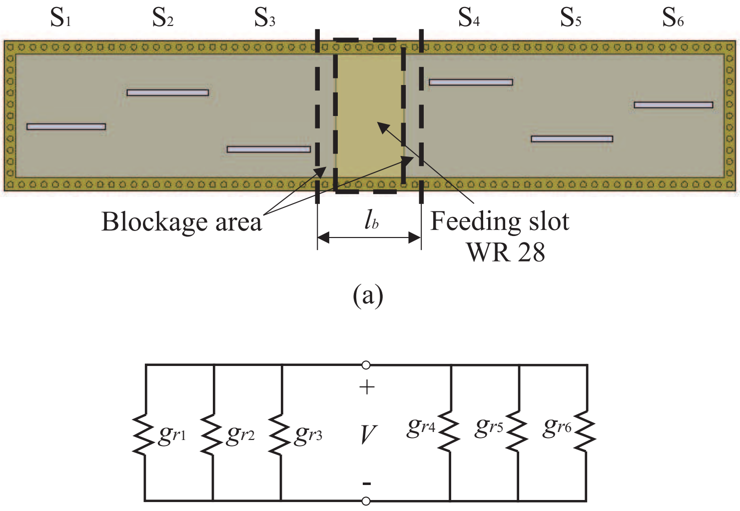

(a)

(b)

FIGURE 4.10: The centre-fed 6-element linear array: (a) geometrical configuration, (b) equivalent circuit model.

between the third pair of slots by l_b. For the linear array, l_b could be reduced to nil. For the planar array in later designs, however, l_b does exist because of the feeding power divider. The appearance of this blockage area pushes centre slots further apart (now $\lambda_g/2 + l_b$) and will consequently result in a increase in the sidelobe level [129, 132].

The initial return loss, S_{11}, and radiation patterns in E-plane and H-plane from the HFSS simulation are shown as the dashed lines in Fig. 4.11.

As can be observed in Fig. 4.11(b), S_{11} from the initial design deviates from 35 GHz by about 0.7 GHz, which obviously is the result by ignoring the mutual coupling. As for the radiation pattern, the peak gain achieved is 14.5 dB which meets the prescribed requirements. The sidelobe suppression in the H-plane, however, is only 21.9 dB which will be improved by the following optimisation.

3) Optimisation with mutual coupling

There are all together six parameters, *i.e.*, three pairs of l_r and x_r that can be utilised to optimise the performance of the small linear array. The radiation characteristics of a single slot will certainly be affected in the situation of an array, though not much. It is found, through empirical knowledge, that l_r has more influence on the resonant position, where S_{11} reaches its minimum, whereas x_r causes more effects on the radiation pattern.

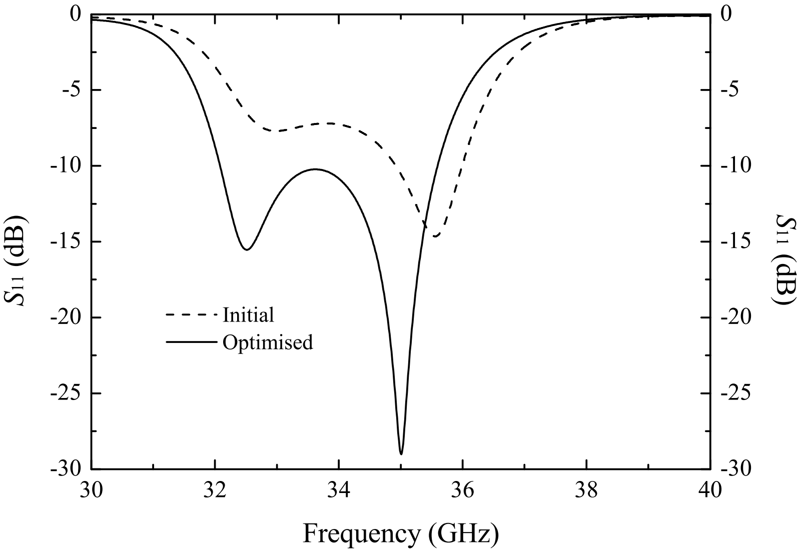

(a) S_{11}

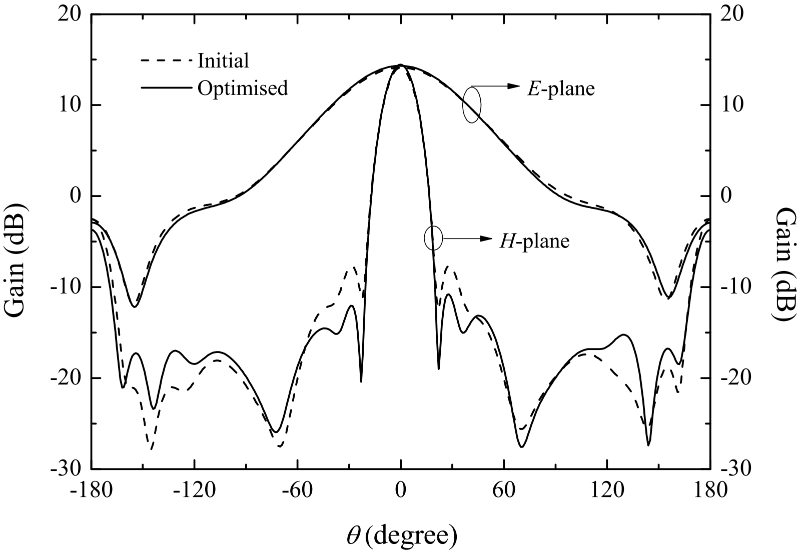

(b) Radiation pattern at 35 GHz

FIGURE 4.11: The radiation performance of a centre-fed 6-element linear array.

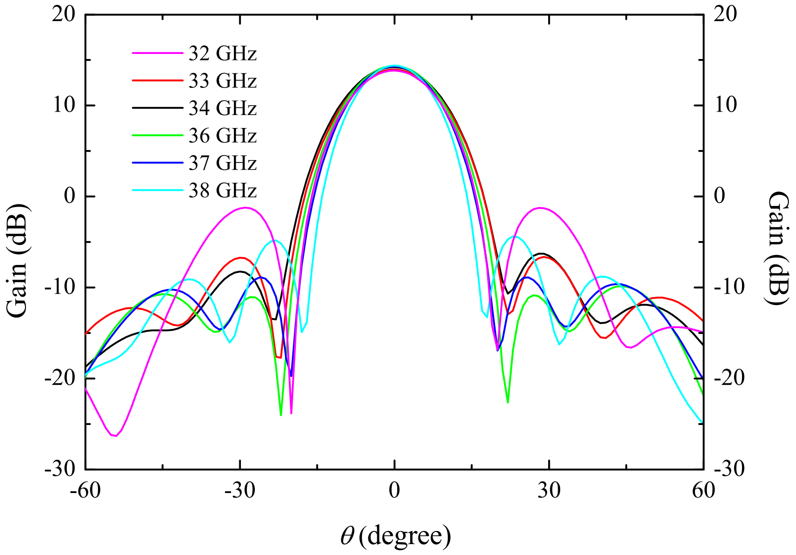

FIGURE 4.12: The simulated H-plane radiation pattern at various frequencies for the centre-fed 6-element linear array.

With that in mind, the optimisation process can be split into two separate stages: S_{11} optimisation and radiation-pattern optimisation. Generally speaking, increasing the length of a resonant slot will decrease the resonant frequency. So l_r is increased marginally of each slot at the same time to find the response of S_{11}. This could be repeated multiple times and try to avoid a sudden big increment at a time. After that, adjust x_r of each slot one by one to find the possible change of sidelobe suppression. If it's getting worse, adjust x_r in the other direction. Normally, the sidelobe suppression is not much from predefined value after the optimisation of S_{11}. So a few times of repeats will achieve the goal.

The optimised values of l_r and x_r are shown in the last two rows of Table 4.1 as l_{ro} and x_{ro}. It can be seen that all the optimised values are slightly higher than the initial ones.

The optimised performance is shown as the solid lines in Fig. 4.11. The resonance is now shifted to exactly 35 GHz, although there is also a weak one at around 32.4 GHz which can be viewed as an enhancement of the frequency bandwidth. Further, the resonance is now much deeper than the initial one, which indicates an excellent input match. As for the radiation pattern, the peak gain and E-plane pattern don't change much while the sidelobe suppression in the H-plane has now increased to 25.4 dB. So to summarise, the optimisation has successfully reached its objective. Nevertheless, it's worth noting that the backlobe of the radiation

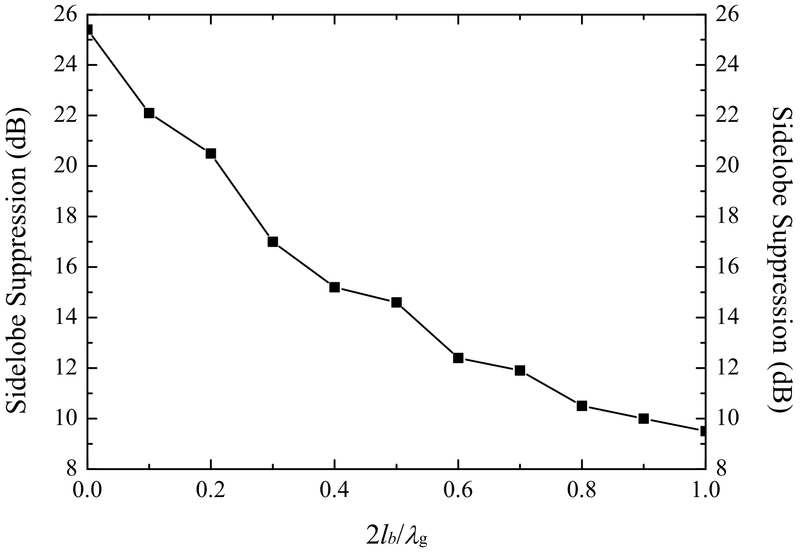

FIGURE 4.13: The degradation of H-plane sidelobe suppression at 35 GHz with the increase of normalised blockage length, $2l_b/\lambda_g$, of the centre-fed 6-element linear array.

pattern for both planes is very high. This is due to the narrow width of the HSIW and can be significantly improved in the later design of planar arrays.

An important feature of centre feeding is that the long-line effect disappears, which means that the main beam doesn't change its orientation along with frequency. This can be clearly observed in Fig. 4.12: The main beam at various frequencies keep the same angle, *i.e.*, exactly broadside to the HSIW, although the sidelobe level might fluctuate considerably. Also, the peak gains keep stable at 14.5 dBi.

Together with this feature, there is a main drawback for centre-feeding arrays, which is the introduction of the blockage area as shown in Fig. 4.10. Although this can be avoided in the linear array, the planar arrays will have to face this grey area where no slots are radiating and an increase in the sidelobe level occurs, as shown in Fig. 4.13.

As can be found, the sidelobe suppression deteriorates quickly from 25.4 dB to 9.5 dB when the length of the blockage area increases from nil to one half-wavelength. So in order to maintain a high sidelobe suppression, l_b should be kept as small as possible. Apart from that, re-optimisation is probably needed when l_b, the width of the feeding power divider, is determined and the inter-subarray coupling appears in the design of a planar array.

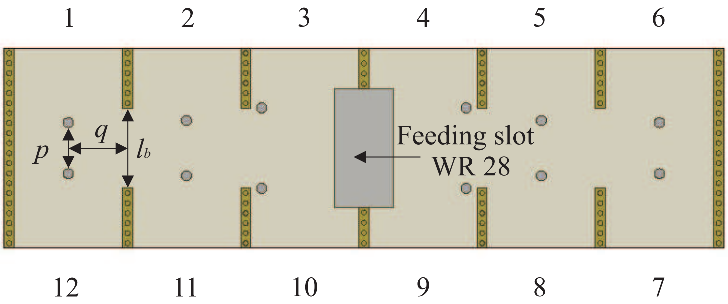

FIGURE 4.14: The top view of the multiway power divider for the use of 6 × 6 planar HSIW slot array.

4.3.2 Planar Array

In this section, a 6 × 6 planar HSIW slot array is designed based on the 6-element linear array designed in last section. Firstly, a multiway power divider is designed and placed at the centre of the planar array, which also satisfies the requirements on the amplitude and phase for each subarray. Then, all 6 subarrays are put together and optimised with the inter-subarray coupling to achieve a high-gain and high-selection planar array.

4.3.2.1 A Multiway Power Divider

M. Ando *et.al.* proposed a multiway power divider based on RWG in 1997 [138]. The basic mechanism is to use a coupling window coupling energy from the feeding waveguide to the radiating waveguide and one or two metallic posts near the window to suppress the reflection. This power divider was later extended to post-wall waveguide in [139] and has been widely used in his own antenna designs [128–133] and by K. Wu *et.al.* based on SIW slot antennas [140–142].

A multiway power divider for the use of waveguide slot arrays should be able to provide: (a) an alternating 180° phase change, since each subarray should be fed in phase and 360° phase change will make the power divider too wide; (b) an amplitude distribution which agrees with the prescribed aperture distribution.

Here a simplified multiway power divider is proposed as shown in Fig. 4.14, which employs only two aligned metallic posts to meet the requirements. The removal of the coupling window will also simplify the fabrication process, since to realise a hollow structure on LTCC has already proved to be difficult.

As shown in Fig. 4.14, there are 6 radiating HSIWs corresponding to 6 subarrays symmetrically located on both sides of the feeding slot. l_b stands for the length

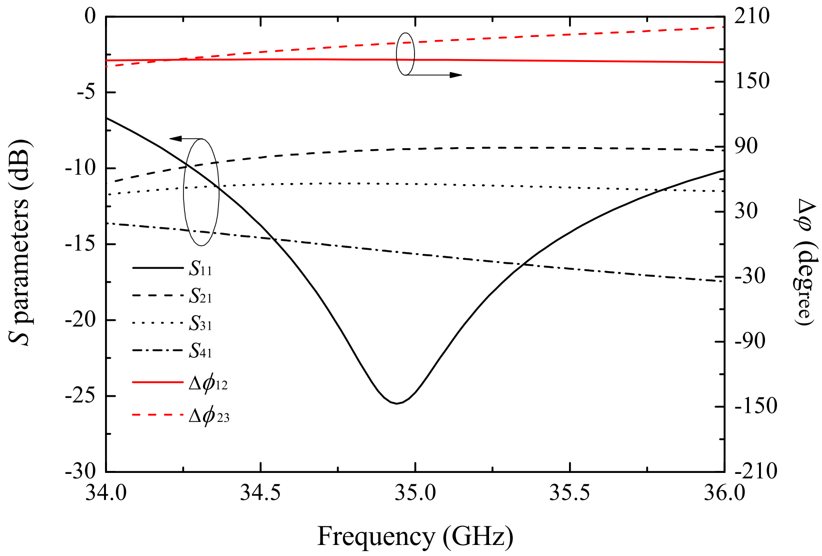

FIGURE 4.15: The simulated performance of the multiway power divider for the use of 6 × 6 planar HSIW slot array.

of the blockage area, through which the injected energy is distributed following a set aperture-excitation pattern. There are 6 pairs of posts, one for each HSIW, responsible for the energy distribution. Further, the horizontal location, q, relative to the host HSIW has more influence on the phase response and the vertical distance, p (symmetrical with respect to the centreline of the blockage area to keep the phase stability), causes more effects on the magnitude response. Special caution should be paid to the closest pair to the feeding slot, as they are key to suppress the return loss.

Here the 25-dB Taylor distribution ($\tilde{n} = 4$) continues to be applied, which results in an energy-distribution of Port 1, 0.0194; Port 2, 0.0797; Port 3, 0.1510 in terms of power ratio or Port 1, -17.12; Port 2, -10.99; Port 3, -8.21 in terms of dB. Note that the energy distribution of the other ports can be obtained based on symmetry.

After optimised through the HFSS simulation, the magnitude and phase response of this multiway power divider is shown in Fig. 4.15 and the finalised blockage area and post locations are: $l_b = 4.6$, $p_1 = 1.5$, $q_1 = 3.3$, $p_2 = 1.6$, $q_2 = 3.5$, $p_3 = 3.1$, $q_3 = 6.1$, all in mm.

As shown in Fig. 4.15, S_{11} has a deep resonance at around 35 GHz and S_{21}, and S_{31} stay rather flat in the studied band and close to the prescribed magnitudes (-8.48 dB and -11.03 dB achieved, respectively). S_{41}, however, is inclined and the middle value is 15.8 dB, slightly drifting from the objective. As for the phase

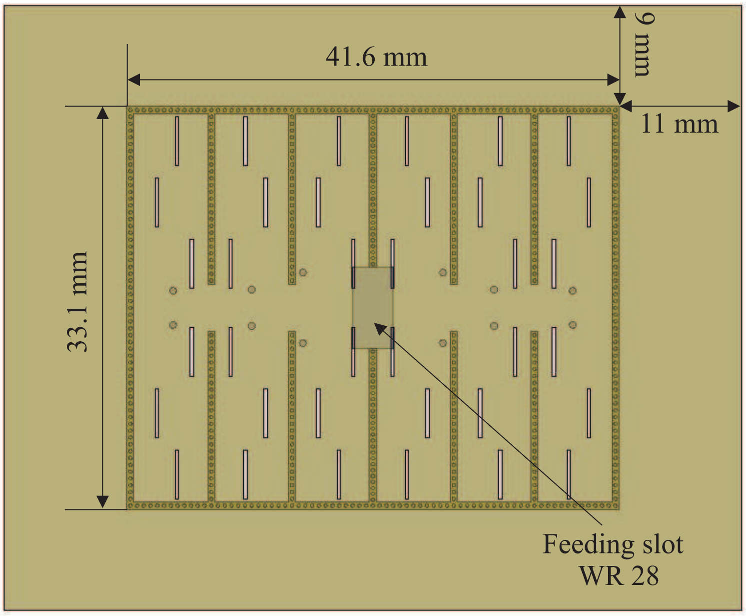

FIGURE 4.16: The top view of the 6 × 6 planar HSIW slot array.

response, $\Delta\phi_{12}$, 172°, is flat throughout the band, whereas $\Delta\phi_{23}$ is inclined as the shape of S_{41}. The middle value of $\Delta\phi_{23}$, however, is 185°, which might narrow down the operating bandwidth of the slot array but still could be used.

4.3.2.2 A 6 × 6 Planar Array

a) Configuration

All 6 linear subarrays are assembled into a planar panel, where the relative positions of slots should be given caution to. Since the power divide generates alternating 180° phase switch, the neighbouring subarrays should be on the opposite side of the radiating HSIW. Further, the slot arrangement inside a single subarray is also different from that of a linear array: the slots are now symmetrical with respect to the feeding slot, as shown in Fig. 4.16, instead of sequentially located as shown in Fig. 4.10(a). The reason is that the orientation of the feeding slot is changed by 180° and thus the phase response changes accordingly.

Note that there is a 9 × 11 mm^2 marginal area surrounding the planar array which is for the convenience of fabrication. This area will slightly enhance the upward radiation (gain) and suppress the backlobe.

As discussed in Section 4.3.1, the blockage area (the power divider) should be kept as small as possible and has been given as $l_b = 4.6$ mm (about $0.43\lambda_g$) in Section

4.3.2.1. This is very high and will result in a big surge in the sidelobe level. A technique to reduce the adverse effect the power divider has brought is to extrude the slots outward into the blockage area to reduce the distance between the split slots. As shown in Fig. 4.16, the middle slots have small fractions of themselves into the power divider. Through this technique, the length of the blockage area, l_b, can be reduced by 3 via distances (3 × 0.6 mm) to 2.8 mm, which can greatly relieve the sidelobe degradation.

Another technique is proposed by M. Ando in [129], wherein an E- to H-plane cross-junction is used in the power divider. Hence, the blockage area is reduced to the narrow side of the feeding waveguide and the sidelobe level can be improved from 10 dB to 15 dB. Apart from that, he also proposed a multi-layer power divider corporately feeding the slots to remove the blockage area completely in [133]. The common feature to his techniques is that they are all realised in traditional RWGs and are considerably complicated, which will not be employed here.

b) Optimised performance

With the existence of inter-subarray coupling, re-optimisation is needed and follows the basic principle given in Section 4.3.1. The only difference lies in the optimisation of E-plane radiation pattern, which is now jointly affected by the power divider and slot locations. Advice to that is to adjust slots first to see the performance and if not satisfied, change the location of post-pairs of the power divider.

After optimisation, the finalised parameter values are given as $x_{r_1} = 0.57$, $x_{r_2} = 1.25$, $x_{r_3} = 1.85$, $l_{r_1} = 4.11$, $l_{r_2} = 4.28$, $l_{r_3} = 4.42$, all in mm and the parameters from the power divider keep unchanged.

The simulated S_{11} and peak gain of this 6 × 6 slot array is shown in Fig. 4.17 as the black lines. As can be seen, S_{11} resonates at 35 GHz and the impedance bandwidth is about 1.5 GHz, which belongs to the narrow-band antenna array. The peak gain for this array is 18.4 dBi at 35 GHz, 3.9 dB increase compared with that of a single linear array. Across the operating frequency band, the peak gain centres at 35 GHz and drops quickly toward both directions, which also indicates a narrow-band characteristic in line with the features of the waveguide slot array and power divider.

The radiation patterns of the E-plane and H-plane are shown in Fig. 4.18. Note that the peak gain has been normalised. The best sidelobe suppression that can

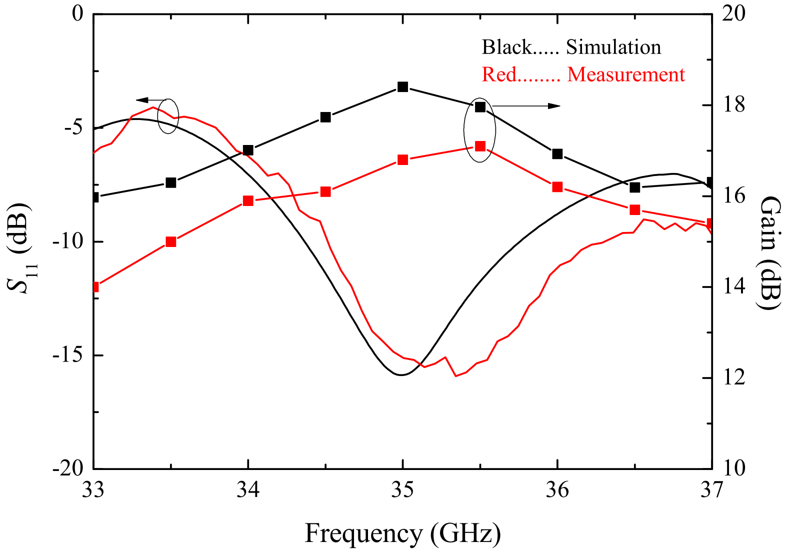

FIGURE 4.17: S_{11} and the gain of the 6 × 6 planar HSIW slot array.

be found is about 13 dB in both planes at 35 GHz and the degradation toward the higher frequency is much larger than that toward lower frequency. As can be observed, the main beam at all 3 frequencies is fixed at the broad side of the HSIW and the backlobe drops significantly compared with that of the linear array in Section 4.3.1.

The moderate sidelobe suppression in the H-plane can be expected after the extrusion technique is used, otherwise it will be below 10 dB, as demonstrated in [129, 131, 133]. As for the sidelobe suppression in the E-plane, it is also less than designed value. This is probably because of the phase instability, as shown in Fig. 4.15 and the extrusion of radiating slots. Note that high sidelobe suppression is probably causing a reduction of peak gain, so if the gain is the main concern, the demand on the sidelobe suppression can be loosened.

c) Measurement

A progressive-lamination LTCC technique is used to manufacture the 6 × 6 planar HSIW slot array, as shown in Fig. 4.19. The Dupont$^{\text{TM}}$ GreenTape$^{\text{TM}}$ 9K7 LTCC system with a relative dielectric constant of 7.1 is employed as the dielectric, while the silver paste with a conductivity of 3.7e7 S/m is adopted as the conductive material.

As shown in Fig. 4.19, the vias of the multiway power divider are implemented through copper wires whose positions are indicated by the red circles. On the

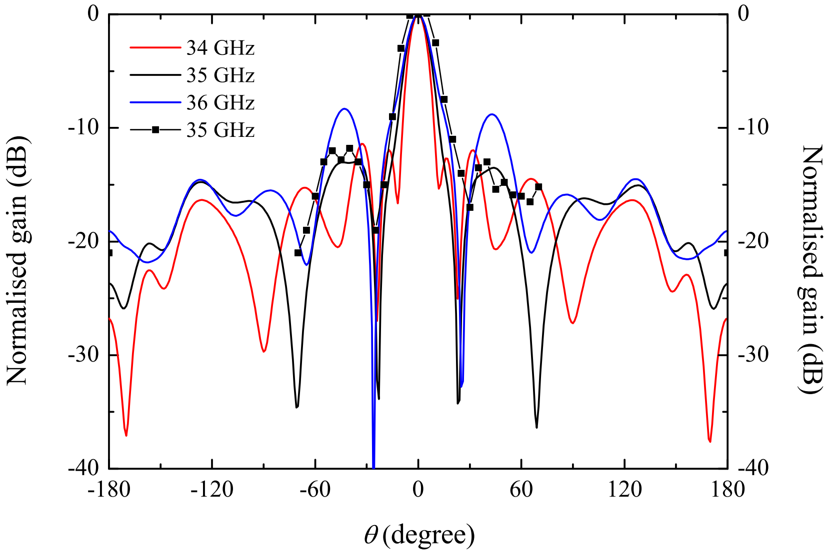

(a) *E*-plane

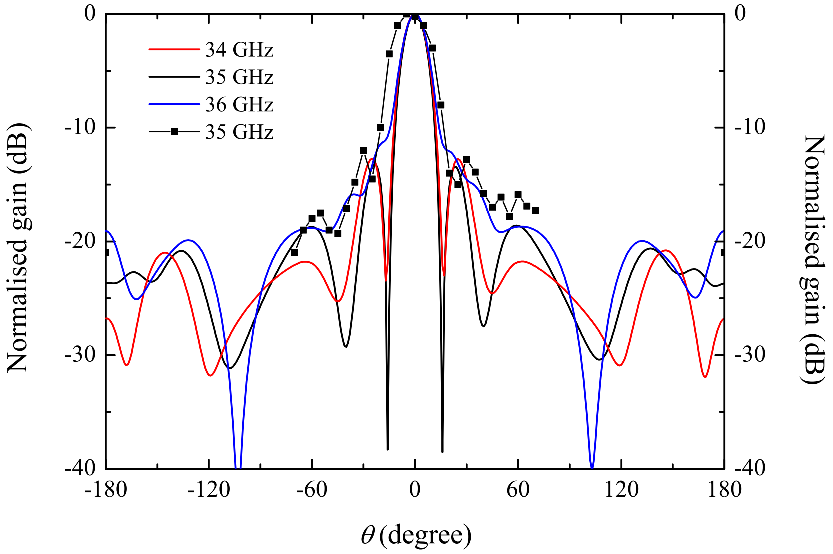

(b) *H*-plane

FIGURE 4.18: The radiation pattern of the 6 × 6 planar HSIW slot array: solid line for the simulation; solid line with squares for the measurement.

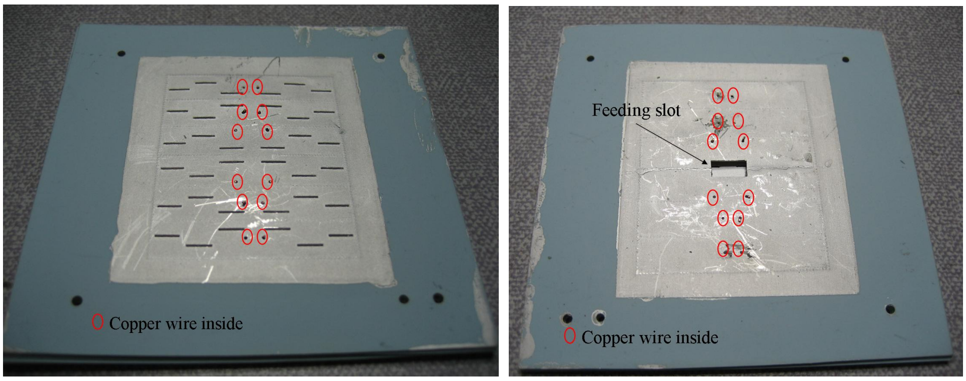

(a) top (b) bottom

FIGURE 4.19: The fabricated 6 × 6 planar HSIW slot array.

bottom side of the sample, a feeding slot is located at the centre to be connected with a standard WR28 through elastic strings or adhesive tapes.

The measurement setup is shown in Fig. 4.20, where a small wooden anechoic box with an internal size of 1.2 × 1.2 × 1.8 mm^3 is housing the measurement equipments and devices under test. The blue tapered absorbers attached to the inner sides of the wooden box are specially made for mm-wave applications. An Agilent PNA working up to 67 GHz is used as the source. A pair of Q-par horn antennas attached to two perspex poles work at the Ka band are used as the standard gain antennas which have a stable gain of 20 dBi. The gain of antenna under test (AUT) can be determined when replacing Antenna 2 and comparing the gain difference.

In order to measure the radiation pattern of an antenna, the AUT has to stay beyond the far-field distance of the source antenna; so does the source antenna. The far-field distance is defined as the spherical wave front radiated by antenna becomes approximately a plane wave front and given as [99]:

$$R_f = \frac{2D^2}{\lambda} \tag{4.8}$$

where D is the largest linear dimension of the antenna. So the far-field distance of an measurement system is the larger one of those for the two antennas.

In our case, the slot array measures 42.1 × 56.2 mm^2 which gives D 70.2 mm and works at a centre frequency of 35 GHz which gives λ 8.6 mm. Then, using (4.8), the far-field distance of the slot array, R_f is obtained as 1.15 m. Since the dimension is obviously larger than the horn antenna, the far-field distance of the slot array is thus that of the system. The distance between the two perspex poles

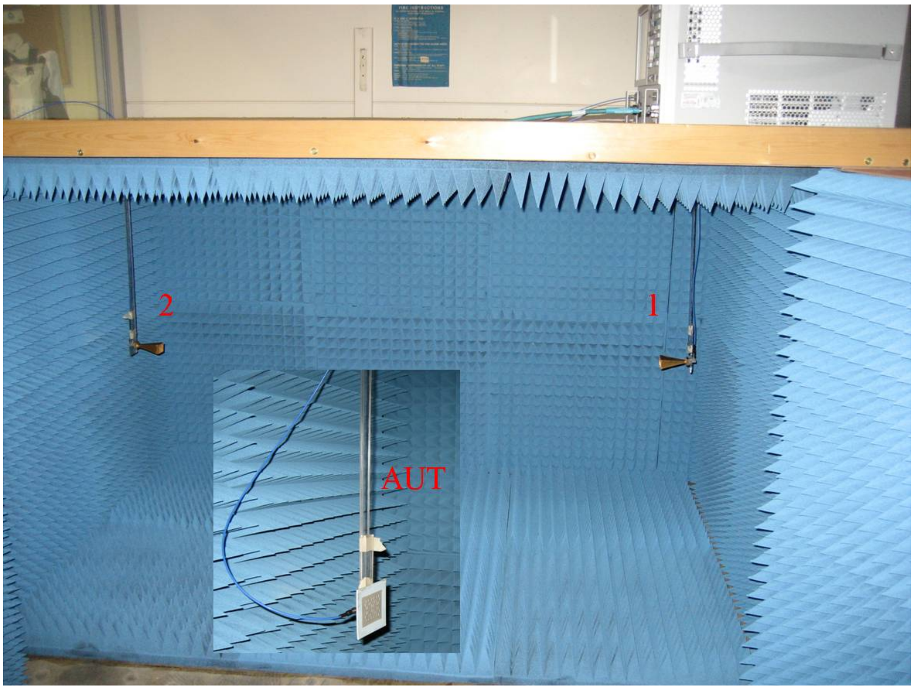

FIGURE 4.20: The measurement setup of the 6 × 6 planar HSIW slot array.

is 1.4 m which satisfies the requirements for the radiation pattern measurement in the far-field.

The measured S_{11} and peak gain of the slot array is shown in Fig. 4.17 as the red lines. As can be observed, the measured response seems to shift slightly upwards with a centre frequency of about 35.5 GHz and the measured gain is generally lower than that from the simulation with the peak gain of 17.1 dBi, 1.3 dB lower than the peak simulated gain. Apart from that, the measured and simulated results are in a good agreement.

The measured radiation pattern at 35 GHz is at a 5° increment up to 70° and is shown in Fig. 4.18 as the solid lines with squares. It can be seen that the sidelobes in both the E-plane and H-plane are about 11.5 dB, 1.5 dB higher than those from the HFSS simulation and the main beams are both slightly wider. Furthermore, the main beam in the H-plane, has shifted toward one side for 5°. Possible reasons for the disagreement and degradation may come from the unaccounted shrinkage of the LTCC and poor via connection between adjacent LTCC layers.

4.4 Conclusion

In this chapter, a 6 × 6 planar array based on a slotted HSIW is designed, fabricated, and measured. A simulated gain of 18.4 dB and a sidelobe suppression of 13 dB in both E and H planes are achieved. Fabrication and measurement have also been performed to verify the design.

For this centre-fed array, an inherent drawback is that the sidelobe suppression cannot be too high with the existence of the blockage area. The investigations on how to alleviate this problem with the LTCC HSIW technology will be studied in the future.

Chapter 5

A Dielectric Insular Resonator Antenna Array Fed by DIIG

This chapter is organised as follows: Section 5.1 presents an introduction to the dielectric resonator antenna (DRA), in terms of its history, advantages/challenges, and feeding schemes. After that, Section 5.2 explains how resonant modes are generated in a DR and radiate as a DRA. Then, Section 5.3 employs two theoretical models to analyse the DRA and dielectric insular resonator antenna (DIRA). Results from the two models are compared with each other and those from publications. Finally, a double-sided Taylor-distributed DIRA array fed by the DIIG is designed, fabricated and measured in Section 5.4.

5.1 Introduction

Over the last few decades, the dielectric resonator antenna (DRA) has been drawing massive interest to prompt significant progress in microwave and mm-wave antenna technologies. What's more, a recent surge of DRA publications in Fig. 5.1 is arguably showing that the interest on this subject tends to be in an explosively-growing mode. The preference on the DRA mainly lies in the fact of its versatility, efficiency and design flexibility compared with traditional microstrip antennas and other low-gain narrow-band antennas [143].

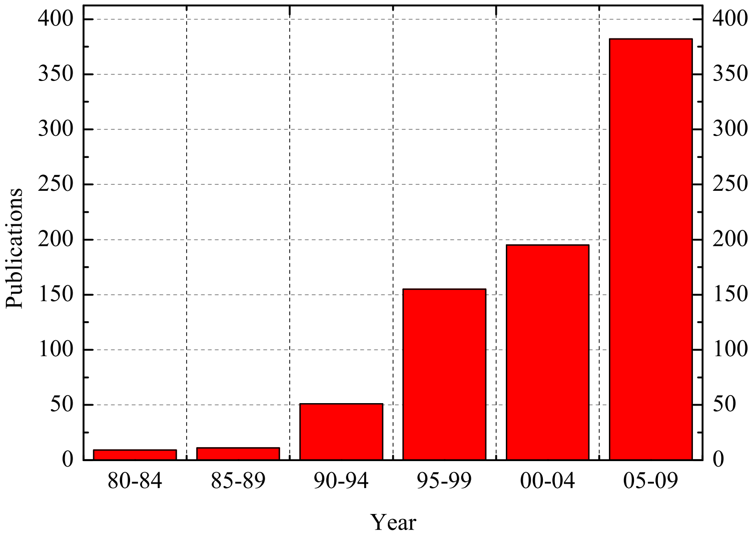

FIGURE 5.1: The number of publications on DRAs in recent years [143].

5.1.1 Historical Review

1939 saw the birth of a new term, “Dielectric Resonator (DR)”, by Ritchmyer of Stanford University who found that dielectric objects in the form of toroids could function as microwave resonators and thus are potential to be developed as oscillators and filters [144]. Little interest, however, was triggered by Ritchmyer’s theoretical investigations over the next two decades and no actual applications were seen in real practice. Not until the early 1960s did worldwide engineers start to pay attention to DRs, together with extensive theoretical and experimental research conducted on various shapes of them. A real breakthrough in the dielectric ceramic industry early 1970s certainly accelerated this process and made massive reliable production of DR circuits possible. During this time, DRs, typically cylindrical, are fabricated out of high dielectric constant materials ($\epsilon_r \geq 35$) and usually shielded to maintain the high quality factor needed for applications in oscillators, filters, *etc.* [145].

By removing the shielding and with proper feeding schemes, these DRs are found to be functioning as efficient radiators. In fact, the theoretical investigations on the radiation characteristics of DRs were carried out long ago in the 1960s as a sideline and practically suppressed for the prevailing application of oscillators and filters until 1983 [146, 147]. In this year, S. Long *et al.* published a paper on the cylindrical DRA which studied and examined at length the radiation performances of DRs as antennas [148]. After that, they continued with the research on this subject to explore DRAs in other shapes: rectangle [149] and hemisphere [150]. All their serial work laid the foundation for future extensive investigations on various aspects of DRAs in various forms [122, 151].

In the late 1980s and early 1990s, the mainstream of the DRA research was focused on the feeding mechanisms, the eigenmodes of and analytical and numerical techniques to determine the input impedance, Q factor and radiation patterns of DRAs with simple shapes. Much of this work was summarized in [152] by R. Mongia *et al.* By the mid- to late 1990s, linear and planar arrays of DRAs started to draw people's attention and publications on simple two-element arrays up to complex planar phased arrays of over 300 elements with electronic phase-steering capabilities were also seen during this period of time [143].

Entering into this new century, many more researchers started to turn their interest to DRAs and an unprecedented rate of publications has been prompted as shown in Fig. 5.1. New areas of DRA research came into being, such as enhanced-gain techniques, finite-ground-plane effects, tunable DRAs, reconfigurable patterns, ultra-wideband designs, polarization agility, and dual-function designs (where the dielectric resonator antenna is used both as a resonator and as an antenna), *etc.* Also, new shapes of DRAs have been introduced, including conical, tetrahedral, hexagonal, pyramidal, elliptical, and stair-stepped shapes, or hybrid antenna designs, using dielectric resonator antennas in combination with microstrip patches, monopoles, or slots. With the fast-growing wireless communications, new specific applications have also emerged: integration into mobile handsets for PCS, IMT2000 and WLAN applications; use in cellular base-station antennas; UWB applications; radar applications; breast-cancer imaging; RFID; spatial power combining; direction finding; and all-dielectric wireless receivers [143].

With more and more researchers and funding joining in, the research on DRAs will continue to be a hot subject and promote the development of modern antenna technologies and wireless communications.

5.1.2 Advantages and Challenges

Quite a variety of DRA shapes have been studied and manufactured. Some of them are commonly seen and shown in Fig. 5.2. Although they do vary in forms, some basic advantages are shared in contrast with traditional microstrip antennas and other low-gain narrow-band antennas, together with challenges.

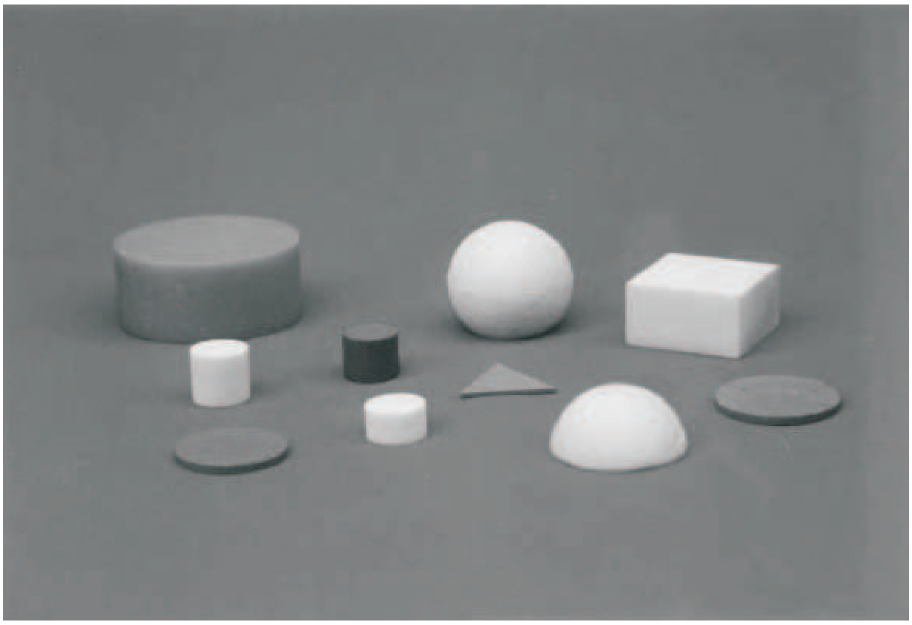

FIGURE 5.2: Various shapes of DRAs, including cylindrical, rectangular, hemispherical, low-profile circular-disk, low-profile triangular, and spherical-cap DRAs [151].

Advantages:

- Efficient radiation

  The DRA is immune to surface-wave losses and maintains reduced conductor losses, which contributes a lot to a high radiation efficiency. This advantage becomes even more pronounced when it comes to the millimetre-wave or higher band, as the conductor loss deteriorates quickly with respect to the increasing frequency [143, 151].

- Wide band

  The DRA radiates through the whole surface except for the grounded part, whereas the microstrip antenna radiates only through two narrow edges. This gives DRAs a much wider bandwidth compared with microstrip antennas. A typical impedance bandwidth for a DRA with a dielectric constant of 10 is around 10%; while the widest for a simple rectangular DRA reported till today is 42% [145, 151, 153].

- Flexible design

  A wide range of ϵ_r (from 4 to 100) can be used, thus allowing the designer the flexibility in controlling the size and bandwidth of DRAs. In addition, various modes can be excited which produce different radiation patterns for flexible coverage requirements. Moreover, the Q-factor of some of these modes depend on the aspect ratio of the DRA, thus allowing one more degree of flexibility in the design. Finally, many existing feeding schemes can be used (slots, probes, microstrip, coplanar waveguides, dielectric image guide, *etc.*), which makes DRAs easy to be integrated with existing technologies and adds another degree of flexibility to their design [143, 145].

Of all the different shapes of DRAs, rectangular DRAs offer extra advantages over DRAs in other shapes, such as cylindrical and spherical ones. One advantage is that it has two degrees of dimensional freedom. For any given resonant frequency and fixed dielectric constant, two of the three dimensions of the rectangular DRA can be chosen independently (one for the cylindrical DRA and none for the hemispherical DRA), which provides more flexibility in terms of aspect ratios and thus bandwidth control [151, 154]. The other is that mode degeneracy, which can enhance the cross-pol levels of an antenna and should be strongly avoided, can be removed in rectangular DRAs; while it always exists in a spherical DRA and in the hybrid modes of a cylindrical DRA [146, 154, 155].

Further details with regard to mode analysis and radiation characteristics will be explained in Section 5.3.

Challenges:

- Fabrication complexity

  The standard fabrication process for a DRA array is to machine all the radiating elements from a block of the dielectric material and then individually place and bond them to the feeding structure. This could be a labour-intensive and relatively expensive procedure. Moreover, air gaps are easily introduced as fabrication imperfections which severely affect DRAs' performances, especially when it comes to the millimetre-wave band. In fact, air gaps are potential to increase the radiation efficiency and bandwidth; the unwanted ones, however, could be a trouble-maker [143, 156].

- Integration with MMICs

  Micro-machining techniques are starting to be used in the fabrication process of DRAs, which could extend their frequency range well beyond 100 GHz. How to surface-mount small DRA blocks to silicon based substrates in the forms of MMICs is challenging. If successful, however, it will fulfil the demand of DRAs on chip for future generation of very compact RF applications [143, 156].

DRAs can fit in a wide range of physical or electrical requirements of various wireless communication applications. From as low as 55 MHz to 94 GHz, from a single radiating element to a planar array of 529 elements, DRAs have demonstrated a large degree of flexibility and adaptability which can still be improved on as they don't represent fundamental theoretical or practical limits. Although fabrication complexity is increased compared with the printed technology, it could be resolved as research is conducted and new or existing technologies are applied into this area. All this will certainly make the DRA a promising and viable alternative to traditional low-gain narrow-band antennas.

5.1.3 Feeding Schemes

For most practical applications, energy must be coupled into or out of a DRA element through one or more ports for it to be working as an antenna (a possible exception is the DRA used in a reflectarray configuration). The type and location of the port with respect to the DRA will determine which mode will be excited and how much energy will be coupled between the port and the antenna, that is the resonate frequency and radiation Q-factor of a DRA. Although there are no simple closed-form expressions to accurately decide on these quantities (numerical techniques are required), it can still be qualitatively analysed through approximate field distributions of the modes of both the coupling structure and the isolated DRA [122, 151]. This section outlines some commonly-seen feeding schemes which might use aperture, coaxial probe, coplanar waveguides, microstrip line or DIG for energy coupling. Fig. 5.3 illustrates some of these feeding schemes.

5.1.3.1 Aperture Coupling

Here the aperture can be of various shapes, such as narrow rectangular slot, loop, cross, or C-shape cut in the ground plane of a microstrip line or on the broad surface of a waveguide. It is worth noting that the aperture should be kept electrically small to avoid excessive radiation beneath the ground plane in the case of microstrip line feeding. Also, if the aperture is too large, it will overly load the DRA to significantly shift the resonant frequency and Q-factor compared to the theoretical calculation. If the aperture is electrically small, it will behave like a magnetic current running parallel to the length of the slot, which excites the magnetic fields in the DRA. Locating below the ground plane, aperture coupling

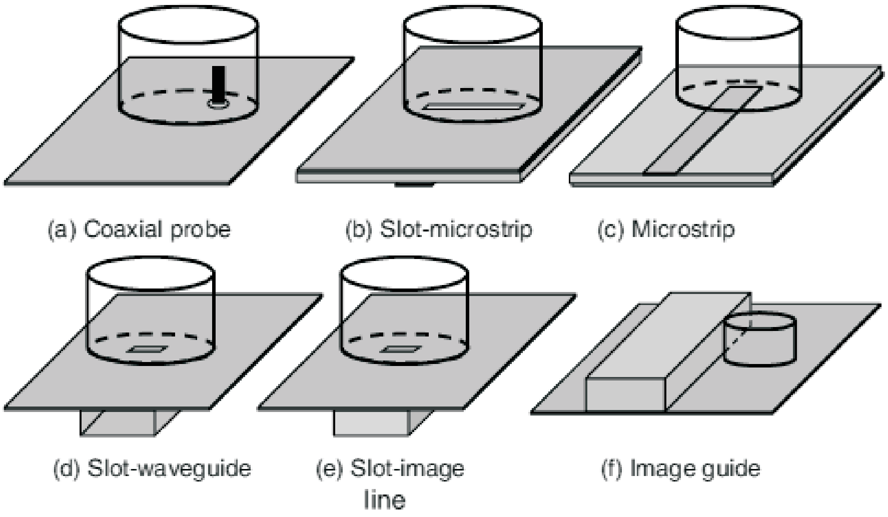
(a) Coaxial probe (b) Slot-microstrip (c) Microstrip

(d) Slot-waveguide (e) Slot-image line (f) Image guide

FIGURE 5.3: Various feeding schemes of the DRA [122].

offers the advantage of protecting the radiating element from any unwanted coupling or spurious radiation of the feed. Moreover, aperture coupling is widely used for integrating DRAs with printed feeding structures [122, 145].

5.1.3.2 Probe Coupling

In this coupling scheme, the probe, considered as an electric current running vertical to the DRA ground, usually consists of the centre pin of a coaxial transmission line that extends through the ground plane or a thin metal post soldered to a flat metal strip. The strength of coupling and nature of modes depend on the length and location of the probe and can be thus optimized. Generally, the probe length is chosen to be less than the height of the DRA, to avoid probe radiation. (A notable exception is the hybrid monopole-DRA, where the probe acts as both a feed and a monopole radiator.) Also, in terms of practicality, locating the probe feed adjacent to the DRA is preferred since embedding the probe into the DRA requires drilling into it. (This, however, cannot be avoided for the $TM_{01\delta}$ mode of cylindrical DRAs where the probe must be at the centre of the DRA.) [122, 151]

An advantage of the probe coupling method is that the antenna system can be directly connected to a 50 Ω circuit without the aid of any matching network [122].

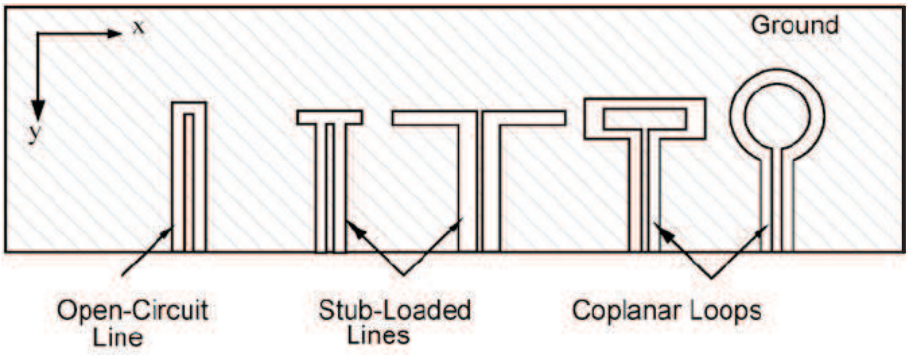

FIGURE 5.4: Various coplanar structures for coupling to the DRA [145].

5.1.3.3 Coplanar Coupling

An advantage of coplanar coupling (normally through coplanar waveguides) is that it enables easy integration with MMICs compared with coaxial probe coupling. Open-circuit coplanar waveguides can be used to directly feed DRAs, together with stubs or loops at the end of the line for additional control of impedance matching as shown in Fig. 5.4. The coupling level and nature of modes can be adjusted by moving the DRA over the coplanar structure [122, 145].

5.1.3.4 Microstrip Line Coupling

The microstrip line coupling mechanism is the simplest method to feed DRAs which offers easy and cost-effective fabrication of DRA arrays because feedlines can be simply printed over the substrate. In this method, the level of coupling from the microstrip line to the DRA can be controlled by adjusting the spacing between the DRA and the line for the side-coupled case or the length of the line underneath the DRA for the direct-coupled case. A more dominant parameter affecting the degree of coupling is the permittivity of the DRA. The higher permittivity, the stronger coupling. This can be problematic when a single low-dielectric-constant demands a wideband operation. For series-fed linear arrays of DRAs, however, the lower level of coupling may not be an impediment, since each DRA element only radiates a small amount from the microstrip feed line [122, 151].

Apart from the merits microstrip line coupling exhibits, there is also a disadvantage: The polarization of the array is dictated by the orientation of the microstrip line and moreover, this excitation scheme may also generate surface waves in the microstrip line substrate, which is highly undesirable [122].

5.1.3.5 DIG/DIIG Coupling

The DIG coupling to the DRA offers advantages over the microstrip line scheme in that they do not suffer from severe conductor loss, especially in the mm-wave band. What's more, this conductor loss could be further reduced by introducing a low-permittivity inset between the dielectric guide and the ground plane, namely employing dielectric insular image guide (DIIG) [106]. Similar to the microstrip line coupling, DRAs can be fed either from sideways or underneath through DIG. Here the coupling level between the guide and the DRA is usually small, which, however, can be increased by operating the guide closer to its cutoff frequency. This feeding scheme is promising and has found its way in many applications, especially in series-fed linear DRA arrays [122, 145].

5.1.4 Conclusion

An introduction to the basic principles of DRs/DRAs is presented in this section, including a historical review, potential advantages and challenges and various feeding schemes. Of all the shapes and feeding schemes DRAs may have, the rectangular DRA and DIG/DIIG stand out in terms of design flexibility and mode-degeneracy suppression. Apart from that, they could also share the same processing technology because of the similar cross section. So the following design will be focusing on this promising type of DRA and its feeding scheme of DIIG.

5.2 Resonant Modes of a Rectangular DR

The resonant mode is generated for a microwave resonator, including the DR, when the stored electric energy is equal to the magnetic energy. Generally, there will be an infinite number of resonant modes and each of them corresponds to a particular resonant frequency. Only the lowest order or a couple of low-order modes will be of interest in the scientific research and practical applications. As for the DR, there are no metallic surfaces to completely confine electromagnetic fields inside, which gives rise to the leakage or radiation in a specific field pattern at a specific mode. That's basically how a DRA is formed [122].

A rectangular DR can be viewed as a truncated DG engulfed in the air, as shown in Fig. 5.5(a), (b). So the modes in a rectangular DR is similar to that in a DG, except that the wave will be standing (suppose there is a field variation) along the z direction instead of travelling. Theoretical methods to analyse the propagation characteristics of the DG/DIG, such as Marcatili's method [112] and the EDC method [113], can be easily transferred to that of the DR. In order for the DR to be used as a DRA in the microwave and millimetre-wave band and also for the facility of feeding, the DR is practically placed on top of a pure or insulated metal together with the feeding DIG/DIIG, as shown in Fig. 5.5(c), (d) [104, 151]. The DRA with an insulated metal ground is named as DIRA (Dielectric Insular Resonator Antenna).

On one hand, the rectangular DR enjoys more design flexibility compared with the spherical or cylindrical DR, which comes from the three independent dimensions; on the other hand, this edge-rich shape brings in more discontinuities and hence, more complexity of its field distribution. In fact, all 6 components of electric and magnetic fields exist in the rectangular DG and hence, the rectangular DR [118]. In contrast, only TE, TM or the combination of these two modes reside in the spherical and cylindrical DR [146, 155]. By neglecting the weakest electric or magnetic components, however, the modes of the rectangular DR can be grouped into TE-like and TM-like ones, as demonstrated in Chapter 3 for the DG/DIG.

Based on the nomenclature used for the rectangular DG/DIG [112], the propagating modes can be classified into TM^y_{mn} and TE^y_{mn} modes. For the TM^y_{mn} mode, E_y and H_x are the principal transverse field components, whereas E_x and H_y are taken as the strongest transverse components when the TE^y_{mn} mode is separated. Following this nomenclature, the resonant modes of a rectangular DR as a truncated section of a DG is thus specified as TM^y_{mnl} and TE^y_{mnl} modes. The mode indices, m, n, and l, refer to the number of field extremas or half cycle variations of electric and magnetic components inside the DR along x, y, and z directions, respectively. At resonant frequencies, the fields tend to be standing inside the DR (except when m, n, or l equals 0), whereas decaying exponentially with distance outside it [104].

For the record, it's not just the TM^y_{mnl} and TE^y_{mnl} modes that can reside inside a rectangular DR. R. Mongia, *et.al.*, point out that TE and TM modes to other directions, *i.e.*, x, z, are also possible if the three dimensions of the resonator are not very different from each other [154, 157].

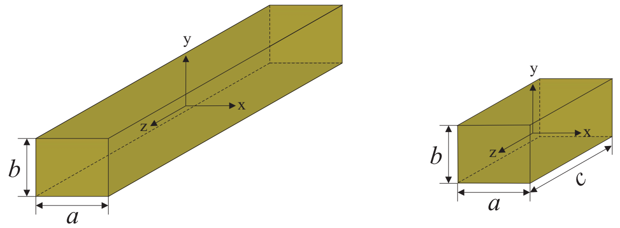

(a) An infinite DG (b) DR (truncated DG)

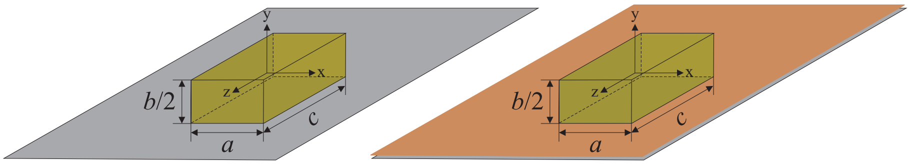

(c) DRA (on a metal plane) (d) DIRA (with an insular layer)

FIGURE 5.5: The 3D geometry of a DG, DR, DRA and DIRA.

5.3 Models of Rectangular DRA and DIRA

Since a rectangular DR can be viewed as a truncated DG, as shown in Fig. 5.5, the rectangular DG model is generally used to describe the wave behaviours in and around the DR. As for the characterization of DGs, there are approximate and numerical methods, as demonstrated in Chapter 3. When it comes to high-permittivity rectangular DRs, the imperfect magnetic-wall condition, (5.12a), can be applied to the DR surfaces and hence, simplify the calculation process. This is sometimes called the magnetic-wall model [154, 157]. Both these two models are elaborated in the following section.

5.3.1 The DG Model

If the DG is truncated in the z direction to form a DR and hence, a DRA, as shown in Fig. 5.5, there could also be a standing-wave pattern triggered inside the DR and an exponentially-decaying wave outside it along that direction, as is the case along the x and y directions.

Following the analysis on the DIG in Chapter 3, assumptions can be made that the propagation constants along the x and y directions, k_{x1} and k_{y1}, stay unchanged, while a similar characteristic equation can then be set up along the z direction.

For clarity and simplicity, assume that $a > b$, $c > b$ and only the EDC-H method is applied and presented; otherwise, the EDC-V method will be used.

5.3.1.1 DRA

The rectangular DRA to be studied is shown in Fig. 5.5(c). Detailed derivation has been demonstrated in Chapter 3 and for simplicity, only the final results will be given here.

For the TM^y_{mnl} mode, the characteristic equations in the x and y directions have already been given by (3.12) and (3.25) or (3.29). Now that in the z direction is given through the EDC-H method by

$$\begin{aligned} &1 - \frac{k_{z1}}{k_{z0}} \tan\left(k_{z1}c/2\right) = 0, \quad \text{even mode} \\ &1 + \frac{k_{z0}}{k_{z1}} \tan\left(k_{z1}c/2\right) = 0, \quad \text{odd mode} \end{aligned} \tag{5.1}$$

where

$$k_{z0} = \sqrt{(\epsilon_{re} - 1)k_0^2 - k_{z1}^2} \tag{5.2}$$

or for the convenience of calculation, transformed into

$$k_{z1}c = -2\arctan\left(\frac{k_{z1}}{k_{z0}}\right) + l\pi \tag{5.3}$$

where

$$\begin{aligned} &l = 2l' - 1, \quad l' = 1,\ 2,\ 3,\ \cdots \quad \text{even mode} \\ &l = 2l', \qquad\quad l' = 1,\ 2,\ 3,\ \cdots \quad \text{odd mode} \end{aligned}$$

Note that k_{x1}, k_{y1}, and k_{z1} should also satisfy the separation equation

$$\epsilon_r k_0^2 = k_{x1}^2 + k_{y1}^2 + k_{z1}^2 \tag{5.5}$$

Solve the equation array, (3.12), (3.25) (or (3.29)), (5.3) and (5.5) for k_0 and hence, the resonant frequency

$$f_0 = \frac{k_0 c_0}{2\pi} \tag{5.6}$$

where c_0 is the speed of light in the free space.

For the TE^y_{mnl} mode, the characteristic equations in the x and y directions have already been given by (3.46) and (3.48). Now that in the z direction is given through the EDC-H method by

$$\begin{aligned} 1 + \frac{\epsilon_{re} k_{z0}}{k_{z1}} \tan\left(k_{z1} c/2\right) = 0, &\quad \text{even mode} \\ 1 - \frac{k_{z1}}{\epsilon_{re} k_{z0}} \tan\left(k_{z1} c/2\right) = 0, &\quad \text{odd mode} \end{aligned} \tag{5.7}$$

where k_{z0} is defined in (5.2); or for the convenience of calculation, it's transformed into

$$k_{z1} c = -2 \arctan\left(\frac{k_{z1}}{\epsilon_{re} k_{z0}}\right) + l\pi \tag{5.8}$$

where

$$\begin{aligned} l &= 2l', & l' &= 1,\ 2,\ 3,\ \cdots \quad \text{even mode} \\ l &= 2l' - 1, & l' &= 1,\ 2,\ 3,\ \cdots \quad \text{odd mode} \end{aligned}$$

After that, the resonant frequency of the TE^{y}_{mnl} mode follows the same derivation process as the TM^{y}_{mnl} mode.

As for the TE and TM modes to the x and z directions, they can be derived and expressed in a similar way and therefore, wll not be repeated here.

One thing to be noted is that the subindex which corresponds to the superindex can be 0, *e.g.*, for the TE^{x}_{mnl} mode, m can start from 0, whereas for the TE^{z}_{mnl} mode, it's z that can be 0, unless restrained by the metallic ground plane. This is an obvious difference between the DRA and DIG, which means that the fields can now be uniformly distributed in one specific direction in the DRA.

5.3.1.2 DIRA

The rectangular DIRA to be studied is shown in Fig. 5.5(d).

For the TM^{y}_{mnl} mode, the characteristic equations in the x and y directions have already been given by (3.53) and (3.56). Now that in the z direction is given through the EDC-H method by (5.1), where

$$k_{z0} = \sqrt{(\epsilon_{re1} - \epsilon_{re2}) k_0^2 - k_{z1}^2} \tag{5.10}$$

After that, the resonant frequency follows the same derivation process as the TM^{y}_{mnl} mode of the DRA.

For the TE^y_{mnl} mode, the characteristic equations in the x and y directions have already been given by (3.53) and (3.56). Now that in the z direction is given through the EDC-H method by

$$\begin{aligned} 1 + \frac{\epsilon_{re1} k_{z0}}{\epsilon_{re2} k_{z1}} \tan\left(k_{z1} c/2\right) = 0, &\quad \text{Even Mode} \\ 1 - \frac{\epsilon_{re2} k_{z1}}{\epsilon_{re1} k_{z0}} \tan\left(k_{z1} c/2\right) = 0, &\quad \text{Odd Mode} \end{aligned} \tag{5.11}$$

where k_{z0} is defined in (5.10).

After that, the resonant frequency follows the same derivation process as the TM^y_{mnl} mode of the DRA.

5.3.2 The Magnetic-Wall Model

5.3.2.1 The Magnetic-Wall Condition

DRAs used to be designed with dielectric materials of a very high permittivity to reduce the size at low frequencies. Although this is already not necessary when frequencies have risen up to millimetre-waves, it is helpful to simplify the theoretical analysis as magnetic-wall conditions can be applied on all the surfaces of high-permittivity materials [158, 159]. The magnetic wall conditions are as follows:

$$\bar{E} \cdot \hat{n} = 0 \tag{5.12a}$$

$$\hat{n} \times \bar{H} = 0 \tag{5.12b}$$

where $\hat{n}$ denotes the normal to the surface of the resonator.

It should be noted that rectangular DRs can only satisfy (5.12a) which is the imperfect magnetic-wall condition, whereas spherical and cylindrical DRs can support both conditions in (5.12) [158, 159].

5.3.2.2 DRA

Suppose the rectangular DRA shown in Fig. 5.5(c) has a high dielectric constant (normally $\epsilon_r \geq 10$), so that the magnetic-wall method can be applied.

In [154], the analysis of the TE^{z}_{mnl} mode has been given as an example and those of the TE^{x}_{mnl} and TE^{y}_{mnl} modes can be obtained in a similar way. Note that the magnetic-wall model is not suitable for the TM modes of rectangular DRs/DRAs, as the imperfect magnetic-wall condition can only regulate the behaviour of the electric field.

Firstly, the field components inside the DRA can be derived through the z directed magnetic potential [154] as

$$\begin{aligned}
H_x &= \frac{k_x k_z}{j\omega\mu_0} A \sin(k_x x)\cos(k_y y)\sin(k_z z)\\
H_y &= \frac{k_y k_z}{j\omega\mu_0} A \cos(k_x x)\sin(k_y y)\sin(k_z z)\\
H_z &= \frac{k_x^2 + k_y^2}{j\omega\mu_0} A \cos(k_x x)\cos(k_y y)\cos(k_z z)\\
E_x &= A k_y \cos(k_x x)\sin(k_y y)\cos(k_z z)\\
E_y &= -A k_x \sin(k_x x)\cos(k_y y)\cos(k_z z)\\
E_z &= 0
\end{aligned} \tag{5.13}$$

where A is an arbitrary constant and k_x, k_y, and k_z are the wavenumbers inside the DRA in the x, y, and z directions, respectively.

Since $E_z = 0$, the surfaces at $|z| = c/2$ automatically satisfy the imperfect magnetic-wall condition, (5.12a). In conjunction with that, $E_x = 0$ at the surface of $y = 0$, which satisfies the electric-wall condition at the metallic ground plane. After that, by applying (5.12a) to the remaining surfaces of the DRA, *i.e.*, $y = b/2$ and $|x| = a/2$, the following results are obtained:

$$\begin{aligned}
k_x &= \frac{m\pi}{b}, \quad m = 0,\ 1,\ 2, \cdots\\
k_y &= \frac{n\pi}{c}, \quad n = 1,\ 3,\ 5, \cdots
\end{aligned} \tag{5.14}$$

In order to find k_z, the DG model in Section 5.3.1 is borrowed to set up a standing-wave pattern along the z direction and hence, the characteristic equation is obtained as follows:

$$k_z c = -2\arctan\left(\frac{k_z}{k_{z0}}\right) + l\pi \tag{5.15}$$

where

$$\begin{aligned} k_{z0} &= \sqrt{(\epsilon_r - 1)k_0^2 - k_z^2} \\ l &= 0,\ 1,\ 2,\ \cdots \end{aligned}$$

Note that m and l can't take 0 simultaneously for any of the resonant modes.

Similarly, for the TE^x_{mnl} mode, $E_x = 0$ and then

$$\begin{aligned} k_y &= \frac{n\pi}{b}, \quad n = 1,\ 3,\ 5, \cdots \\ k_z &= \frac{l\pi}{c}, \quad l = 0,\ 1,\ 2, \cdots \end{aligned} \tag{5.17}$$

and

$$k_x a = -2 \arctan\left(\frac{k_x}{k_{x0}}\right) + m\pi \tag{5.18}$$

where

$$\begin{aligned} k_{x0} &= \sqrt{(\epsilon_r - 1)k_0^2 - k_x^2} \\ m &= 0,\ 1,\ 2,\ \cdots \end{aligned}$$

Finally, for the TE^y_{mnl} mode, $E_y = 0$ and then

$$\begin{aligned} k_x &= \frac{m\pi}{a}, \quad m = 0,\ 1,\ 2, \cdots \\ k_z &= \frac{l\pi}{c}, \quad l = 0,\ 1,\ 2, \cdots \end{aligned} \tag{5.20}$$

and

$$k_y b = -2 \arctan\left(\frac{k_y}{k_{y0}}\right) + n\pi \tag{5.21}$$

where

$$\begin{aligned} k_{y0} &= \sqrt{(\epsilon_r - 1)k_0^2 - k_y^2} \\ n &= 2,\ 4,\ 6,\ \cdots \end{aligned}$$

After that, apply the separation equation, (5.5), to find k_0 of each mode and then the resonant frequency, f_0.

It can be observed that for the TE^y_{mnl} mode, n can only be an even number, whereas for the TE^x_{mnl} and TE^z_{mnl} modes, n turns out to be odd. This results from that the metallic ground plane works a short circuit.

5.3.2.3 DIRA

Since the DIRA includes a dielectric layer with a considerably low permittivity, the magnetic-wall model is not suitable here and therefore won't be discussed.

5.3.3 Theoretical Calculation and Comparison

The DRA and DIRA shown in Fig. 5.5(c), (d) are taken to be analysed in terms of the resonant frequency with the DG model and magnetic-wall model, respectively.

5.3.3.1 Comparison with Published Results

Firstly, the computed results are compared with those from experiments carried out in [154] and [157].

It should be corrected that $\mathrm{TE/M}^{x/y/z}_{111}$ modes are not the lowest-order modes as claimed by [154] and [157]. It will be clearly shown that the modes with a zero subindex among m, n, or l may have lower resonant frequencies for certain dimensions and will be verified in this subsection. In fact, with the DRA and DIRA, n can only be an odd number starting from 1 for the TM^y_{mnl} mode and an even number starting from 2 for the TE^y_{mnl} mode. This means that numerous and complex modes in the DR as presented by [154] and [157] can now be greatly simplified.

As shown in Tab. 5.1, a set of resonant frequencies of the DRA with various dimensions and dielectric constants is calculated and compared with experimental results. Note that due to a different nomenclature, the TE^x_{131} and TE^x_{132} modes are equivalent to TE^x_{121} and TE^x_{122}in [157]. Both the DG model and magnetic-wall model of the DR/DRA precedingly presented in this section are employed for the calculation.

It can be found in Tab. 5.1 that the dielectric constant of the DR plays an important role in the accuracy of two different methods. When the dielectric

Table 5.1: Theoretical and experimental resonant frequencies of the DRA.

a (mm)	b (mm)	c (mm)	ϵ_r	Mode	Resonant frequencies (GHz) / Difference with experiment(%)		
					DG Model	Magnetic-Wall Model	Experiment [154, 157]
6	4	6	37.1	$\mathrm{TE}_{111}^{x/z}$	7.81 / -4.8	8.01 / -2.3	8.20
6	3	6	37.1	$\mathrm{TE}_{111}^{x/z}$	9.41 / -5.6	9.72 / -2.5	9.97
12	16	10	12.7	TM_{113}^{y}	9.46 / +4.9	— / —	9.02
8	24	10	12.7	TE_{131}^{x}	7.35 / +0.8	7.62 / +4.5	7.29
8	24	10	12.7	TM_{212}^{y}	9.99 / +8.6	— / —	9.20
8	24	10	12.7	TE_{132}^{x}	10.27 / +3.2	10.68 / +7.3	9.95
15.24	15.24	3.10	10.8	TE_{111}^{z}	6.69 / +7.7	6.95 / +11.9	6.21

constant takes a high value (37.1, in this case), the theoretical calculations are all below the experimental results, where the DG model generates the lowest value; it's the other way around while the dielectric constant is low (12.7 and 10.8, in this case), where the magnetic-wall model brings about the highest value.

The reason why the magnetic-wall method tends to be more accurate among high-permittivity materials is obvious as the magnetic-wall condition only exists for materials with a very high dielectric constant as explained in [158, 159]. As for the DG model which is originally established for the application of an optical transmission line, the dielectric constant of the rectangular rod is normally close to the surrounding air to ensure a total internal reflection occurs only at grazing angles as assumed in [112, 113]. So the DG model of a rectangular DR seems to be valid only with low-permittivity materials.

5.3.3.2 Calculation of Fundamental Modes

A low-loss DIIG designed in Chapter 3 will be used here as the feeding line and hence, transforms the DRA into DIRA. The fundamental mode propagating in the DIIG is TM_{11}^{y} with a main H_x component, which couples into the nearby DIRA with the same corss-section and triggers the resonant modes with H_x as one of their main field components: TM_{11l}^{y}, TM_{11l}^{z}, and TE_{11l}^{x} modes. It can be further revealed that the remaining field components are E_y, H_z for the TM_{11l}^{y} modes, H_y, E_z for the TM^{z} modes, and E_y, E_z for the TE^{x} modes. These modes should be carefully separated in the DIRA array design in order to avoid the radiation interference.

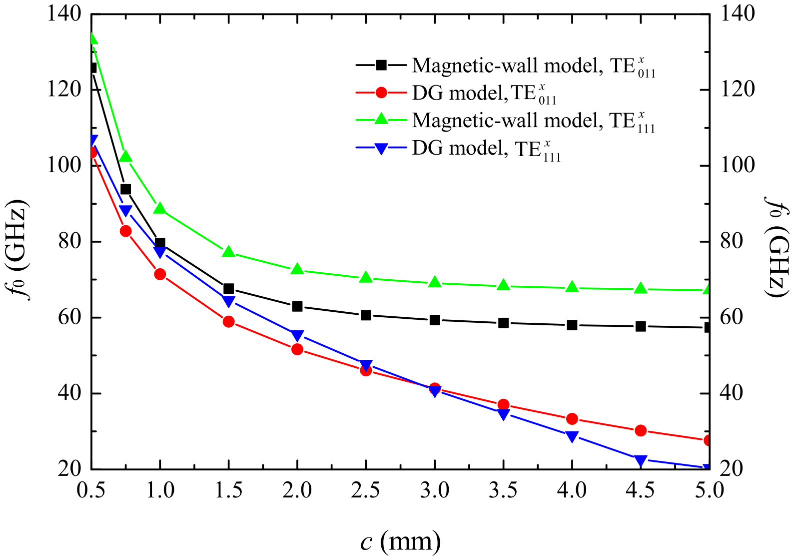

(a) DRA

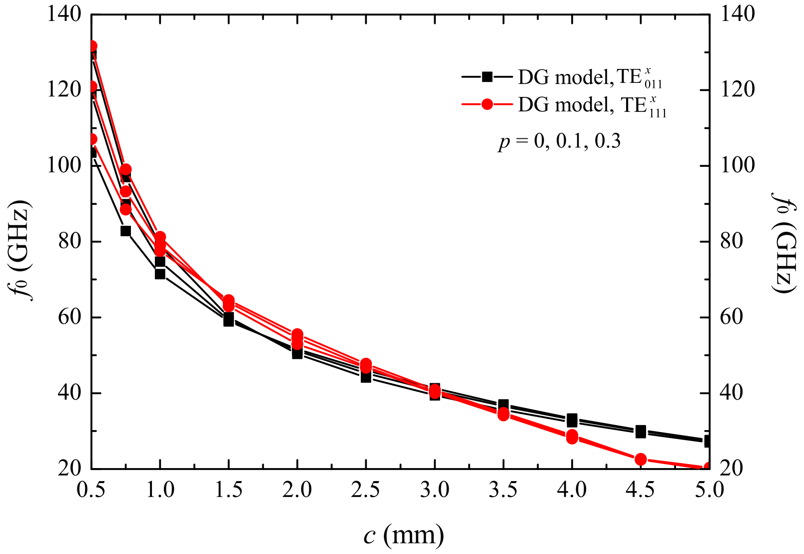

(b) DIRA

FIGURE 5.6: The resonant frequencies of TE$^x_{mnl}$ modes vs. the length of the DRA and DIRA ($a = 1$ mm, $b/a = 1$, $\epsilon_{r_1} = 7.1$, $\epsilon_{r_2} = 2.2$).

Since the Dupont$^{\text{TM}}$ 9K7 LTCC and RT/duroid 5880 are going to be used, the DRA and DIRA shown in Fig. 5.5(c), (d) have dielectric constants of $\epsilon_{r_1} = 7.1$ and $\epsilon_{r_2} = 2.2$. The DG model is employed together with the magnetic-wall model as a comparison.

As shown in Fig. 5.6(a), the computed results from the magnetic-wall model and

DG model vary greatly, especially for long DRAs. One obvious reason for the large discrepancy is that the dielectric constant considered now has decreased to 7.1, where the magnetic-wall condition doesn't hold anymore. Apart from that, the abrupt dimension change also contributes.

As for the TE^x_{011} and TE^x_{111} modes analysed by the DG model, there is a turning point in terms of the length, c, where the two modes exchange their role as the fundamental mode. When c is close to a and b, the TE^x_{011} mode has the lowest resonant frequency; while the TE^x_{111} mode quickly descends into the fundamental mode when c is well larger than a and b. Since the TE^x_{011} and TE^x_{111} modes have similar field patterns inside the DRA, their radiation pattern won't differ much. The TE^x_{011} mode, however, doesn't exist when excited by the DIIG, as its fundamental mode is TM^y_{11}.

As explained before, the DRA turns into DIRA when fed by the DIIG. The resonant frequency, f_0, of the DIRA with various insular ratios, p's, are illustrated in Fig. 5.6(b). As can be seen, f_0 doesn't change much as p increases from 0 to 0.3. As a result, the effect of a insular layer on the DRA in terms of resonant frequency can be negligible.

To present a direct view of the inner field distributions, the rigorous HFSS simulation is used and the results are shown in Fig. 5.7 in terms of some low-order modes. The dimension of the DR is $a = 4$ mm, $b/2 = 3$ mm, and $c = 6$ mm with the dielectric constant, $\epsilon_r = 37.1$. As shown in Fig. 5.7, there is no field variation (electric field is taken as an example here) along the x and z directions for the TE^x_{011} and TE^z_{110} modes, respectively. As for the $TE^{x/z}_{111}$ and TM^y_{111} modes, they share a similar field pattern and there is one field variation along all three directions shown in Fig. 5.7(c). The last field pattern in Fig. 5.7 is for the TE^x_{012} mode.

5.3.3.3 DIRA in Ka Band

Following the design of the DIIG in Chapter 3, a DIRA with the same cross-section is designed to resonate in the Ka band centring at 35 GHz. Tab. 5.2 lists a set of the possible modes resonating at 35 GHz with $a = 1.32$ mm, $b = 3.08$ mm, $p = 0.16$, $\epsilon_{r_1} = 7.1$, and $\epsilon_{r_2} = 2.2$, exactly the same as the DIIG.

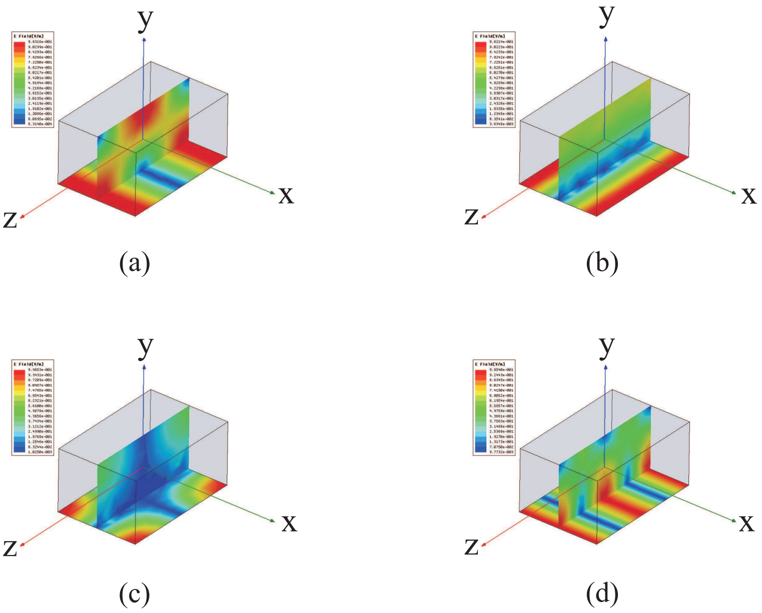

FIGURE 5.7: The field distribution inside the DRA: (a) TE^x_{011}; (b) TE^z_{110}; (c) $\mathrm{TE}^{x/z}/\mathrm{TM}^y_{111}$; (d) TE^x_{012}.

TABLE 5.2: The length of the DIRA for possible modes resonating at 35 GHz.

Mode order	111			112			113			114		
Mode type	TM^y	TM^z	TE^x	TM^y	TM^z	TE^x	TM^y	TM^z	TE^x	TM^y	TM^z	TE^x
c (mm)	0.9	2	1.7	3.5	4.3	4.3	5.9	6.6	6.8	8.3	8.9	9.4

Since the guided wavelength at 35 GHz for the TM^y_{11} mode is calculated to be 6.16 mm, the 113 and higher-order modes need double-wavelength feeding line and thus are not suitable for compact antenna designs.

As for the 111 and 112 modes, TM^z and TE^x stay too close to be differentiated, which leaves the TM^y modes as the only option. In the following section, they will be further reduced into one specific mode as the best candidate based on the coupling between the feeding line and radiating elements.

5.4 Design of a DIRA Array

In this section, a double-sided DIRA array fed by the DIIG is designed and simulated to demonstrate the merit of high gain and wide band.

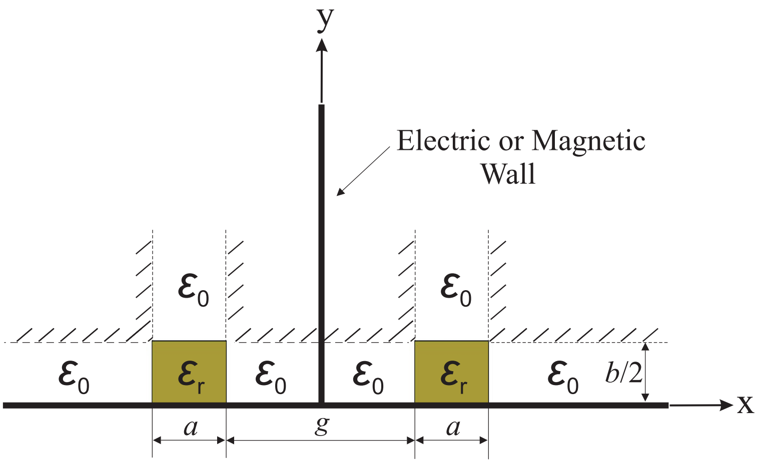

FIGURE 5.8: Symmetric or asymmetric modes for the coupling between two DIGs [113].

5.4.1 Coupling

5.4.1.1 Coupling between the DIG and DRA

Firstly, consider the coupling between two DIGs with the same cross-section, as shown in Fig. 5.8. The reason for choosing the same cross-section is to achieve maximum coupling, which has been concluded in [160]. Now the structure under investigation is symmetrical with respect to the $x = 0$ plane and hence, the fields propagating along the DIGs can be classified into symmetrical (even) and asymmetrical (odd) groups depending on whether it's a electric or magnetic wall at the $x = 0$ plane. Further, the symmetrical and asymmetrical modes will inevitably generate different phase velocities, which is the root of coupling [112, 113].

We now apply the EDC method, where the EDC-H and EDC-V methods are to be selected depending on whether a is larger or smaller than b. For simplicity, here assume $b \leq a$ and then the EDC-H method is employed. In addition, only the TM^y_{mn} mode will be considered, as the fundamental operating mode in the DIG is TM^y_{11}.

On the preceding premises, the coupling analysis between two DIGs are carried out. The characteristic equations defining the wavenumber in the y direction, k_{y1}, and the effective dielectric constant, ϵ_{re}, have already been given by (3.11) and (3.15). Now the wavenumber in the x direction, k_{x1}, needs to be rewritten, in the light of the new configuration in that direction, as [113]:

$$k_{x1}a = -\arctan\left(\frac{k_{x1}}{k_{x0}}\right) - \arctan\left(\frac{Dk_{x1}}{k_{x0}}\right) + m\pi, \quad m = 1,\ 2,\ 3,\ \cdots \tag{5.23}$$

where

$$\begin{aligned} D &= \coth(k_{x0}g/2), \quad \text{even mode} \\ &= \tanh(k_{x0}g/2), \quad \text{odd mode} \end{aligned}$$

and k_{x0} is defined in (3.16)

So k_{x1} now comprises two values, k_{xe} for the even mode and k_{xo} for the odd mode. Hence, the phase constant, β (equals k_z in a low-loss situation), can be derived in two forms:

$$\begin{aligned} \beta_e &= \sqrt{\epsilon_{re}k_0^2 - k_{x_e}^2}, \quad \text{even mode} \\ \beta_o &= \sqrt{\epsilon_{re}k_0^2 - k_{x_o}^2}, \quad \text{odd mode} \end{aligned} \tag{5.24}$$

In order to be connected with the propagation in a single DIG, β_e and β_o can be rewritten as [112]:

$$\left.\begin{matrix} \beta_e \\ \beta_o \end{matrix}\right\} = \beta \left[1 \pm 2\frac{k_x^2}{\beta^2}\frac{1}{k_{x0}a}\frac{\exp(-k_{x0}g)}{1 + k_x^2/k_{x0}^2} \right],$$

where β and k_x are the phase constant and x-direction wavenumber of the single DIG, respectively.

Then we define the coupling coefficient, K, between the two DIGs as:

$$\begin{aligned} -jK &= \frac{\beta_e - \beta_o}{2} \\ &= 2\frac{k_x^2}{\beta^2}\frac{1}{k_{x0}a}\frac{\exp(-k_{x0}g)}{1 + k_x^2/k_{x0}^2} \end{aligned} \tag{5.25}$$

and the length, L, necessary for complete power transfer from one DIG to the other is then derived as:

$$L = \frac{\pi}{2|K|}. \tag{5.26}$$

Now the second DIG is truncated to form a DRA and the coupling mechanism follows the same rule as that of two DIGs.

As predicted, the coupling is enhanced exponentially by decreasing either the gap, g, or the real attenuation constant, k_{x0}, whereas by changing the length, c, of the

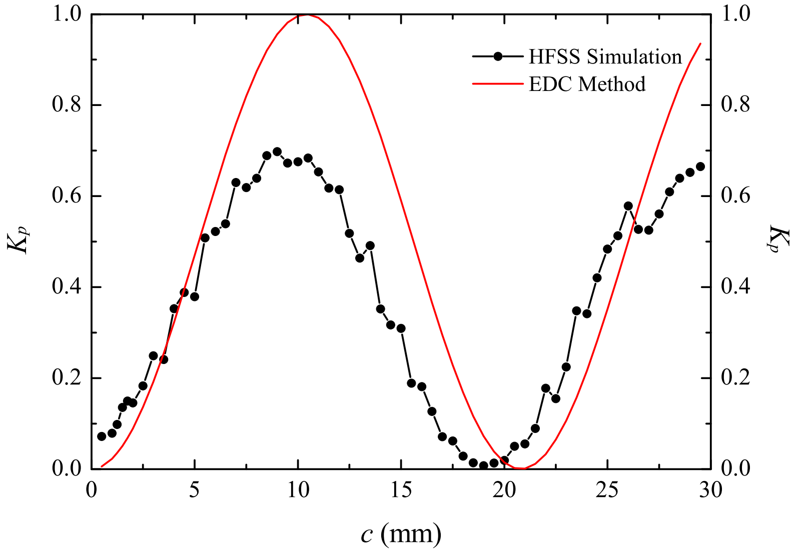

(a) $g = 0.5$ mm and c varies

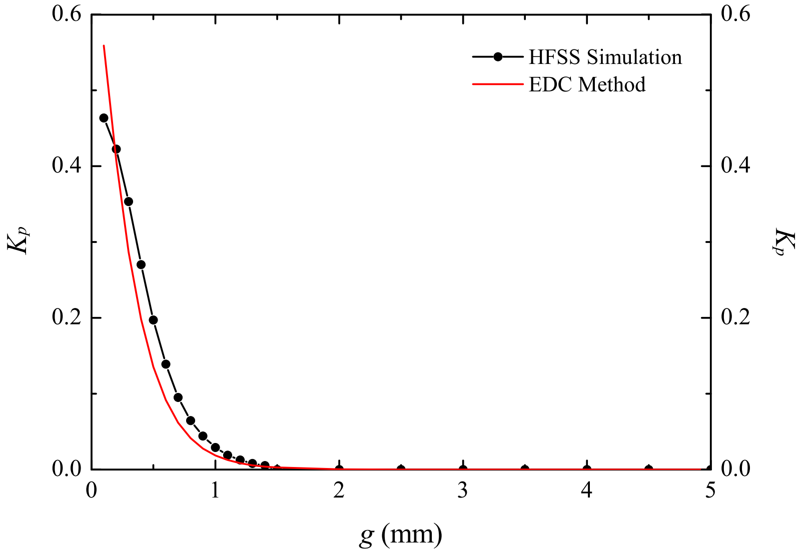

(b) $c = 3$ mm and g varies

FIGURE 5.9: The power coupling coefficient, K_p, of the TM_{11}^y mode between the DIG and DRA ($a = b = 1$ mm, $\epsilon_r = 7.1$).

DRA, the coupling fluctuates square-sinusoidally as [161, 162]

$$K_p = \sin^2\left(\frac{\pi c}{2L}\right) \tag{5.27}$$

where K_p is the power coupling coefficient which stands for the ratio of coupled power to the DRA from the feeding DIG.

In order to verify those conclusions, a 3D simulator, HFSS, based on the FEM method is used to calculate this coupling problem for the fundamental TM_{11}^{y} mode, as shown in Fig. 5.8. The configurational parameters are that $a = b = 1$ mm and $\epsilon_r = 7.1$. Results are shown in Fig. 5.9.

In Fig. 5.9(a), g is fixed to be 0.5 mm and the corresponding L for complete power transfer (where $K_p = 1$) is calculated through the EDC method to be 10.4 mm. Then, substitute it for L in (5.27) to obtain the theoretical result. As expected, the curve takes the shape similar to a square sinusoid. The result from HFSS has also been provided as a comparison. It can be seen that the peak and valley positions agree well, while the peak value from the HFSS simulation can only go up to 0.7 compared to theoretical 1. There are two main factors that contribute to this disagreement: one is the unaccounted dielectric and metallic loss in theoretical calculation is revealed in the more practical HFSS simulation; the other is that radiation into free space is given rise to because of the coupling.

In Fig. 5.9(b), c is fixed to be 3 mm. By changing g, L is changed and K_p is affected in the end. Results from HFSS and the EDC method agree well and they all descend quickly as the gap, g increases, which is predicted by the preceding conclusion.

5.4.1.2 Coupling between the DIIG and DIRA

Through (5.25) and (5.26), L is obtained for the DIRA as 7.5 mm. Then, K_p with various c's and g's is analysed and shown in Fig. 5.10. As can be seen, results from HFSS and the EDC method agree well in terms of the shape and positions of peaks and valleys. The coupled power from the EDC method is obviously lower for the same reason in the DRA case. Furthermore, the level of free-space radiation is now much higher since there are two resonators for the coupling. As a result, the coupling coefficient is much lower than that of the DRA. One thing to be noted is that K_p doesn't drop quickly to 0 in Fig. 5.10(b). In fact, a residual coupled power still exists even when the DIIG and DIRA are 5 mm apart. The

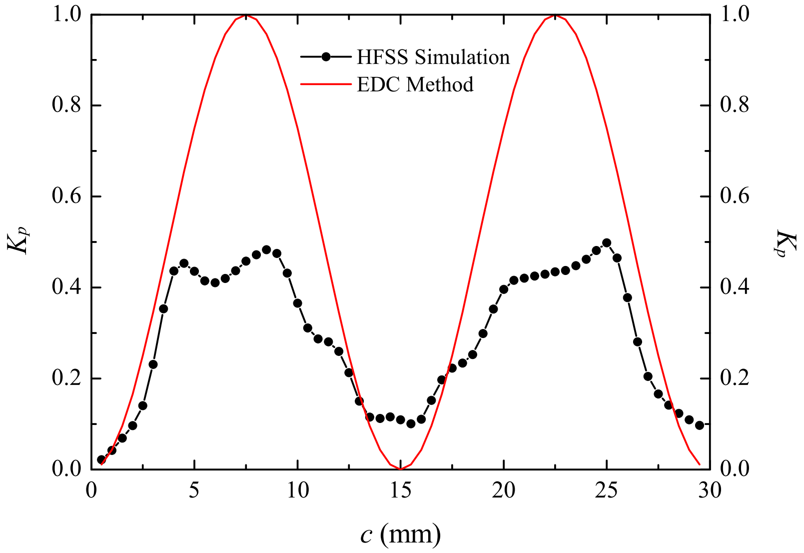

(a) $g = 0.5$ mm and c varies

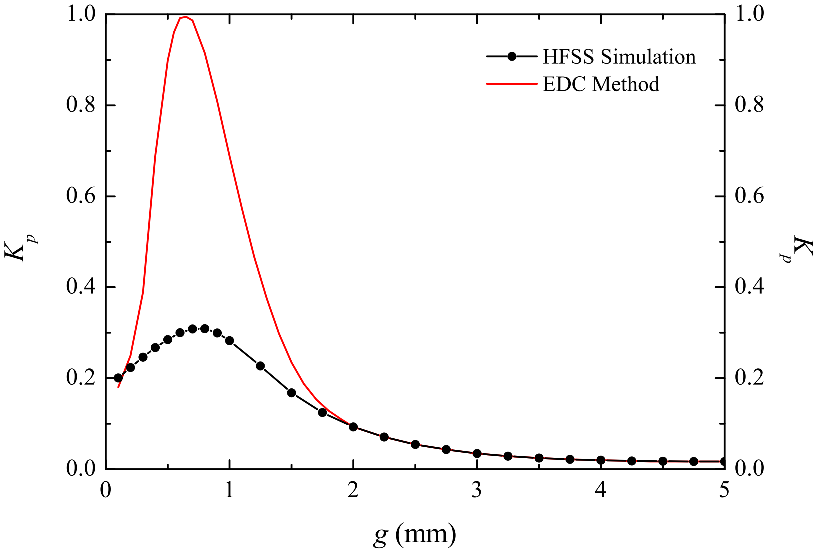

(b) $c = 3.5$ mm and g varies

FIGURE 5.10: The power coupling coefficient, K_p, of the TM^y_{11} mode between the DIIG and DIRA ($a = b = 1$ mm, $p = 0.2$ $\epsilon_r = 7.1$).

reason is that the insular layer binds the DIIG and DIRA together and works as a chanel where power couples. This will inevitably slows down the fade-away speed of power coupling.

As presented in Section 5.3.3.3, the resonant frequency of 35 GHz under the DIIG-feeding scheme has only left two options for the resonant modes of the DIRA:

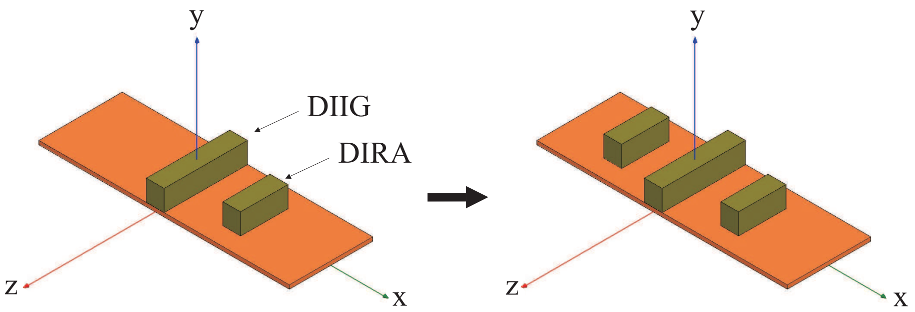

FIGURE 5.11: The transformation from single-sided to double-sided DIRA.

TM^y_{111} and TM^y_{112}. In order to achieve high level of coupling, the TM^y_{112} mode is chosen as its resonant length, c, is closer to L compared with the TM^y_{111} mode. It's also worth mentioning that still K_p is very low for the TM^y_{112} mode, even at its peak value (about 0.3). To obtain higher antenna gain and more flexibility in antenna design, higher power coupling is needed.

5.4.2 Double-sided Taylor-distribution

In order to achieve higher coupling, the original DIRA fed by the DIIG in [162, 163] is improved by adding a mirror array of DIRA blocks on the other side. As a result, the DIRA array now becomes double-sided, as shown in Fig. 5.11. The two DIRA block arrays are coupled to the DIIG by an H_x component and are thus resonant in the same TM^y_{112} mode. With more receptors to couple, the power coupling coefficient, K_p is now certainly higher.

This is verified through the HFSS simulation on the double-sided DIRA shown in Fig. 5.11, where the DIIG is one guided-wavelength long (6.16 mm). Results are shown in Fig. 5.12. It can be seen that the peak K_p has increased to nearly 0.45, whereas the peak position has shifted upwards from $c = 0.8$ mm to 1.1 mm.

For a practical antenna array, it is always desirable to have a main beam as narrow as possible, a gain as high as possible and side lobes as low as possible, which, in many cases, is hard to realise. Since several decades ago, two methods have been developed and widely used to achieve the optimum: The Dolph-Tchebysheff distribution [164] and Taylor distribution [165, 166]. For the Dolph-Tchebysheff distribution, the width of the main beam is the narrowest that a symmetric array can get at the prescribed side-lobe level, whereas the drawback of this method is that all its side lobes are at the same level, even extending to infinity. The Taylor

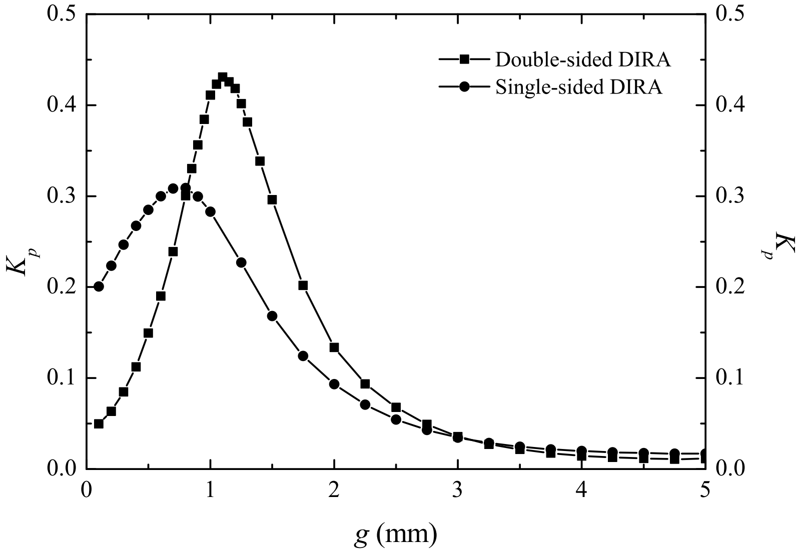

Figure 5.12: The comparison of the power coupling coefficient, K_p, between the single-sided and double-sided DIRA.

distribution, however, has side lobes which are gradually vanishing, by sacrificing some main-beam width.

In this design, the Taylor distribution is chosen to minimise the side-lobe level.

To start the Taylor distribution, the number of DIRA elements in the array needs to be determined based on the prescribed gain. Here at least a 15 dB gain is needed, which requires 10 elements or more. Next is to prescribe the side-lobe level at 20 dB or 25 dB.

Then, the original Taylor distribution of 10 array elements for 20-dB and 25-dB side-lobe level are calculated and shown in Tab. 5.3. Note that the power distribution is recalculated here. The reason is because when the energy travels through an element, a portion is absorbed and thus the energy injected into the next element is the residual from the total. Hence, the power ratio is calculated based on the residual. Results are also shown in Tab. 5.3. Note that all the power feeding is realised through the coupling between the DIIG and DIRA, *i.e.*, K_p.

As can be observed in Tab. 5.3, K_p of the last element in the recalculated Taylor distribution is 1. This is not hard to achieve, as the last element will be open ended and radiate most of the power easily. For the other elements, however, it has to stay below the peak K_p of the double-sided DIRA in Fig. 5.12. This will

TABLE 5.3: The Taylor distribution of 10 array elements in terms of power.

Element	20 dB (original)	20 dB (recalculated)	g (mm)	25 dB (original)	25 dB (recalculated)
1	0.070	0.070	2.47	0.030	0.030
2	0.051	0.054	2.67	0.046	0.047
3	0.096	0.110	2.15	0.096	0.104
4	0.129	0.165	1.89	0.147	0.177
5	0.154	0.235	1.66	0.182	0.267
6	0.154	0.308	1.47	0.182	0.364
7	0.129	0.372	1.32	0.147	0.461
8	0.096	0.444	1.10	0.096	0.558
9	0.051	0.418	1.20	0.040	0.605
10	0.070	1.000	0.50	0.030	1.000

rule out the application of the 25-dB distribution, as Elements 7, 8, and 9 are on top of the threshold.

After finalising the side-lobe level, the next step is to find the corresponding gap, g, which enables that amount of power coupling, by referring to Fig. 5.12. It's worth noting that one K_p might prompt two g's. For the convenience of fabrication and also to minimise the influence of fabrication errors, all g's are to be chosen from the gentle slope rather than the sharp one.

The final set of g's are also shown in Tab. 5.3, where g for Element 10 is flexible in a wide range as the open-end DIRA easily radiates out all the energy.

5.4.3 Simulation and Comparison

The DIRA array needs transitions to be connected with WR28 for practical measurement and application, as shown in Fig. 5.13. As can be seen, only one tapered transition is added at the input end of the DIRA array in order to be fed from a standard WR28, as the energy almost dies out at the other end. Note that the transition is tapered at both horizontal and vertical planes to ensure a smooth feeding.

After optimised by the HFSS simulation, the performance of this double-sided Taylor-distributed DIRA array is given by Fig. 5.14.

In Fig. 5.14(a), the gain of both double-sided and single-sided DIRA array are shown from 30 to 40 GHz. As can be found, the peak gains centre around 35

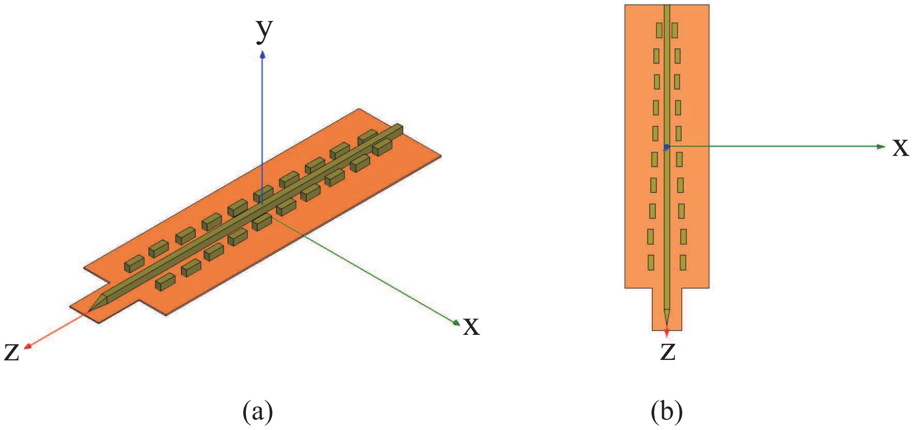

FIGURE 5.13: The geometric configurations of the double-sided Taylor-distributed DIRA array: (a) 3D view, (b) top view.

GHz and those of the double-sided array are all higher than the single-sided one. Average gain increase is from 1.5 to 2.5 dB. The maximum gain this DIRA array can achieve is 17.3 dBi at 36 GHz. As for the impedance bandwidth represented by S_{11}, it is very wide, nearly throughout the whole 10-GHz band.

The radiation pattern is shown in Fig. 5.14(b) as the solid lines, where 34, 35, and 36 GHz are all included. The side-lobe suppression has been observed as the best side-lobe level is 17.5 dB at 35 GHz. Possible reason for the 2.5 dB degradation is that the cross coupling between nearby elements are not accounted for in the design process (optimisation of the cross coupling is too complicated for a 10-element array and thus will not be carried out here) and the transition added afterwards might disturb the field pattern of radiation. As there is no side-lobe suppression technique applied in the H-plane, a 10-dB sidelobe can be found. An interesting characteristic for the E-plane radiation pattern is that as frequency varies, the peak-gain position changes accordingly. This, in fact, occurs to all antenna arrays fed at one end, which in some literatures are called Long-Line Effect, [128]. Hence, the solution to suppress the centre-shifting is to feed the array at the centre, which has been employed for the waveguide-based slot antenna arrays in Chapter 4. As for the level of the cross-polarisation, it is found to be well below the desired polarisation in the E-plane, while in the H-plane, the level of cross-polarisation starts low at the centre and increases quickly toward higher angles, which might be acceptable given that the main direction of radiation is confined at the centre. The simulated radiation efficiency is about 92.54%, which has demonstrated the low-loss characteristic of this type of antenna.

Finally, the magnetic field pattern responsible for the power coupling is obtained

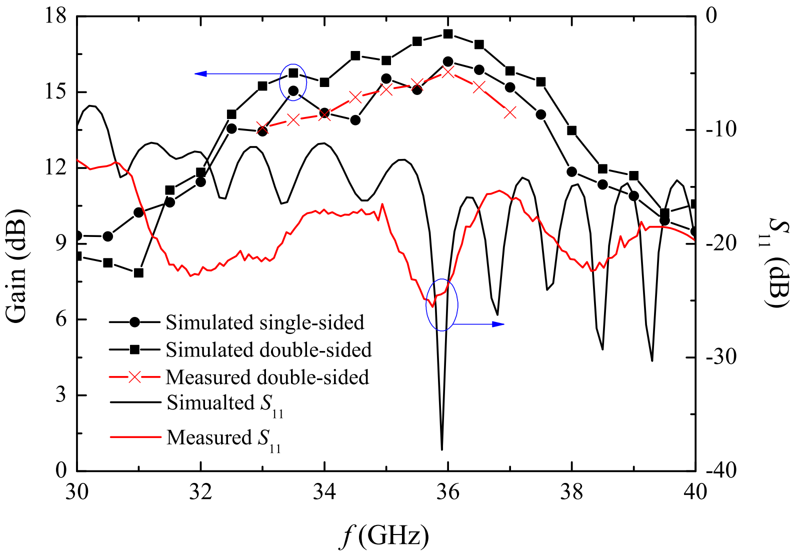

(a) Gain and S_{11}

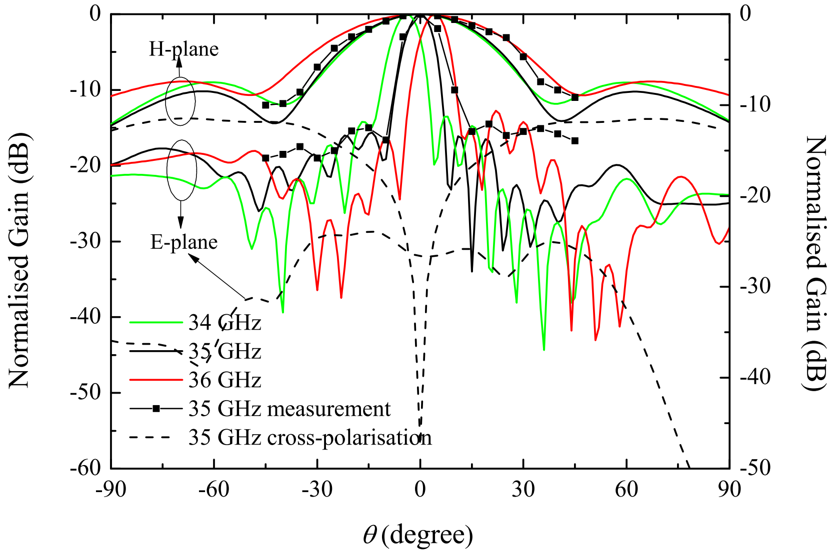

(b) Radiation pattern

FIGURE 5.14: The performance of the double-sided Taylor-distributed DIRA array.

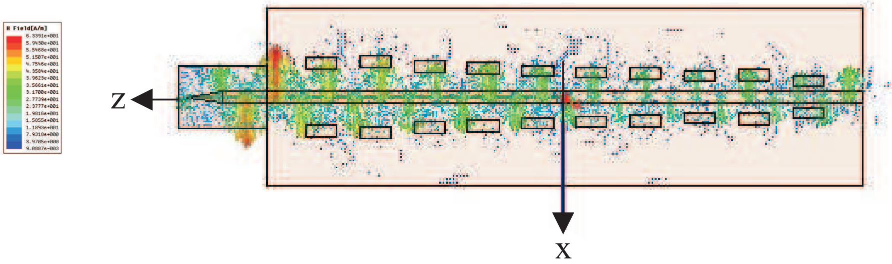

FIGURE 5.15: The magnetic field pattern of the double-sided Taylor-distributed DIRA array.

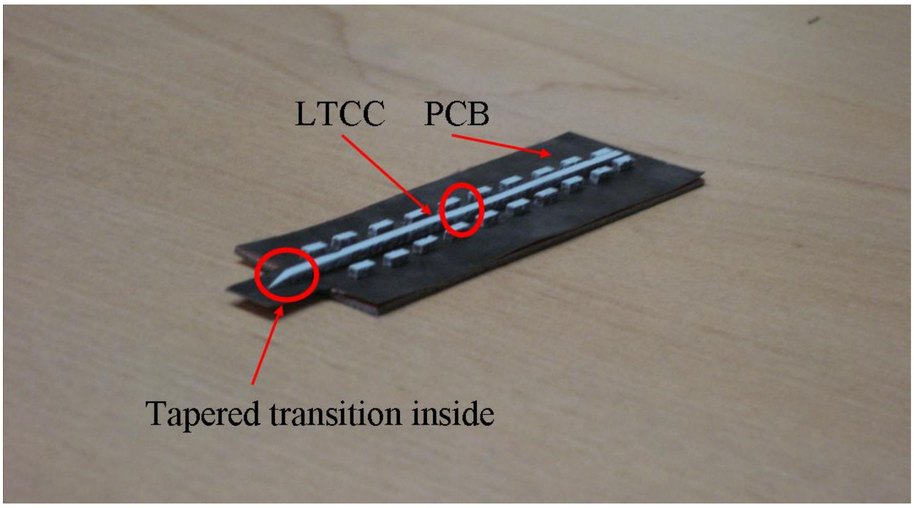

FIGURE 5.16: The fabricated 10-element double-sided DIRA array.

through the HFSS simulation and presented in Fig. 5.15. As observed in this figure, the magnetic field is mainly in the x direction, *i.e.*, H_x. It is strong at the input of the array and gradually dies out as the field travels through the array. In the end, the last bit of power radiates at the open end. Since the array elements are all one-wavelength away, they are in phase or the H_x components are in the same direction, as shown in Fig. 5.15.

5.4.4 Measurement

A standard LTCC technique is used here to fabricate the 10-element double-sided DIRA array, as shown in Fig. 5.16. The feeding DIIG is designed in Chapter 3 and directly employed here.

The measurement setup is shown in Fig. 5.17, which is similar to that used for the HSIW slot array in Section 4. Using (4.8), the double-sided DIRA array (20.1 × 77.8 mm ^{2}) generates a R_f of 1.16 m, which is smaller than that between

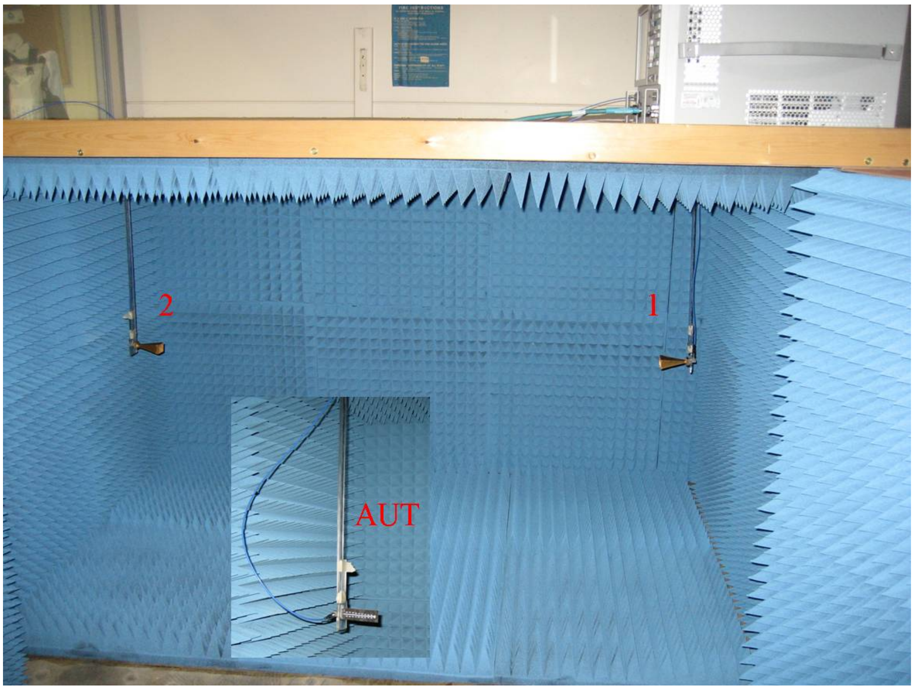

FIGURE 5.17: The measurement setup of the 10-element double-sided DIRA array.

two perspex poles and hence, satisfies the requirement for the radiation pattern measurement in the far-field.

The measured S_{11} and peak gain of the DIRA array is shown in Fig. 5.14(a) as the red lines. As can be observed, the measured S_{11} tends to have multiple resonances which is in line with that from the HFSS simulation. The measured gain of the double-sided array also centres around 36 GHz, although the peak gain is 1.5 dB lowered to 15.8 dBi compared with 17.3 dBi from the HFSS simulation.

The measured radiation pattern at 35 GHz is at a 5° increment up to 45° and is shown in Fig. 5.14(b) as the solid lines with squares. It can be seen that the main beams in both E- and H-planes get wider toward the transition end and hence, the sidelobe suppression on that side degrades by about 1.5 dB to 16 dB. Also, the measured radiation pattern cannot fully demonstrate the peaks and valleys among the sidelobes. Possible reasons for the disagreement and degradation may come from the unaccounted shrinkage of the LTCC and the bond between the LTCC and PCB board might not be completely intact.

5.5 Conclusion

In this chapter, a short review of the DRA is introduced. Then, the DRA and DIRA are studied in depth in terms of resonant modes, resonant frequencies, and field patterns. After that, a 10-element double-sided Taylor-distributed DIRA array is designed, simulated, and measured. Results agree well, which verifies the design of this antenna array.

Chapter 6

Conclusions and Future Work

This thesis has described research on two types of waveguides and their applications to antenna arrays. The main contributions of the work can be summarised as follows:

1) A new type of metallic rectangular waveguide, the HSIW, has been proposed and studied. By adding a hollow air cavity to the traditional SIW, the HSIW has proved to be comparable in loss to a standard air-filled RWG and hence offers low-loss performance in mm-waves. An HSIW prototype manufactured in a progressive-lamination LTCC technique has demonstrated a loss of approximately 2 Np/m or 17 dB/m in the Ka band, higher than WR28. However, the potential of HSIW to be integrated with other microwave components is highly advantageous compared with standard RWGs.

   To theoretically analyse the HSIW, a new method is proposed which decomposes the HSIW into a RWG and SIW; therefore, two steps need to be followed. Firstly, the HSIW is viewed as a two-dielectric loaded RWG. After solving this boundary value problem, the two-dielectric loaded RWG is transformed into a uniformly-filled RWG by introducing the effective dielectric constant (EDC), ϵ_e. Then, by modifying the empirical formula in [89] relating SIW and RWG, the dimensions of the HSIW can be finally determined.

2) An existing type of the dielectric waveguide, the DIIG, is studied to find out its low-loss performance in the Ka band. A prototype made in a standard LTCC technique has demonstrated an attenuation constant of approximately 3 Np/m or 26 dB/m in the Ka band, which is higher than the metallic waveguides, such as the HSIW. As the frequency increases, however, the conductor loss rises

more quickly than the dielectric loss. So there is a turning point where the dielectric transmission line starts to be better.

To theoretically analyse the DIIG, the traditional EDC method originally used for the DIG is improved and completed, which takes into account all aspect ratios of the DIG. Through this method, the DIIG is divided into different areas which are then solved individually and finally combined together for the final phase constant. Apart from that, the attenuation constant is also derived and given in detailed analytical expressions for both the DIG and DIIG. It has been found that the increase of the insular layer in the DIIG can reduce the loss but narrow the single-mode bandwidth. Therefore, a compromised insular ratio (the ratio of the thickness between the insular layer and the main dielectric) is given as $0.1 \sim 0.3$.

3) A 6×6 slot antenna array based on the HSIW is designed, fabricated and measured seeking for a high-gain performance. The analysis and design starts with a single slot, for which theoretical calculations and HFSS simulations are compared. Then, the single slot is extended into a linear array and eventually a planar array. To eliminate the tilting of the main beam, the slot array is fed from the centre at the back side of the HSIW, which results in a blockage area. To alleviate the resulting sidelobe increase, a slot extrusion technique is introduced. A simplified multiway power divider is demonstrated to feed the array elements following a Taylor distribution and the detailed optimisation procedure to reach prescribed antenna specifications is also provided. To verify the antenna design, the 6×6 planar array is fabricated and measured. Due to the low loss of the HSIW comparable to the standard WR28, a high gain of 17.1 dBi has been achieved.

4) A double-sided DIRA array fed by the DIIG is designed, fabricated and measured seeking for a high-gain performance. The analysis and design starts with the rectangular dielectric resonator (DR), then extends to the DRA and finally the DIRA. This is performed through the complete EDC method, verified by the HFSS simulation based on the finite element method (FEM). In order to enhance the gain, the DIRA array is made double-sided, *i.e.*, adding another mirror array on the other side of the DIIG. The Taylor distribution technique is employed here to suppress the sidelobes. Finally, the 10-element linear DIRA array is fabricated and measured, where a high gain of 15.8 dBi has been achieved.

It is worth noting that the difference between the DRA and DIG or the DIRA and DIIG, in terms of the application of the complete EDC method, is that the characteristic equations are now written in all three directions for the latter while it is two directions for the former. We have also found that the insular ratio has little effect on the resonant frequency of the DIRA compared with that of the DRA, which facilitates the design of the DIIG.

Furthermore, these proposed waveguides and their corresponding antenna arrays can then be integrated with other active and passive microwave components, such as, filters, mixers, power amplifiers, *etc.*, to form a complete communication system in MCM technology.

For future research, the author would like to pinpoint some suggestions that may be helpful for researchers who are interested in this area:

1) As mentioned above, the average loss of the DIIG is higher than that of the HSIW in the Ka band. It will be turned around, however, at the higher frequencies, above mm-waves. Some HSIW designs at 300 GHz have been attempted and the loss is terribly high. So, it can be foreseen that dielectric guides will be the main waveguiding structures at these frequencies, unless super conductors at room temperature proves to be a success.

2) As found in the measured results of the HSIW, there are quite a few resonances throughout the Ka band, which greatly affects the extraction of the propagation constant as the resonances might not occur at the same frequency for different lengths. So, a horizontal feeding structure rather than a vertical one with a pair of backside slots might be favourable, as it could avoid, to a great extent, the resonances, if not entirely. Also, increasing the length differences between adjacent samples and the number of samples all seem to be promising. These rules are also applicable to the measurement of the DIIG.

3) Further study can be undertaken to reduce the sidelobe levels of both antenna arrays. For the HSIW slot array, the technique presented by M. Ando in [133] can be taken into consideration, although it is complicated. For the DIRA array, a simplified optimisation method needs to be found to make a feasible implementation using 3D modelling.

4) A proper automatic positioner is needed for the small anechoic chamber to accurately locate the angles for the radiation pattern measurement and save time.

Ideally, embedded automatic software to control the positioner and measure the gain should be developed.

5) As mentioned a few times in this thesis, both antenna arrays have the potential to be integrated with other microwave components to form a complete front-end or transceiver in MCM technology. This was the ultimate goal of the research, and by investigating two types of transmission line, a significant and novel contribution to the subject of antenna-in-package design has been made.

Bibliography

[1] A. Huurdeman, *The Worldwide History of Telecommunications.* Wiley-IEEE Press, 1 ed., 2003.

[2] Y. Kwok and V. Lau, *Wireless Internet and Mobile Computing: Interoperability and Performance.* Wiley-IEEE Press, 1 ed., 2007.

[3] W. Mohr, J. Monserrat, A. Osseiran, and M. Werner, "Imt-advanced and next-generation mobile networks [guest editorial]," *Communications Magazine, IEEE*, vol. 49, pp. 82 –83, Feb. 2011.

[4] A. Hashimoto, H. Yoshino, and H. Atarashi, "Roadmap of imt-advanced development," *Microwave Magazine, IEEE*, vol. 9, pp. 80 –88, Aug. 2008.

[5] L. Garber, "News briefs," *Computer*, vol. 46, no. 8, pp. 18–20, 2013.

[6] T. Rappaport, S. Sun, R. Mayzus, H. Zhao, Y. Azar, K. Wang, G. Wong, J. Schulz, M. Samimi, and F. Gutierrez, "Millimeter wave mobile communications for 5g cellular: It will work!," *Access, IEEE*, vol. 1, pp. 335–349, 2013.

[7] H. Zhao, R. Mayzus, S. Sun, M. Samimi, J. K. Schulz, Y. Azar, K. Wang, G. N. Wong, F. J. Gutierrez, and T. S. Rappaport, "28 ghz millimeter wave cellular communication measurements for reflection and penetration loss in and around buildings in new york city," in *IEEE International Conference on Communications (ICC)*, 2013.

[8] R. Freeman, *Radio System Design for Telecommunication.* Wiley-IEEE Press, 1 ed., 2007.

[9] T. Cooklev, *Wireless Communication Standards:A Study of IEEE 802.11, 802.15, 802.16.* Wiley-IEEE Standards, 1 ed., 2004.

[10] P. Smulders, “Exploiting the 60 ghz band for local wireless multimedia access: prospects and future directions,” *Communications Magazine, IEEE*, vol. 40, pp. 140 –147, Jan. 2002.

[11] E. H. Ong, J. Kneckt, O. Alanen, Z. Chang, T. Huovinen, and T. Nihtila, “Ieee 802.11ac: Enhancements for very high throughput wlans,” in *Personal Indoor and Mobile Radio Communications (PIMRC), 2011 IEEE 22nd International Symposium on*, pp. 849 –853, Sept. 2011.

[12] L. Garber, “Wi-fi races into a faster future,” *Computer*, vol. 45, pp. 13 –16, Mar. 2012.

[13] M. Peter, W. Keusgen, and J. Luo, “A survey on 60 ghz broadband communication: Capability, applications and system design,” in *Microwave Integrated Circuit Conference, 2008. EuMIC 2008. European*, pp. 1 –4, Oct. 2008.

[14] J. Gilb, *Wireless Multimedia:A Guide to the IEEE 802.15.3 Standard*. Wiley-IEEE Standards Association, 2004.

[15] Y. Kwok and V. Lau, *Wireless Internet and Mobile Computing: Interoperability and Performance*. Wiley-IEEE Press, 1 ed., 2007.

[16] Y. Zhang, “Antenna-in-package technology for modern radio systems,” in *Antenna Technology Small Antennas and Novel Metamaterials, 2006 IEEE International Workshop on*, pp. 37 – 40, 6-8, 2006.

[17] G. Pearson and W. Brattain, “History of semiconductor research,” *Proceedings of the IRE*, vol. 43, pp. 1794 –1806, Dec. 1955.

[18] L. Lukasiak and A. Jakubowski, “History of semiconductors,” *Journal of Telecommunications and Information Technology*, pp. 3 –9, Jan. 2010.

[19] G. Busch, “Early history of the physics and chemistry of semiconductors-from doubts to fact in a hundred years,” *European Journal of Physics*, vol. 10, p. 4, Oct. 1989.

[20] M. Riordan and L. Hoddeson, “The origins of the pn junction,” *Spectrum, IEEE*, vol. 34, pp. 46 –51, jun 1997.

[21] J.-S. Rieh and S. Kim, “Technology and design considerations for millimeter-wave circuits,” in *Solid-State and Integrated-Circuit Technology, 2008. ICSICT 2008. 9th International Conference on*, pp. 1352 –1356, Oct. 2008.

[22] P. Staecker, "Device technology and integration techniques for commercial mm-wave systems," in *Millimeter Waves, 1997 Topical Symposium on*, pp. 51 –54, Jul. 1997.

[23] R. Carrillo-Ramirez and R. Jackson, "A highly integrated millimeter-wave active antenna array using bcb and silicon substrate," *IEEE Transactions on Microwave Theory and Techniques*, vol. 52, pp. 1648 – 1653, 2004.

[24] Y. Zhang, M. Sun, and L. Guo, "On-chip antennas for 60-ghz radios in silicon technology," *Electron Devices, IEEE Transactions on*, vol. 52, pp. 1664 – 1668, Jul. 2005.

[25] M. Barakat, C. Delaveaud, and F. Ndagijimana, "60 ghz high resistivity silicon on insulator interdigitated dipole antenna," *Microwave and Optical Technology Letters*, vol. 52, no. 5, pp. 1197 – 201, 2010.

[26] M. H. Barakat, C. Delaveaud, and F. Ndagijimana, "Radiation measurement of 60 ghz high resistivity silicon on insulator double slot antenna," *Microwave and Optical Technology Letters*, vol. 53, no. 12, pp. 2861 – 2865, 2011.

[27] E. Herth, N. Rolland, and T. Lasri, "Circularly polarized millimeter-wave antenna using 0-level packaging," *Antennas and Wireless Propagation Letters, IEEE*, vol. 9, pp. 934 –937, 2010.

[28] A. Adane, F. Galle ande, and C. Person, "Bandwidth improvements of 60ghz micromachining patch antenna using gap coupled u - microstrip feeder," in *Antennas and Propagation (EuCAP), 2010 Proceedings of the Fourth European Conference on*, pp. 1 –5, Apr. 2010.

[29] A. Adane, F. Gallee, C. Person, V. Puyal, and C. Vil-leneuve, "Implementation of broadband microstrip-u coupled patch array on si/bcb membrane for beamforming applications at 60 ghz," in *Antennas and Propagation (EUCAP), Proceedings of the 5th European Conference on*, pp. 1263 –1267, Apr. 2011.

[30] B. Pan, Y. Li, G. Ponchak, J. Papapolymerou, and M. Tentzeris, "A 60-ghz cpw-fed high-gain and broadband integrated horn antenna," *Antennas and Propagation, IEEE Transactions on*, vol. 57, pp. 1050 –1056, Apr. 2009.

[31] K. Gilleo, "The circuit centennial tribute to 100 yeas of innovation," *CircuiTree Magazine*, Jun. 2003.

[32] "History of printed circuit boards," *https://www.eiconnect.com/pcbhistory.aspx.*

[33] "Printed circuit board history - printed wiring board," *http://www.trianglecircuits.com/pcb-history.html.*

[34] M. Ando and J. Hirokawa, "High-gain and high-efficiency single-layer slotted waveguide arrays in 60 ghz band," in *Antennas and Propagation, Tenth International Conference on (Conf. Publ. No. 436)*, vol. 1, pp. 464 –468 vol.1, Apr. 1997.

[35] P. Hall and C. Hall, "Coplanar corporate feed effects in microstrip patch array design," *Microwaves, Antennas and Propagation, IEE Proceedings H*, vol. 135, pp. 180 – 186, Jun. 1988.

[36] Q.-H. Lai, W. Hong, Z.-Q. Kuai, Y. S. Zhang, and K. Wu, "Half-mode substrate integrated waveguide transverse slot array antennas," *Antennas and Propagation, IEEE Transactions on*, vol. 57, no. 4, pp. 1064–1072, 2009.

[37] Y. Ding and K. Wu, "T-type folded substrate integrated waveguide (tf-siw) slot array antenna," *IEEE Transactions on Antennas and Propagation*, vol. 58, pp. 1792 – 1795, 2010.

[38] X.-P. Chen, K. Wu, L. Han, and F. He, "Low-cost high gain planar antenna array for 60-ghz band applications," *Antennas and Propagation, IEEE Transactions on*, vol. 58, pp. 2126 –2129, Jun. 2010.

[39] X.-P. Chen, L. Li, and K. Wu, "Multi-antenna system based on substrate integrated waveguide for ka-band traffic-monitoring radar applications," in *Microwave Conference, 2009. EuMC 2009. European*, pp. 417–420, 2009.

[40] O. Kramer, T. Djerafi, and K. Wu, "Very small footprint 60 ghz stacked yagi antenna array," *Antennas and Propagation, IEEE Transactions on*, vol. 59, pp. 3204 –3210, Sept. 2011.

[41] J. Grzyb, D. Liu, U. Pfeiffer, and B. Gaucher, "Wideband cavity-backed folded dipole superstrate antenna for 60 ghz applications," in *Antennas and Propagation Society International Symposium 2006, IEEE*, pp. 3939 –3942, Jul. 2006.

[42] J. Akkermans, M. van Beurden, and M. Herben, "Design of a millimeter-wave balanced-fed aperture-coupled patch antenna," in *European Conference. on Antennas and Propagation*, pp. 1 –6, Nov. 2006.

[43] D. Liu, J. Akkermans, and B. Floyd, "A superstrate patch antenna for 60-ghz applications," in *Antennas and Propagation, 2009. EuCAP 2009. 3rd European Conference on*, pp. 2592 –2594, Mar. 2009.

[44] D. Liu, J. Akkermans, H.-C. Chen, and B. Floyd, "Packages with integrated 60-ghz aperture-coupled patch antennas," *Antennas and Propagation, IEEE Transactions on*, vol. 59, pp. 3607 –3616, Oct. 2011.

[45] Q. Lai, C. Fumeaux, W. Hong, and R. Vahldieck, "60 ghz aperture-coupled dielectric resonator antennas fed by a half-mode substrate integrated waveguide," *Antennas and Propagation, IEEE Transactions on*, vol. 58, pp. 1856 –1864, Jun. 2010.

[46] A. Agouzoul, M. Nedil, Y. Coulibaly, T. Denidni, I. Ben Mabrouk, and L. Talbi, "Design of a high gain hybrid dielectric resonator antenna for millimeter-waves underground applications," in *Antennas and Propagation (APSURSI), 2011 IEEE International Symposium on*, pp. 1688 –1691, Jul. 2011.

[47] X. Liang, D. Yang, R. Jin, and J. Geng, "A 60-ghz wideband dielectric resonator antenna with inclined radiation," in *Antenna Technology (iWAT), 2012 IEEE International Workshop on*, pp. 124 –127, Mar. 2012.

[48] I. Wolff, "From antennas to microwave systems - ltcc as an integration technology for space applications -," in *Antennas and Propagation, 2009. EuCAP 2009. 3rd European Conference on*, pp. 3 –8, Mar. 2009.

[49] Y. Imanaka, *Multilayered low temperature cofired ceramics (LTCC) technology.* Springer Science+Business Media, Inc., 2005.

[50] H. BIROL, *fabrication of low temperature co-fired ceramic (ltcc)-based sensor and micro-fluidic structures.* PhD thesis, Swiss Federal Institute of Technology, 2006.

[51] Y. Zhang, "Antenna-in-package technology: The key to success of 60-ghz radio," in *Microwave Conference Proceedings (APMC), 2010 Asia-Pacific*, pp. 954 –957, Dec. 2010.

[52] Y. Zhang, M. Sun, K. Chua, L. Wai, D. Liu, and B. Gaucher, "Antenna-in-package in ltcc for 60-ghz radio," in *Antenna Technology: Small and Smart Antennas Metamaterials and Applications, 2007. IWAT '07. International Workshop on*, pp. 279 –282, Mar. 2007.

[53] M. Massiot, "Evolution of ltcc technology for industrial applications," in *Microwave Conference, 2002. 32nd European*, pp. 1 –2, Sept. 2002.

[54] M. Sun, Y. Zhang, K. Chua, L. Wai, D. Liu, and B. Gaucher, "Integration of yagi antenna in ltcc package for differential 60-ghz radio," *Antennas and Propagation, IEEE Transactions on*, vol. 56, pp. 2780 –2783, Aug. 2008.

[55] M. Sun, Y. Zhang, Y. Guo, K. Chua, and L. Wai, "Integration of grid array antenna in chip package for highly integrated 60-ghz radios," *Antennas and Wireless Propagation Letters, IEEE*, vol. 8, pp. 1364 –1366, 2009.

[56] Y. Zhang, M. Sun, K. Chua, L. Wai, and D. Liu, "Antenna-in-package design for wirebond interconnection to highly integrated 60-ghz radios," *Antennas and Propagation, IEEE Transactions on*, vol. 57, pp. 2842 –2852, Oct. 2009.

[57] J. Xu, Z. N. Chen, X. Qing, and W. Hong, "Bandwidth enhancement for a 60 ghz substrate integrated waveguide fed cavity array antenna on ltcc," *Antennas and Propagation, IEEE Transactions on*, vol. 59, pp. 826 –832, Mar. 2011.

[58] A. Lamminen and J. Saily, "High gain 60 ghz ltcc chain antenna array with substrate integrated waveguide feed network," in *Antennas and Propagation (EUCAP), 2012 6th European Conference on*, pp. 2569 –2573, Mar. 2012.

[59] G. Brzezina, R. Amaya, D. Lee, K. Hettak, J. Sydor, and L. Roy, "A 60 ghz system-on-package balanced antipodal vivaldi antenna with stepped dielectric director (bava-sdd) in ltcc," in *Microwave Conference (EuMC), 2011 41st European*, pp. 547 –550, Oct. 2011.

[60] J.-H. Lee, N. Kidera, G. DeJean, S. Pinel, J. Laskar, and M. Tentzeris, "A v-band front-end with 3-d integrated cavity filters/duplexers and antenna in ltcc technologies," *Microwave Theory and Techniques, IEEE Transactions on*, vol. 54, pp. 2925 – 2936, Jul. 2006.

[61] M. Martinez-Vazquez and C. Oikonomopoulos-Zachos, "60 ghz embedded antennas on ltcc substrate," in *ICECom, 2010 Conference Proceedings*, pp. 1 –4, Sept. 2010.

[62] C. Oikonomopoulos-Zachos and M. Martinez-Vazquez, "Effect of technological tolerances in the design of a 60 ghz ltcc antenna," in *Antennas and Propagation Society International Symposium (APSURSI), 2010 IEEE*, pp. 1 –4, Jul. 2010.

[63] M. M. Vazquez, S. Holzwarth, C. Oikonomopoulos-Zachos, and A. Rivera, "Wideband, balanced-fed 60 ghz antennas for integrated transceivers on ltcc substrate," in *Antennas and Propagation (EuCAP), 2010 Proceedings of the Fourth European Conference on*, pp. 1 –5, Apr. 2010.

[64] C. Oikonomopoulos-Zachos, D. Titz, M. Martinez-Vazquez, F. Ferrero, C. Luxey, and G. Jacquemod, "Accurate characterisation of a 60 ghz antenna on ltcc substrate," in *Antennas and Propagation (EUCAP), Proceedings of the 5th European Conference on*, pp. 3117 –3121, Apr. 2011.

[65] F. Wollenschlager, R. Muller, R. Stephan, A. Ariza, A. Schulz, R. Thoma, J. Muller, and M. Hein, "A wideband 60 ghz differential stripline-to-waveguide transition for antenna measurements in low-temperature co-fired ceramics technology," in *Antennas and Propagation (EUCAP), 2012 6th European Conference on*, pp. 3537 –3541, Mar. 2012.

[66] B. Sanadgol, S. Holzwarth, A. Milano, and R. Popovich, "60 ghz substrate integrated waveguide fed steerable ltcc antenna array," in *Proceedings of the Fourth European Conference on Antennas and Propagation (EuCAP)*, 2010.

[67] F. Bechtold, "A comprehensive overview on today's ceramic substrate technologies," in *Microelectronics and Packaging Conference, 2009. EMPC 2009. European*, pp. 1 –12, Jun. 2009.

[68] S. Koch, I. Kallfass, R. Weber, A. Leuther, M. Schlechtweg, and M. Uno, "An analogue, 4:2 mux/demux front-end mimic for wireless 60 ghz multiple antenna transceivers," in *Microwave Symposium, 2007. IEEE/MTT-S International*, pp. 1121 –1124, Jun. 2007.

[69] S. Koch, I. Kallfass, A. Leuther, M. Schlechtweg, S. Saito, and M. Uno, "A four-antenna transceiver mimic for 60 ghz wireless multimedia applications," in *Microwave Integrated Circuit Conference, 2008. EuMIC 2008. European*, pp. 502 –505, Oct. 2008.

[70] S. Koch, I. Kallfass, R. Weber, A. Leuther, M. Schlechtweg, and S. Saito, "A fully integrated, compound transceiver mimic utilizing six antenna ports for 60 ghz wireless applications," in *Compound Semiconductor Integrated Circuit Symposium, 2009. CISC 2009. Annual IEEE*, pp. 1 –4, Oct. 2009.

[71] B. Pan, Y. Li, G. Ponchak, M. Tentzeris, and J. Papapolymerou, “A low-loss substrate-independent approach for 60-ghz transceiver front-end integration using micromachining technologies,” *Microwave Theory and Techniques, IEEE Transactions on*, vol. 56, pp. 2779 –2788, Dec. 2008.

[72] A. Patrovsky and K. Wu, “Active 60 ghz front-end with integrated dielectric antenna,” *Electronics Letters*, vol. 45, pp. 765 –766, 16 2009.

[73] F. F. He, K. Wu, W. Hong, L. Han, and X.-P. Chen, “Low-cost 60-ghz smart antenna receiver subsystem based on substrate integrated waveguide technology,” *Microwave Theory and Techniques, IEEE Transactions on*, vol. 60, pp. 1156 –1165, Apr. 2012.

[74] D. G. Kam, D. Liu, A. Natarajan, S. Reynolds, and B. Floyd, “Organic packages with embedded phased-array antennas for 60-ghz wireless chipsets,” *Components, Packaging and Manufacturing Technology, IEEE Transactions on*, vol. 1, pp. 1806 –1814, Nov. 2011.

[75] R. Suga, H. Nakano, Y. Hirachi, J. Hirokawa, and M. Ando, “A small package with 46-db isolation between tx and rx antennas suitable for 60-ghz wpan module,” *Microwave Theory and Techniques, IEEE Transactions on*, vol. 60, pp. 640 –646, Mar. 2012.

[76] K. Kunihiro, S. Yamanouchi, H. Dodo, T. Miyazaki, N. Hayama, M. Fujii, Y. Aoki, Y. Takahashi, K. Numata, K. Haraguchi, T. Ohtsuka, K. Ikuina, and H. Hida, “A 0.08-cc fully integrated ltcc transceiver front-end module for 5-ghz wireless lan systems,” in *Radio Wireless. RAWCON Conference*, 2003.

[77] Y.-H. Cho, J.-W. Kim, and Y.-H. Park, “An ultra-miniaturized transceiver module for bluetooth applications using 3-d ltcc system-on-package technology,” in *IEEE MTT-S International Microwave Symposium Digest*, 2008.

[78] D. Yuefei, L. Chunming, X. Qilin, and H. jun, “Double mode x-band t/r module based on ltcc,” in *CIE International Conference on Radar*, 2006.

[79] S. Hanzhang, X. Mengjiang, L. Yuejin, and L. Wei, “Design of a front-end of a ku-band transceiver based on ltcc technology,” in *11th International Conference on Electronic Packaging Technology & High Density Packaging*, 2010.

[80] S. Zhang, Y. Cui, and Y. Guan, "A ka band transceiver using ltcc technology," in *International Symposium on Microwave, Antenna, Propagation and EMC Technologies for Wireless Communications*, 2007.

[81] A. Stark, A. Dreher, H. Fischer, A. Geise, R. Gieron, M. Heckler, S. Holzwarth, C. Hunscher, A. Jacob, K. Kuhlmann, O. Litschke, D. Lohmann, W. Simon, F. Wotzel, and D. Zahn, "Santana: Advanced electronically steerable antennas at ka-band," in *Antennas and Propagation, 2009. EuCAP 2009. 3rd European Conference on*, pp. 471–478, March 2009.

[82] S. Holzwarth, A. Jacob, A. Dreher, C. Hunscher, H. Fischer, A. Stark, B. Rohrdantz, A. Geise, K. Kuhlmann, R. Gieron, O. Litschke, D. Lohmann, W. Simon, P. Buchner, M. Heckler, and L. Greda, "Active antenna arrays at ka-band: Status and outlook of the santana project," in *Antennas and Propagation (EuCAP), 2010 Proceedings of the Fourth European Conference on*, pp. 1–5, April 2010.

[83] Y. C. Lee, W. il Chang, and C. S. Park, "Monolithic ltcc sip transmitter for 60ghz wireless communication terminals," in *Microwave Symposium Digest, 2005 IEEE MTT-S International*, pp. 1015 –1018, Jun. 2005.

[84] J.-H. Lee, S. Pinel, J. Laskar, and M. Tentzeris, "Design and development of advanced cavity-based dual-mode filters using low-temperature co-fired ceramic technology for v-band gigabit wireless systems," *Microwave Theory and Techniques, IEEE Transactions on*, vol. 55, pp. 1869 –1879, Sept. 2007.

[85] K. Wu, D. Deslandes, and Y. Cassivi, "The substrate integrated circuits - a new concept for high-frequency electronics and optoelectronics," in *Telecommunications in Modern Satellite, Cable and Broadcasting Service*, 2003.

[86] H. Uchimura, T. Takenoshita, and M. Fujii, "Development of a laminated waveguide," in *IEEE MTT-S International Microwave Symposium Digest*, 1998.

[87] J. Hirokawa and M. Ando, "Single-layer feed waveguide consisting of posts for plane tem wave excitation in parallel plates," *IEEE Transactions onAntennas and Propagation*, vol. 46, pp. 625 – 630, 1998.

[88] Y. Cassivi, L. Perregrini, P. Arcioni, M. Bressan, K. Wu, and G. Conciauro, "Dispersion characteristics of substrate integrated rectangular waveguide," *Microwave and Wireless Components Letters, IEEE*, vol. 12, no. 9, pp. 333–335, Sept. 2002.

[89] F. Xu and K. Wu, "Guided-wave and leakage characteristics of substrate integrated waveguide," *IEEE Transactions on Microwave Theory and Techniques*, vol. 53, pp. 66 – 73, 2005.

[90] K. Wu, Y. J. Cheng, T. Djerafi, X. P. Chen, N. Fonseca, and W. Hong, "Millimeter-wave integrated waveguide antenna arrays and beamforming networks for low-cost satellite and mobile systems," in *Proceedings of the Fourth European Conference on Antennas and Propagation (EuCAP)*, 2010.

[91] D. Stephens, P. Young, and I. Robertson, "Millimeter-wave substrate integrated waveguides and filters in photoimageable thick-film technology," *IEEE Transactions on Microwave Theory and Techniques*, vol. 53, pp. 3832 – 3838, 2005.

[92] Y. Cheng, W. Hong, and K. Wu, "Design of a substrate integrated waveguide modified r-kr lens for millimetre-wave application," *IET Microwaves, Antennas & Propagation*, vol. 4, pp. 484 – 491, 2010.

[93] Z. Zhen-Yu, K. Wu, and N. Yang, "A millimeter-wave sub-harmonic self-oscillating mixer using dual-mode substrate integrated waveguide cavity," *IEEE Transactions on Microwave Theory and Techniques*, vol. 58, pp. 1151 – 1158, 2010.

[94] B. Liu, W. Hong, Y.-Q. Wang, Q.-H. Lai, and K. Wu, "Half mode substrate integrated waveguide (hmsiw) 3-db coupler," *IEEE Microwave and Wireless Components Letters*, vol. 17, pp. 22 – 24, 2007.

[95] W. D'Orazio and K. Wu, "Substrate-integrated-waveguide circulators suitable for millimeter-wave integration," *IEEE Transactions on Microwave Theory and Techniques*, vol. 54, pp. 3675 – 3680, 2006.

[96] K. Sellal, L. Talbi, T. Denidni, and J. Lebel, "Design and implementation of a substrate integrated waveguide phase shifter," *ET Microwaves, Antennas and Propagation*, vol. 2, pp. 194 – 199, 2008.

[97] M. Abdolhamidi, M. ; Shahabadi, "X-band substrate integrated waveguide amplifier," *IEEE Microwave and Wireless Components Letters*, vol. 18, pp. 815 – 817, 2008.

[98] D.-S. Eom, J. Byun, and H.-Y. Lee, "Multilayer substrate integrated waveguide four-way out-of-phase power divider," *IEEE Transactions on Microwave Theory and Techniques*, vol. 57, pp. 3469 – 3476, 2009.

[99] D. M. Pozar, *Microwave Engineering.* Wiley India Pvt. Limited, 3rd ed., 2009.

[100] J. van Bladel and T. J. Higgins, "Cut-off frequency in two-dielectric layered rectangular wave guides," *Journal of Applied Physics*, vol. 22, pp. 329 –334, Mar. 1951.

[101] R. Marks, "A multiline method of network analyzer calibration," *Microwave Theory and Techniques, IEEE Transactions on*, vol. 39, no. 7, pp. 1205–1215, Jul. 1991.

[102] M. Janezic and J. Jargon, "Complex permittivity determination from propagation constant measurements," *Microwave and Guided Wave Letters, IEEE*, vol. 9, no. 2, pp. 76–78, Feb. 1999.

[103] A. Savitzky and M. J. E. Golay, "Smoothing and differentiation of data by simplified least squares procedures.," *Analytical Chemistry*, vol. 36, no. 8, pp. 1627–1639, 1964.

[104] S. K. Koul, ed., *Millimeter Wave and Optical Dielectric Integrated Guides and Circuits.* Wiley-Interscience: New York, 1st ed., 1997.

[105] D. D. King, "Dielectric image lines," *Journal of Applied Physics*, vol. 23, pp. 699 –700, Jun. 1952.

[106] R. Knox, "Dielectric waveguide microwave integrated circuits - an overview," *Microwave Theory and Techniques, IEEE Transactions on*, vol. 24, pp. 806 – 814, Nov. 1976.

[107] K. Ogusu, "Numerical analysis of the rectangular dielectric waveguide and its modifications," *Microwave Theory and Techniques, IEEE Transactions on*, vol. 25, no. 11, pp. 874–885, 1977.

[108] T. Itoh, "Inverted strip dielectric waveguide for millimeter-wave integrated circuits," *Microwave Theory and Techniques, IEEE Transactions on*, vol. 24, no. 11, pp. 821–827, 1976.

[109] S. Peng and A. Oliner, "Guidance and leakage properties of a class of open dielectric waveguides: Part i–mathematical formulations," *Microwave Theory and Techniques, IEEE Transactions on*, vol. 29, no. 9, pp. 843–855, 1981.

[110] H. Haus and D. Miller, “Attenuation of cutoff modes and leaky modes of dielectric slab structures,” *Quantum Electronics, IEEE Journal of*, vol. 22, pp. 310 – 318, Feb. 1986.

[111] W. McLevige, T. Itoh, and R. Mittra, “New waveguide structures for millimeter-wave and optical integrated circuits,” *Microwave Theory and Techniques, IEEE Transactions on*, vol. 23, no. 10, pp. 788–794, 1975.

[112] E. A. J. Marcatili, “Dielectric rectangular waveguide and directional coupler for integrated optics,” *Bell System Technical Journal*, vol. 48, pp. 2071 – 2102, Sept. 1969.

[113] R. M. Knox and P. P. Toulios, “Integrated circuits for the millimeter through optical frequency range,” in *Proceedings of the Symposium on Submillimeter Waves*, Mar. 1970.

[114] J. Xia, S. McKnight, and C. Vittoria, “Propagation losses in dielectric image guides,” *Microwave Theory and Techniques, IEEE Transactions on*, vol. 36, pp. 155 –158, Jan. 1988.

[115] R. Mittra, Y.-L. Hou, and V. Jamnejad, “Analysis of open dielectric waveguides using mode-matching technique and variational methods,” *Microwave Theory and Techniques, IEEE Transactions on*, vol. 28, pp. 36 – 43, Jan. 1980.

[116] J. E. Goell, “circular-harmonic computer analysis of rectangular dielectric waveguides,” *Bell System Technical Journal*, vol. 48, pp. 2133 –2160, Sept. 1969.

[117] M. Ikeuchi, H. Sawami, and H. Niki, “Analysis of open-type dielectric waveguides by the finite-element iterative method,” *Microwave Theory and Techniques, IEEE Transactions on*, vol. 29, pp. 234 – 240, Mar. 1981.

[118] A. Oliner, S.-T. Peng, T.-I. Hsu, and A. Sanchez, “Guidance and leakage properties of a class of open dielectric waveguides: Part ii–new physical effects,” *Microwave Theory and Techniques, IEEE Transactions on*, vol. 29, pp. 855 – 869, Sept. 1981.

[119] W. Watson, “Resonant slots,” *Electrical Engineers - Part IIIA: Radiolocation, Journal of the Institution of*, vol. 93, no. 4, pp. 747–777, 1946.

[120] A. F. Stevenson, “Theory of slots in rectangular wave-guides,” *Journal of Applied Physics*, vol. 19, no. 1, pp. 24–38, 1948.

[121] A. Oliner, “The impedance properties of narrow radiating slots in the broad face of rectangular waveguide: Part i–theory; part ii: comparison with experiment,” *Antennas and Propagation, IRE Transactions on*, vol. 5, no. 1, pp. 4–20, 1957.

[122] J. L. Volakis, ed., *Antenna Engineering Handbook.* McGraw-Hill Professional, 4 ed., 2009.

[123] R. Elliott, ed., *Antenna Theory & Design.* Wiley-IEEE Press, revised ed., 2003.

[124] H. Booker, “Slot aerials and their relation to complementary wire aerials (babinet’s principle),” *Electrical Engineers - Part IIIA: Radiolocation, Journal of the Institution of*, vol. 93, no. 4, pp. 620–626, 1946.

[125] R. J. Stegen, “Longitudinal shunt slot characteristics,” *Hughes Technical Memorandum*, vol. 93, no. 261, 1951.

[126] G. Stern and R. Elliott, “Resonant length of longitudinal slots and validity of circuit representation: Theory and experiment,” *Antennas and Propagation, IEEE Transactions on*, vol. 33, no. 11, pp. 1264–1271, 1985.

[127] H. Yee, “Impedance of a narrow longitudinal shunt slot in a slotted waveguide array,” *Antennas and Propagation, IEEE Transactions on*, vol. 22, no. 4, pp. 589–592, 1974.

[128] M. Ando, Y. Tsunemitsu, M. Zhang, J. Hirokawa, and S. Fujii, “Reduction of long line effects in single-layer slotted waveguide arrays with an embedded partially corporate feed,” *Antennas and Propagation, IEEE Transactions on*, vol. 58, no. 7, pp. 2275–2280, 2010.

[129] Y. Tsunemitsu, S. Matsumoto, Y. Kazama, J. Hirokawa, and M. Ando, “Reduction of aperture blockage in the center-feed alternating-phase fed single-layer slotted waveguide array antenna by e- to h-plane cross-junction power dividers;,” *Antennas and Propagation, IEEE Transactions on*, vol. 56, no. 6, pp. 1787–1790, 2008.

[130] S. Park, Y. Tsunemitsu, J. Hirokawa, and M. Ando, “Center feed single layer slotted waveguide array,” *Antennas and Propagation, IEEE Transactions on*, vol. 54, no. 5, pp. 1474–1480, 2006.

[131] K. Hashimoto, J. Hirokawa, and M. Ando, "A post-wall waveguide center-feed parallel plate slot array antenna in the millimeter-wave band," *Antennas and Propagation, IEEE Transactions on*, vol. 58, no. 11, pp. 3532–3538, 2010.

[132] J. Hirokawa, "Analysis and fabrication of millimeter-wave slotted waveguide array antennas," in *Electromagnetic Theory (EMTS), 2010 URSI International Symposium on*, pp. 906–909, 2010.

[133] J. Hirokawa, M. Zhang, Y. Miura, and M. Ando, "Double-layer slotted waveguide array antennas with corporate-feed by diffusion bonding of laminated thin metal plates," in *Antennas and Propagation (EuCAP), 2010 Proceedings of the Fourth European Conference on*, pp. 1–5, 2010.

[134] R. Elliott and L. Kurtz, "The design of small slot arrays," *Antennas and Propagation, IEEE Transactions on*, vol. 26, no. 2, pp. 214–219, 1978.

[135] R. Elliott, "An improved design procedure for small arrays of shunt slots," in *Antennas and Propagation Society International Symposium, 1983*, vol. 21, pp. 297–300, 1983.

[136] R. Elliott and W. O'Loughlin, "The design of slot arrays including internal mutual coupling," *Antennas and Propagation, IEEE Transactions on*, vol. 34, no. 9, pp. 1149–1154, 1986.

[137] S. Rengarajan and D. Nardi, "On internal higher order mode coupling in slot arrays," *Antennas and Propagation, IEEE Transactions on*, vol. 39, no. 5, pp. 694–698, 1991.

[138] K. Sakakibara, Y. Kimura, A. Akiyama, J. Hirokawa, M. Ando, and N. Goto, "Alternating phase-fed waveguide slot arrays with a single-layer multiple-way power divider," *Microwaves, Antennas and Propagation, IEE Proceedings*, vol. 144, no. 6, pp. 425–430, 1997.

[139] S. Park, Y. Okajima, J. Hirokawa, and M. Ando, "A slotted post-wall waveguide array with interdigital structure for 45 deg; linear and dual polarization," *Antennas and Propagation, IEEE Transactions on*, vol. 53, no. 9, pp. 2865–2871, 2005.

[140] W. Hong, J. Xu, Q. Lai, and P. Chen, "Design and implementation of low sidelobe slot array antennas with full and half mode substrate integrated

waveguide technology," in *Microwave Conference, 2007. European*, pp. 428–429, 2007.

[141] Z. Chen, W. Hong, Z. Kuai, J. Chen, and K. Wu, "Circularly polarized slot array antenna based on substrate integrated waveguide," in *Microwave and Millimeter Wave Technology, 2008. ICMMT 2008. International Conference on*, vol. 3, pp. 1066–1069, 2008.

[142] J. Xu, W. Hong, P. Chen, and K. Wu, "Design and implementation of low sidelobe substrate integrated waveguide longitudinal slot array antennas," *Microwaves, Antennas Propagation, IET*, vol. 3, no. 5, pp. 790–797, 2009.

[143] A. Petosa and A. Ittipiboon, "Dielectric resonator antennas: A historical review and the current state of the art," *Antennas and Propagation Magazine, IEEE*, vol. 52, pp. 91 –116, Oct. 2010.

[144] R. D. Richtmyer, "Dielectric resonators," *Journal of Applied Physics*, vol. 10, pp. 391 –398, Jun. 1939.

[145] A. Petosa, *Dielectric Resonator Antenna Handbook*. Artech House Publishers, 2007.

[146] M. Gastine, L. Courtois, and J. Dormann, "Electromagnetic resonances of free dielectric spheres," *Microwave Theory and Techniques, IEEE Transactions on*, vol. 15, pp. 694 –700, Dec. 1967.

[147] O. Sager and F. Tisi, "On eigenmodes and forced resonance-modes of dielectric spheres," *Proceedings of the IEEE*, vol. 56, pp. 1593 – 1594, Sept. 1968.

[148] S. Long, M. McAllister, and L. Shen, "The resonant cylindrical dielectric cavity antenna," *Antennas and Propagation, IEEE Transactions on*, vol. 31, pp. 406 – 412, May 1983.

[149] M. McAllister, S. Long, and G. Conway, "Rectangular dielectric resonator antenna," *Electronics Letters*, vol. 19, pp. 218 –219, Mar. 1983.

[150] M. McAllister and S. Long, "Resonant hemispherical dielectric antenna," *Electronics Letters*, vol. 20, pp. 657 –659, Aug. 1984.

[151] K. M. Luk and K. W. Leung, eds., *Dielectric Resonator Antennas*. Research Studies Press, 2002.

[152] R. K. Mongia and P. Bhartia, “Dielectric resonator antennasa review and general design relations for resonant frequency and bandwidth,” *Int. J. Microw. Mill.-Wave Comput.-Aided Eng.*, vol. 4, p. 230247, 1994.

[153] Y. Gao, B.-L. Ooi, W.-B. Ewe, and A. Popov, “A compact wideband hybrid dielectric resonator antenna,” *Microwave and Wireless Components Letters, IEEE*, vol. 16, pp. 227 – 229, Apr. 2006.

[154] R. Kumar Mongia and A. Ittipiboon, “Theoretical and experimental investigations on rectangular dielectric resonator antennas,” *Antennas and Propagation, IEEE Transactions on*, vol. 45, pp. 1348 –1356, Sept. 1997.

[155] D. Kajfez and P. Guillon, eds., *Dielectric resonators.* Norwood, MA: Artech, 1986.

[156] Y. Antar and D. Guha, “Composite and hybrid dielectric resonator antennas: Recent advances and challenges,” in *Radio Science Conference, 2006. NRSC 2006. Proceedings of the Twenty Third National*, vol. 0, pp. 1 –7, Mar. 2006.

[157] R. Mongia, “Theoretical and experimental resonant frequencies of rectangular dielectric resonators,” *Microwaves, Antennas and Propagation, IEE Proceedings H*, vol. 139, pp. 98 –104, Feb. 1992.

[158] J. Van Bladel, “On the resonances of a dielectric resonator of very high permittivity,” *Microwave Theory and Techniques, IEEE Transactions on*, vol. 23, pp. 199 – 208, Feb. 1975.

[159] J. Van Bladel, “The excitation of dielectric resonators of very high permittivity,” *Microwave Theory and Techniques, IEEE Transactions on*, vol. 23, pp. 208 – 217, Feb. 1975.

[160] M. Wyville, A. Petosa, and J. Wight, “Dig feed for dra arrays,” in *Antennas and Propagation Society International Symposium, 2005 IEEE*, vol. 2A, pp. 176–179 vol. 2A, 2005.

[161] S. E. Miller, “Coupled wave theory and waveguide applications,” *Bell System Technical Journal*, vol. 33, pp. 661 – 719, May 1954.

[162] A. Al-Zoubi, A. Kishk, and A. Glisson, “A linear rectangular dielectric resonator antenna array fed by dielectric image guide with low cross polarization,” *Antennas and Propagation, IEEE Transactions on*, vol. 58, no. 3, pp. 697–705, 2010.

[163] M. Birand and R. Gelsthorpe, "Experimental millimetric array using dielectric radiators fed by means of dielectric waveguide," *Electronics Letters*, vol. 17, no. 18, pp. 633–635, 1981.

[164] C. L. Dolph, "A current distribution for broadside arrays which optimizes the relationship between beam width and side-lobe level," *Proceedings of the IRE*, vol. 34, no. 6, pp. 335–348, 1946.

[165] T. Taylor, "Design of line-source antennas for narrow beamwidth and low side lobes," *Antennas and Propagation, Transactions of the IRE Professional Group on*, vol. 3, no. 1, pp. 16–28, 1955.

[166] A. Villeneuve, "Taylor patterns for discrete arrays," *Antennas and Propagation, IEEE Transactions on*, vol. 32, no. 10, pp. 1089–1093, 1984.